ABSTRACT

Title of Thesis: CHARACTERIZATION OF PORE STRUCTURE AND CRACK PROPAGATION IN CONCRETE USING X-RAY COMPUTED TOMOGRAPHY

Opio Konata Hunter, Master of Science, 2004

Thesis directed by: Professor Amde M. Amde, PhD
Department of Civil and Environmental Engineering

This thesis utilized the method of computed tomography to quantify the pore structure and the development of cracks in concrete specimens due to delayed ettringite formation. The pore structure is responsible for the passage of harmful substances through the concrete matrix, while delayed ettringite formation causes expansion and internal cracking in concrete structures; particularly in prestressed and precast concrete elements. Computed tomography is a relatively new technique that can be utilized to determine the pore structure and crack propagation in concrete specimens within the mm to micrometer range.

The experiment was successful in quantifying the pore structure in the specimens. The pore sizes and total porosity of each specimen were determined along with the pore size distribution on diameter and volume. A comparison was then made with the mercury intrusion porosimetry technique. However, the second objective of analyzing internal cracking due to delayed ettringite formation was not met.

CHARACTERIZATION OF PORE STRUCTURE AND CRACK PROPAGATION IN CONCRETE USING X-RAY COMPUTED TOMOGRAPHY

by

Opio K. Hunter

Thesis submitted to the Faculty of the Graduate School of the
University of Maryland, College Park in partial fulfillment
of the requirements for the degree of
Master of Science
2004

Advisory Committee:

Professor Amde M. Amde, Advisor
Professor Chung C. Fu
Professor Mohamad S. Aggour

TABLE OF CONTENTS

LIST OF FIGURES

LIST OF TABLES

LIST OF ABBREVIATIONS AND SYMBOLS

DEF .....Delayed Ettringite Formation

CT .....Computed Tomography

MIP .....Mercury Intrusion Porosimetry

ASTM .....American Society for Testing and Materials

SEM .....Scanning Electron Microscopy

QXRD .....Quantitative X-ray Diffraction

C-S-H .....Calcium Silicate Hydrate

C_3S .....Tricalcium Silicate

C_2S .....Dicalcium Silicate

C_3A.....Tricalcium Aluminate

C_4AF .....Tetracalcium Aluminoferrite

CH.....Calcium Hydroxide

w/c.....Water to Cement Ratio

BS.....British Standards

ASR.....Alkali Silica Reaction

θ.....View angle of X-Ray

t .....Impact Parameter with respect to fixed Cartesian coordinates

$P(\theta,t)$ .....Projection Measurement of the Sample along the X-ray's Path

I_o .....Incident Intensity

I .....Final Intensity

s.....Distance between the X-ray Source and the detector

F(x,y) .....Arbitrarily Defined Function with respect to Cartesian coordinates

μ .....Linear Attenuation Coefficient

ρ.....Electron Density

Z .....Effective Atomic Number

E .....Energy of the Incoming X-ray beam

a.....Quantity with a relatively small Energy Dependence

f_i .....Fraction of the Total Number of Electrons Contributed by Element i

Z_i.....Atomic Number of Element i

Bpp.....Bits per pixel

CHAPTER 1

Introduction

1.1 General

It has become quite commonplace for the service life of concrete structures to be significantly reduced from its intended life span. Effectively, structural retrofit programs are set forth much earlier than anticipated. However in more recent times, inaccurate structural designs or structural instabilities are rarely the cause. The failure of concrete to perform at its design standards (due to a breakdown of its properties) is a durability issue.

The rate in which substances are allowed to pass through the concrete pores will determine its durability, this is known as the permeability of concrete. Therefore one way in maintaining a durable structure is by keeping its permeability low. Concrete is a non-homogeneous material, made up of two different pore systems, gel pores and capillary pores. These pores have a continuum of sizes with very irregular geometry. Gel pores, which are inherent in the cement mix are very small, and have little to do with the porosity. The permeability is dependent on the capillary pores which are remnants of water filled spaces that exist between partially hydrated cement grains.

A major concern in the concrete industry is the passage of extraneous substances via fluids or gasses through the capillary pore systems. One of the focuses of this paper is to determine the porosity and pore size distribution of this type of pore system. Some of the major deteriorating processes in concrete are caused by physical or chemical damage. Where these types of attacks are identified, they are almost always due to the passage of fluids or gasses through the concrete matrix.

Sulfate attack, attacks by acids and bases, and leaching are a few common chemical attacks, while the freezing and thawing cycle is the most pronounced physical attack on concrete structures. The determining factor on the level of chemical or physical attack on a structure would be the environment in which it is placed. Concrete structures situated along the coastal regions, or out at sea will be subjected to chloride attack. Similarly concrete members that are in contact with the ground, for example retaining walls foundations will be subjected to sulfate attack.

It is important to note that whether chemical or physical attack, the most severe problems are the ones that produce internal cracking in concrete. The development of internal cracking is a major cause of premature concrete degradation. There are many processes that can be responsible for the internal cracking of concrete in the field and includes; alkali-aggregate reaction, corrosion, delayed ettringite formation (DEF), sulfate attack, the freeze/ thaw cycle, and carbonation of concrete.

Observing internal cracking caused by DEF is the other focus of this thesis. While there is a general consensus in the concrete industry on the mechanisms that are responsible for the other process, the factors affecting DEF are not quite clear.

Some researchers attribute the destruction of heat-cured concrete to the growth of ettringite crystals in microcracks, which in turn causes the expansion. Other researchers suggest that it is the expansion of the cement paste due to the formation of ettringite that causes cracking in the concrete. They believe that the increase of the ettringite itself could not produce sufficient pressure for expansion. This debate indicates that continued research is necessary to provide a more comprehensive theory on the mechanisms affecting delayed ettringite formation.

1.2 Ettringite

Ettringite naturally forms during the early stages of the hydration process, while the cement is still in a fluid state. It is a very complex mineral and is formed due to the interactions of calcium, aluminum and sulfate in the cement. Formation of ettringite greatly influences some of the properties of the fresh cement paste, and of the hardened concrete, such as strength, durability, and setting time. The early formation of ettringite is not harmful and does not produce any problems in the concrete. However, ettringite may decompose and reform in concrete months, even years later, this is what is what is referred to as delayed ettringite formation (DEF) or secondary ettringite formation. It is generally believed that the formation of DEF can cause expansion in concrete. Many experiments have shown that when cement pastes, mortar, and concrete are first exposed to high temperatures during curing and consequently exposed to moist conditions, they exhibit expansion and cracking. Similar results are also found in concrete that has a high sulfate content in the cement mix. After investigating the deteriorated concrete samples by optical microscopy and scanning electron microscopy (SEM), ettringite has been found to form around aggregates in the concrete, and also to fill in between spaces in the cracks.

1.3 Concrete Background

In the simplest of terms, concrete is made up of cement, water, fine aggregate (sand), and course aggregate (gravel). These components are mixed together in certain proportions to optimize cost, strength, workability and durability.

Cement is a hydraulic material with adhesive properties. This means that when it is added to water, a chemical reaction occurs which allows it to bond mineral fragments into a compact unit (Neville 1996). Portland cement is the type of hydraulic cement that is used universally, and its principal constituents are silicates and aluminates of lime.

Aggregates comprise 70-80% of the volume of concrete, and costs much less than cement. In contrast to cement paste, aggregates are more durable, and possess a higher volume stability. Aggregates are classified by gradation/ particle size distribution, which is determined by a sieve analysis. The No. 4 sieve separates course and fine aggregates in that course aggregates are retained on it while fine aggregates pass through.

There is no explicit stipulation for the water used in the concrete mix; however the quality of the water is important. Impurities in the water can corrode rebars, have an adverse effect on the strength of the concrete, and also influence the setting time of the cement. The mix water should be free from harmful organic compounds or any excessive amounts of inorganic substances.

Conventional theory specifies that Portland cement needs 28 days for its complete hydration and hence maximum strength development. However to achieve this, concrete has to be cured in an appropriate surrounding during the early stages of hardening. Curing is achieved by providing an environment that will promote the hydration of cement products by controlling the temperature and humidity around the concrete. Uneven hydration will occur in concrete if a controlled environment is not maintained. This will result in pockets of unreacted cement grains in the concrete, and hence a lower strength development.

Admixtures are another important component in concrete. While not as essential as cement, water and aggregate, admixtures are often placed in the concrete mix to offer extra protection to the hardened concrete. An admixture is a compound that is substituted for a portion of the cement in the concrete mix. Its purpose is to achieve a specific modification of the normal properties of concrete. The use of admixtures in the concrete mix has become a standard practice and has been proven to achieve considerable physical and economic benefits in regards to concrete.

1.4 Problem Statement

The reduction in durability of concrete members is the overall problem being addressed in this report. The emphasis is directed on precast and prestressed elements which are typically employed in bridge, highway and parking structures. The two specific problems being addressed are highlighted below:

- One of the major concerns with concrete structures is the porosity. Many of the extremely degenerative concrete mechanisms develop through the pore system formed. Therefore understanding the nature of the pore structure formation under similar conditions as applied to prestressed and precast concrete is necessary, and is one of the focuses of this research.
- The expansion and internal cracking caused by the delayed ettringite formation significantly reduces the durability of concrete structures. Delayed ettringite formation has initiated the premature deterioration of many prestressed and precast concrete elements including bridge girders, railway sleepers and cladding panels. DEF is a universal problem as many countries have reported this type of

damage in bridge elements. However the processes that influence the formation of ettringite are not fully understood and researchers have proposed many different theories on the causes of DEF. The other focus of this research is to observe and quantify internal cracks due to ettringite formation.

1.5 Research Approach

This report is a continuation of an experiment undertaken my Azzam 2002, where the main purpose was to create different environments in which ettringite is believed to flourish, and investigate the extent of its formation. The paper presented here is not specifically focused on ettringite, but on the development of voids in the concrete. These voids are present as cracking due to ettringite, or as pores caused by cement hydration. Factors affecting both will be discussed extensively.

Computed tomography was utilized because it presents a visual representation of the interior of samples which allows the researcher to distinguish between the different shapes and sizes of pores in a concrete structure. The technology can also provide a three dimensional analysis of any solid object, an accomplishment that was previously unattainable with other methods used in determining pore structure.

Type of aggregate, cement chemistry, concrete curing and environmental conditions have been recognized as potential causes for DEF, these issues will also affect the type of pore system developed in concrete. Microcracks, exposure to moist conditions after heat-treatment and mobile sulfate release from calcium silicate hydrate (C-S-H) have been identified as essential for DEF damage to concrete, and are provided through the Dugan test method. The Dugan test was designed to provide a rapid indication of

potential for the generation of excessive ettringite in a Portland cement concrete mix design in a shortened time period. The experiment was done in two series; series one consisted of four concrete specimens while series two had three samples. All the concrete samples were exposed to a modified Dugan test described later in this report.

1.6 Objectives and Scope

The research presented in this report utilizes the relatively new technique of x-ray microtomography to quantify the pore structure of concrete. This is done by determining the pores sizes, the porosity and the pore size distribution of the specimens. In particular, the effects of aggregate type, curing condition, potassium content and admixtures on the pore structure of concrete were investigated.

Identifying and observing the internal cracking caused by ettringite formation is another objective of this experiment.

CHAPTER 2

The Chemistry of Cement

2.1 Introduction

The previous chapter gave an overview of the components used in the concrete mix, and the purpose of each component. This chapter intends to provide a more in-depth explanation of the chemistry of the cement mix, and its relevance to durability and the formation of the pore systems. The type of Portland cement used, and the mix proportions are principal factors in determining the type of barrier characteristics developed in concrete. The proportion of the components in the concrete mix and their properties controls the initial pore structure of the concrete, while the hydration process as influenced by curing conditions controls the final pore structure. These issues are explored in detail in the following sections.

2.2 Manufacture of Cement

It is important to review the raw materials that comprise the cement, and of the processes involved in its manufacture. This will allow a better understanding of the overall behavior of the cement, namely the chemical nature of the hydration process, the subsequent compound formations and the physical structure of the hardened cement paste. All of which are necessary to properly explain the pore structure formation in cement.

2.2.1 Raw Materials

Cement is manufactured from any naturally occurring calcium carbonate containing (calcareous) material, and a clayey (argillaceous) material. The calcium carbonate ($CaCO_3$) is considered the primary material, as it is the principal source of calcium oxide (CaO) which contributes 62-67% of oxides by weight in the finished product. All forms of limestone, chalk, marble, shell deposits and calcareous muds are perfect examples of a primary raw material. The use of a primary raw material will depend mainly on its bulk availability, and the feasibility of setting up a plant in a particular location. However, other considerations are crystal size, porosity and hardness. Soft materials can be easily excavated, and would not require any preliminary process before being sent to the plant, whereas hard materials would need to be blasted and crushed before it can be ready for use. Trace amounts of iron oxide (Fe_2O_3) and carbon are sometimes found in the raw materials.

The argillaceous component being different types of clay minerals is the principal source of silica (SiO_2). Chemically, clays are iron bearing aluminum silicates containing water in their crystal structure, and normally possessing trace elements of potassium, sodium and magnesium. Clay minerals are therefore also source elements of Al_2O_3, and Fe_2O_3 with K_2O, Na_2O and MgO as minor impurities. Clays and silts are preferred for use as a raw material because their particles are already finely divided. Clays that contain a mixture of two layer minerals of the Kaolinite group, and three layer minerals of the Illite and montmorillonoid (swelling clays) group are usually used. The criterion that determines the usefulness of the clay in the manufacture of cement is its cat-ion exchange capacity (Worrall 1969, 1986). Shales are sometimes used as a source of silica if the

sulphur and alkali levels are not too high. Marl, can also be used because it is made up of both a clayey and a calcareous material.

Sometimes it is necessary to add iron oxide from an external source whenever the raw materials fail to yield an adequate amount. When this is necessary, iron oxide is usually added in the form of iron pyrite cinders (Bye 1999).

Note that all the sources of silica previously discussed are not pure forms of silica, they all contain iron and aluminum oxides. These oxides can lead to durability problems and abnormal setting in cement, and does not contribute to the strength capabilities of the cement. Quartz, which is one of the pure sources of silica in nature, is not used because it will increase the burning temperature of the feed in the kiln. Iron and aluminum oxides are used as fluxing agents which allows the raw materials to fuse together at a lower temperature, resulting in a more economical process.

2.2.2 The Process

There are two processes that can be used in the manufacture of the cement, a wet and a dry process. In the wet process, significant volumes of water are mixed separately with each raw material creating slurries that are then blended to get the correct proportions. However an excessive amount of energy is required with this process thus it is no longer utilized in modern cement plants, and a more economical dry grinding process is employed. The main difference between the two is that water is used in the wet process to help break down the material while in the dry process better grinding procedures are employed.

Essentially the raw materials are crushed and mixed together in specific proportions; this mixture is then sent into a slowly rotating, inclined kiln to be burned at 1450° C. It is here that a chemical reaction occurs, and the material then sinters and fusses into balls of 3 to 25mm in diameter, known as clinker. The clinker is then sent through a cooling chamber then into a ball mill, where a small percentage of gypsum is added to it. The clinker and gypsum goes through a series of grinding processes until a fine powder remains. The resulting product is known as Portland cement.

The name Portland cement comes from the resemblance of the hardened cement to the Portland stone quarried at Dorset, England. Joseph Aspdin patented the name in 1824, and was originally used to refer to cement made from finely divided clay and limestone that was heated in a furnace until carbon dioxide is given off. Note that this temperature is much lower than necessary for clinkering to occur. The name Portland cement has remained even though gypsum is added after burning, and the process is now more refined. (W.E Worall 1986, G.C Bye 1999)

2.3 The Composition of Cement

It is also essential to discuss the different phases that have been created, in terms of the compounds formed rather than on the oxides produced during the manufacture of Portland cement. Reason being, all chemical reactions and processes that occur with cement are best explained in terms of its major compounds.

2.3.1 Equilibrium of Products

The raw materials that are burnt form a series of very complex compounds that reaches a state of equilibrium in the kiln. From phase equilibrium analysis it has been determined that the rate of cooling of the clinker will affect this equilibrium. In modern cement plants the cooling of the clinker is too rapid for complete crystallization to occur. This cooling process in effect destroys equilibrium. However, in calculating the composition of the cement products, it is assumed that the cooled material duplicates the state of equilibrium of the clinker at high temperatures. Essentially, it is taken that complete crystallization occurs, and the actual volumes of oxides that are produced in the clinker are used to calculate the composition of the cement. (F.M Lea 1970).

2.3.2 Main Compounds

There are four compounds that are generally considered to be the major constituents of cement. These are Tricalcium Silicate ($3CaOSiO_2$), Dicalcium Silicate ($2CaOSiO_2$), Tricalcium Aluminate ($3CaOAl_2O_3$), and Tetracalcium Aluminoferrite ($4CaOAl_2O_3Fe_2O_3$). The shorthand notation used by cement chemists as an abbreviation for these oxides are (C_3S, C_2S, C_3A, C_4AF) respectively. It should be noted that the silicates in cement are not pure compounds and have oxides in solid form. These oxides will also affect the performance of the cement, and should not be overlooked.

2.3.3 Proportioning of the Compounds

The actual proportion of the different compounds varies, and depends on the quantity of the raw materials, and also the cooling temperature of the cement during

manufacture. Work done by R.H. Bogue led to the invention of a method to calculate the composition of Portland cement, and is known as “Bogue Composition” (R.H Bogue 1955). Calculation using Bogue equations overestimates the C_2S and underestimates the C_3S. This happens because some of the calcium oxide found in C_3S is replaced by other oxides; as previously stated, pure silicates do not occur as the finished product of manufacture.

There have been advances in cement research which modifies Bogue’s equations, this work was done by Taylor, which takes into account the presence of substituent ions in the nominally pure main compounds for the rapidly cooled clinkers produced in modern cement plants. (Taylor 1989)

2.4 Hydration of Cement

The hydration of the cement compounds is probably the most important concept in understanding the chemistry of the cement and its controls. Cement hydration involves the setting and hardening of the hydrated products, the heat evolution during the different stages of hydration and the eventual pore filling effect of the concrete. The size and amount of these pores that remain after hydration will affect durability, and since durability is the overall focus of this paper, a thorough understanding of this concept is necessary.

2.4.1 Hydration Products

Cement goes through a chemical reaction when combined with water to produce a bonding material. Effectively, the silicate, aluminate and ferrite compounds decompose,

forming products of hydration in the presence of water. These hydrates will harden with time, gaining strength as it forms into a firm mass. The hydration products are calcium silicate hydrate (C-S-H), calcium hydroxide (CH), and calcium sulfoaluminate hydrates. The reactions representing the hydration of Portland cement have been proven by many researchers to be chemically similar to the hydration of the individual compounds under comparable conditions. Therefore the hydration of each compound can be considered separately. It is understood however that interactions between hydrating compounds is possible, but the overall reactions are generally the same (Steinour 1952, Bogue and Lerch 1934).

Different kinds of pores and solids form at different stages during hydration. The processes that take place during cement hydration in the first 24hours should be given special attention, because they determine the fluidity of the paste, the setting and beginning of hardening. As will be shown, all of these factors contributed to the development of the pore structure.

2.4.2 Hydration of Tricalcium Silicate and Dicalcium Silicate

The C_3S and the C_2S are the two main cementitious compounds in cement, and the physical behavior of the overall cement during hydration is contributed to that of only these two compounds, (Flint and Wells 1934, Neville 1996). Both the C_3S and the C_2S react with water to produce C-S-H and CH in different proportions, the C-S-H is the compound responsible for the strength characteristics in concrete. However the C_3S hydrates much faster and is therefore responsible for the strength in the early stages of hydration, within the first few days and weeks. The C_2S takes a much longer time to

hydrate and is responsible for long term development of strength, taking months or years. The equations representing the hydration of the two silicates are:

$$2C_3S + 6H \rightarrow C_3S_2H_3 + 3CH \quad \text{……...…….2.1}$$

$$2C_2S + 4H \rightarrow C_3S_2H_3 + CH \quad \text{……2.2}$$

Both the C_3S and the C_2S require approximately the same amount of water for hydration, however the C_3S produces more than twice as much CH than that of C_2S. Considering the reactions individually, the ratio of the amount of C-S-H to CH produced in the C_3S reaction is about 3 to 2 (Equation 2.1); whereas the ratio is 5 to 1 in the C_2S reaction (Equation 2.2) (Neville 1996).

2.4.3 Hydration of Tricalcium Aluminate and Tetracalcium Aluminoferrite

When C_3A reacts with water a condition known as flash setting occurs, this is due to the rapid and excessive formation of calcium aluminate hydrates. This reaction causes the concrete to form too fast which is undesirable. The hydration is as follows:

$$C_3A + 21H \rightarrow C_4AH_{13} + C_2AH_8 \quad \text{……2.3}$$

Gypsum is added to aid in the hydration of C_3A. The gypsum slows down the reaction between C_3A and water by producing calcium sulfoaluminate hydrate (ettringite) which builds up as a layer on the C_3A impeding hydration and is shown as:

$$C_3A + 3C\bar{S}H_2 + 26H \rightarrow C_6A\bar{S}_3H_{32} \quad \text{……2.4}$$

When all the gypsum has been used up, the ettringite layer is no longer stable, and another reaction takes place. The ettringite reacts with C_3A to produce monosulfoaluminate, with the hydration as follows:

$$2C_3A + C_6A\bar{S}_3H_{32} + 4H \rightarrow 3C_4A\bar{S}H_{12} \quad \text{.....2.5}$$

In essence the C_4AF will give a similar type of reaction as C_3A, however since it is much less reactive it will only come in contact with a small amount of gypsum. C_4AF reacts with water in the presence of gypsum to produce calcium sulfoferric as well as calcium sulfoaluminate (Neville 1996, Young 2002)

2.4.4 Rate of Hydration and Heat Evolution

The hydration of cement compounds is exothermic, liberating energies of up to 500J/g of cement. The hydration process does not progress at a steady rate or even a steadily changing rate, nevertheless it can be followed by observing the rate of evolution of heat during the early stages. Some researchers have broken down the hydration process in five different stages. A typical plot of the rate of heat evolution against time is shown in Figure 2.1.

The order in which the compounds react is C_3A, C_3S, C_4AF, and then C_2S. A large liberation of heat is shown during the first stage. This is due to the initial wetting and hydration at the surface of the cement particles, which elapses within a few minutes. The high heat of hydration observed is due mainly because of the C_3A and C_3S and to a lesser extent the C_4AF and C_2S. When ettringite is liberated it forms a layer around the surface of the C_3A essentially preventing its reaction. At the same time the ions of the C_3S are diffused in solution with hydroxide ions. This gives rise to stage II, the dormant period in which cement is fluid and workable; this stage lasts for one or two hours.

The reason for the occurrence of a dormant stage is that a sufficient amount of ions has to be liberated before the hydration products of CH and C-S-H can be formed.

When enough ions have been produced, the hydration of C_3S proceeds once again with the CH crystallizing from solution and C-S-H forming around the surface of the C_3S. This is the beginning of Stage III. As identified in Figure 2.1, the hydration of C_3S continues slowly and the rate of heat evolved increases gradually and typically reaches a maximum at an age of 10hours. As hydration continues, the C-S-H layer gets thicker and provides a barrier from which ions must pass through to get to growing crystals. Water must also penetrate this barrier to get to the unreacted cement grains (Young 2002). The ending of stage three is signified by the peak of the rate of heat evolved as shown in Figure 2.1.

In stage IV, the hydration of the C_3S has slowed down hence a reduction in the amount of heat evolved; more importantly the gypsum content is proportioned to be depleted in this stage and is responsible for the third peak in Figure 2.1. This peak is caused by the renewed reaction of C_3A with ettringite as represented by Equation. 2.5, and would occur in concrete somewhere between the ages of 18 to 30hrs.

After this point, the rate at which cement hydrates decreases continuously, and even after long time periods there exists appreciable amounts of unreacted cement grains.

Experiments have shown that after 28 days of being in contact with water, the cement grains have been shown to hydrate to a depth of 4µm, and 8µm after a year (Giertz-Headstrom 1939). Under normal conditions 100% cement hydration is unattainable. However for cements with grain sizes smaller than 50µm this can be achieved, if the cement is continually grinded in water for five days (Powers 1949).

The C_2S and C_4AF are much less reactive compounds and after the initial heat liberation in stage I, their contribution diminishes greatly. These compounds take a much

longer time to hydrate, and for this reason the physical properties of cement are taken at an age of 28 days. It is said that hydration still continues after this point, however the changes in physical properties are very minute.

2.5 Calcium Silicate Hydrate

2.5.1 Morphology

The composition of the calcium silicate hydrate formed during the hydration of cement varies, and causes difficulty in defining its structure. Notice that the formula of $C_3S_2H_3$ given in eqn 2.1 is only approximate, and its stoichiometry will depend on the mix design procedures, curing conditions, impurities, and age of the hydrated cement. Therefore the convention is to write C-S-H which has been utilized in this report.

Another difficulty faced with defining its structure is that the C-S-H particles are so finely divided that even with the more recent techniques a definite structure can not be established. These techniques include scanning electron microscope (SEM) and energy dispersive X-ray spectrometer.

Since the composition of C-S-H fluctuates limiting its ability to form crystals, this allows us to define C-S-H as being amorphous. However researchers have made a more detailed classification of its structure which includes: fibrous particles, flattened particles, a rectangular network, and irregular grains, all of which are difficult to define. The predominant form is that of fibrous particles, typically ranging from 0.5 to 2µm long and less than 0.2µm across (Diamond 1976).

2.5.2 Physical Behaviors and Properties of C-S-H

As stated previously C-S-H particles are finely divided, this allows for a very high surface area in hydrated cement paste. Therefore it is the surface properties of the C-S-H that dominates its overall behavior.

The C-S-H in concrete is one of the major hydration products taking up 65% of the hydrated cement paste by volume. It provides the major cohesive force that binds everything together. 90 to 95% of the strength of hardened cement paste is supplied by the C-S-H.

2.6 Calcium Hydroxide

2.6.1 Morphology

The structure of calcium hydroxide is much more easily defined than C-S-H, it is made up of well-crystallized particles having an exact composition. Its chemical formula is $Ca(OH)_2$, but abbreviated as CH. The crystals that grow within body of the cement paste can be characterized as having a crystalline structure which may vary from large flat platy crystals to large thin elongated crystals. This morphology is affected by admixtures and temperature of hydration. Crystals will also grow in voids known as capillary pores. These crystals have a distinct hexagonal shape and are sometimes large enough to be seen by the naked eye (Young 2002).

2.6.2 Physical Behavior and Properties

Calcium Hydroxide occupies 20-25% of the cement paste volume, and does not directly contribute to the strength of the hydrated cement paste. However it is said that its pore filling effect provides some strength gain to the hydrated cement.

The CH keeps the ph in cement high, approximately 12.5, which protects the steel in concrete from corrosion. The ph can be reduced if the CH reacts with carbon dioxide from the atmosphere to form insoluble calcium carbonate, this is known as carbonation.

2.7 Setting

It is important to distinguish the setting and hardening periods in cement hydration. Setting can be defined as the period in which the cement paste loses its fluidity to gain rigidity, whereas hardening is regarded as the gain of strength of a set cement paste. This definition implies that setting occurs before hardening. After the initial hydration has passed, where sufficient contact has been formed between the hydration products, the paste is more rigid. This stage is the setting stage, which occurs with the onset of an increase in the rate of reaction due to C_3S hydration, hence the beginning of Stage III. Both initial and final setting occurs within this stage; final setting would have occurred before the rate of heat evolved reached its maximum. At the time of final setting the rigidity would have increased to an extent where the cement paste is now a solid. This process is best followed schematically as is shown in Figure 2.2

Figure 2.2 shows the interaction of the hydration products of the cement grains, and its effect on rigidity. Although the cement is in a solid state at the point of final set, it

still has a very low strength. The strength increase after this point is now due to hardening.

2.8 Structure of Hydrated Cement

This report is based on the physical nature of the cement paste; more specifically the final structure the cement products occupy at the completion of the desired 28-day hydration. The processes described thus far have created sufficient understanding as to how the cement products interact in producing the hydrated paste. Some specifics about the final structure are outlined below.

The hydrated product consists of very poorly crystallized hydrates of various compounds, which are collectively referred to as the cement gel. The composition of which consists of the calcium silicate hydrate phase, calcium hydroxide crystals, unhydrated cement, small amount of minor impurities, and the residue of water-filled spaces in the fresh paste. These spaces are known as capillary pores, however in between the aggregated hydration products there exist smaller voids called gel pores.

2.8.1 Capillary Pores and the Pore Filling Effect

When cement is initially mixed with water it is in a fluid state, and the porosity is very high because the cement grains are separated from one another. As hydration products begin to form around the grains, a pore filling effect occurs because the hydration products occupy a larger volume than the grains. Therefore as time elapses, the gaps between the grains get smaller and the volume of the capillary system is reduced. It is these gaps that are known as capillary pores. Capillary pores represent that part of the

total volume not occupied by the products of hydration. This process can also be followed by the lower part of Figure 2.2

Other important factors that contribute to the structure of the hydrated cement include the mix proportions, namely the water to cement (w/c) ratio and the degree of hydration as controlled by curing conditions. Theses two factors will determine the actual size and length of the capillary pores formed in the concrete. Capillary pores take on different sizes, studies done by Glasser indicates that mature cement paste contains few pores larger than 1µm and most pores being smaller than 100nm (Glasser 1992).

2.8.1.1 Water/Cement Ratio

Works done by many researchers have proved that cement paste with a w/c ratio of 0.38 will produce enough hydration products to ensure that no unhydrated cement will be left or capillary pores will be present. If the w/c ratio is less than this value then complete hydration will never be achieved. However if the w/c ratio is 0.38 or higher the volume of hydration products formed will not be sufficient to fill in between gaps and there will be capillary pores left even after complete hydration.

In practice the w/c ratio is usually taken to be between 0.38 and 0.70 because within this range a discontinuous capillary pore system can be achieved, and cement paste is also more workable.

2.8.1.2 Curing of Concrete

Concrete must be properly cured if it is to develop its optimum strength and durability properties. Curing is the name given to procedures used in promoting the

hydration of cement. This includes a control of temperature and moisture movement from and into the concrete. The aim is to keep concrete saturated or as nearly saturated as possible until the water filled pores in the cement paste is filled by products of hydration.

If concrete is not cured, the w/c ratio will be disturbed due to water loss from evaporation or by absorption of water by aggregates, formwork or subgrade. If the water loss is such that it reduces the relative humidity within the capillary pores below 80%, the hydration process will be brought to an end.

2.8.2 Gel Pores

As stated earlier, the gel pores are interconnected interstitial spaces between gel particles, they are a part of the cement paste. The ability of the cement paste to take on a large volume of water and use it during hydration indicates its porous nature. The evaporation of the water occurs through these gel pores. The gel pores are much smaller than capillary pores, and takes on sizes less than 3nm in diameters.

When considering its volume percentage, it can be said gel pores take up about 30% of the total volume of cement paste. This is generally true for various cements, and unlike the capillary pores, gel pores are unaffected by the w/c ratio or the progress of hydration. This would mean that gel of similar properties is formed at each stage of hydration, and continued hydration does not affect the products already formed. As the total volume of gel increases with hydration, total volume of gel pores also increase (Neville 1996). The distinction between the Gel pores and Capillary pores can be seen from Figure 2.3.

2.9 Cement Fineness

Fineness is simply a measure of the size the cement grains in any particular cement. The size is determined by the final process in cement manufacture, the grinding stage. The size of cement particles is very important because it affects the rate of hydration of cement. The hydration process commences at the surface of the cement grains, and it is the total surface area of the cement grain that represents the material available for hydration. Therefore smaller grains will have a larger surface area per unit mass and would play a more significant role in the rate of hydration and strength development. This shows that finer particles are necessary for a faster hydration rate and a rapid strength development; however, long term strength is unaffected.

There is however a downside in having a cement with finer particles. Along with an increase in the rate of hydration comes a higher rate of heat liberation and all the problems that are associated with it. Finer cements are also more susceptible to alkali-aggregate reactions and ettringite formation. These aspects will be discussed in the next section and in chapter three.

2.10 Cement Types

Discussing the different types of cement available for use is also necessary because as will be shown, the composition of each cement type differs and different performances can be expected. The type of cement influences the degree of hydration achieved at a given age, hence the formation of pores will also be affected.

The American Society For Testing and Materials (ASTM) has designated eight different types of Portland cements, according to specification ASTM C150-02a these are

Types I,II, III, IV, V, IA, IIA, IIIA. These types are designed to meet different chemical and physical requirements. Ordinary Portland cement -Type I, is the normal, general purpose cement, suitable for various uses. It is without a doubt the most common cement in use as it accounts for 90% of the cement used in the United States and the United Kingdom. Type I cement is suited for general construction where concrete is not subjected to specific exposures from sulfates in soils or water.

Type II cement is known as moderate heat of hydration and moderate sulfate resistance. This means that the rate of heat development is lower than Type I, but with a similar rate of strength gain. In very large structures it is important to use a cement that gives off a small amount of heat in the hydration process. Therefore Type II cement is used in large piers, and heavy retaining walls and abutments. Due to the sulfate resistance of Type II cement, it is also utilized in drainage structures, where sulfate concentrations are expected to be more than average.

Type III cement is a high-early-strength cement, and causes concrete to harden and gain strength more rapidly than all other cement types. The increase in the rate of strength gain of type III cement is due to an increase in the C_3S content, and the fact that the cement is grinded more finely in the clinker. C_3S is responsible for the strength gain of cement, and is greater than 55% in type III cement. Also, the fineness of type III cement is between 450 to 600 m^2/kg while that of type I is between 300 to 400 m^2/kg (ASTM Specs). Fineness allows for a significant increase in strength at 20 hours after pouring. Type III cement is used in situations where the concrete needs to be utilized as quickly as possible, as in airport runways and roadways.

Types IA, IIA, IIIA are three air entrained Portland cements that correspond in composition to types I, II, and III respectively, however small amounts of cement is replaced by an air-entraining admixture. During the hydration process, this material mixes with the water to produce small, well distributed and separated air bubbles. This type of cement is suitable for concrete subjected to freeze-thaw action, and will include all outdoor concrete.

Type IV concrete is manufactured to produce a very low heat of hydration. This cement was developed for use in large gravity dams where the amount of heat evolved has to be kept at a minimal. Severe cracking will occur in the interior of large structures due to a rise in temperature caused by the heat development from the hydration process in cement. To achieve this lower heat of hydration, the C_3S, and C_3A contents are lowered as these compounds are the more rapidly hydrated compounds. In effect the C_2S content is increased, and is principally responsible for the strength development. Since C_2S hydrates very slowly, type IV cement will also have a lower rate of strength development.

ASTM type V cement is a sulfate resistant cement. If sulfate salts come in contact with calcium silicate hydrates in hydrated cement paste, a reaction can occur that will cause volume changes, and complete disintegration of the concrete. This is known as sulfate attack. To create sulfate resistant cement, the C_3A content is kept low so as to produce less calcium silicate hydrates. ASTM specifications on type V cement stipulates that the maximum amount of C_3A used is 5%, also that the sum of the C_4AF content and that of twice the C_3A should be kept at 25% of total composition. Type V cement is used in concrete that is expected to encounter high sulfate levels due mainly to soil or groundwater.

Other types of cements include white Portland cement, which has identical properties as ordinary Portland cement, only difference is the color. The raw materials containing iron and manganese oxides are avoided, because these minerals are responsible for the gray color in cement. White cement is sometimes requested for architectural purposes.

Blended cements and expansive cements are also available. Blended cements are obtained by mixing two or more types of cementitious materials. The primary material is Portland cement, which is blended with either blast furnace slag or a pozzolon, (ASTM C595). Expansive cements increase in volume significantly more than Portland cement during the early hydration period after setting. There are three kinds of expansive cement as defined by ASTM C 845, these are types K, M, and S. Expansive cements are used to compensate for volume decreases caused by drying shrinkage and therefore minimize cracking.

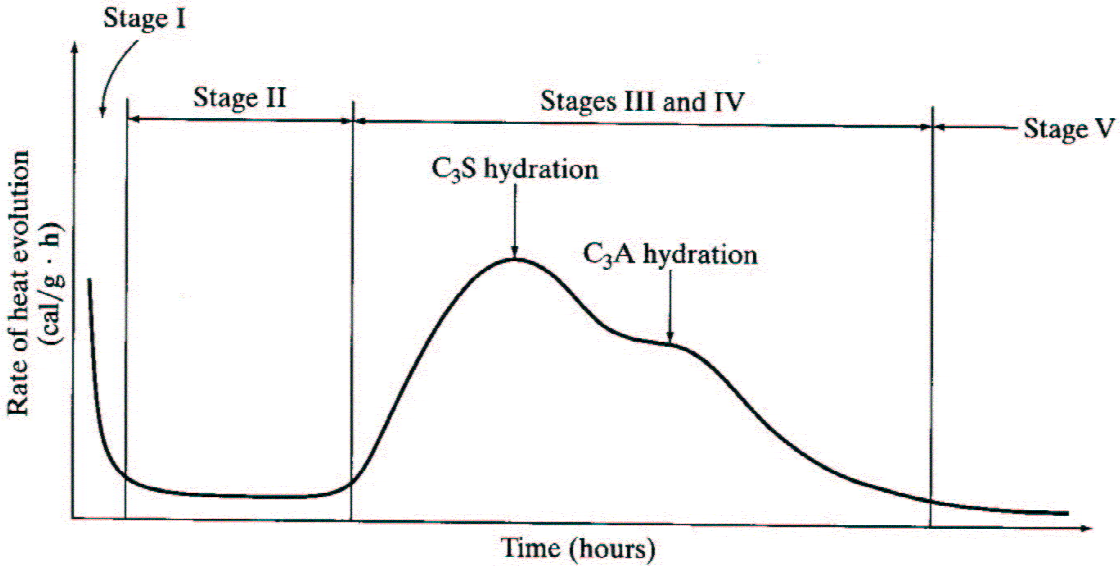

Figure 2.1 Rate of Heat Evolution Against Time During Portland Cement Hydration (After S. Mindess, D. Darwin and J.F. Young 2002)

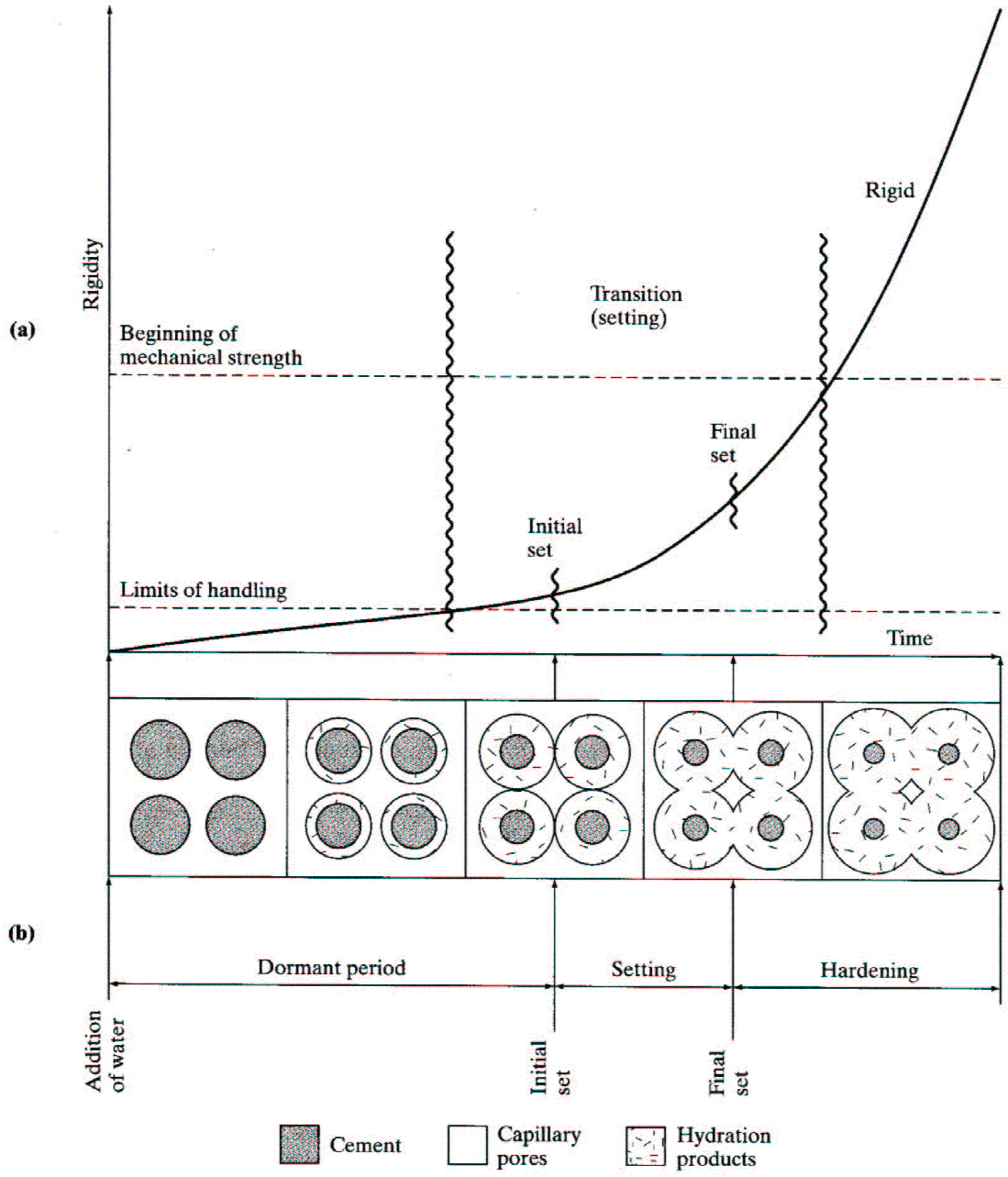

Figure 2.2 Schematic Descriptions of: (a) Setting and Hardening, and (b) Structure Formation During Cement Hydration (After R.J. Gray, J.F. Young, A. Bentur and S. Mindess 1998)

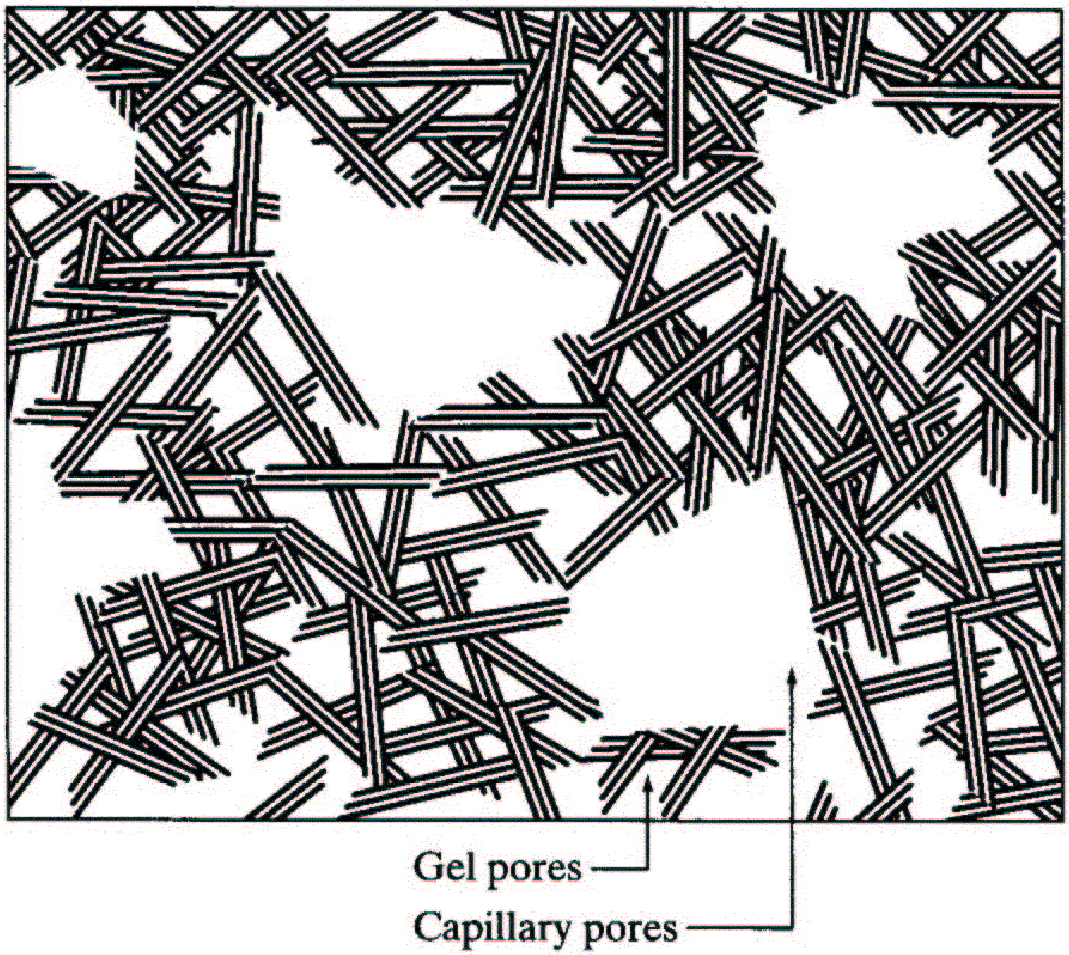

Figure 2.3 Model of the Paste Pore Structure Based on Platy Gel
(After T.C. Powers 1958)

CHAPTER 3

Processes Affecting Individual Concrete Components and Influencing Pore Structure and Delayed Ettringite Formation

3.1 Introduction

As mentioned previously, there are many factors affecting the way concrete hydrates and subsequently hardens. The nature in which concrete hydrates will certainly affect its physical properties, however we are primarily concerned with the permeability and durability of the concrete. The first chapter discussed in general some of the issues affecting concrete durability and ettringite formation, while chapter two gave a very in-depth analysis of how the chemistry of cement hydration contributes to these issues. This chapter explains the role admixtures play, which is the effect the different types have, on permeability and ettringite formation. Curing conditions and aggregate types will also contribute to the formation of the structure of the fully hydrated cement and will also be discussed here. The role that the cement type and the addition of potassium plays in the concrete specimens will be explained and should validate the overall experimental procedure that follows.

3.2 Admixtures

Admixtures are not as essential in the cement mix as compared to cement water and aggregate, however the use of admixtures have increased worldwide that it is rare to see a cement mix which contains no admixtures. Admixtures are added to a batch prior to or during the mixing of the essential materials. The term admixture should not be confused with the term addition, which is an older terminology that was used

synonymously with admixture. The two terms are not used interchangeably here and are presented as two different processes. An additive as defined by American Society for Testing and Materials (ASTM) is a material that is interground or blended in limited amounts into a hydraulic cement during manufacture either as a “processing addition” or as a “functional addition.” Processing additions are used to aid in the manufacture and handling of cement, a grinding aid or fluxing agent are examples of a processing addition and should not in theory affect the behavior of the cement. A functional addition modifies the properties of the finished cement, which is exactly what an admixture does; however the admixture is added just before mixing while the addition is added during manufacture.

The use of admixtures has increased tremendously because almost every property of concrete can be modified to some extent, imparting considerable physical and economical benefits with respect to the concrete. Although admixtures are not cheap, they do not incur additional expenditure because their use will result in enormous savings.

3.2.1 Types of Admixtures

There are a large number of admixtures available on the market, each aimed at a specific concrete property or a combination of properties and can be somewhat confusing. They can however be classified in groups which will make their analysis simpler, these groups are: air entraining agents, chemical admixtures, and mineral admixtures.

3.2.1.1 Air Entraining Admixtures

Air entraining admixtures are classified under ASTM C260-94 and British Standards BS 5075: Part 2, and are used to improve the durability of concrete by increasing its frost resistance. Concrete is very susceptible to damage due to freezing and thawing cycles, therefore air entraining admixtures should be included in any concrete that is to be exposed to such conditions. The damage of the freeze-thaw cycle is caused by internal cracking from an increase in hydraulic pressure due to freezing of the water available inside capillary pores. Air entraining agents provides additional voids in the concrete for water to move into so that damage of concrete will not occur. All entraining agents are surfactants or surface active agents which concentrate at the air water interface, lowering the surface tension, and stabilize the air bubbles formed during mixing. The molecules of surfactants repel each other preventing the bubbles from coming together and creating a uniform distribution of entrained air. The minimum volume of voids required to give effective frost resistance is 9% of the volume of mortar (Klieger 1978).

3.2.1.2 Chemical Admixtures

Chemical admixtures are covered under ASTM C494-92 and BS 5075: Part 1 and 3, and includes accelerators, water reducers and retarders. Accelerators are classified as an ASTM type C admixture, which is beneficial during cold weather concreting operations, when concrete is being placed at 2 to 4º. It is also advantageous in the manufacture of precast concrete where rapid removal of formwork is desired.

Conventional accelerators increase the rate of hydration of C_3S allowing for an earlier strength development.

It might be beneficial in certain situations to delay the rate of setting or heat evolution during cement hydration by including a retarding admixture (ASTM Type B) into the mix. This is the case when massive structures are being placed, or when concrete is being placed in hot climates. Retarders prolong the time during which concrete can be transported placed and compacted.

Water reducing admixtures are another type of chemical admixtures which as the name implies reduces the water content of the mix typically by 5 or 10%. Water reducing admixtures are used to reduce the water/cement ratio of concrete while still maintaining the desired workability. This will produce more durable concrete as lower w/c will yield less capillary pores. This type of admixture is also utilized when the “flowability” of concrete needs to be improved, as in the case where concrete is pumped. This means the workability of the cement paste has to increase while keeping w/c fixed.

3.2.1.3 Mineral Admixtures

Mineral admixtures are finely grounded solid materials added into concrete in relatively large amounts, usually 20 to 100 percent by weight of Portland cement. It is frequently used to improve the impermeability and chemical durability of the fully hardened concrete, also to increase its ultimate strength. Improvements in workability of the fresh concrete can also be obtained. The principal sources of mineral admixtures are from the waste products of certain industrial processes namely; various types of metallurgical processes, and power plants where coal and rice husk are used as fuel

(Ramachandran 1984). Nonetheless, raw or calcined natural minerals known as pozzolans are still being used as a mineral admixture. Mineral admixtures can be categorized as exhibiting either a purely pozzolanic reaction, or both a cementitious and pozzolanic reaction.

Cementitious reactions occur in materials that have hydraulic properties of their own and produce hydration products similar to that of cement, thus contributing an additional strength gain in concrete. Pozzolans are siliceous materials which inherently have no cementitious properties of their own. However they provide a source of silica which when placed in the cement mix will chemically react with the calcium hydroxide produced during cement hydration, this is known as the pozzolanic reaction. The result this effect has on the concrete is that the C-S-H content is increased at the expense of the calcium hydroxide, thereby producing stronger and more durable concrete.

The different types of mineral admixtures available include; natural or calcined materials, silica fume, blast furnace slag, fly ash, and rice husk ash. Granulated blast furnace slag, and high-calcium fly ash (containing 10-40% CaO) exhibits both cementitious and pozzolanic reactions. Although these admixtures have been used over time, not all have been recognized by ASTM as admixtures. The ASTM specification C 618 recognizes only three classes of mineral admixtures, these are:

1. Class N: Raw or calcined natural pozzolans such as diatomaceous earths, opaline cherts, clays and shales, tuffs and volcanic ashes or pumicites.
2. Class F: Fly ash produced from burning anthracite or bituminous coal
3. Class C: Fly ash normally produced from lignite or sub-bituminous coal which may contain analytical CaO contents higher than 10%.

Some of the specimens that were tested contained different percentages of Class F fly ash, the composition and effect of the fly ash in the concrete will be discussed extensively. Fly ash was chosen because it was readily available at the testing facility.

3.2.1.3.1 Source and Particle Characteristics of Fly Ash

Fly ash is the inorganic residue which is obtained from the combustion of powdered coal in power plants. During combustion the volatile matter and carbon are burned off producing energy, while the mineral impurities are fused together and quickly transferred to a lower temperature zone where it solidifies into spherical particles. Most of the solidified matter subsequently flies out in the flue gas stream, and is known as “fly ash”. It is obtained by using electrostatic precipitators to trap and remove the ash from the gas stream.

The surface properties and particle size distribution influences the behavior of fly ash in concrete and is worth reviewing. In general fly ash consists of solid glass spheres which are mostly transparent and have sizes varying from under 1µm to 100µm. However, particle size distribution shows that most of the material is made of spheres having sizes less than 20µm. Class F fly ash, appropriately called low calcium fly ash has a lower proportion of alkali sulfate impurities deposited on its surface than high calcium fly ash. This indicates why the surface area of low calcium fly ash is smaller, thus making it a superior void filler (Mehta 1983).

3.2.1.3.2 Effect of Fly Ash in the Concrete Mix

The void filling effect of fly ash in concrete is very appealing to cement users, and is one of the reasons for its popularity. This characteristic is excellent for a lean concrete mix because it is capable of improving the workability without an excessive increase in water, unlike most natural pozzolanic materials. It is expected that the X-ray tomographic results will show a reduction in the void sizes of the samples containing fly ash when compared to samples without any admixture.

As stated earlier the size of fly ash particles are less than 20 µm while those of cement are less than 45µm. This finer particle size distribution has the effect of increasing the physical properties of cement by reducing the water requirements needed for a given consistency of concrete. Thus the smaller particle sizes and surface area of the fly ash allows it to be an excellent void filler, and by virtue of this it also reduces the water requirements in the cement. A 30 percent substitution of fly ash was made for cement in a field application, and it was found to reduce the water requirements by 7 percent (Berry 1982).

Note however that only low-calcium fly ash is capable of a void filling effect and water reducing capabilities, while high-calcium fly ash, because of its higher surface area tends to have the opposite effect on concrete.

3.2.1.3.3 Effect of Fly Ash on Fresh Concrete Properties

Workability, a characteristic of fresh concrete, can be greatly improved by the inclusion of fly ash as it depends mainly on cohesiveness. The volume of the cement paste in concrete principally controls cohesiveness. Therefore whenever a replacement of

cement is made with a lower density mineral admixture such as fly ash, it has the effect of increasing the paste volume. On an equal weight basis the volume of fly ash can exceed the volume of Portland cement by 30 percent (Lane 1982), thus increasing cohesiveness and workability.

Bleeding and Segregation can also be reduced in concrete containing fly ash. The inclusion of fly ash offers smaller particles in the mix that holds the paste and aggregate particles together. Thus preventing formation of bleed water channels and reduces the risk of segregation. It would therefore be more beneficial to include fly ash in lean cement mixes or in concrete deficient in fine particles.

In general the use of mineral admixtures will result in the set retardation of the concrete, this is especially true with Class F fly ash. Initial set can be increased by at least 2 hours, and final set by 5 hours or more (Diamond, 1981). A low strength development and a low rate of heat development accompany the set retardation. These aspects will be further discussed in the following section.

3.2.1.3.4 Effect of Fly Ash on Strength and Permeability

The overall strength and permeability of concrete is adversely affected by the presence of large voids in the hydrated cement paste and microcracks in the interfacial transition zone. The use of fly ash transfers large voids into small ones, and reduces the microcracking in the interfacial transition zone.

In concrete containing no admixture, the C-S-H and the calcium hydroxide phases are very compact and do not properly fill in-between void spaces. Whenever the pozzolanic reaction as described earlier takes place, the denser calcium hydroxide phase

is converted into C-S-H of low density which fills into capillary pores and cavities (Feldman, 1981). The formation of more C-S-H essentially increases the strength while the pore filing effect increases permeability of the concrete.

The strength development due to the pozzolanic reaction of a low-calcium fly ash is not immediate, its contribution usually takes place two weeks after cement hydration has started. For this reason concrete with fly ash as an admixture has to be cured for longer periods to take into account the extra time needed for pozzolanic activity to be in effect. This is not true however for high-calcium fly ash which can be described as a highly reactive pozzolan. It seems the availability of hydroxyl, sulfate and calcium ions in the plastic cement paste triggers the hydration. Hydration takes place relatively quickly and can start after only 3 days of cement hydration (Ramachandran 1984).

3.2.1.3.5 Effect of Fly Ash on Durability

The interfacial transition zone in concrete is the region around the course aggregate separating it from the hydrated cement paste, and is responsible for durability characteristics in concrete. This region is less dense than the bulk of the hydrated paste and is sometimes classified as the weak link in concrete. Many researchers contribute this to the fact that the calcium hydroxide produced in cement hydration usually forms in the interfacial transition zone. Ordinary concrete is susceptible to microcracking in this region due to tensile stresses induced by normal thermal and humidity changes. However, the inclusion of fly ash will alter consistency and water requirements, bleeding and segregation, and also time of setting. All of these characteristics have the ability to

improve the structure and mechanical properties of cement thereby strengthening the interfacial transition zone.

3.2.1.3.6 Effect of Fly Ash on Expansion of Concrete due to Ettringite Formation

After extensive studies by Tikalsky in 1989, it was concluded that the use of any high calcium fly ash makes concrete potentially susceptible to expansion and that high-calcium fly ash should not be used when there is a risk of sulfate attack. Gress also suggested in 1997 that high-calcium fly ash might contribute to premature distress in concrete pavements due to the formation of ettringite. High-calcium fly ash has also been reported to have a higher amount of aluminum and sulfur (Diamond 1983, Tishmack 1999). Furthermore, increasing the calcium content leads to an increase in the alkali level which in turn enhances the ettringite formation (Lee 1986, 1989). This results in the overwhelming conclusion that formation of ettringite increases when class C fly ash is used.

High-calcium fly ash can reduce the permeability of concrete, the chloride diffusivity and increase the concrete's resistance to freeze/thaw cycles. However many researches have reported variations in class C fly ash hydration (Bergeson 1988, Isenberger 1981, and Schlorholtz 1993). This suggests that more research is needed in the hydration of class C fly ash.

3.3 Aggregates

Aggregates are the most predominant material utilized in the concrete mix taking up 70-80% of the volume of concrete. Therefore it is expected that its characteristics will

have a major influence on the properties of the concrete. Aggregates were once thought of as being inert materials dispersed in the cement mix for economic reasons. However an appreciation of aggregates as a building material is now the predominant view of the concrete community. As will be shown, aggregates are not inert, and their physical, chemical, and thermal properties will affect the performance of the concrete. A poor quality aggregate can severely reduce the strength and durability capabilities of the concrete. While more aggregate is placed in the concrete than cement for economical reasons, it also provides other advantages, as it is more durable than the cement paste and it increases the volume stability of the concrete.

3.3.1 Different Types of Aggregates

The most widely used aggregate type in concrete applications are natural aggregates. This includes any material that has been produced without having its particles altered by artificial means, this is exclusive of washing, crushing and sieving. Natural aggregates are derived from rocks that may contain a single mineral or many different minerals. This is called a mineralogical classification and will are outlined below.

3.3.1.1 Classification of Aggregates

Aggregates can be classified into a number of different groups, the most common being a mineralogical or petrological classification and also by specific gravity. A summary of some of the common minerals classified by ASTM C 294 is as follows:

- Silica Minerals
- Feldspar

- Ferromagnesian minerals
- Micaceous minerals
- Clay minerals
- Zeolites
- Carbonate minerals
- Sulfate minerals
- Iron sulfide minerals
- Iron oxides

In using this classification, it should be noted that no particular group or mineral type is more suitable as an aggregate than another, as unsuitable aggregate types can be found in all groups.

A more useful classification would be via specific gravity/relative density, in which aggregates are classified as heavyweight, normal weight, or lightweight. Lightweight aggregates are available as natural materials (expanded clays and shales), or as synthetic materials obtained from the by-products of industrial processes (foamed slag and sintered pulverized fuel). The criteria being that the specific gravity of these materials should be between 1.2 and 2.0. Lightweight aggregates have a density of around 70 pcf (1120 kg/m^3) and are used when the strength to weight ratio is of more significance than overall strength, for example in the construction of slabs for high rise buildings. Heavyweight materials are those with a high specific gravity value of about 3.0. This type of material is used when a high mass to volume ratio is needed, for instance in constructing radiation-shielding materials. Normal weight aggregates have specific gravity values ranging from 2.4 to 2.8 and includes materials such as natural

sands gravels and crushed stones. Normal weight aggregates have densities in the range of 95 to 105 pcf (1520 – 1680 kg/ m^3) and are used in most concrete applications. Most of the concrete produced in the United States is made with normal weight aggregates, as is the case with the samples in this experiment.

3.3.2 Typical Properties Required for Mix Design

Aggregates are particulate in nature, and its effectiveness is to a considerable extent related to the size and gradation, or size distribution, of its particles. The size of aggregate particles are generally taken as some measure of their diameters which can range from tens of millimeters to particles less than one-tenth of a millimeter. The maximum aggregate size used will vary and depends on the job function of the concrete. If the aggregate is too large at a particular cross section of a concrete element, then the member properties may not be representative of the entire material. Therefore to prevent this condition it is suggested that the maximum aggregate size should not be greater than one-fifth of the smallest dimension of the member. In any mix a variation in the size of the aggregate particles is necessary, this is known as the particle size distribution often referred to as grading.

In the manufacture of good quality concrete the grading of its aggregates should be such that it incorporates two distinct size groups, fine aggregate known as sand and course aggregate. Fine aggregates are no larger than 5mm or 3/16 in and coarse aggregates are at least 5mm or 3/16 in. The division is made by the No. 4 ASTM sieve, which is 4.75mm in size. It should be noted that the term aggregate is often used to refer to coarse aggregates in distinction to sand, this of course is not correct.

With respect to aggregates, this report is concerned with the influence that fine aggregates have on the mix design, and therefore different types of sands were used. Depending on its origin, aggregates will have various impurities that will cause devastating physical and chemical effects on concrete. The following section discusses these deleterious impurities.

3.3.3 Deleterious Substances in Aggregates

Impurities may reside in the aggregate itself or may be inherent in the environment in which it has been exposed. These substances may interfere with the bond between aggregate and the cement paste, and may also hinder the hydration of the cement in the mix. Extremely harmful process can also occur with the development of chemical reactions between the aggregate and cement paste. As a result, deleterious substances can be responsible for unstable volume changes, freeze-thaw deterioration, mechanical degradation and chemical degradation.

3.3.3.1 Organic Impurities

Aggregates derived from natural means are more inclined to contain harmful organic impurities. These impurities may delay the setting and hardening of concrete by interfering with the chemical reactions of cement hydration. A reduction in the strength capabilities and the overall degradation of the concrete can also be a result of organic impurities. Such materials are usually found in sand in the form of tannic acid and its derivatives (decay of vegetable matter), humus, peat and organic loam are known for

these impurities (ASTM C40). Coarse aggregates are less likely to have these impurities particularly when washed.

3.3.3.2 Fine Materials

Fine materials in the range of 2 to 80 µm may be present in the aggregate as loose dust, and may form a coating on the aggregate particles that will interfere with the bond between the cement paste and aggregate. Clays, sands and fine dust represents the major types of surface coatings that can cause strength reduction and durability issues in the concrete. These particles are undesirable even when they are present as loose particles in the fine aggregate and not affixed to the course aggregate. Loose particles present in excessive quantities will increase the water requirements significantly; this is due to the large surface area of finer particles.

3.3.3.3 Unsound Particles

Aggregate particles are said to be unsound if they lead to disruptive expansion from volume changes brought on by environmental changes, and also if they simply fail to maintain their integrity. The main concrete damages due to unsound particles are surface pop-outs and D-cracking in pavements. Low density materials, for example shale are regarded as unsound. If these are found near the surface of the concrete they might disintegrate or pop-out. Soft particles such as clay lumps, wood or fibrous materials, and coal are also labeled as unsound and can cause a lot of physical degradation in concrete as they affect the durability and wear resistance of concrete.

3.3.3.4 Chemical Reactivity of Aggregates

The various different processes capable of being formed from the reaction of aggregates with cement paste is of particular importance. The Alkali-silica reaction is the most pronounced development having been studied and researched for many years. Delayed ettringite formation is another very detrimental process that severely reduces the durability of concrete structures. In order to observe the breakdown of durability due to cracking, an ettringite friendly environment was created for the samples. Therefore a discussion of these processes is warranted.

3.3.3.4.1 Alkali-Silica Reaction

The alkali-silica reaction (ASR) is a chemical reaction that occurs when the alkalis present in cement or other sources attacks the active siliceous minerals in the aggregate, producing gels that expand and eventually cracks the concrete. Potassium and sodium are the alkalis present in Portland cement and their contributions are usually expressed as a single value (equivalent alkalis). Opals and chalcedony and tridymite are the reactive forms of silica and are found in opaline, cherts, siliceous limestones, and tuffs (Goldbeck 1956). The silica's have different levels of reactivity depending on degree of crystallinity, internal porosity, crystallite size,, and internal crystal strain. Opal being both amorphous and porous is the most reactive form of natural silica.

The alkaline hydroxides in pore water derived from the potassium and sodium in the cement attacks the siliceous materials in the aggregate. An alkali-silica gel is then formed in the pores of aggregates or on the surface of the aggregate particles. This is characterized by a dark rim around the aggregate particle which destroys the bond

between the aggregate and the cement paste. The gel that is formed has a tendency to absorb water thereby increasing in volume. This process applies internal pressures on the aggregate and cement paste which can lead to expansion and cracking. It is important to note that the alkali-silica reaction will only occur in the presence of water, while advanced stages of ASR results in extensive map cracking.

3.3.3.4.2 Delayed Ettringite Formation

DEF takes place due to either external sulfate attack or internal sulfate attack. However external sulfate attack is known as traditional sulfate attack, and takes place when environmental sulfate from soil or water penetrates into concrete and reacts with the cement paste. DEF is sometimes called internal sulfate attack, and may take place due to many factors, the most important being excessive amounts of slowly soluble sulfate in the clinker phase of Portland cement, excessive amounts of sulfate ions in the concrete from; cement, aggregates or in mineral admixtures and exposure to temperatures above that necessary for the decomposition of ettringite.

Ettringite formed during the early stages of hydration is harmless, it is neither associated with a damaging sulfate attack nor does it produce any damaging expansion. As explained in chapter two this type of harmless ettringite formation occurs from the reaction of gypsum and anhydrous calcium aluminates. Conversely, late ettringite formation occurs at a late age, after several months or years. This process occurs in a hardened concrete from the reformation of primary ettringite which decomposed or failed to form during exposure to high curing temperatures or excessive heat of hydration.

As stated previously, alkalis are present in the cement as sodium and potassium. These alkalis are normally present in the clinker as neutral sulfates Na_2SO_4 and K_2SO_4 or the mixed salt $(Na, K)_2SO_4$ (Pettifer, 1980). The values of the alkalis are usually expressed as a single value, but this level can be increased by various other sources which include aggregates, mixing water, admixture, contaminated de-icing salts, and environmental pollution. An increase in the alkali content decreases the solubility of calcium hydroxide (CH) and accelerates the formation of ettringite (Daerr 1977). Researchers have also concluded that expansion of DEF was more serious with high alkali cements. Thus it is clear that the overall alkali content in the form of sulfates is a determining factor for ettringite development.

The damage to concrete caused by delayed ettringite formation (DEF) is very similar to that caused by ASR because both produce internal pressures and expansions within concrete. Many studies show that there is a strong co-relation with ASR and DEF as ASR initiates the cracks that are later filled by ettringite (Shayan 1996).

3.4 Potassium Carbonate

To aid in the formation of ettringite, potassium carbonate was added to increase the alkali content in the samples. The inclusion of potassium by this method was preferred to using a cement with a high potassium content because cements of this nature would include additional variables in the experiment. The issue is that potassium in high potassium cement is present as potassium sulfate. Consequently any effects observed may be due to a combination of both potassium and sulfate.

The carbonate salt was used because it is the ultimate form of the carbonated concrete. Precipitation of the carbonate occurs during the curing of the concrete in the form of calcium carbonate as follows:

$$K_2CO_3 + Ca^{2+} + 2OH^- \rightarrow 2KOH + CaCO_3 \quad \text{.....3.1}$$

The Potassium hydroxide and calcium carbonate are the results of the reaction which is similar to that which occurs with the normal form of potassium as potassium sulfate.

$$K_2SO_4 + Ca^{2+} + 2OH^- \rightarrow 2KOH + CaSO_4 \quad \text{.....3.2}$$

3.5 Effects of Curing on Delayed Ettringite Formation

Delayed ettringite formation has come to be principally known for its deleterious expansions of concrete that has been previously heat-cured then subsequently exposed to moisture. Many researchers have concluded that treating concrete at a temperature above 70º C, then afterward immersing it in moist conditions promotes delayed ettringite formation (Heinz 1986, Lawrence 1990, Diamond 1996, Ronne 1999).

A heat curing method is often used to accelerate the strength development of concrete elements. It has been mainly used in the production of prestressed concrete elements to achieve early strength allowing for the timely releasing of the prestressed loads. High temperature curing accelerates the hydration of Portland cement and the formation of C-S-H, hence an earlier strength development. However problems with delayed ettringite formation almost co-exist with this method as C-S-H absorbs more sulfate ions at higher temperatures, that is above 65º C (Fu 1995). The sulfate ions are very weakly bonded and releases slowly at later ages, which initiates the delayed ettringite formation.

Research performed in Europe reported that the main cause of delayed ettringite formation is the decomposition of early ettringite by excessive temperature during heat curing. They also suggested that DEF is affected by sulfate content and sulfates to aluminates ratio (Heinz 1987). Others also reported that excessive heat curing at temperatures above 70º C was the main cause of the disintegration of concrete due to DEF (Tepponen 1987). The length of precuring and the rate of temperature rise were also cited as important factors affecting delayed ettringite formation.

Damage caused by the formation of DEF due to heat treatment is identified by the formation of gaps around the aggregate particles. The gaps will be empty, partially filled, or completely filled with ettringite needles extending from the surface of the aggregate particles (Heinz 1986, Diamond 1993). The gaps created are proportional to the aggregate particles.

As explained earlier DEF can be formed from an increase in alkali content in the concrete, however curing and subsequent expose conditions are chiefly responsible for DEF.

CHAPTER 4

Experimental Program

4.1 Introduction

The technique used to analyze the concrete samples is a three dimensional imaging technique called X-ray microtomography. This method is a completely non-destructive means of visualizing the internal structure of any dense, solid object. X-ray microtomography, otherwise known as high resolution x-ray computed tomography (C.T), has been modified from a similar process utilized in the medical field; the Computed Axial Tomography, or more commonly known as CAT scans. The main differences lie with the x-ray emitting source, and the type of detector utilized in picking up these x-rays. In comparison with medical devices, high resolution C.T scans can reach orders of magnitude of up to two or three times greater than that capable with conventional CAT scanners.

Some of the techniques already utilized in measuring the size of pores in concrete includes: mercury intrusion porosimetry (MIP), scanning electron microscope (SEM), optical microscopy, gas absorption, and the more recently developed nuclear magnetic resonance imaging microscope. All these methods have been necessary because of the trade offs between the range of observation for each technique and the wide length scale required for complete measurement (Mindess and Young, 1981).

X-ray microtomography presents an alternative approach in determining the porosity and pore size distribution of concrete specimens. A better image is obtained by using this new technique because it significantly enhances the picture of the pore structure in the millimeter to micron range. In addition more accurate conclusions can be

drawn about the distribution of pore sizes in concrete and its relationship to permeability and durability issues.

X-ray microtomography is distinctive in that, when compared with other microscopic analysis techniques, it offers unique imaging capabilities. Principally, accurate three dimensional maps of densities and elemental distributions can be nondestructively determined from samples. Hundreds of two dimensional maps of an object's x-ray absorptivity are reconstructed producing the three dimensional image. Also, with the implementation of synchrotron x-ray sources, scanning time is reduced to an hour. This rate is comparable with other conventional optical and electron microscopies.

4.2 Description of Microtomography

When a high resolution C.T scan is made of an object (in this case a concrete specimen), hundreds of two-dimensional radiographic images are produced. These images are referred to as "slices" which reveals the interior of the object as if it has been sliced open along the image plane. The images produced were determined from each of the elements' attenuation coefficients. The difference in density within each element of the object is the main factor that creates a difference in x-ray absorptivity that allows for a level of contrast in the image. Therefore x-ray absorption is a function of the elemental composition of the object, which is directly related to the microstructure of the material. A vast number of elements have had their x-ray absorptivity values calculated and documented (McCullough 1975, Hubell 1969, Ketcham 1997, Landis 2000).

4.2.1 Obtaining Tomographic Data

A tomographic image of an object is produced by placing the sample on a rotating stage or platform that is not only capable of full rotations but can also translate in the vertical direction. A schematic representation of the CT system is shown in Figure 4.1. X-rays, which are usually in the form of a planar fan, are directed toward the sample. The intensities of the rays are measured before penetrating the sample (incident intensity), and after passing through the sample (final intensity). The emitting source is held fixed while the platform is rotated at small angular increments repeating the intensity measurements on each turn. This allows the x-rays to penetrate the sample along several different paths in several different directions. A slice is complete only after the intensity measurements of a full rotation of the platform is collected, the rotating stage is then shifted vertically by a fixed quantity and this procedure is repeated to create additional slices of the entire sample.

4.2.2 Mathematical Principles of Microtomography

The overall objective is to obtain an image from the information collected of the intensity measurements of an object, which will be referred to as the intensity data. This is achievable when considering the relationship between the incident and final intensities of an x-ray beam; and the x-ray attenuation coefficient within an object as described by the exponential attenuation law, otherwise known as Beer's law. When considering a ray defined by its direction θ and an impact parameter *t* with respect to a Cartesian coordinate system (x,y) in the observed plane of the sample, Beer's law can be written as:

$$P(\theta,t) = \ln\left(I_o / I\right) = \int_s F(x,y)ds \quad \text{.....4.1}$$

Where (I_o) is the incident intensity and (I) is the final intensity, F(x,y) is the linear attenuation coefficient and (s) is a distance variable along the x-ray path. The value of the line integral is equal to the function P(θ,t) and is known as the projection measurement or optical depth of the sample along the ray's path. This Equation is more commonly written as:

$$P(\theta,t) = \ln\left(I_o / I\right) = \int_s \left[-\mu(s)\right] ds \text{ ……..4.2}$$

Where μ(s) is equal to the arbitrarily defined function F(x,y). The values of μ(s) are the unknowns in Equation 4.2, that is, the values of the linear attenuation coefficient at each point along each x-ray path. The unknown μ(s) values are constrained by many equations having the form of Equation 4.2 since the platform is rotated numerous times during several different intensity measurements. To acquire an image from the intensity data, values of μ(s) that provide solutions to the equations has to be determined.

Advanced mathematical principles have to be implemented to derive solutions from these equations. The method utilized in medical devices or tomographic systems that are not capable of reaching sub-micrometer resolutions is called the "filtered back-projection". This technique generates a unique set of μ(s) values, given a specified digital noise filter. However, for true microscopic resolution another type of mathematical reconstruction formula has to be used, namely the "projection slice theorem." This theorem shows that the Fourier transform of the target along a ray or slice in frequency space at an angle θ, is identical to the Fourier transform of the projections of the target viewed from that angle. Therefore theoretically it is possible to generate an image of the attenuation coefficient μ(s) from measurements of the projections P(θ,t). (Flannery, 1987, Ketcham 1997).

4.2.3 Differences in Attenuation Coefficients

In regards to CT imaging, to attenuate a beam is to decrease its intensity as a result of absorption of energy; also the attenuation coefficient of a material can be defined as the rate at which it absorbs energy from a ray. This leads to the theory behind the scans which illustrates that denser materials will have higher linear attenuation coefficient (μ) values and absorbs more energy. Therefore a CT scan is a map of the spatial distribution of μ values which reveals the differences in density within the object. Images are typically scaled so that brightness is proportional to x-ray absorption, thus bright regions corresponds to high density phases while dark regions would correspond to low density phases. A hole or pore space in a sample would appear to be practically black.

It is true that differences in features within a sample are due mainly to its electron density at each point (ρ), however other factors are also involved in determining values for μ. These are, the effective atomic number of the material encompassing the object at the specific point (Z), and the energy of the incoming x-ray beam (E). This relationship is shown in the following simplified Equation.

$$\mu = \rho\left(a + \left(b * Z^{3.8} / E^{3.2}\right)\right) \quad \text{.....4.3}$$

"a" is a quantity with a relatively small energy dependence and "b" is a constant(Wellington & Vinegar, 1987, McCullough, 1975). If a sample consists of a mixture of atomic species, then Z is defined by:

$$Z^{3.8} = \sum_i f_i * \left(Z_i\right)^{3.8} \quad \text{.....4.4}$$

Where f_i is the fraction of the total number of electrons contributed by element *i* with atomic number Z_i. Therefore in parts of a sample that consists of varying densities and chemical composition, these parts will have distinct linear attenuation coefficients and will be shown in the image to have contrasting brightness.

4.3 Developments

Medical computed tomographic scanners use conventional bremsstrahlung x-ray sources, scintillation crystals, and phototubes as detectors, and high speed data acquisition and processing to create individual planar maps. Theses maps are defined on grids of order 500 by 500 pixels with approximately 1-mm resolution.

The idea of using x-ray beams to create higher resolution images than those used in medical devices is not a new idea. In fact there is no intrinsic restriction with the system that would inhibit us in obtaining superior resolution than that obtained with medical devices. It was shown that utilizing synchrotron radiation theoretically could be used to generate data that could produce micrometer resolution (Flannery 1987). The only restriction that standard C.T devices would face is that the detector would not be able to efficiently spot these rays to achieve a greater resolution.

4.3.1 Synchrotron Radiation Source

To achieve microtomographic images there needs to be a source that is capable of generating x-rays with high resolution and a detector that is able to efficiently spot these

rays. The development of a digital imaging x-ray detector capable of spotting rays at submicrometer resolution has been developed and microtomographic systems now utilize extremely bright synchrotron radiation as the x-ray source, along with a high resolution detector.

The synchrotron source provides a well collimated, brighter x-ray beam of higher flux than with conventional x-ray sources. It is this higher flux and better collimation which provides more x-rays per unit area on the object which allows for better spatial resolution. Also the higher flux and continuous spectrum of the synchrotron source allows the beam to be monochromated to a narrow frequency band, which significantly improves the sensitivity of the tomographic device making it capable of distinguishing subtle variations in absorptivity within the specimen. The beam energy can be optimized for a particular object. There is an extensive range over which the beam energy can be tuned to optimize the x-ray absorption of each sample being scanned, depending on size and composition (Landis 2000, 2003).

4.3.2 High Resolution Detector

As stated earlier it is necessary to utilize an imaging x-ray detector system that will allow the finer spatial resolution of the microtomography to be realized. A high-resolution x-ray detector records two-dimensional images making efficient use of the area-filling collimated x-ray beam. It records the data simultaneously in multiple stacked planes, which is suitable for the reconstruction of three-dimensional images. This simultaneous recording of data helps to keep the overall scanning time at a minimum and allows the technique to be competitive with other established microscopies.

4.3.3 Increased Data Volume

Since microtomographic systems require the generation and detection of x-rays with higher spatial resolution it would be expected that there will be an increase in the volume of data stored, and also in the processing time of the data. However due to more advanced methods this larger volume can be processed in a short time frame.

Medical procedures typically produce maps in a few contiguous planes each containing 10^6 volume elements. Maps of even a millimeter-sized object with micrometer resolution require 10^9 volume elements for a complete three-dimensional image. Fortunately better tomographic reconstruction procedures have been developed that makes it possible to analyze tomographic data much more rapidly than with the conventional filtered back-projection method, one such method is the projection slice method (Flannery, 1987).

4.4 Problems Within the Reconstructed Image

A tomographic scan provides a reasonable representation of the interior of a sample, however it is important to realize that the images can be somewhat flawed due to the limitations of the CT system. To be able to properly interpret information and draw sensible conclusions from the images an understanding of the complexities and limitations of the technique is necessary.

4.4.1 Image Quality

The size and type of the emitting source and detector along with the imaging geometry, affects resolution and hence image quality in a CT image. Image geometry refers to the relative distances between the X-ray source, the sample, and the detector.

The signal to noise ratio in the attenuated beam and the image reconstruction procedure also contributes to the quality of the image produced.

X-ray signals are inherently noisy because both the x-ray generation and scattering events that produce absorption within the sample are stochastic processes. These variations can obscure variations arising from the sample itself. The electronics used for amplification in the detectors also contributes additional noise, which all results in noisy intensity measurements. The noise in the measurements limits the scanner's ability to differentiate between elements that have closely similar attenuation coefficients, thus degrading the resolution of the image.

The signal to noise ratio will affect image quality in such a way that if the X-ray flux and counting time for each intensity measurement is increased, the signal to noise ratio will be increased and the resolution improved.

In some CT devices the resolution is controlled primarily by the size of the apertures on the detector and their distance from the source. Adjusting the vertical dimension of these slits changes the slice thickness, thereby establishing the vertical resolution. The horizontal dimension can also be established by adjusting the in-plane resolution. Some researchers try to increase resolution by decreasing the aperture sizes on the detectors, but this has the negative effect of lowering the X-ray flux on each detector reducing the signal to noise ratio hence lowering resolution (Herman 1980).

4.4.2 Limits on Sensitivity

Sensitivity is the term given to the ability of the CT system to differentiate between materials that have closely similar linear attenuation values. This of course

depends on the precision in which μ values are calculated. Modern CT devices have the ability to differentiate between μ values that differ by 0.1 percent. Researchers have created tables showing the μ values of a number of minerals (McCullough 1975, Hubbell 1969).

In some cases, to determine the μ values, the sensitivity has to be increased by making multiple scans. Materials that have vastly dissimilar electron densities and chemical composition can have very similar μ values according to Equation 4.3. This may occur if one has a higher electron density that is offset by having a smaller effective atomic mass. In this particular case the sensitivity of the instrument can be improved by emitting more than one X-ray beam with differing photon energies. Equation 4.2 also shows that different values of μ will be obtained for high and low energy rays. Thus a combination of these scans will yield the appropriate μ value.

4.4.3 Creation of Artifacts

A frequently occurring flaw in CT results is that regions in the center of a sample will appear to have a lower attenuation coefficient than an identical region at the edge of the sample. This occurs because most materials attenuate X-rays more strongly at lower energies than at higher energies, thus the energy-distribution spectrum of the beam changes as it passes through the object. The beam that emerges has a higher quantity of high-energy (hard) x-rays, therefore this occurrence is known as beam hardening.

This unequal absorption effect is similar to having a polychromatic beam. However, Equation 4.2 applies to monochromatic radiation only, and the change in the energy distribution of the X-rays creates an apparent decrease in attenuation in the middle

of the object being scanned. This region is known as an artifact. (Herman 1980, Ketcham 1997).

4.5 Description of Device

The computed tomographic device utilized in this experiment is located at the Turner Fairbank Highway Research Center in McLean Virginia. The devise consists of a dual focus 420-kV continuous X-ray source and a 512 channel digital detector.

This device is not capable of sub-micrometer resolution, only reaching spatial resolutions of 0.250mm. However, for the purpose of this experiment, a 0.250mm spatial resolution is more than adequate. Furthermore, the filtered back projection reconstruction algorithm is sufficient in transforming the raw data into a TIF image.

4.6 Image Analysis Software

The software used to analyze the C.T scans is the Image-Pro Plus version 5.0 for Microsoft Windows operating system. Image-Pro Plus provides technologically advanced analysis techniques which allow the user to acquire and enhance image data obtained from a camera, microscope, VCR or scanners before analyzing. The product reads and writes image data in all standard image file formats including TIF, JPE, BMP, and TGA.

4.6.1 Capabilities of the Software

Some standard features include its ability to work with gray scale data in 8, 12, 24, or 32-bit floating point depths, and also with color data in palletized or 24, 32, 48-bit format. In addition the RGB, HIS, HSV, and YIQ are different models that allow image pro to manipulate its color data.

Image enhancement can be carried out using powerful color and contrast filters, including Fast Fourier Transforms (FFT), morphology, field flattening, background subtraction and other spatial and geometric operations. Other features include the ability to calibrate the spatial scale to any unit of measure, tracing and counting objects manually or automatically, and measuring objects' attributes.

The data can then be collected and classified in a number of different forms including numerically, statistically, or graphically for example as a histogram or scattergram (Image-Pro Plus start-up guide 1993).

4.6.2 Image Processing

Digital image processing is a specific means of altering information within an image by the use of a computer. An object can be visually represented with pictorial information as in the case of photographic images, however to represent objects by the use of a computer, numerical information will be necessary.

4.6.2.1 Description of Image

Images are represented in a computer by a horizontal grid, or array of very small regions known as picture elements. The entire grid is known as a "bitmap" and the picture elements are more commonly known as pixels. The position of each pixel in the bitmap can be identified by its row (x) and column (y) number. It is conventional to have the reference point from the upper-left position of the bitmap, which is considered position (0, 0) that is (row 0, column 0).

When a CT scan of a section of an image is taken, as described earlier based on the attenuation coefficient of the element, it is given a bright or a dark value, resulting in

an image with different shades of grey levels. The software examines the image created in grid fashion, where each pixel is individually sampled and its brightness measured and quantified. This results in the assigning of an integer value to the pixel, which represents the brightness or darkness of the image at that point. This value is subsequently stored in the related pixel of the image bitmap.

It is also important to know that the width and height of the grid is chosen when the CT scan is made, and cannot be altered thereafter. The width and height of the pixels in the bitmap are known as its spatial resolution.

4.6.2.2 Pixel Depth and Image Class

The pixel depth or bits per pixel (BPP) is the number of bits used to represent a pixel value in an image. Anywhere from 1 to 32 bits can be used to store each pixel value depending on the complexity of the image and the capability of the measuring device. The bit depth signifies the amount of gray shades in a gray scale image, or the number of unique colors that are in a colored image. Due to the nature of computed tomographic analysis, the images obtained are gray scale images. Gray scale pixel values represents the level of grayness in an image which ranges from completely black to completely white. This group of images is sometimes called monochromatic.

The number of bits per pixel used to represent each pixel value also determines the “image class” of the image. The image class of all scans obtained from the computed tomographic system in this study is labeled “Gray Scale 8,” having 8 BPP. Although the software supports Gray Scales 12, 16, and 32 image classes, the 8 BPP image class is most commonly utilized. 8BPP images are preferred because its one byte per pixel size allows for easy computer manipulation. It also does a more than adequate job in

representing any gray scale image, as its 256 distinct levels of gray are more than the human eye can distinguish. In Gray scale 8 images, a pixel with a value of zero is completely black and a pixel with a value of 255 is completely white.

4.6.2.3 Image Enhancing Techniques

In most cases an image will require some type of enhancement so that the ability to extract and interpret data from it can be improved. As described earlier there are many complexities inherent in the computed tomographic results. The stochastic process of the system along with the emitting source, detector size and type causes blurring in the images. This sometimes hinders the CT system's ability to distinguishing between certain objects. Since our goal is to obtain the amount and size of pores, a clear defining line is needed between pore and cement paste. As defined by most literature, a procedure known as segmentation is required to identify this defining line.

Segmentation is generally known as one of the difficult procedures in obtaining results from CT tomography. To aid in this process the software offers many different enhancement techniques designed to tease out and refine information in the image. These have been placed in three main groups, which are:

- Intensity Index Modification
- Spatial Filter Application
- Image Frequency Manipulation

Image-Pro Plus offers a collection of enhancement techniques in each group which allows enhancement for a variety of purposes and applications. It was observed that best results were obtained by utilizing several techniques in combination rather than any one in particular.

4.6.2.3.1 Intensity Index Modification

Altering the intensity Index means changing the way the software interprets the intensity values in an image. Image-Pro Plus offers three different intensity manipulation tools known as Contrast Enhancement tools. These are brightness, contrast and gamma correction commands.

The Brightness command as the name implies expresses the amount of light or the degree of brightness contained in an image. The degree of difference between the bright and dark components in an image is known as the contrast, and is controlled by the contrast command. The gamma correction control is a specialized type of enhancement developed to improve the contrast in the very dark or very light areas of an image.

For the CT images obtained in this study, it was only necessary to alter the intensity index by changing the brightness and contrast commands.

4.6.2.3.1.1 Image Histograms

Image histograms measure and illustrate the brightness and contrast characteristics of an image graphically. They are very useful tools as they demonstrate what kind of brightness and contrast deficiencies are present in an image. The x-axis represents intensity values (from 0 to 255 for 8BPP images) and the y-axis measures the number of pixels in the image having a specific intensity.

If there is clustering around a narrow portion of the histogram this would indicate a contrast deficiency, also the region in which the clustering occurs will determine if the image is too dark, too light or too gray. This process was utilized to determine if a brightness or contrast adjustment is necessary. An example of an unaltered image and its histogram is shown in Figure 4.2 and 4.3 respectively.

From visual inspection it can be seen that the image is too gray. Also from an analysis of the intensity histogram there is clustering somewhere around the 160 intensity value, showing a narrow bandwidth from the 115 to the 200 intensity value. It can therefore be deduced that the image has a brightness/contrast deficiency.

After modifying the intensity index of the image, the resulting image and histogram are shown in Figures 4.4 and 4.5 respectively. Visually the image shown is now brighter than before and an inspection of the new histogram confirms the increase in brightness. The entire histogram has shifted to the right, into the brighter region of the graph. The mid-range value is now at the 200 intensity value, and the range has become wider being between 130 and 255.

4.6.2.3.2 Spatial Filter Application

The objective of a spatial filter is to alter the rate of change that occurs in the intensity transitions within an image. Images often contain hard edges, which are regions in which abrupt changes in intensity occur. Soft edges or areas in which there are gradual changes also exist. Application of a spatial filter will detect and modify the intensity transitions at these edges by making a soft edge appear sharper, or making a hard edge smoother. The filter process takes place by adjusting a pixel's value based on the values of the pixels that surround it; Image-Pro Plus refers to this as the "pixel neighborhood."

Spatial filters used to enhance images generally utilize the convolution process, as is the case with the Image Pro Plus software. The convolution process operates on the entire neighborhood by multiplying each pixel by a matrix of filtering coefficients. The matrix is of the same size of the neighborhood to which it is being applied, and consists

of integer value coefficients. This is known as the filter kernel. The multiplication results are then summed and divided by the sum of the filter kernel. This result is scaled and boosted and replaces the center pixel in the image neighborhood.

Since the interfaces between the voids and the cement paste or aggregate are blurred, a spatial filter was required. The “Higauss Filter” best fitted the needs of this experiment and was used on all images.

4.6.2.3.2.1 Higauss Filter

The Higauss filter is designed to accentuate all edges by significantly enhancing the intensity transitions in the image. This type of filter is used to enhance fine details within an image or to re-focus an image that has been blurred. Essentially the low-pass results are subtracted from the original image (via use of the convolution process not by actual subtraction). The Higauss filter was chosen over the sharpening filter because it introduces less noise in the filtering process. The filtered image is shown in Figure 4.6. It can be seen that the voids are more defined and there is less blurring in the image.

4.6.2.3.3 Image Frequency Manipulation

Frequency manipulation is only necessary when there is any form of reoccurring noise in an image that is something that displays itself as a regular or periodic pattern. Due to the nature of the CT system, this type of noise was not present in the images therefore it was not necessary to utilize any frequency filtering tools.

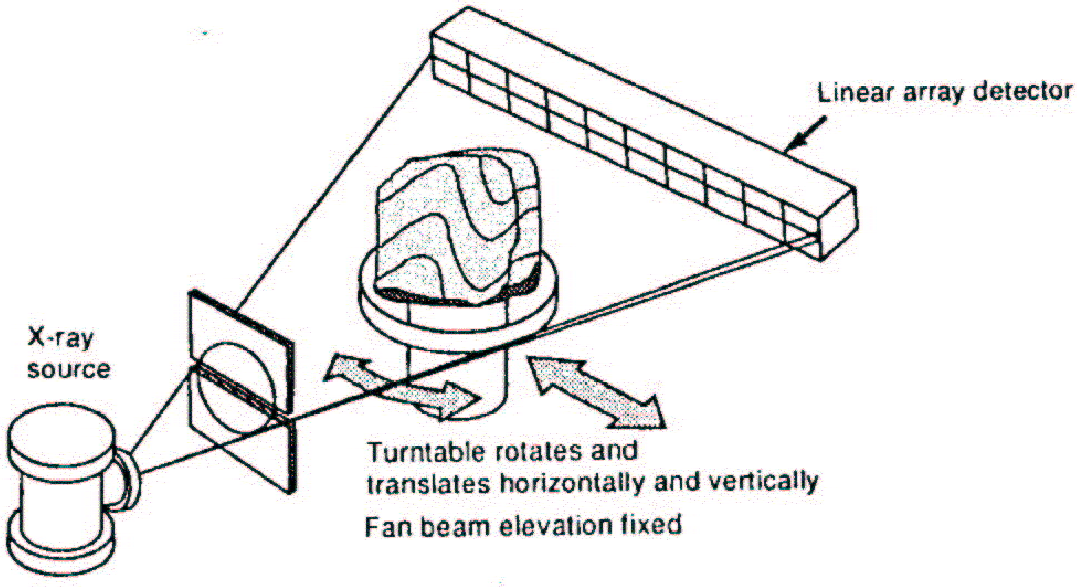

Figure 4.1 Schematic Representation of a Computed Tomographic System
(After C. Denison, W.D Carlson and R.A Ketcham 1997)

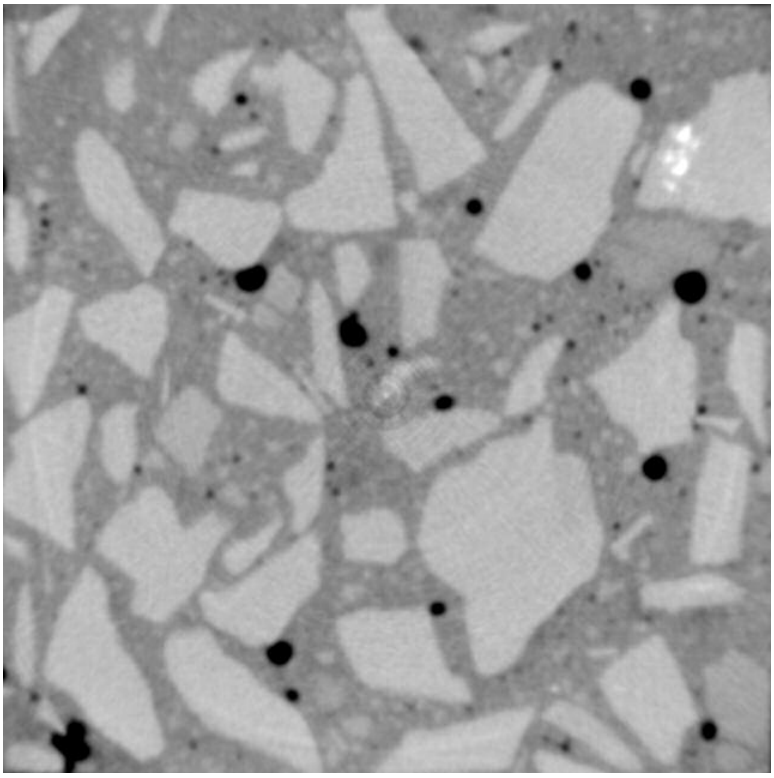

Figure 4.2 Unaltered X-ray Computed Tomographic Image of a Section through a Concrete Prism

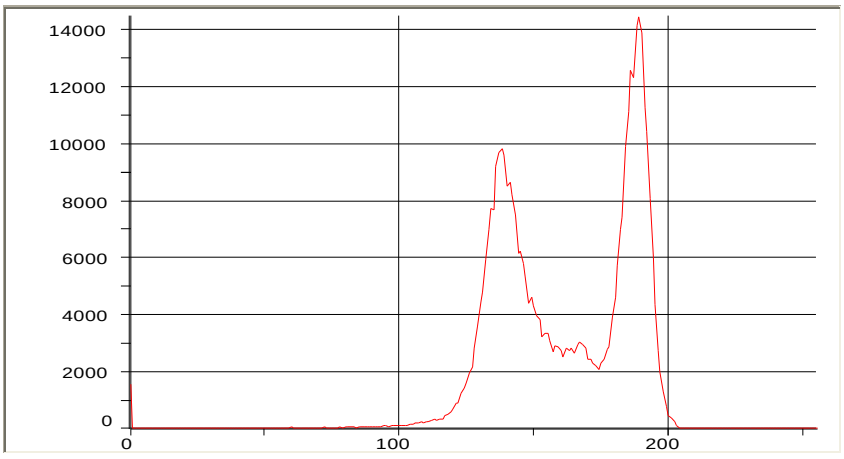

Figure 4.3 Intensity Histogram of an Unaltered Computed Tomographic Image

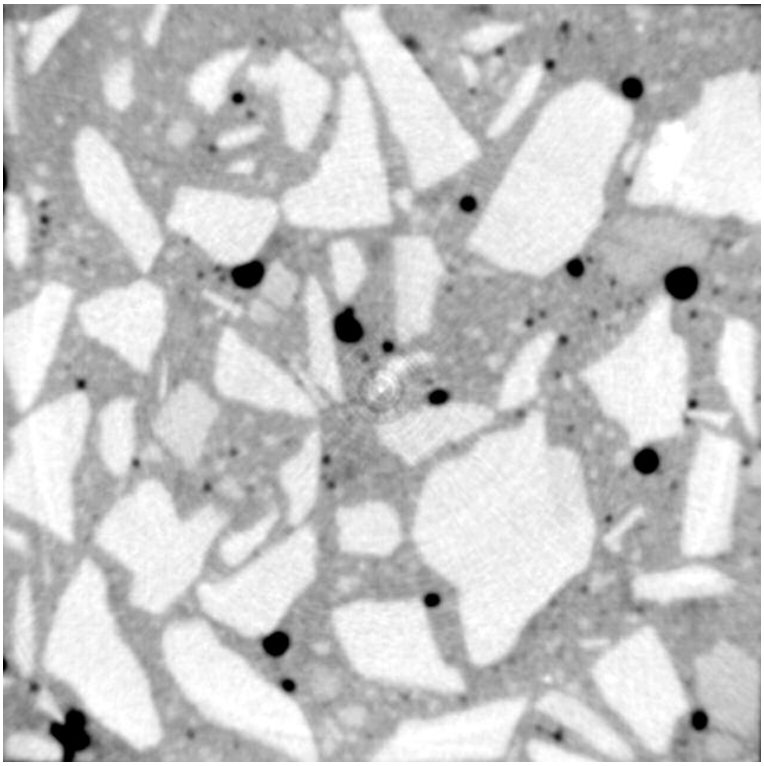

Figure 4.4 X-ray Computed Tomographic Image of a Section through a Concrete Prism with an Intensity Index Modification

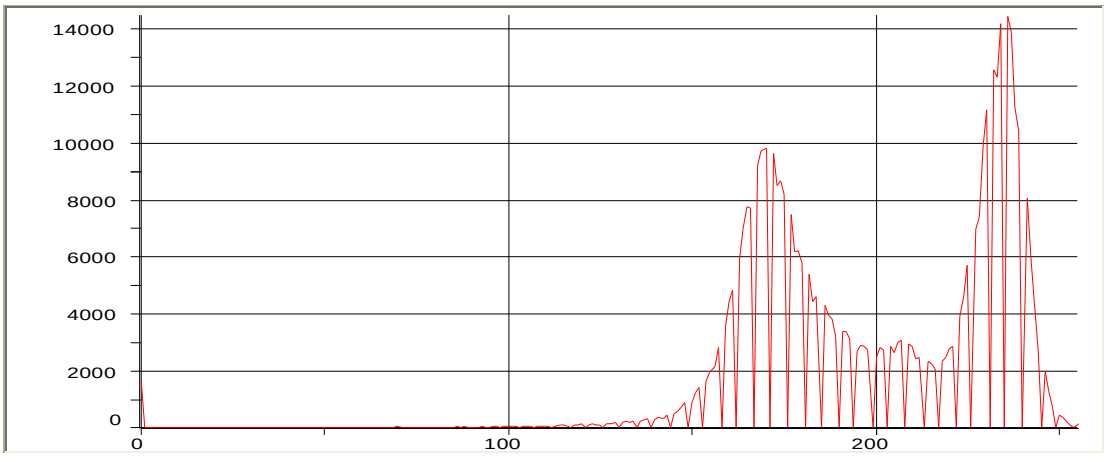

Figure 4.5 Intensity Histogram of a Computed Tomographic Image with an Intensity Index Modification

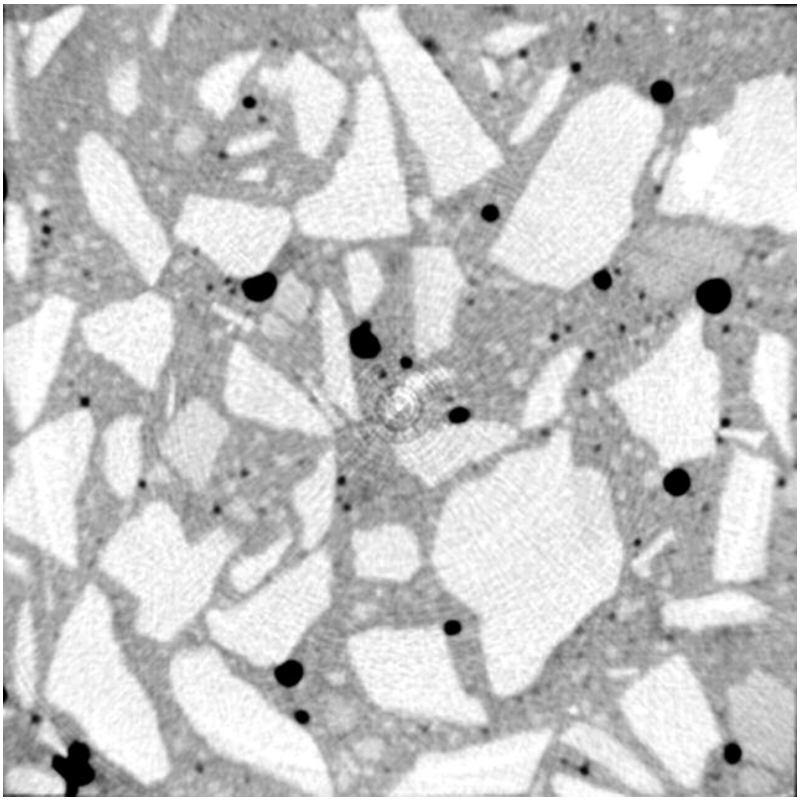

Figure 4.6 Filtered X-ray Computed Tomographic Image of a Section through a Concrete Prism

CHAPTER 5

Materials, Preparation of Samples and Testing Procedures

5.1 Introduction

This chapter outlines all the materials and procedures that were employed in the preparation of the samples. To ensure the capability of obtaining credible results, the materials chosen and procedures followed are in accordance to the American Society of Testing and Materials (ASTM). Firstly, all the materials are described including chemical composition of aggregates and cement. The test procedures utilized in preparing the concrete specimens are also described, along with all other measures that were applied to the samples after being cast.

All the specimens in this study had a water to cement ratio (w/c) of 0.5, and were prepared using the modified sample preparation method. The Duggan Heat Cycle was carried out exactly one week after the samples were cast to accelerate the cracking due to delayed ettringite formation.

This experiment aims at quantifying the development of the pore structure in concrete specimens under specific environments via the use of modern computed tomography. An atmosphere that is perceived to be conducive to ettringite development is first created for the concrete specimens. Then an assessment of the pore structure formation is undertaken which involves calculating the pore size distribution and the void percentages in each sample. The detection of cracking and observation of crack patterns due to delayed ettringite formation is also attempted.

5.2 Materials

The methods utilized in this experiment and the reasons for their use are explained below. The conformance to ASTM standards is important as it allows the experiment to replicate somewhat the procedures and materials utilized in practice. The materials discussed are fine and coarse aggregates, cement type, fly ash, the potassium carbonate addition, and the casting molds.

5.2.1 Fine Aggregate

The types of sand used were Laurel, Medford and Frederick sand which are either siliceous or crashed sands that conforms to ASTM C33. Laurel sand is both the natural and siliceous sand used in this study, while Frederick and Medford Sands are manufactured crashed sands. Laurel sand was obtained from Laurel sand and gravel, Laurel, Maryland. The laurel sand used had a moisture absorption of 0.9% and a specific gravity of 2.62%. Both manufactured sands are crashed limestone, with Medford sand being obtained from Medford quarry, New Windsor Maryland and Frederick sand being obtained from Frederick quarry, Frederick Maryland. The Medford sand had a moisture absorption of 0.9% and a specific gravity of 2.72, while Frederick sand had a moisture absorption of 1.3% and a specific gravity of 2.65.

Observing the degree in which materials with expansive tendencies have in concrete as opposed to those with non-reactive tendencies is one of the purposes of series two. Consequently both a reactive and a non-reactive aggregate were necessary in this experiment. According to the Maryland State Highway Administration, the alkali silica reactivity (ASR) results for Laurel, Frederick, and Medford sands are 0.18%, 0.09% and

0.01% respectively. The Maryland State Highway Administration has certain recommendations as to the use of an aggregate depending on its alkali silica reactivity. According to the Maryland State Highway Administration, aggregates with less than 0.10% ASR can be used without restriction, and those with more than 0.35% should not be used. Aggregates having an ASR value between 0.10% and 0.35% are taken as reactive aggregates. Therefore Laurel sand is considered a reactive aggregate, Frederick sand is considered an intermediary reactive sand, while Medford sand is a non-reactive sand. Additional information on the different types of fine aggregates is shown in Tables 5.1 to 5.3.

5.2.2 Coarse Aggregate

Only one type of coarse aggregate is used in this experiment. All samples consist of limestone aggregates having a maximum diameter of one inch, a dry rodded weight of 102.3lb/ft and a specific gravity of 2.72. Additional coarse aggregate information is presented in Table 5.4.

5.2.3 Fly Ash

Class F Fly ash was used to prevent DEF from occurring in the concrete samples. Since class F Fly ash had the least amount of sulfur when compared to the other admixtures, it is less likely to promote DEF. This type of Fly ash was obtained from Brighton Point, Brighton Point, Massachusetts, and its chemical composition is shown in Table 5.5. For the samples created in series two, different percentages of fly ash were added as a partial replacement of the Portland cement.

5.2.4 Cement

Portland cement type III is used in all samples in this experiment. As described earlier type III cement is more susceptible to delayed ettringite formation than any other cement because of its higher sulfate content and finer cement grains. The chemical composition of the type III Portland cement is shown in Table 5.6

5.2.5 Potassium Carbonate

Anhydrous, granular reagent grade potassium carbonate (K_2CO_3) was used. This type of potassium was used because it results in a chemical reaction similar to that which occurs with the normal reaction of potassium as potassium sulfate that is found in Portland cement.

5.2.6 Molds

Steel molds used conformed to ASTM C470 specifications and had dimensions of 3” x 3” x 11.25”. Provisions for stainless steel studs and an effective gage length of 10 inches were used to fabricate the prisms.

5.3 Experimental Program

This experimental program was geared towards analysis via computed tomography, and was divided into two different series. The specimens were prepared to observe cracking and pore formation due to: curing conditions, different types of fine aggregate, and the addition of different amounts of fly ash. The concrete samples were made and cured according to ASTM C192-88, which specifies the method of making and

curing concrete test specimens in the laboratory. The prism molds were in accordance with ASTM C490-86, which is standard practice for the use of apparatus determining the length change of hardened cement paste, mortar, and concrete. There was however a modification to the Duggan test method, as concrete prisms with studs at the ends were utilized instead of concrete cores.

For the first series, the specimens were prepared with different types of fine aggregates while keeping all other parameters constant. Potassium Carbonate was added at 1% of the weight of cement to accelerate cracking due to expansion. The specimens were also subjected to heat curing. The Duggan test was carried out after one week of casting.

In series two the fly ash was added to the mix in different proportions. All specimens were subjected to water curing. The Duggan Heat Cycle was also performed after one week of casting.

5.3.1 Duggan Heat Cycle

The Duggan Heat Cycle consists essentially of three cycles. For the first two cycles the specimens are placed in the oven at 82 °C for one day, they are then cooled for 1 ½ hours followed by an entire day of soaking in water at room temperature. For the third cycle, the specimens were left in the oven for 3 days at 82°C then they were stored under water at room temperature for a period up to 2 years.

The Duggan Heat Cycle was employed to simulate the effects of DEF in the shortest possible time period, accelerating expansion and cracking.

5.3.2 Modified Sample Preparation

The samples were prepared according to ASTM C 192-88. However the prisms have two steel studs at its end instead of drilled cores as suggested by Duggan. The studs are utilized as a more practical method of taking length measurements.

5.4 Preparation of Samples

All samples prepared for laboratory testing were prepared according to ASTM C192-90, which is the customary practice for making and curing concrete test specimens in the laboratory. The mixer used for all concrete batches was a power driven revolving drum tilting concrete mixer, with a three cubic feet capacity. All the mixes were machine mixed according to ASTM C192-90. The samples were covered with plastic sheets before they were subjected to the curing regime.

5.4.1 Series One

The primary purpose of this series was to examine the effects that different aggregate types had on the formation of voids in concrete. Three concrete batches were prepared for testing. The mix materials and proportions for all three samples were the same with the exception that the fine aggregates used differ. Laurel sand was used as the natural, siliceous and reactive aggregate, while Frederick and Medford sands were used as the intermediary and non-reactive aggregates for the other two samples. 1% potassium carbonate (K_2CO_3) by weight was added to the mixing water to increase the potassium levels to 1.4% as K_2O. Type III Portland cement was used in all samples, which were

prepared according to the modified test method. Mixing proportions for each specimen is given in Table 5.7

The specimens were then steam cured after casting then subjected to the Duggan Heat Cycle. The samples were then left to cool overnight, and then stored under water at room temperature.

5.4.2 Series Two

The objective of this series is to study the effects of pore and void formations due to the replacement of cement with varying amounts of fly ash. In this series four different samples were created with type III Portland cement. All samples were made with similar mixing materials and proportions in accordance with the modified test method. Laurel sand was used in this series to enhance the DEF reaction. The only difference in the samples were the percentage of fly ash that was substituted for cement, each sample contained 0%, 10% 20%, 30% respectively. Class F fly ash was used to mitigate ettringite formation in the samples.

After casting, all the prisms were moist cured to enhance hydration. The prisms were then subjected to the Duggan Heat Cycle after one week of casting. Thereafter they were immersed in water for the duration of the test. Additional information is available for the mix proportions of series two in Table 5.7.

5.5 X-Ray Computed Tomography

X-ray computed tomography presents a non-destructive way of visualizing, quantifying and analyzing the microstructure that makes up the interior of solid objects,

including concrete specimens. CT scans are capable of revealing the shape and size of the concrete pores, the porosity distribution in a concrete sample and the nature of the interfacial zone between aggregate and the cement paste.

In relation to this experiment, the primary purpose is to reveal the porosity in concrete specimens due to varying factors and to capture any interior cracking due to ettringite formation.

5.5.1 Scanning of Samples

The samples created where rectangular prisms having a cross sectional dimension of 76.2 x 76.2 mm (3 x 3in) and a length of 285.75 mm (11.25in). Taking horizontal sections every 4.7625 mm (0.1875 in) created sixty scans from a sample. This process was followed for both series that contains a total of seven specimens. TIF images with pixel dimensions of 1024 x 1024 and having resolutions of 72 dots/inch were created. To obtain accurate information from these images they were taken through a series of meticulous processing techniques as described in previous sections.

5.5.2 Image Processing

Image processing involves the application of various forms of enhancement techniques on the images so that realistic information can be extracted. All the scans created from the device at the Turner Fairbank testing facility consisted of a cross section of a sample in the middle of a dark background. An example of an unaltered image is shown in Figure 5.1. The dark background is initially removed as it clarifies the image and allows for proficiency in the calculation and collection of the different measurements

within the image. The removal of the background is known as cropping. The cropped images had pixel dimensions of 657 x 657, an example is shown in Figure 5.2.

Before segmentation is performed, the images are enhanced by the use of Image Pro Plus features. The intensity histogram is altered to make the images brighter through the use of the contrast enhancement tools. The brightness command is changed to a value of 57, the contrast command to a value of 62 and the gamma control remained at 1. These changes are made permanent by storing them to the image bitmap. A filtering procedure was then applied to the images to accentuate the edges so that voids could be clearly defined. The Higauss filter was employed at a strength value of 4. This filter was considered the most appropriate because it introduced less noise within the images. The images are then saved as enhanced versions of their original files.

5.5.3 Calibration of Images

The spatial measurements of images created by the CT system and represented in Image Pro Plus are automatically expressed in terms of pixels. Calibration establishes the unit of measure in the images, which allows for a quantitative means of comparison after taking measurements.

The calibration was done by using the image's cross-sectional dimension as a reference. This is done by drawing a line alongside the width of the image and indicating the number of calibrated units it represents. This reference line corresponded to 76.2mm (the width of the images), then the corresponding pixel to mm (p/m) ratio would be displayed. Not all images had the exact (p/m) ratio because some were skewed at an

angle to the horizontal. This discrepancy is very minute, and did not severely interfere with the measurements.

5.5.4 Segmentation

The segmentation or thresholding procedure involves identifying or selecting certain regions in the image based upon their relative pixel intensities. In this experiment the purpose of segmentation is to separate void spaces from cement paste, therefore we are only interested in two regions. The problem is defining a threshold value that will reasonably represent the boundary that signifies where the void space ends and the cement phase begins.

Image Pro Plus assists in defining this line with a feature that can manually select a range on the intensity histogram which will act as the threshold limit. By a series of trial and error analysis it was determined that pixels with intensity values falling in the range of 0 to 97 will be taken as pores.

5.5.5 Counting Measuring and Collection of Data

The void spaces are then counted based on the criteria above. An image identifying voids are shown in Figure 5.3, each void is treated as an object and is given an object number. Various number of measurements are associated with each object, the ones of primary concern were; area, aspect ratio, mean diameter, maximum diameter, perimeter, roundness and per area object measurements.

Two of the more common measurements are the area and the perimeter. The area calculates the cross-sectional area of voids having various shapes, and the perimeter computes the length of the outline of the voids.

The aspect ratio is the ratio between the major and minor axis of an ellipse that is equivalent to the void. The mean diameter is calculated as the average length of the diameter measured at 2 degree intervals and passing through the void's centroid, while the maximum diameter is taken as the length of the longest line joining two points of the void's outline and passing through its centroid.

Roundness is taken as the square of the perimeter divided by the product of 4, π, and the area of the void. A value greater than one is not considered round. The per area object measurement gives the ratio of the void to the total cross-sectional area of the specimen. All these measurements will assist in the analysis and will allow for a comparison with other experiments.

The listing of these measurements for each object in a scan is known as the measurement data sheet. The data for each scan is then saved and stored in an excel document for analysis.

Technical Information Sheet For Laurel Sand			
Rock Type:	Natural		
Color:	Natural		
Average Gradation	Dry Analysis		
ASTM C136	% Passing		
3/8 (in)	100		
#4	92.1		
#8	74.4		
#16	60.9		
#30	42.6		
#50	15.9		
#100	2.6		
#200	0.6		
F.M.	0.1		
	Bulk	SSD	Apparent
Specific Gravity (AASHTO T85)	2.64	2.64	2.65
Absorption (AASHTO T85)	0.14%		.
Alkali silika reactivity (MSMT 212/ ASTM C1260	0.18%		

Table 5.1 Technical Information Sheet for Laurel Sand

RGI Medford Quarry	Manufactured ASTM C33 stone sand	
Technical Information sheet		
Rock Type:	Carbonate	Calcitic Marble
Color:	Variations of light gray, beige, pink, white	
Average Gradation	Dry Analysis	Wet Analysis
ASTM C136	% Passing	% Passing
3/8 (in)	100	100
#4	98.8	99.1
#8	80.1	81.7
#16	53.5	54
#30	36.9	38.5
#50	23.3	25.4
#100	8.6	10.2
#200	2.1	3.7
F.M.	2.99	2.91
	Bulk	SSD	Apparent
Specific Gravity (AASHTO T85)	2.678	2.694	2.722
Absorption (AASHTO T85)	0.60%		
Alkali silika reactivity (MSMT 212/ ASTM C1260	0.00% expansion		
Sodium Sulfate soundness (AASHTO T104)	0.07% loss		
Unit weight, dry rodded (AASHTO T19)	111#/CF		
Fine Aggregate Angularity (ASTM C1252 method A)	46.2% Voids		
Sand equivalency (AASHTO T176)	84%		
Fractured faces (PMT 621)	100%		
Organic Impurities (AASHTO T21)	color plate 1		

Table 5.2 Technical Information Sheet for Medford Sand

RGI Frederick Quarry Manufactured ASTM C33 stone sand Technical Information sheet			
Rock Type:	Carbonate	Calcitic Limestone	
Color:	Light to dark gray		
Average Gradation	Dry Analysis	Wet Analysis	
ASTM C136	% Passing	% Passing	
3/8 (in)	100	100	
#4	98.6	98.8	
#8	91	91.5	
#16	48.1	49.7	
#30	24	24.7	
#50	10.8	12	
#100	3.8	5	
#200	2	2.8	
F.M.	3.15	3.18	
	Bulk	SSD	Apparent
Specific Gravity (AASHTO T85)	2.664	2.687	2.729
Absorption (AASHTO T85)	0.90%		
Alkali silika reactivity (MSMT 212/ ASTM C1260	0.09% expansion		
Sodium Sulfate soundness (AASHTO T104)	1.2% loss		
Unit weight, dry rodded (AASHTO T19)	108#/CF		
Fine Aggregate Angularity (ASTM C1252 method A)	45.6% Voids		
Sand equivalency (AASHTO T176)	94%		
Fractured faces (PMT 621)	100%		
Organic Impurities (AASHTO T21)	color plate 1		

Table 5.3 Technical Information Sheet for Frederick Sand

RGI Frederick Quarry ASTM #57 Stone Technical Information Sheet			
Rock Type:	Carbonate	Calcitic Limestone	
Color:	Light to dark gray		
Average Gradation	Dry Analysis	Wet Analysis	
ASTM C136	% Passing	% Passing	
1 (in)	0	100	
3/4 (in)	7.3	92.7	
1/2 (in)	48.6	44.1	
3/8 (in)	26	18.1	
#4	15.1	3	
#8	1.9	1.1	
Pan	1.1		
	Bulk	SSD	Apparent
Specific Gravity (AASHTO T85)	2.712	2.722	2.74
Absorption (AASHTO T85)	0.40%		
200 Wash (ASTM C117)	0.80%		
Polish Value (MSMT 411)	7		
British Pendulum Number (ASTM D 411)	26		
Alkali silika reactivity (MSMT 212/ ASTM C1260	0.09% expansion		
L.A. Abrasion (AASHTO T96/ASTM C131)	26% Wear		
Sodium Sulfate soundness (AASHTO T104)	0.1% loss		
Unit Weight, dry rodded (AASHTO T19)	99#/CF		
MOHs Hardness	4		
Sand Equivalency (AASHTO T176)	94%		
Fractured faces (PMT 621)	100%		

Table 5.4 Technical Information Sheet for Coarse Aggregate

Element	%
Al	30.06
Ba	0.15
Ca	0.91
Fe	3.92
K	3.93
Mg	0.76
Mn	0.02
Na	0.49
P	0.09
S	0.36
Si	56.91
Sr	0.12
Ti	1.93
Total	**99.66**

Table 5.5 Chemical Composition of Class F Fly Ash as Measured by X-ray Fluoresce

Chemical Analysis of Cement	
Analyze	Weight %
SiO_2	20.89
Al_2O_3	4.28
Fe_2O_3	2.6
CaO	61.85
MgO	2.99
SO_3	3.21
Na_2O	0.1
K_2O	0.71
TiO_2	0.26
P_2O_5	0.15
Mn_2O_3	0.19
SrO	0.06
L.O.I (950º C)	2.06
Total	99.36
Alkals as Na_2O	
Insoluble Residue	
Free CaO	0.57
Calculated Compounds per ASTM C 150-97	
C_3S	51
C_2S	21
C_3A	7
C_4AF	8
ss(C_4AF+C_2F)	---

Table 5.6 Chemical Composition of Type III Portland Cement

	Series I			Series II			
Mix	I	II	III	I	II	III	IV
Water (lb)	15	15	16	1	16	16	16
Cement (lb)	29	29	29	15	27	24	21
C. aggregate (lb)	84	80	81	29	88	88	88
F. aggregate (lb)	54	59	57	84	55	55	54
Added P. carbonate by wt. of cement (lb)	1	1	1	54	1	1	1
Fly Ash (lb)					3	6	9

Table 5.7 Mixing Proportions of Each Series

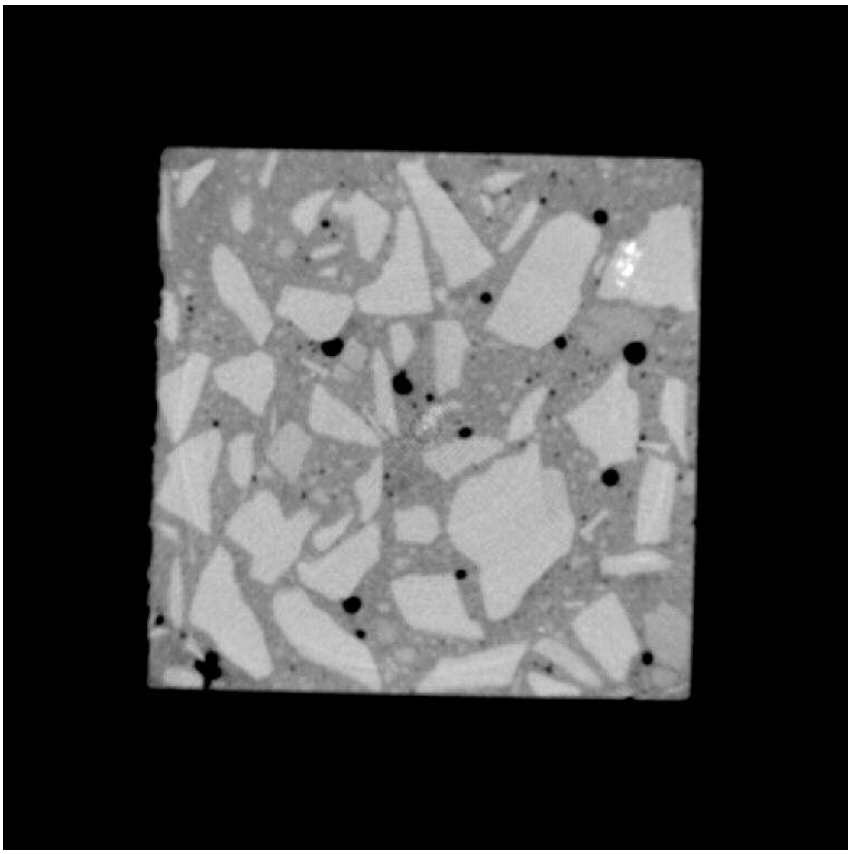

Figure 5.1 Unaltered Scan of an X-Ray Computed Tomographic Image

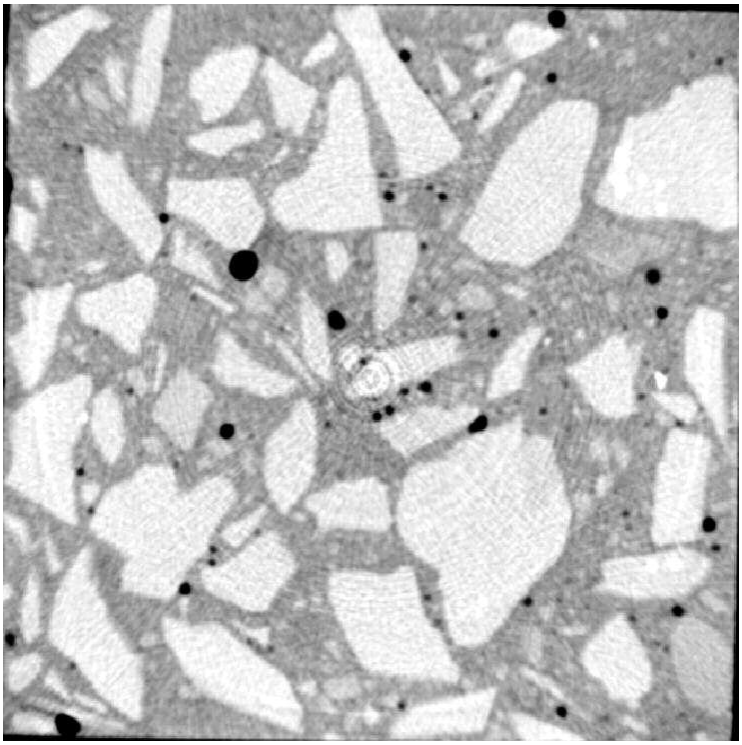

Figure 5.2 X-Ray Computed Tomographic Image that has been Cropped and Enhanced

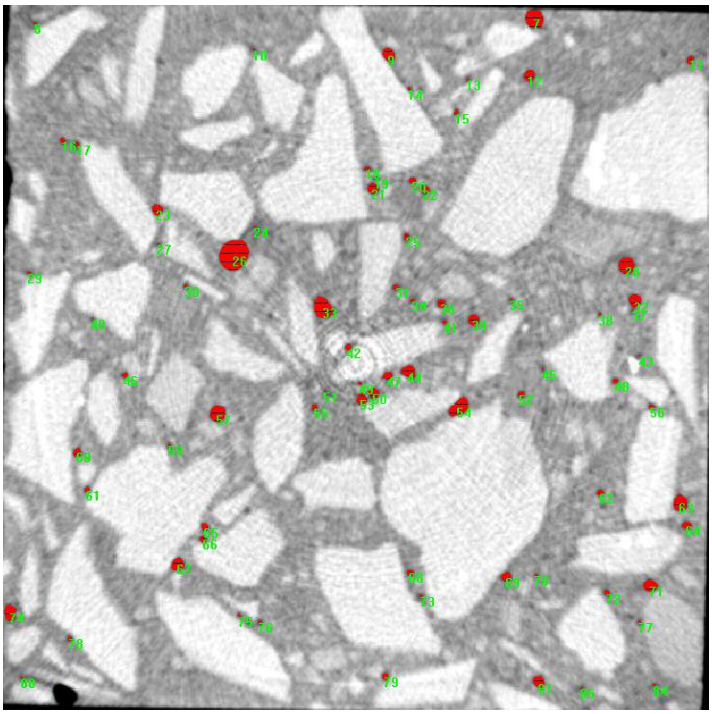

Figure 5.3 X-Ray Computed Tomographic Image Identifying Voids

CHAPTER 6

Results and Discussions

6.1 General

This chapter presents and discusses the results obtained from the investigation that has been performed on both series of experiments. The results are summarized and analyzed while trends and data are revealed. Comparisons of results to other applicable experiments are also investigated.

The experimental program was divided into two series, each being designed to study specific parameters. The purpose of series one is to investigate the effects of the various types of fine aggregates. While series two was designed to study the effect of the inclusion of fly ash in the cement mix.

The results gathered here will also be compared with those done by other test methods aimed at quantifying and analyzing pore structure in concrete. The results gained through computed tomography can be later grouped with those done by Azzam (2002) in an attempt to find correlations to further validate the study on ettringite.

6.2 Series One

The samples that were prepared in this series were all stored under water at room temperature in order to accelerate the delayed ettringite formation and cracking. Laurel, Frederick and Medford sands were chosen as the reactive, intermediary reactive and non-reactive aggregates respectively. However they also represent the natural and manufactured sands, where Laurel sand is the natural sand and Frederick and Medford

sands are manufactured crashed sands. All samples in this series were subjected to steam-curing which replicates the procedures performed during the precasting of concrete.

The results obtained from performing the CT analysis did not materialize as expected. The purpose of carrying out a CT scan on the specimens was to quantify the voids and reveal any internal cracks between the aggregate and cement paste. While the voids where easily determined from the scans, a reasonable quantification of cracks were not made through the CT analysis.

6.2.1 Specimens made with Laurel Sand

The results of the CT scans revealed that although the specimen made with Laurel sand did not quantitatively reveal cracking, it certainly influenced the size of pores formed and also the overall void percentage.

The results of the CT analysis made from the specimen containing Laurel sand is shown in this chapter. The images for each scan are displayed followed by a histogram of the pore size distribution on both diameter and volume. However, only the measurement data for scan #1 is shown as a representative data set for all the scans. Figure 6.1 and Tables 6.1a and b show the image and measurement data sheet for scan no.1 respectively. The data sheet shows that there are 71 voids (labeled as object #s) in this scan and it also lists the measurements corresponding to each void. Significant amounts of information are contained in the data sheet.

Tables 6.2 and 6.3 show the histogram data of the pore size distribution on diameter and volume respectively, while Figures 6.2 and 6.3 plot the charts of these histogram data. Table 6.2 shows that 51.43 % of the voids have diameters between 0.5

and 1mm which is the highest percentage of voids in the first scan. Table 6.3 shows that 24.29 % of the 71 voids have volumes between 0 and 0.5mm^3 which are the highest percentage of voids based on volume percentages.

To obtain the pore size distribution of the entire specimen the histograms of all the scans are compiled and grouped together. The scans of the entire specimen along with the plots of the histogram data are displayed in Figures 6.1 through 6.174, while the actual histogram data is shown in Tables 6.2 through 6.117. Note that for the specimen made with Laurel sand only fifty eight scans were compiled, two had been corrupted during the scanning process. After all the data from the fifty eight scans have been stored, this information was used to generate two other histograms showing the total pore size distribution on diameter and volume for the entire specimen.

Table 6.118 shows the histogram data for the pore size distribution on diameter and Figure 6.175 depicts the corresponding histogram plot. The data shows that pores in the range of 0.5mm to 1mm occupy 46.95% of the total pores, while those in the range of 0.1mm to 0.5mm occupied 29.58%. The other 23.74% where taken up by pores in the range of 1mm to 13mm. It can be seen that the pore size distribution of each scan is representative of the entire scan where approximately 50 % of the pores are within the ranges of 0.5 mm to 1mm in diameter.

The histogram data for the total pore size distribution on volume for the entire specimen is shown in Table 6.119, and its related plot is shown in Figure 6.176. The bin range chosen has yielded relatively even pore size distribution on volume. The volume range that occupies the largest percentage of pores is between 2 and 5mm^3 having 21.93%, the range between 1 and 2mm^3 consisted of the second largest amount of pores

taking up 21.69%. Bin range between 0 and 0.5mm^3 consists of 21.56%, while the range between 0.5 and 1mm^3 occupies 17.11% of the pores by volume. The remaining 17.71% takes up the wide range of 5 to 210mm^3.

6.2.2 Specimens made with Medford Sand

It was clear that the specimen made with Medford sand revealed no cracks whatsoever. The interfacial zone between the aggregates and cement paste did not show any separation. The entire CT results of the specimen containing Medford Sand is not shown, however a similar procedure as that performed in the specimen containing Laurel sand was undertaken.

The measurement data sheet for each of the sixty scans were stored and individual pore size distribution histograms were constructed and analyzed. The grouping of all the measurement data sheets from each scan was done, and the histogram data representing the total pore size distribution on diameter and volume were generated.

The histogram data shown in Table 6.120 and plotted in Figure 6.177 represent the total pore size distribution on diameter. It can be seen that 47.48% of the pores were in the range of 0.5 to 1mm which takes up the largest percentage of pores in the specimen. 27.69% of pores occupied the range of 0.1 to 0.5mm and the other 24.83% is lumped into the wide range of 1 to 13mm.

The histogram data and related plots depicting pore size distribution in relation to volume percentages are shown in Table 6.121 and Figure 6.178. The data shows that the largest pore sizes fell in the range of 2 to 5mm^3 with a percentage of 22.27%. The range of 0.0 to 0.5mm^3 comprised of 21.30%, followed by the range of 1 to 2mm^3 occupying

20.42% of the pores by volume. Pores in the bin range of 0.5 to 1mm^3 were next in line having 16.26%, while the remaining 19.75% of pores fell in the range of 5 to 120mm^3.

6.2.3 Specimens made with Frederick Sand

From both the visual inspections, and quantitative computations obtained from the scans it was also very clear that there were no internal cracking in the specimen containing Frederick sand. A similar procedure is performed on each scan producing pores size distribution plots on both diameter and volume. The data is stored and grouped, and histograms of the entire sample based on diameter and volume are then generated.

The histogram of the total pore size distribution on diameter is shown in Table 6.122 and plotted in Figure 6.179. The plot revealed that 46.61% of the pores fall between the ranges of 0.5 and 1mm, followed by 35.44% of pores being in the range of 0.1 to 0.5mm. Whereas the remaining pores fall between the ranges of 1 to 6mm and consisted of 17.95%.

In the same way the total pore size distribution on volume is shown via histogram data in Table 6.123 and plotted in Figure 6.180. The data shows that similar to the Laurel and Medford sands, the pore size distribution is relatively evenly distributed around the ranges chosen. 25.35% of the pores falls in the range of 0.0 to 0.5mm^3 and 21.26% are in the range of 1 to 2mm^3 which represents the two larger percentages. Followed closely behind in percentages where pores in the range of 2 to 5mm^3 having 21.08%, while pores in the range of 0.5 to 1mm^3 had 17.65%. The other 14.46% were contained in the range of 5 to 60mm^3.

6.2.4 Comparison of Samples Having Different Fine Aggregates

To aid in the comparison of the differences in pore size distribution on diameter for the specimens made with various types of fine aggregate, a Table which grouped the results was created. Table 6.132 compares the pore size distribution for different samples based on diameter.

In terms of actual pore sizes, it was expected that the non-reactive aggregate would have the lowest percentage of large pores (1 to 13mm). However, this was not confirmed by the CT analysis. Frederick sand, which is the intermediary reactive sand, had 17.95% of its pores in the range of 1 to 13mm. While the samples containing the reactive (Laurel sand) and non- reactive (Medford sand) sands had 23.74% and 24.83% of pores in the range of 1 to 13mm

The percentage of small holes (0.1 to 0.5mm) first increased before decreasing when comparing the transition from the reactive aggregate to the non-reactive aggregates. Results from the specimen made with Laurel sand showed that 29.58% of its pores belong in the range of 0.1 to 0.5mm. In comparison 35.44% and 27.69% of the pores belonging to Frederick and Medford sands respectively for that range.

Along with the pore size distribution, calculating the overall porosity is another important measurement that will enable researches to determine how durable a concrete member will be. Porosity, therefore being one of the objectives of this experiment was calculated for each specimen in true tree-dimensional manner.

As described in previous sections, the CT analysis involves taking scans of a sample at specified intervals; with this experiment sixty scans were generated each having a thickness of 4.7625mm (0.1875 in). Also as depicted in the measurement data

sheets, there is an area measurement included for each void in a scan. Therefore in order for the true porosity of a sample to be determined the areas of the voids in each scan have to be multiplied by 4.7625mm to obtain the volume of each void section. Taking a sum of all the void section volumes and dividing by the total volume of the sample will yield the void ratio. The porosity is then easily calculated by multiplying by 100%.

This procedure was carried out for all three samples to obtain their porosities. The porosities are 1.31%, 0.56%, 0.66%, and for Laurel, Frederick and Medford sands respectively. The results were then plotted on a bar graph for comparison, and are shown in Figure 6.181.

6.3 Series Two

The samples that were cast in this series consisted of a control specimen in which no fly ash was present, and three other samples having 10%, 20% and 30% of fly ash respectively. The purpose of this series was to analyze the effects of adding different percentages of Class F fly ash as a partial replacement to the cement.

The mixing materials and proportions are the same for all four specimens. Portland cement type III was used in all batches as this type favors the formation of DEF due to the higher amounts of sulfate that it contains. Also Laurel sand was used as the fine aggregate because it promotes the delayed ettringite formation more readily than Frederick and Medford sands. The alkali level of all the samples were also increased by adding potassium carbonate at 1% of the weight of cement, this condition also promotes the formation of DEF. Class F fly ash was chosen to minimize the formation of DEF as it

contains the lowest amounts of sulfur. Also, all samples in this series were exposed to a water curing regime.

X-ray computed tomography is a technique that can be used to unveil interior cracking and voids in a concrete section. The CT analysis did not reveal any cracking in either the control specimen or in any of the samples made with Fly Ash. However the computed tomography allowed for the determination of pores and a distribution of the pore sizes in each specimen. The information gained from this process is vital for obtaining measurements, making comparisons between samples and for the overall validation of the experiment. The sections that follow provide a more detailed discussion of the results.

6.3.1 Control Sample

Since there was no Fly Ash present in the control specimen, it was expected that there would be internal cracks large enough to be detected by the CT system. Once again the CT scans did not reveal any internal cracking but did reveal void spaces which were captured and analyzed. A measurement data sheet was created for each scan and the histogram data for the pore size distribution on diameter and volume were generated and plotted in chart format. The entire results are not displayed in this thesis, however the format is similar to that displayed for the specimen containing Laurel sand. The results were also grouped together to obtain two histograms displaying the pore size distribution of both the diameter and volume.

The total histogram data of the pore size distribution on diameter for the control specimen is shown in Table 6.124 and plotted in Figure 6.182. It can be seen that 37.33%

of the pores fall in the range of 0.5 to 1mm, 31.53% lie between 0.1 and 0.5mm and the other 31.14% is grouped in the large range of 1mm to 13mm.

Table 6.125 displays the total histogram data of the pore size distribution on volume for the control specimen, and its plot is shown in Figure 6.183. The range that occupies the largest percentage of pores falls between 2 to 5mm^3 having 25.62%, the range of 1 to 2mm^3 had the second largest amount taking up 24.71%. The range of 0.5 to 1mm^3 had 16.39% followed by the range of 0 to 0.5mm^3, which occupies 14.17%. Pores in the range of 5 to 120mm^3 occupied the other 14.46%.

6.3.2 Samples Containing 10%, 20% and 30% Fly Ash

The computed tomographic analysis revealed that there were no internal cracking in any of the samples containing Fly ash. All the images consistently showed a smooth transition from cement paste to aggregate without any openings. Once again the void spaces were captured and analyzed by a similar procedure as mentioned in previous samples.

The pore size distribution data on diameter and volume for each scan in all the specimens were compiled, stored and grouped. The total histogram data for each sample containing fly ash is grouped separately and are depicted below in Tables 6.126 through 6.131 and plotted in Figures 6.184 through 6.189. In all the specimens, the range of 0.5 to 1mm occupied the majority of the pores based on the diameter measurement. The percentages were 33.55%, 44.06% and 47.66% for samples containing 10%, 20% and 30% Fly Ash respectively.

Based on volume percentages most of the pores fell in the range of 2 to 5mm^3, this was the case for all samples in this series. The percentages for specimens containing 10%, 20% and 30% were 27.74%, 26.64% and 21.77% respectively.

6.3.3 Comparison of Samples with Different Fly Ash Percentages

When comparing the specimens in series two, the sample containing 0% Fly Ash is expected to reveal more cracks, have a larger porosity percent, and have a greater percent of its pores occupying larger diameters. As can be seen by Table 6.133 the results did not completely agree with what was expected. Table 6.133 compares the pore size distribution on diameter for each sample containing different percentages of Fly Ash.

Calculating the overall porosity is another important objective of this experiment, it also presented itself as an ideal measure on which to compare the different specimens. The porosity of each specimen in the series is calculated in a manner similar to that of series one. The porosities as shown in Figure 6.190 are 1.01%, 0.73%, 0.51% and 0.69% for samples containing 0%, 10%, 20% and 30% of Fly Ash respectively.

6.4 Discussions

6.4.1 Series One

According to Azzam 2002, scanning electron microscope and quantitative x-ray diffraction methods have observed the formation of ettringite in the sample containing Laurel sand. Azzam's report also noted that the expansion observed for the Laurel specimen was the greatest among the samples in the series. This confirms the presence of ettringite in the samples.

As expected, the Laurel sand had the highest porosity percent which was also more than twice that of Frederick and Medford sands. Since Laurel sand had the highest alkali silica reactivity, the specimen that contained Laurel sand was more susceptible to the environment that favored ettringite development. The common theory stipulates that DEF causes expansion and internal cracking; this would explain the increase in the porosity. However, CT analysis did not reveal any internal cracks in any of the specimens investigated, possible explanations for this includes:

- The development of DEF in a concrete structure can cause expansion and internal cracking to occur. It is then possible for ettringite needles to fill in between these cracks. This would create a difficulty for the CT system in classifying such ettringite filled regions as pores, and would explain the increase in porosity in the sample.
- The Dugan Heat Cycle was designed for samples of much smaller size than those created in this experiment, therefore the effect it would have on large specimens would not be as severe. Consequently it is believed that cracking did occur but was out of the observable range of the CT system. It is possible that crack detection can be made possible via the use of another technique.

The specimen containing Frederick sand had a lower void percentage than that of the Medford Sand. The CT results are consistent with SEM analysis and expansion results done by Azzam 2002. It was shown that the sample containing Medford sand exhibited higher expansion values and higher concentration of ettringite around the aggregate than the sample containing Frederick sand.

6.4.2 Series Two

Azzam reported that ettringite was not detected by SEM or quantitative x-ray diffraction (QXRD) analysis in any of the samples containing Fly Ash. Also, CT technology did not reveal any cracks in these specimens. With the exception of the control sample, the overall trend as the Fly Ash percentage increased was for the larger size pores (1 to 13mm) to decrease and for smaller size pores (0.5 to 1mm) to increase. This will of course yield to a more durable structure as the large pores decrease.

The porosity constantly decreased from a sample containing 0% Fly Ash to 20% Fly Ash, this proves that Fly Ash is essential for enhancing durability in concrete structures. There was however a slight increase in the porosity at 30 %, it is possible that the benefits of replacing cement with class F Fly Ash reaches a limit around 20% by weight. Nevertheless further research will be needed to explain this occurrence.

6.4.3 General

From the vast amounts of results gained, it can be seen that computed tomography is a very powerful tool. The method that is commonly employed to obtain the pore sizes in concrete samples is known as mercury intrusion porosimetry (MIP). With this method of analysis, mercury is forced to penetrate the pores in the concrete specimen, and then measurements are taken. Computed tomography has several advantages over this method as will be discussed.

With computed tomography the results that are gained are actual spatial information from the density and composition of the samples. In comparison, the mercury intrusion technique first assumes the shape of the pores before determining their

diameter. Another critical advantage with the CT analysis is that with the incorporation of Image Pro Plus a distinction can be made between naturally formed round pores and cracks that are noted by their flat and long shape. This division is made possible by the use of shape parameters for example the “Roundness” or the “Aspect ratio” measurement.

It should be noted that the results on pore size distribution were displayed in both diameters and volume units. Showing results in terms of diameters allows for a comparison with the other related techniques, however the true power of the CT system is its ability to incorporate a three dimensional analysis. Performing the total CT analysis on the samples described is vital as it further validates the experiment done by Azzam (2002), and should allow for the observations of correlations between ettringite formation and an increased void ratio. This will eventually allow researchers to have a better understanding about the processes influencing DEF so that more durable concrete can be produced.

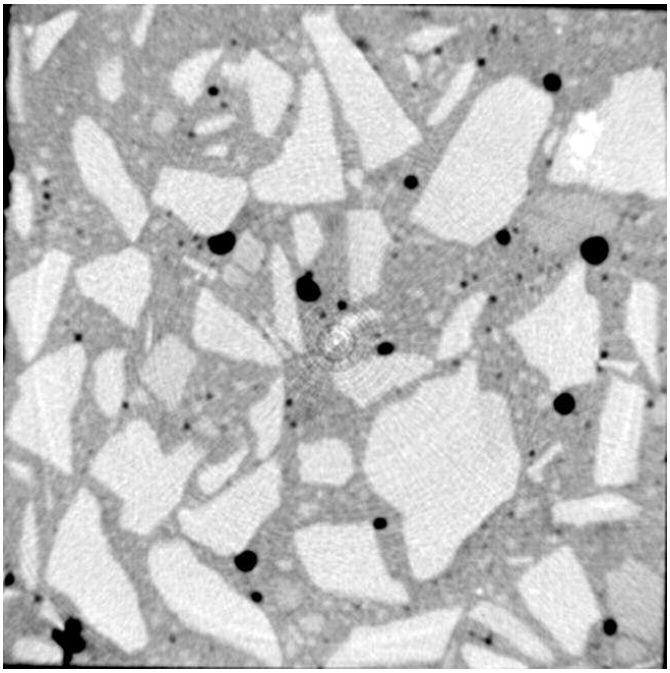

Figure 6.1 X-ray Computed Tomographic Image for Scan #1 of Specimen made with Laurel Sand

Object #	Area (mm^2)	Aspect Ratio	Max Diameter (mm)	Mean Diameter (mm)	Perimeter	Roundness	Per Area (Obj)	Volume (mm^3)
24	8.8999567	1.0352593	3.4291008	3.2590821	10.448102	1	0.0015478	42.3860438
31	7.6863265	1.3171734	3.5527112	3.0089688	10.374489	1.1143067	0.00133674	36.60613
22	7.0525417	1.3620961	3.3495283	2.8851061	9.6321402	1.0468636	0.00122652	33.5877298
61	5.4073982	1.158463	2.7208724	2.5398366	8.0748672	1	0.00094041	25.7527339
49	5.2590656	1.0502453	2.6480346	2.4859502	7.95785	1	0.00091461	25.0462999
10	4.0724044	1.0754481	2.2873776	2.1664331	6.9170833	1	0.00070824	19.394826
66	2.8587742	1.2470946	2.004611	1.7800467	5.8604684	1	0.00049717	13.6149121
20	2.7104416	1.1104922	1.9465929	1.7681971	5.6742826	1	0.00047137	12.9084781
42	2.6430175	1.4481277	2.1030951	1.8033884	5.7180891	1	0.00045965	12.5873708
16	2.3193827	1.0563319	1.6747642	1.6118945	5.1351218	1	0.00040336	11.0460601
59	1.9552937	1.1559873	1.6504321	1.4713027	4.6700087	1	0.00034004	9.31208625
63	1.6721132	1.4292442	1.6422414	1.3655373	4.416225	1	0.0002908	7.96343912
64	1.5372653	1.3251187	1.5140717	1.2781118	4.2590232	1	0.00026734	7.32122599
37	1.2271153	1.1070936	1.2560731	1.1528761	3.7400441	1	0.00021341	5.84413662
12	1.1731762	1.2129281	1.2983057	1.1246154	3.6775708	1	0.00020402	5.58725165
6	1.0383283	1.5527667	1.3240173	1.1655954	3.3399894	1	0.00018057	4.94503853
9	0.75514787	1.1621935	0.92899203	0.89111054	2.8459742	1	0.00013132	3.59639173
40	0.67423916	1.1124306	0.90695745	0.86804461	2.7273316	1	0.00011725	3.211064
68	0.67423916	1.0589545	0.93622166	0.82774717	2.7233982	1	0.00011725	3.211064
4	0.5933305	1.4358251	0.88437402	0.72243297	2.3687294	1	0.00010318	2.82573651
44	0.57984567	1.0899594	0.89512038	0.85818118	2.4750323	1	0.00010084	2.761515
36	0.56636089	1.0771837	0.88322091	0.85157812	2.3316464	1	0.00009849	2.69729374
65	0.56636089	1.0190684	0.82112068	0.7823385	2.4787571	1	0.00009849	2.69729374
18	0.52590656	1.1908394	0.89186502	0.82040155	2.3461077	1	0.00009146	2.50462999

Table 6.1a Measurement Data Sheet for Scan #1 of Specimen made with Laurel Sand

Object #	Area (mm^2)	Aspect Ratio	Max Diameter (mm)	Mean Diameter (mm)	Perimeter	Roundness	Per Area (Obj)	Volume (mm^3)
51	0.51242179	1.1998167	0.88392705	0.81032276	2.2260277	1	0.00008911	2.44040877
35	0.45848262	1.0655525	0.78862154	0.76436365	2.0726991	1	0.00007973	2.18352348
38	0.4180283	1.2026131	0.80845517	0.74035197	1.9888939	1	0.0000727	1.99085978
55	0.4180283	1.0825069	0.7599991	0.73103619	1.850044	1	0.0000727	1.99085978
8	0.40454352	1.1204007	0.75671041	0.71605158	1.8495597	1	0.00007035	1.92663851
54	0.37757394	1.0186497	0.69826603	0.69187403	1.964398	1	0.00006566	1.79819589
57	0.31015003	1.1566895	0.67524433	0.62950873	1.7118878	1	0.00005393	1.47708952
14	0.29666525	1.3813253	0.71877426	0.61956275	1.7006632	1	0.00005159	1.41286825
53	0.29666525	1.1192293	0.64824414	0.61371607	1.5973884	1	0.00005159	1.41286825
34	0.28318045	1.1292325	0.64330262	0.60649192	1.5379736	1	0.00004924	1.34864689
52	0.28318045	1.2876924	0.68011618	0.60414141	1.4644312	1	0.00004924	1.34864689
32	0.26969567	1.46385	0.70284057	0.59148604	1.509065	1	0.0000469	1.28442563
23	0.2427261	1.3879785	0.64926183	0.55851847	1.5774611	1	0.00004221	1.15598305
25	0.21575654	1.2520046	0.58349359	0.5247705	1.4089403	1	0.00003752	1.02754052
2	0.20227176	1.4265712	0.60200781	0.51200205	1.3794599	1	0.00003517	0.96331926
15	0.20227176	1.1470787	0.53992742	0.50531262	1.288867	1	0.00003517	0.96331926
33	0.20227176	1.3190906	0.58025676	0.51007414	1.1765523	1	0.00003517	0.96331926
50	0.20227176	1.137147	0.53875488	0.5062663	1.2273432	1	0.00003517	0.96331926
26	0.18878697	1.286718	0.55344337	0.49178177	1.0334116	1	0.00003283	0.89909794
69	0.18878697	1.3483994	0.56220108	0.48957032	1.1204227	1	0.00003283	0.89909794
7	0.17530218	1.1737211	0.50664234	0.46914858	1.1109977	1	0.00003048	0.83487663
13	0.17530218	1.462396	0.57009089	0.47996217	1.0933679	1	0.00003048	0.83487663
17	0.17530218	1.173722	0.50664246	0.46914852	1.1592764	1	0.00003048	0.83487663
21	0.17530218	1.1737211	0.50664234	0.46914858	1.110996	1	0.00003048	0.83487663
27	0.17530218	1.173722	0.50664246	0.46914852	1.1592779	1	0.00003048	0.83487663
39	0.17530218	1.173722	0.50664246	0.46914852	1.159278	1	0.00003048	0.83487663
46	0.17530218	1.1737213	0.50664234	0.46914852	0.99245334	1	0.00003048	0.83487663
45	0.1618174	1.6485286	0.57556593	0.46235257	1.111218	1	0.00002814	0.77065537
29	0.10787827	1.2649115	0.40947974	0.36660087	0.78257459	1	0.00001876	0.51377026
58	0.10787827	1.2649115	0.40947974	0.36660087	0.78257734	1	0.00001876	0.51377026
47	0.09439348	1.8073928	0.46528304	0.36135817	0.86004049	1	0.00001641	0.44954895
70	0.09439348	2.1807593	0.49702826	0.36247176	0.69674379	1	0.00001641	0.44954895
60	0.0809087	1.6329931	0.3944034	0.31796259	0.58061677	1	0.00001407	0.38532768
19	0.06742391	1.7320507	0.3724775	0.29376376	0.41414413	1	0.00001172	0.32110637
28	0.06742391	1.732051	0.3724775	0.29376373	0.45910287	1	0.00001172	0.32110637
41	0.06742391	1.7320506	0.37247747	0.29376373	0.42892727	1	0.00001172	0.32110637
11	0.05393913	1.0000001	0.24670592	0.24670592	0.2322472	1	0.00000938	0.25688511
56	0.05393913	1.0000001	0.24670592	0.24670592	0.23225483	1	0.00000938	0.25688511
62	0.05393913	1.0000001	0.24670592	0.24670592	0.23224398	1	0.00000938	0.25688511
71	0.05393913	7.136498	0.46449599	0.29031	0.69674402	1	0.00000938	0.25688511
1	0.04045435	4.5135175	0.34837201	0.23224801	0.46449602	1	0.00000703	0.19266384
30	0.04045435	1.7320505	0.28302166	0.22321215	0.116124	1	0.00000703	0.19266384
48	0.04045435	1.7320505	0.28302166	0.22321215	0.16422413	1	0.00000703	0.19266384
3	0.02696956	2.2567587	0.23224799	0.17418599	0.23224801	1	0.00000469	0.12844253
5	0.02696956	2.2567587	0.23224799	0.17418599	0.23224801	1	0.00000469	0.12844253
67	0.02696956	2.2567587	0.23224799	0.17418599	0.23224801	1	0.00000469	0.12844253
43	0.01348478	1	0.116124	0.116124	0.116124	1	0.00000234	0.06422126

Table 6.1b Continuation of Measurement Data Sheet for Scan #1 of Specimen made with Laurel Sand

Bins (mm)	Frequency	Cumulative %	Relative %
0.1	0	.00%	0.00%
0.5	19	27.14%	27.14%
1	36	78.57%	51.43%
1.5	3	82.86%	4.29%
2	5	90.00%	7.14%
2.5	3	94.29%	4.29%
3	2	97.14%	2.86%
6	2	100.00%	2.86%
13	0	100.00%	0.00%

Table 6.2 Histogram Data of Scan #1 for the Pore Size Distribution on Diameter of Specimen made with Laurel Sand

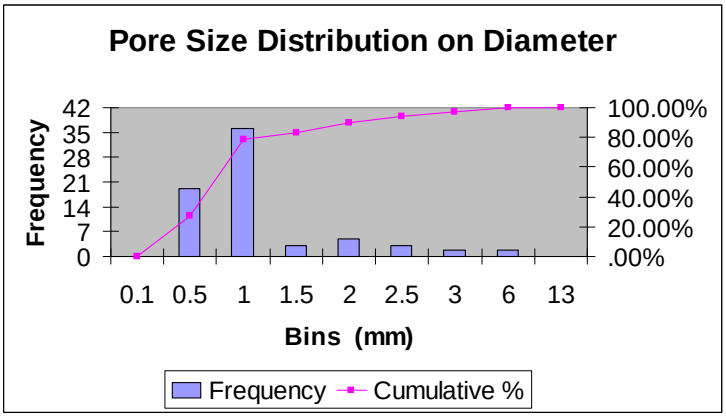

Figure 6.2 Histogram Plot of Scan #1 for the Pore Size Distribution on Diameter of Specimen made with Laurel Sand

Bins (mm^3)	Frequency	Cumulative %	Relative %
0.5	17	24.29%	24.29%
1	16	47.14%	22.86%
2	12	64.29%	17.14%
5	11	80.00%	15.71%
15	9	92.86%	12.86%
30	3	97.14%	4.29%
60	2	100.00%	2.86%
120	0	100.00%	0.00%
210	0	100.00%	0.00%

Table 6.3 Histogram Data of Scan #1 for the Pore Size Distribution on Volume of Specimen made with Laurel Sand

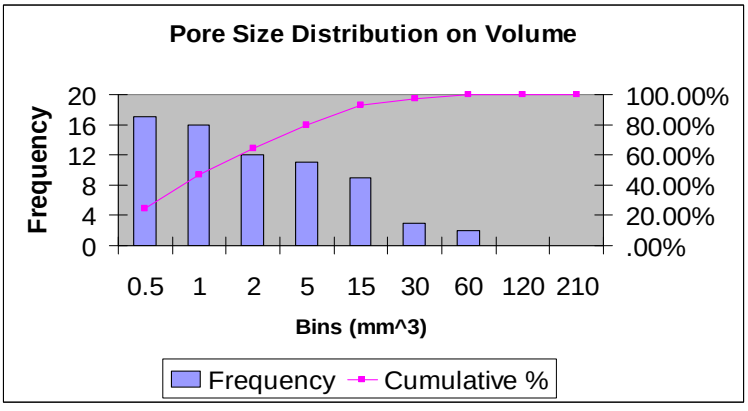

Figure 6.3 Histogram Plot of Scan #1 for the Pore Size Distribution on Volume of Specimen made with Laurel Sand

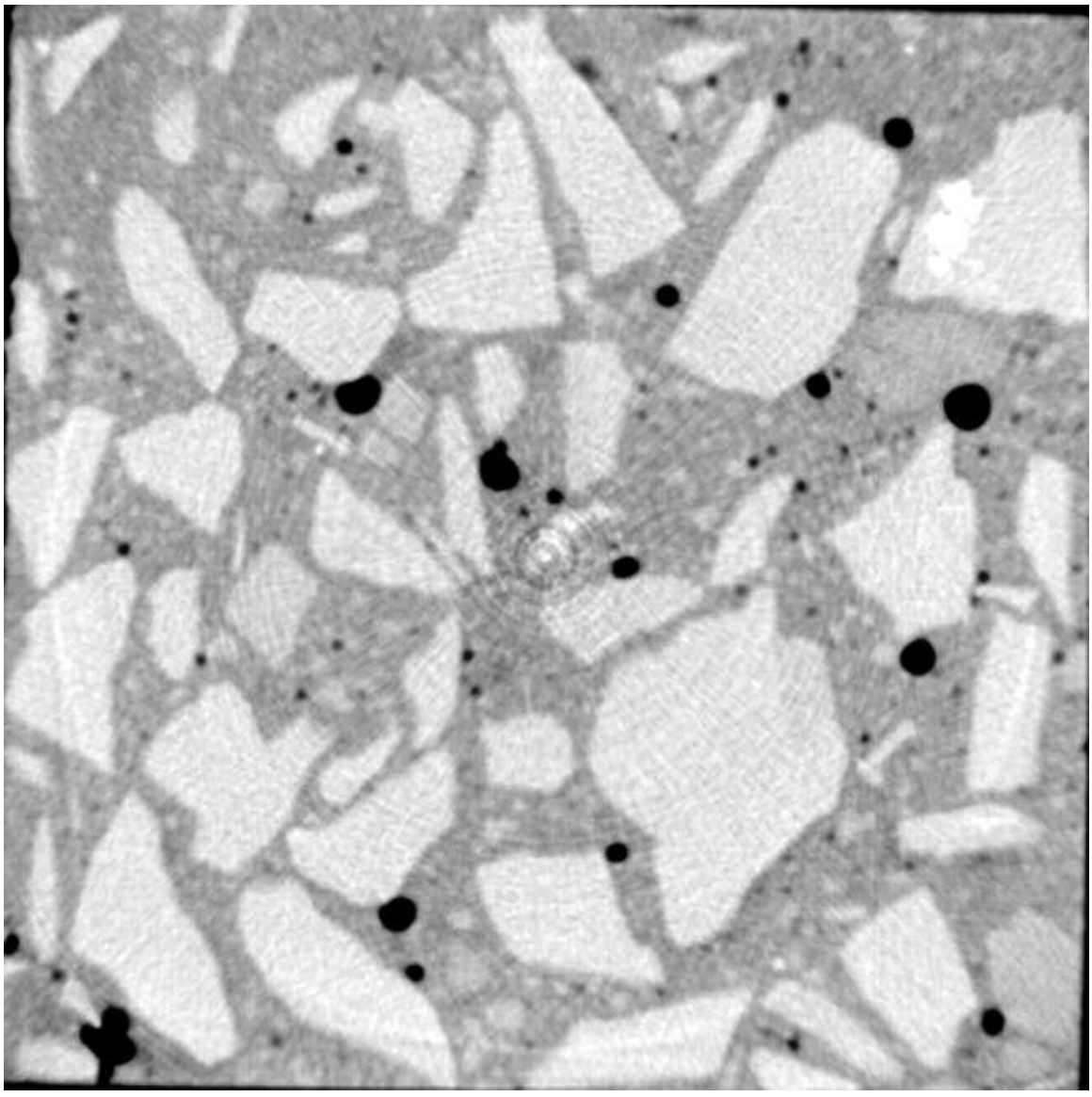

Figure 6.4 X-ray Computed Tomographic Image for Scan #2 of Specimen made with Laurel Sand

Bins (mm)	Frequency	Cumulative %	Relative %
0.1	0	.00%	0.00%
0.5	26	32.50%	32.50%
1	39	81.25%	48.75%
1.5	3	85.00%	3.75%
2	5	91.25%	6.25%
2.5	3	95.00%	3.75%
3	2	97.50%	2.50%
6	2	100.00%	2.50%
13	0	100.00%	0.00%

Table 6.4 Histogram Data of Scan #2 for the Pore Size Distribution on Diameter of Specimen made with Laurel Sand

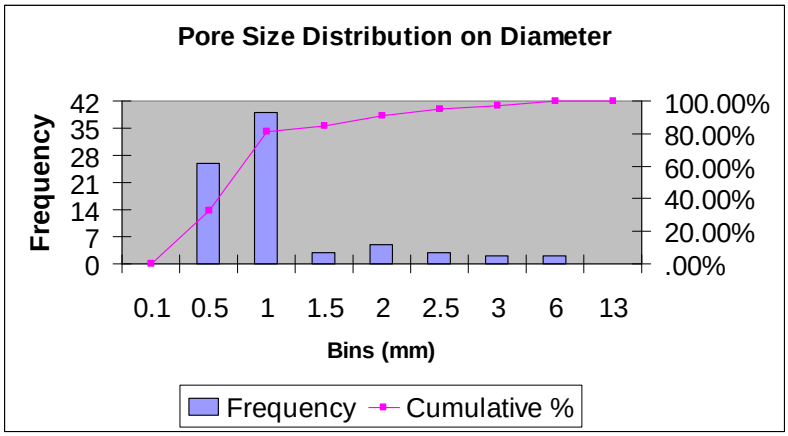

Figure 6.5 Histogram Plot of Scan #2 for the Pore Size Distribution on Diameter of Specimen made with Laurel Sand

Bins (mm^3)	Frequency	Cumulative %	Relative %
0.5	21	26.25%	26.25%
1	13	42.50%	16.25%
2	19	66.25%	23.75%
5	12	81.25%	15.00%
15	10	93.75%	12.50%
30	3	97.50%	3.75%
60	2	100.00%	2.50%
120	0	100.00%	0.00%
210	0	100.00%	0.00%

Table 6.5 Histogram Data of Scan #2 for the Pore Size Distribution on Volume of Specimen made with Laurel Sand

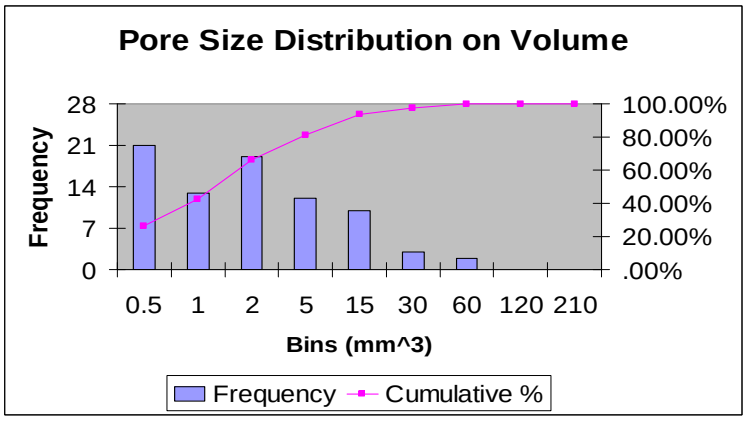

Figure 6.6 Histogram Plot of Scan #2 for the Pore Size Distribution on Volume of Specimen made with Laurel Sand

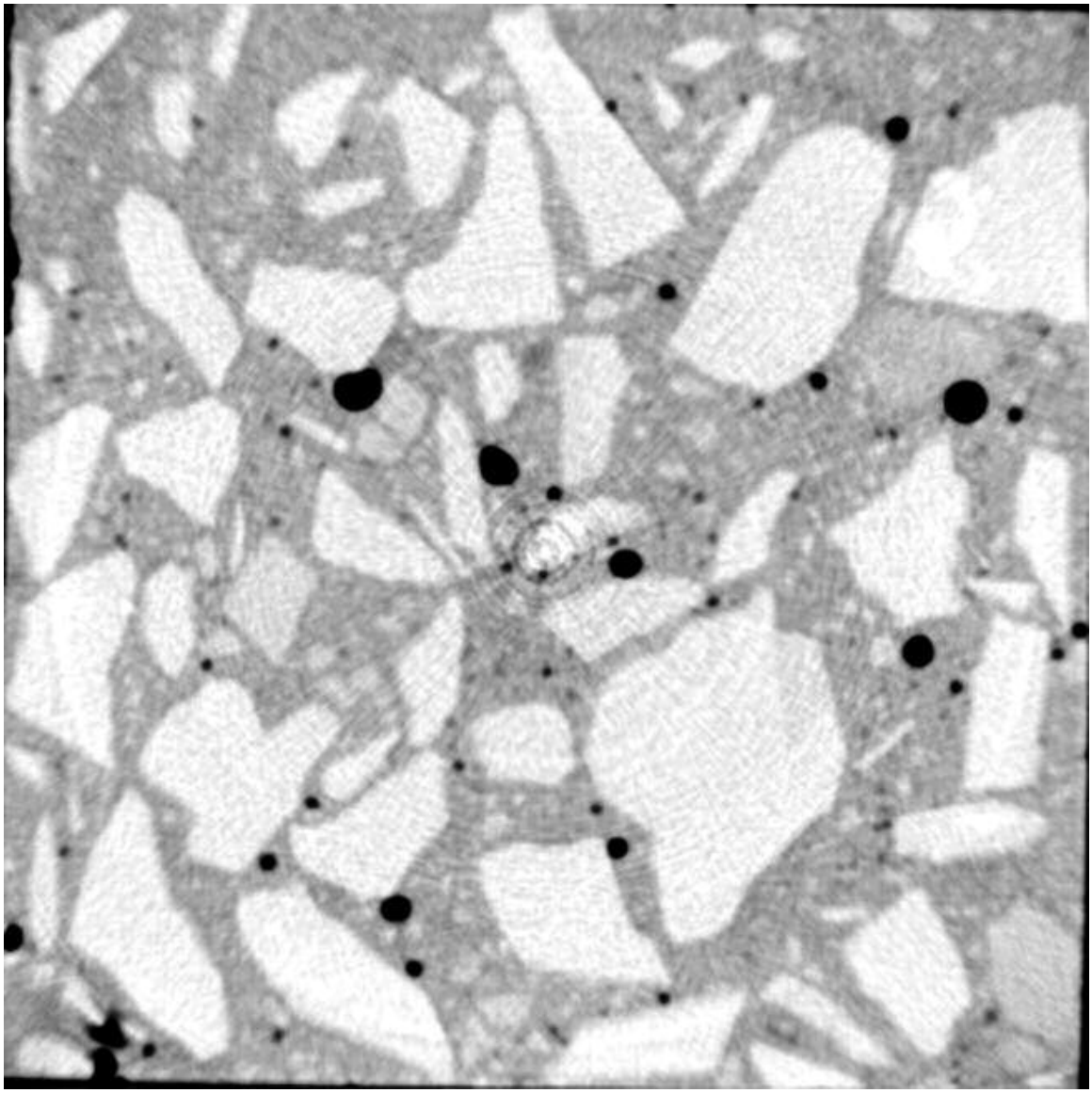

Figure 6.7 X-ray Computed Tomographic Image for Scan #3 of Specimen made with Laurel Sand

Bins (mm)	Frequency	Cumulative %	Relative %
0.1	0	.00%	0.00%
0.5	18	26.09%	26.09%
1	35	76.81%	50.72%
1.5	8	88.41%	11.59%
2	2	91.30%	2.90%
2.5	4	97.10%	5.80%
3	0	97.10%	0.00%
6	2	100.00%	2.90%
13	0	100.00%	0.00%

Table 6.6 Histogram Data of Scan #3 for the Pore Size Distribution on Diameter of Specimen made with Laurel Sand

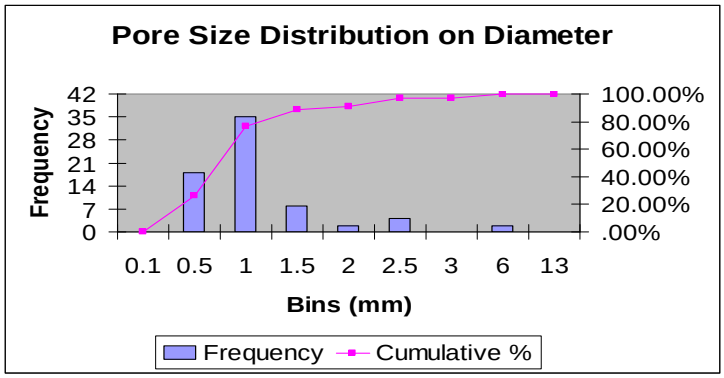

Figure 6.8 Histogram Plot of Scan #3 for the Pore Size Distribution on Diameter of Specimen made with Laurel Sand

Bins (mm^3)	Frequency	Cumulative %	Relative %
0.5	13	18.57%	18.57%
1	14	38.57%	20.00%
2	10	52.86%	14.29%
5	18	78.57%	25.71%
15	9	91.43%	12.86%
30	3	95.71%	4.29%
60	3	100.00%	4.29%
120	0	100.00%	0.00%
210	0	100.00%	0.00%

Table 6.7 Histogram Data of Scan #3 for the Pore Size Distribution on Volume of Specimen made with Laurel Sand

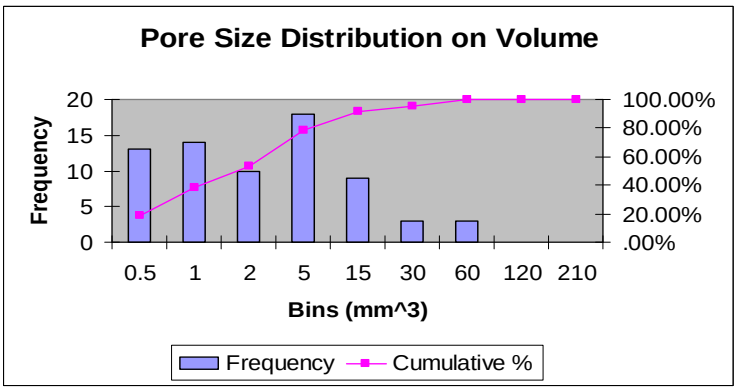

Figure 6.9 Histogram Plot of Scan #3 for the Pore Size Distribution on Volume of Specimen made with Laurel Sand

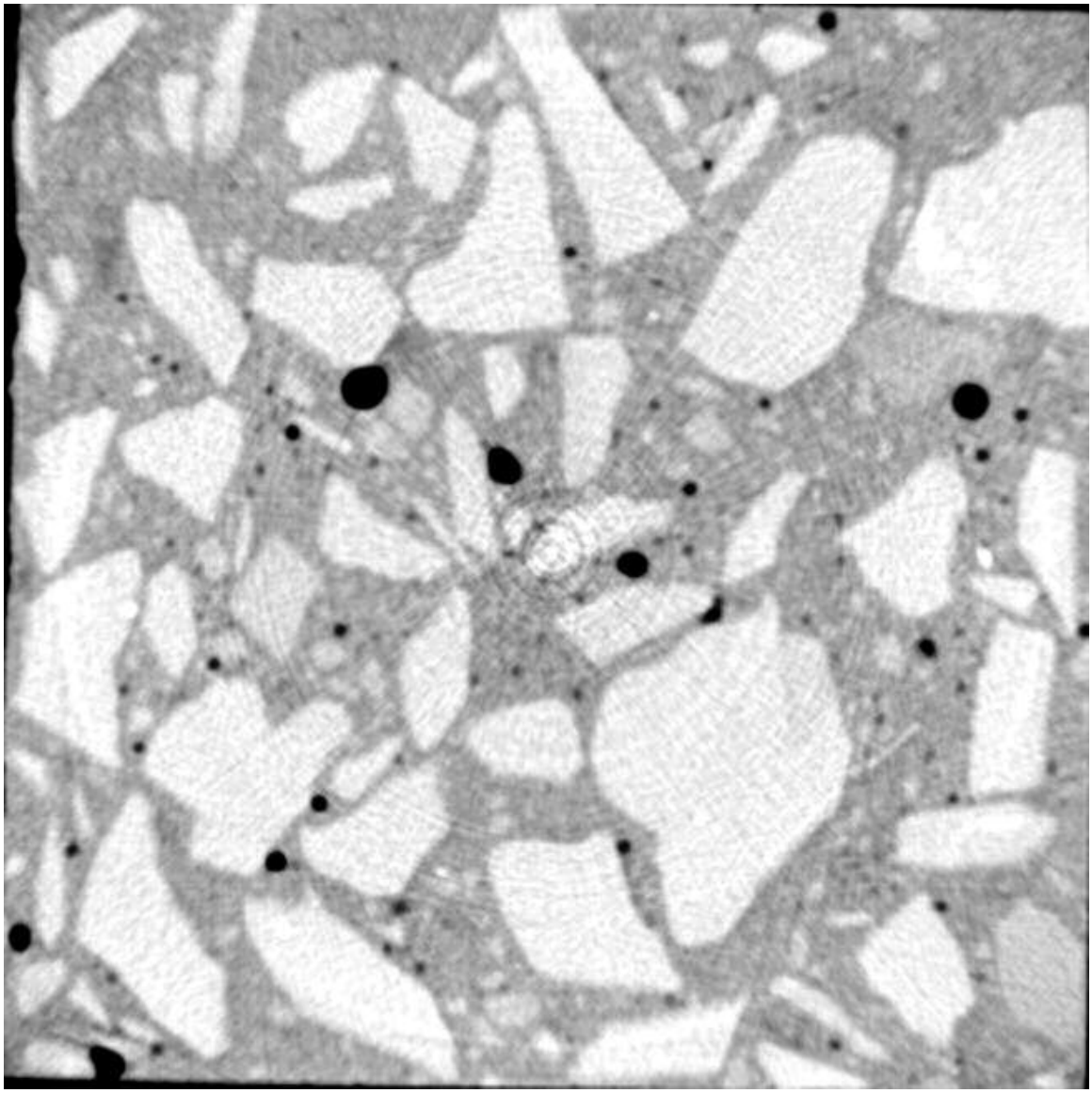

Figure 6.10 X-ray Computed Tomographic Image for Scan #4 of Specimen made with Laurel Sand

Bins (mm)	Frequency	Cumulative %	Relative %
0.1	0	.00%	0.00%
0.5	27	37.50%	37.50%
1	33	83.33%	45.83%
1.5	5	90.28%	6.94%
2	1	91.67%	1.39%
2.5	3	95.83%	4.17%
3	1	97.22%	1.39%
6	2	100.00%	2.78%
13	0	100.00%	0.00%

Table 6.8 Histogram Data of Scan #4 for the Pore Size Distribution on Diameter of Specimen made with Laurel Sand

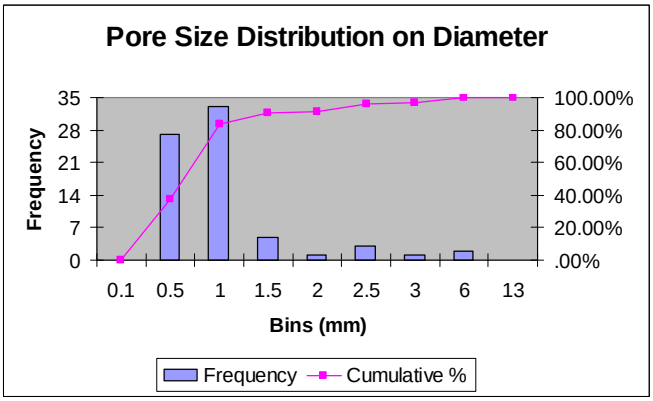

Figure 6.11 Histogram Plot of Scan #4 for the Pore Size Distribution on Diameter of Specimen made with Laurel Sand

Bins (mm^3)	Frequency	Cumulative %	Relative %
0.5	20	27.78%	27.78%
1	10	41.67%	13.89%
2	18	66.67%	25.00%
5	14	86.11%	19.44%
15	6	94.44%	8.33%
30	3	98.61%	4.17%
60	1	100.00%	1.39%
120	0	100.00%	0.00%
210	0	100.00%	0.00%

Table 6.9 Histogram Data of Scan #4 for the Pore Size Distribution on Volume of Specimen made with Laurel Sand

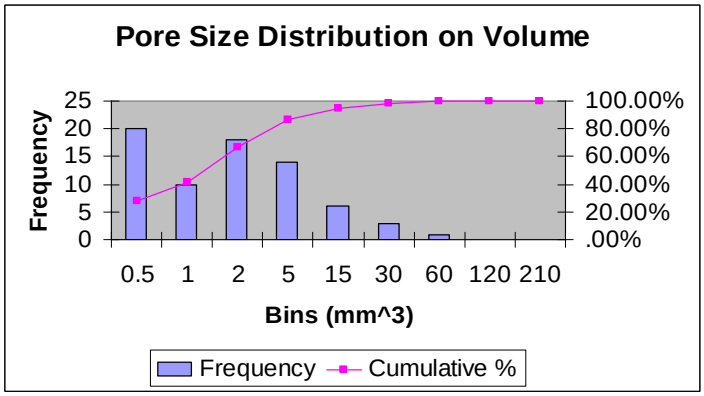

Figure 6.12 Histogram Plot of Scan #4 for the Pore Size Distribution on Volume of Specimen made with Laurel Sand

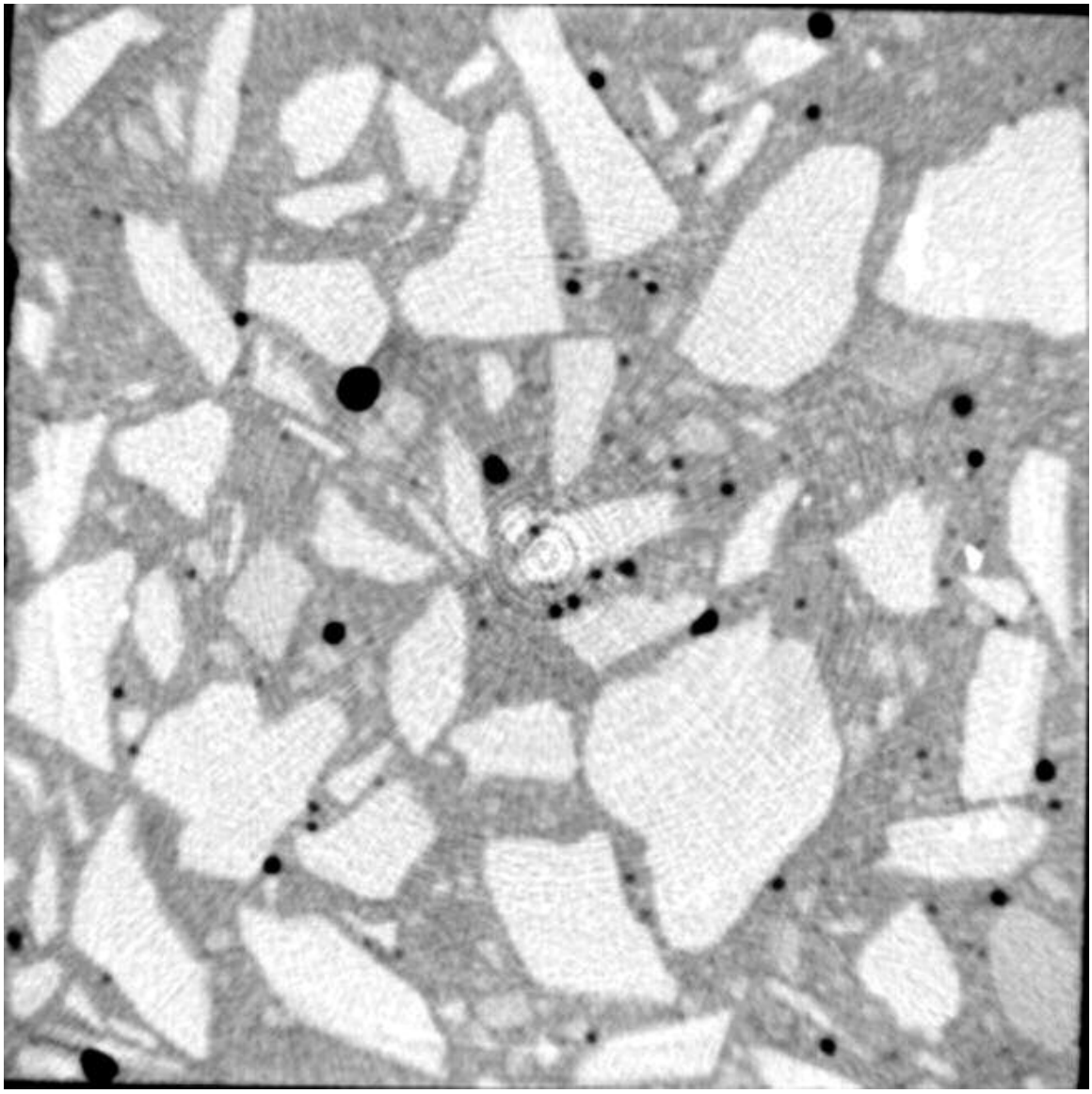

Figure 6.13 X-ray Computed Tomographic Image for Scan #5 of Specimen made with Laurel Sand

Bins (mm)	Frequency	Cumulative %	Relative %
0.1	0	.00%	.00%
0.5	30	39.47%	39.47%
1	27	75.00%	35.53%
1.5	12	90.79%	15.79%
2	4	96.05%	5.26%
2.5	2	98.68%	2.63%
3	0	98.68%	0.00%
6	1	100.00%	1.32%
13	0	100.00%	0.00%

Table 6.10 Histogram Data of Scan #5 for the Pore Size Distribution on Diameter of Specimen made with Laurel Sand

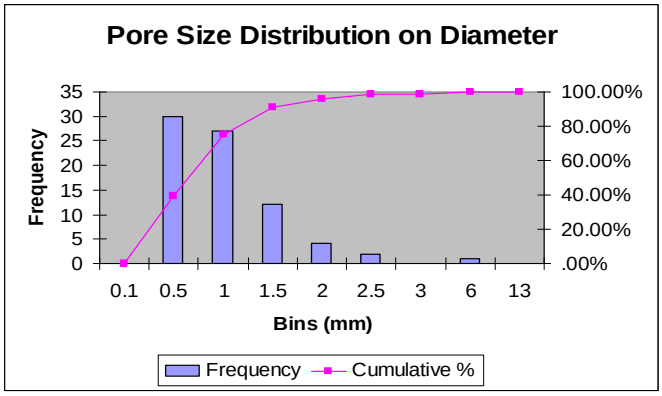

Figure 6.14 Histogram Plot of Scan #5 for the Pore Size Distribution on Diameter of Specimen made with Laurel Sand

Bins (mm^3)	Frequency	Cumulative %	Relative %
0.5	25	32.89%	32.89%
1	5	39.47%	6.58%
2	18	63.16%	23.68%
5	14	81.58%	18.42%
15	12	97.37%	15.79%
30	1	98.68%	1.32%
60	1	100.00%	1.32%
120	0	100.00%	0.00%
210	0	100.00%	0.00%

Table 6.11 Histogram Data of Scan #5 for the Pore Size Distribution on Volume of Specimen made with Laurel Sand

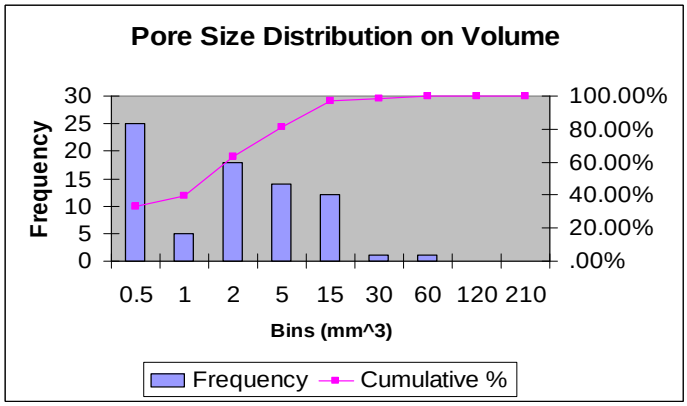

Figure 6.15 Histogram Plot of Scan #5 for the Pore Size Distribution on Volume of Specimen made with Laurel Sand

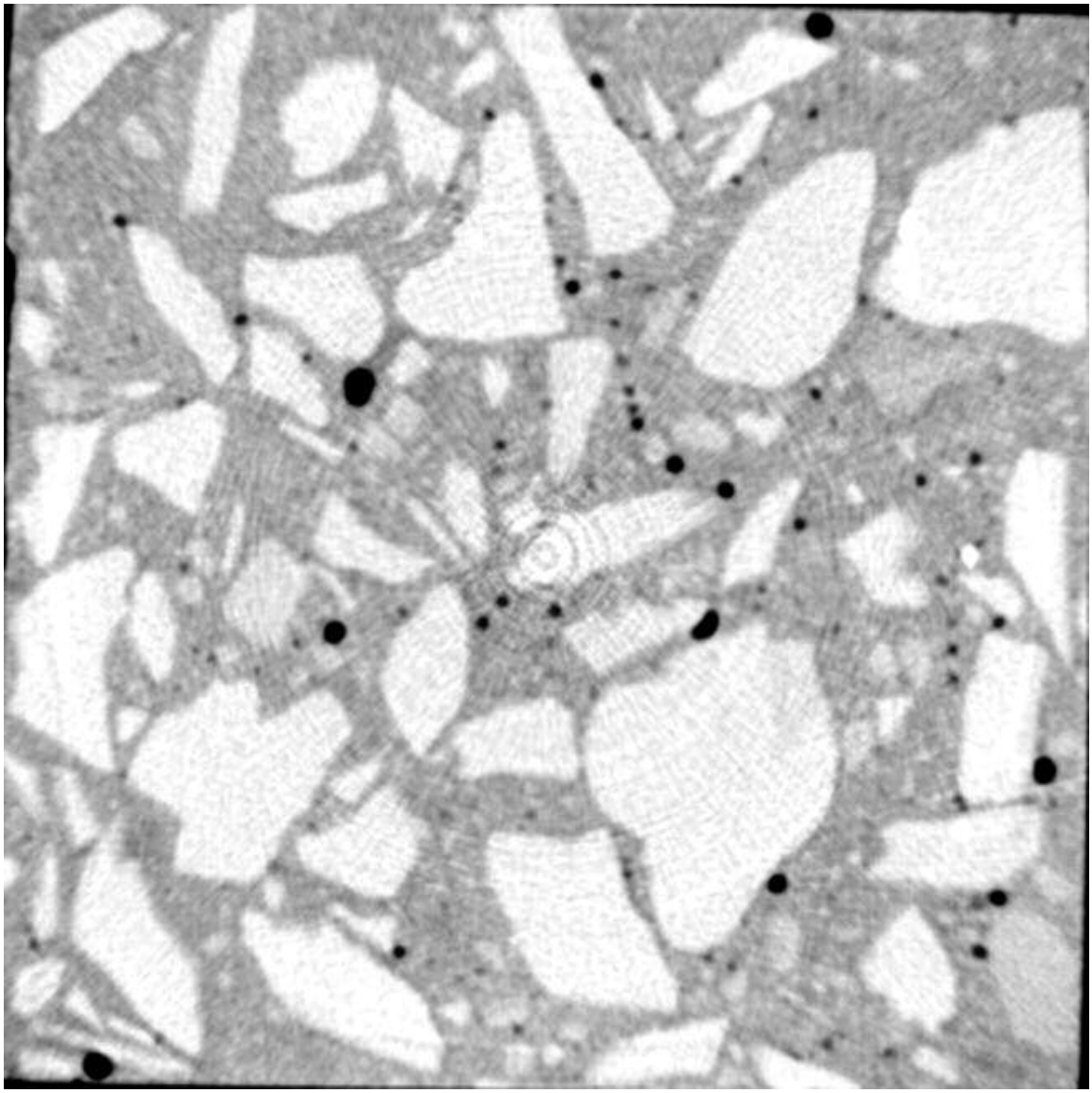

Figure 6.16 X-ray Computed Tomographic Image for Scan #6 of Specimen made with Laurel Sand

Bins (mm)	Frequency	Cumulative %	Relative %
0.1	0	.00%	0.00%
0.5	25	34.72%	34.72%
1	32	79.17%	44.44%
1.5	8	90.28%	11.11%
2	3	94.44%	4.17%
2.5	3	98.61%	4.17%
3	1	100.00%	1.39%
6	0	100.00%	0.00%
13	0	100.00%	0.00%

Table 6.12 Histogram Data of Scan #6 for the Pore Size Distribution on Diameter of Specimen made with Laurel Sand

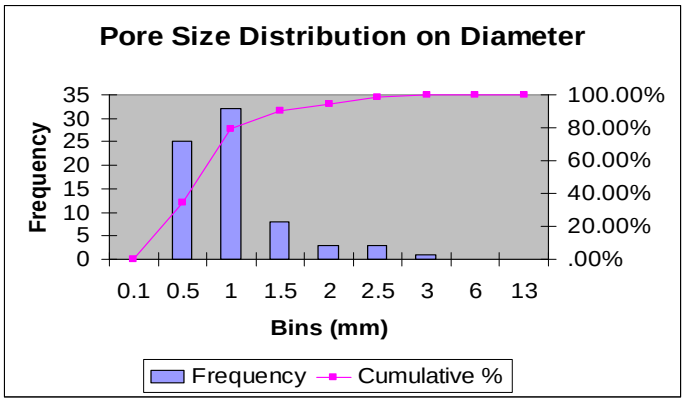

Figure 6.17 Histogram Plot of Scan #6 for the Pore Size Distribution on Diameter of Specimen made with Laurel Sand

Bins (mm^3)	Frequency	Cumulative %	Relative %
0.5	16	22.22%	22.22%
1	13	40.28%	18.06%
2	18	65.28%	25.00%
5	15	86.11%	20.83%
15	8	97.22%	11.11%
30	2	100.00%	2.78%
60	0	100.00%	0.00%
120	0	100.00%	0.00%
210	0	100.00%	0.00%

Table 6.13 Histogram Data of Scan #6 for the Pore Size Distribution on Volume of Specimen made with Laurel Sand

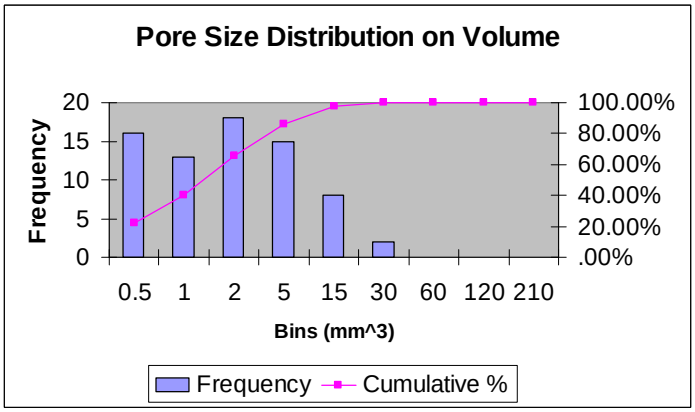

Figure 6.18 Histogram Plot of Scan #6 for the Pore Size Distribution on Volume of Specimen made with Laurel Sand

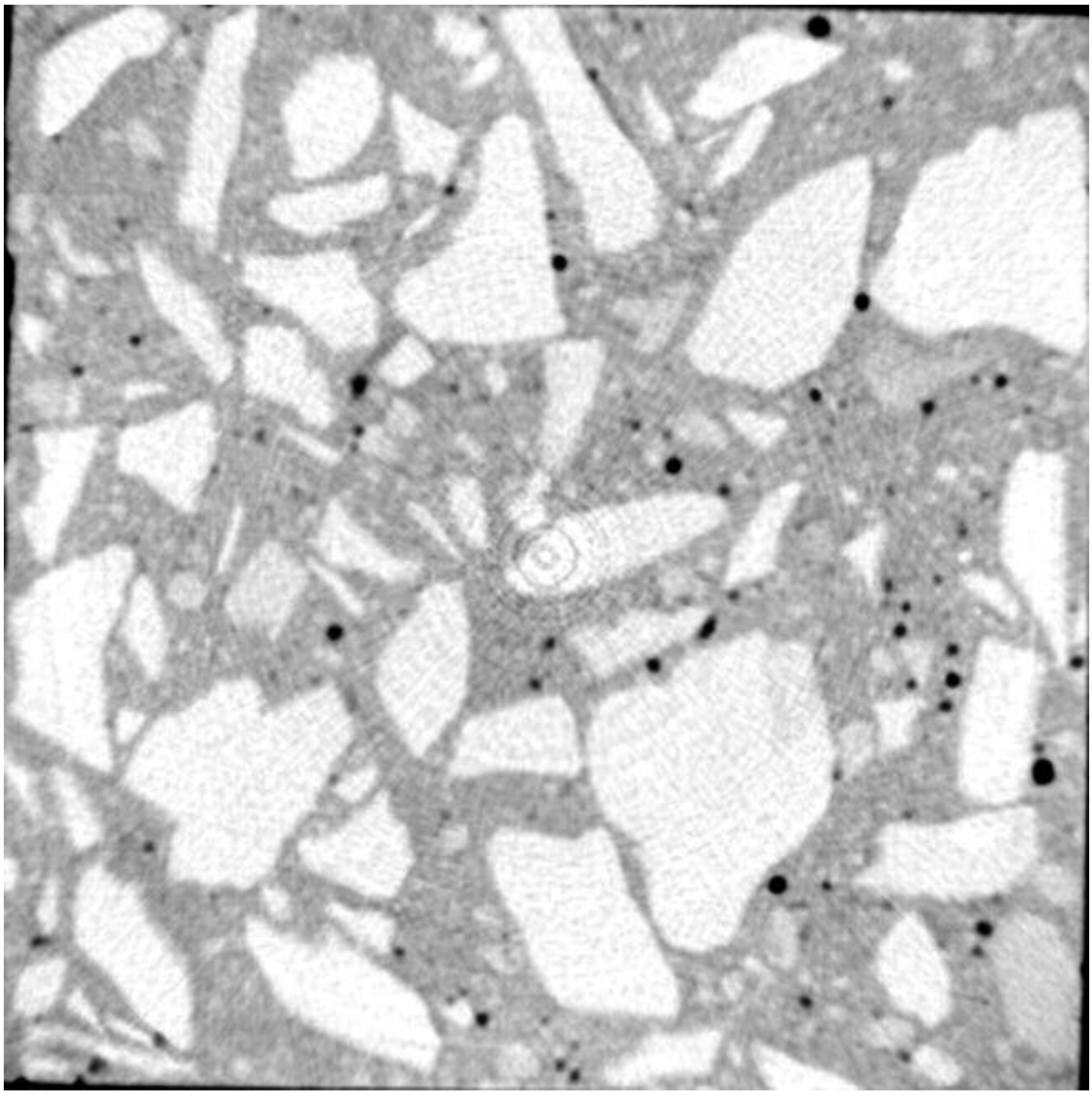

Figure 6.19 X-ray Computed Tomographic Image for Scan #7 of Specimen made with Laurel Sand

Bins (mm)	Frequency	Cumulative %	Relative %
0.1	0	.00%	0.00%
0.5	14	21.88%	21.88%
1	37	79.69%	57.81%
1.5	9	93.75%	14.06%
2	4	100.00%	6.25%
2.5	0	100.00%	0.00%
3	0	100.00%	0.00%
6	0	100.00%	0.00%
13	0	100.00%	0.00%

Table 6.14 Histogram Data of Scan #7 for the Pore Size Distribution on Diameter of Specimen made with Laurel Sand

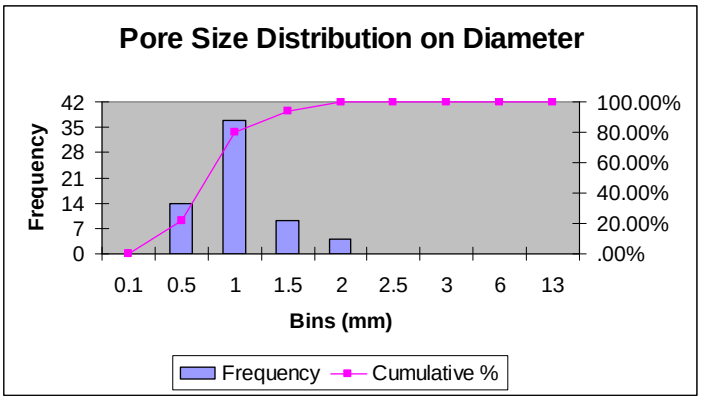

Figure 6.20 Histogram Plot of Scan #7 for the Pore Size Distribution on Diameter of Specimen made with Laurel Sand

Bins (mm^3)	Frequency	Cumulative %	Relative %
0.5	10	15.63%	15.63%
1	9	29.69%	14.06%
2	19	59.38%	29.69%
5	17	85.94%	26.56%
15	9	100.00%	14.06%
30	0	100.00%	0.00%
60	0	100.00%	0.00%
120	0	100.00%	0.00%
210	0	100.00%	0.00%

Table 6.15 Histogram Data of Scan #7 for the Pore Size Distribution on Volume of Specimen made with Laurel Sand

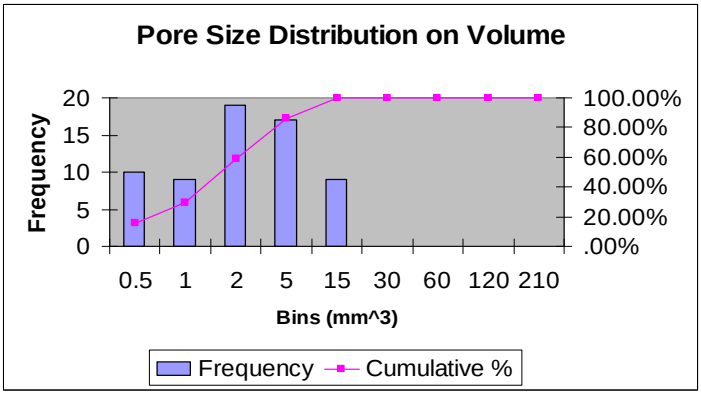

Figure 6.21 Histogram Plot of Scan #7 for the Pore Size Distribution on Volume of Specimen made with Laurel Sand

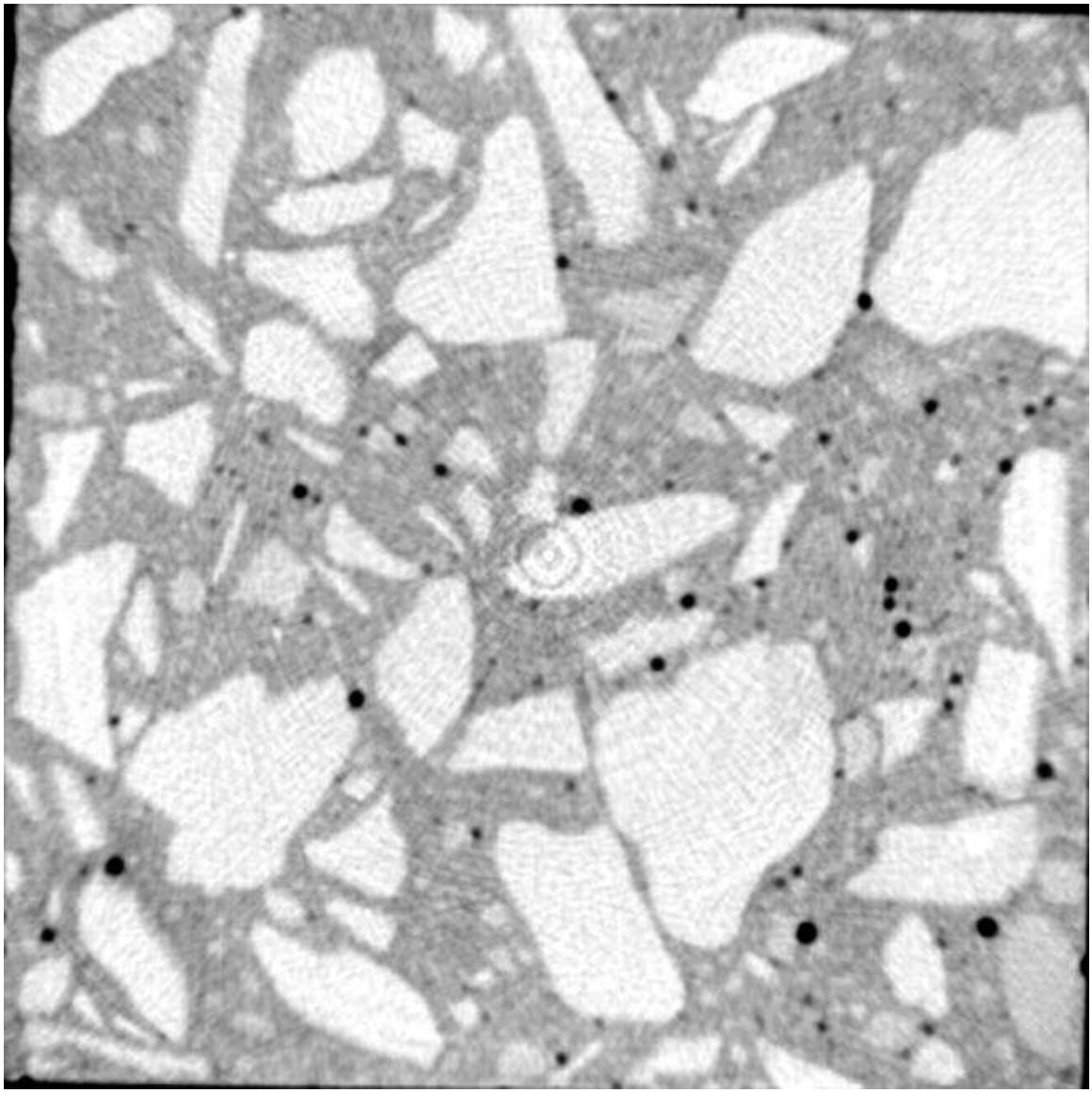

Figure 6.22 X-ray Computed Tomographic Image for Scan #8 of Specimen made with Laurel Sand

Bins (mm)	Frequency	Cumulative %	Relative %
0.1	0	.00%	0.00%
0.5	22	29.73%	29.73%
1	40	83.78%	54.05%
1.5	8	94.59%	10.81%
2	3	98.65%	4.05%
2.5	1	100.00%	1.35%
3	0	100.00%	0.00%
6	0	100.00%	0.00%
13	0	100.00%	0.00%

Table 6.16 Histogram Data of Scan #8 for the Pore Size Distribution on Diameter of Specimen made with Laurel Sand

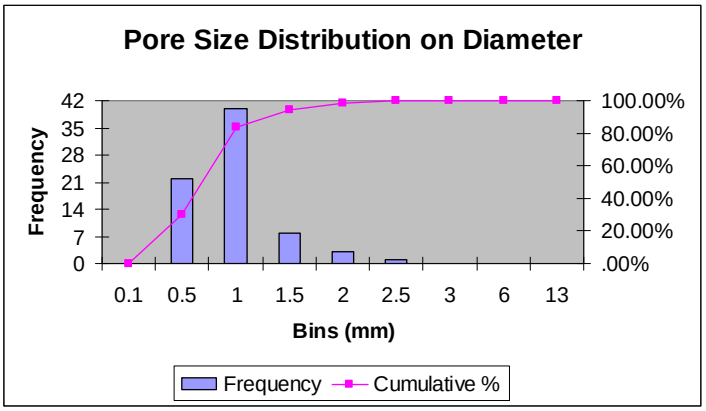

Figure 6.23 Histogram Plot of Scan #8 for the Pore Size Distribution on Diameter of Specimen made with Laurel Sand

Bins (mm^3)	Frequency	Cumulative %	Relative %
0.5	16	21.62%	21.62%
1	16	43.24%	21.62%
2	15	63.51%	20.27%
5	17	86.49%	22.97%
15	10	100.00%	13.51%
30	0	100.00%	0.00%
60	0	100.00%	0.00%
120	0	100.00%	0.00%
210	0	100.00%	0.00%

Table 6.17 Histogram Data of Scan #8 for the Pore Size Distribution on Volume of Specimen made with Laurel Sand

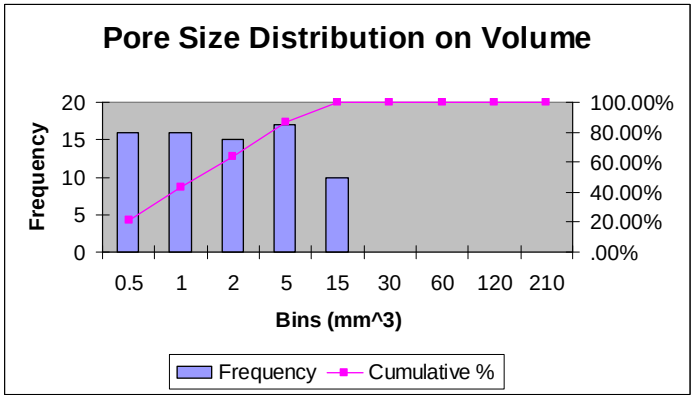

Figure 6.24 Histogram Plot of Scan #8 for the Pore Size Distribution on Volume of Specimen made with Laurel Sand

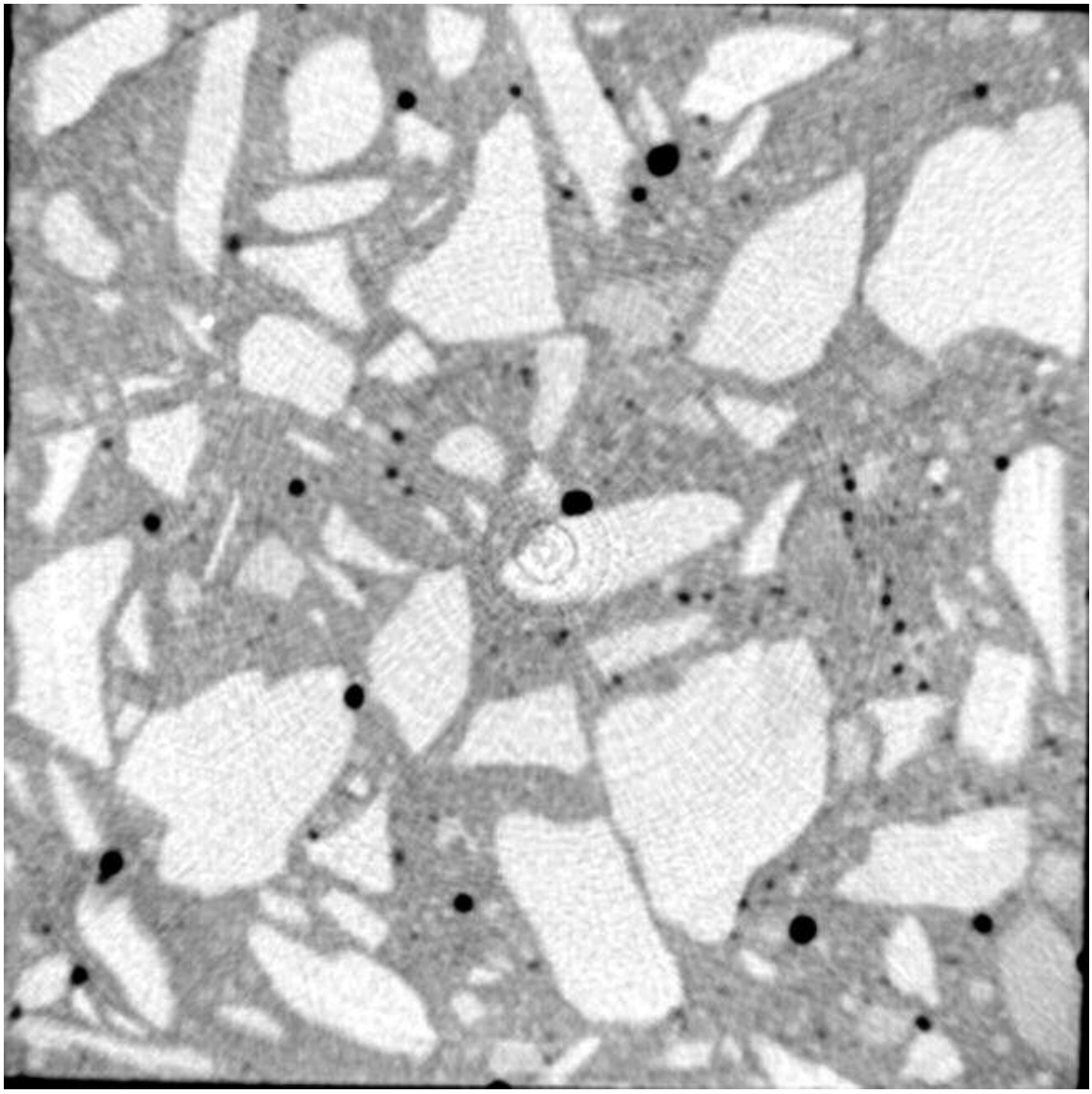

Figure 6.25 X-ray Computed Tomographic Image for Scan #9 of specimen made with Laurel Sand

Bins (mm)	Frequency	Cumulative %	Relative %
0.1	0	.00%	0.00%
0.5	27	35.06%	35.06%
1	30	74.03%	38.96%
1.5	13	90.91%	16.88%
2	3	94.81%	3.90%
2.5	2	97.40%	2.60%
3	2	100.00%	2.60%
6	0	100.00%	0.00%
13	0	100.00%	0.00%

Table 6.18 Histogram Data of Scan #9 for the Pore Size Distribution on Diameter of Specimen made with Laurel Sand

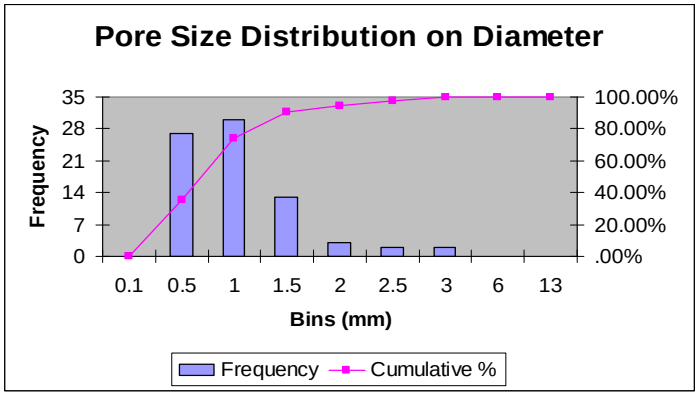

Figure 6.26 Histogram Plot of Scan #9 for the Pore Size Distribution on Diameter of Specimen made with Laurel Sand

Bins (mm^3)	Frequency	Cumulative %	Relative %
0.5	19	24.68%	24.68%
1	11	38.96%	14.29%
2	16	59.74%	20.78%
5	18	83.12%	23.38%
15	9	94.81%	11.69%
30	4	100.00%	5.19%
60	0	100.00%	0.00%
120	0	100.00%	0.00%
210	0	100.00%	0.00%

Table 6.19 Histogram Data of Scan #9 for the Pore Size Distribution on Volume of Specimen made with Laurel Sand

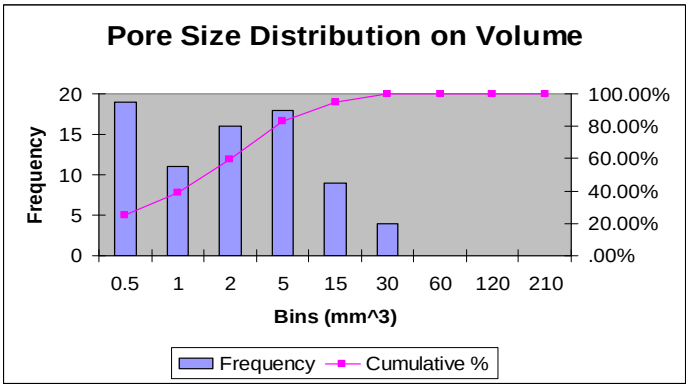

Figure 6.27 Histogram Plot of Scan #9 for the Pore Size Distribution on Volume of Specimen made with Laurel Sand

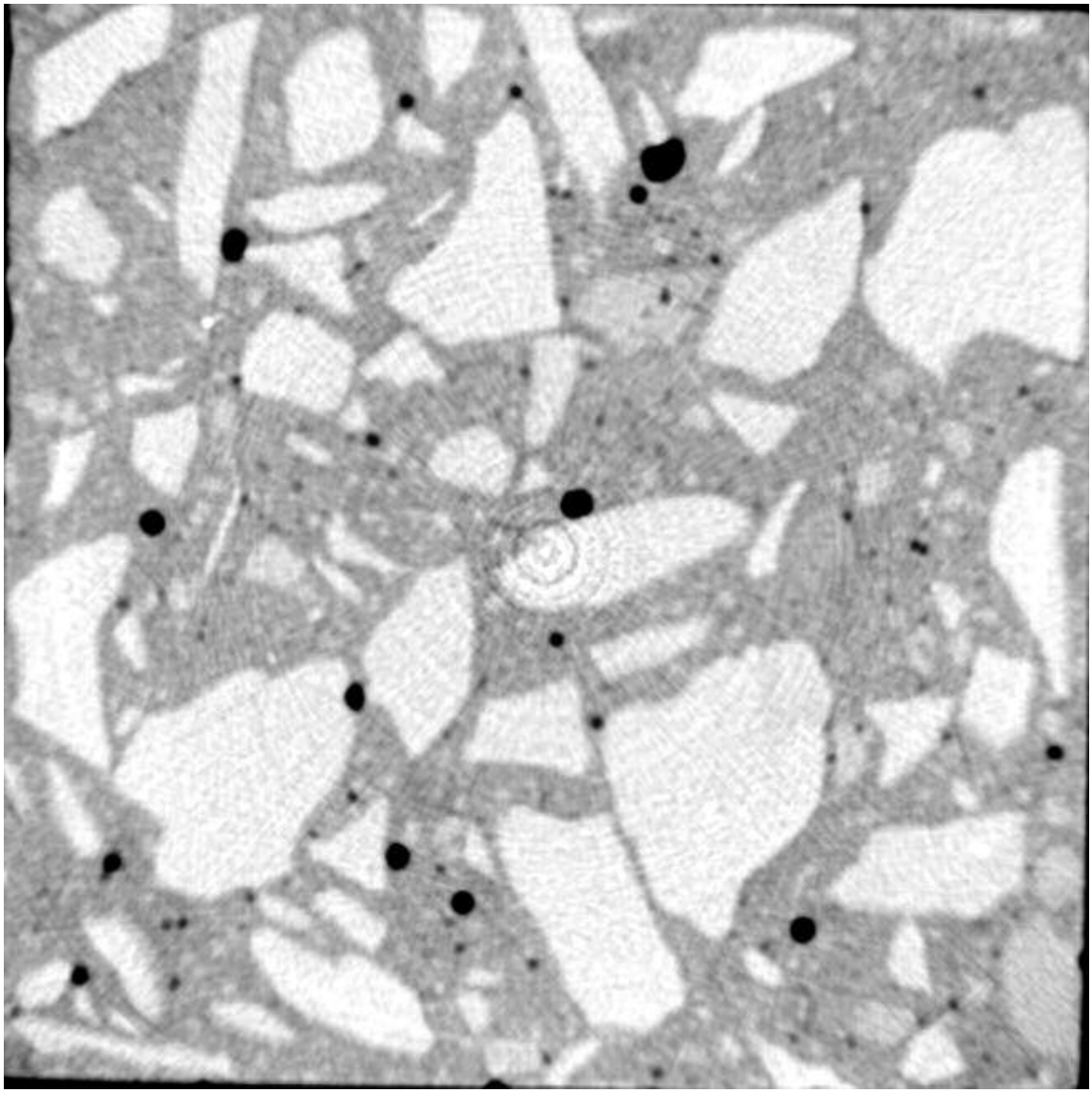

Figure 6.28 X-ray Computed Tomographic Image for Scan #10 of specimen made with Laurel Sand

Bins (mm)	Frequency	Cumulative %	Relative %
0.1	0	.00%	0.00%
0.5	22	32.84%	32.84%
1	30	77.61%	44.78%
1.5	5	85.07%	7.46%
2	5	92.54%	7.46%
2.5	3	97.01%	4.48%
3	1	98.51%	1.49%
6	1	100.00%	1.49%
13	0	100.00%	0.00%

Table 6.20 Histogram Data of Scan #10 for the Pore Size Distribution on Diameter of Specimen made with Laurel Sand

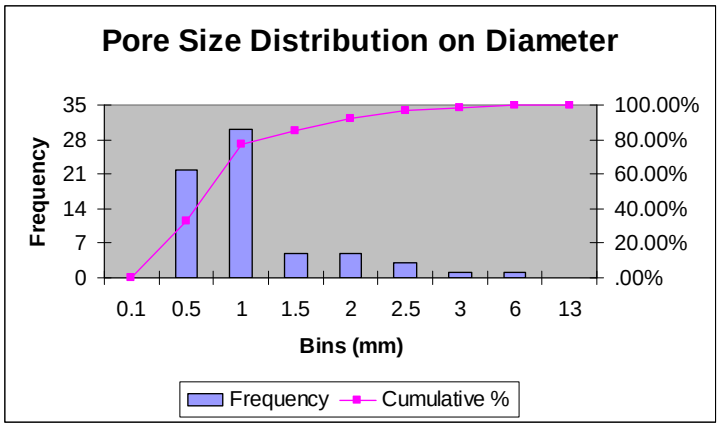

Figure 6.29 Histogram Plot of Scan #10 for the Pore Size Distribution on Diameter of Specimen made with Laurel Sand

Bins (mm^3)	Frequency	Cumulative %	Relative %
0.5	18	26.87%	26.87%
1	10	41.79%	14.93%
2	18	68.66%	26.87%
5	8	80.60%	11.94%
15	10	95.52%	14.93%
30	2	98.51%	2.99%
60	1	100.00%	1.49%
120	0	100.00%	0.00%
210	0	100.00%	0.00%

Table 6.21 Histogram Data of Scan #10 for the Pore Size Distribution on Volume of Specimen made with Laurel Sand

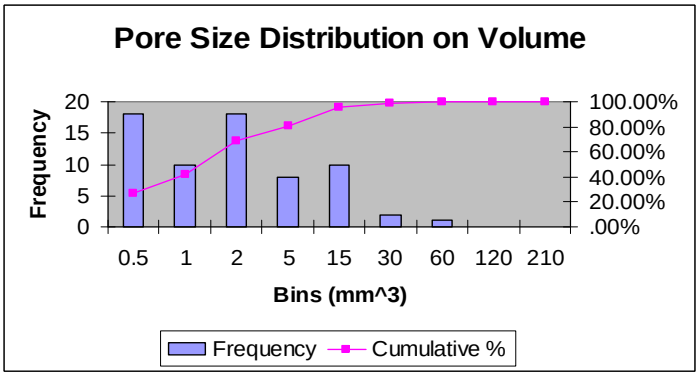

Figure 6.30 Histogram Plot of Scan #10 for the Pore Size Distribution on Volume of Specimen made with Laurel Sand

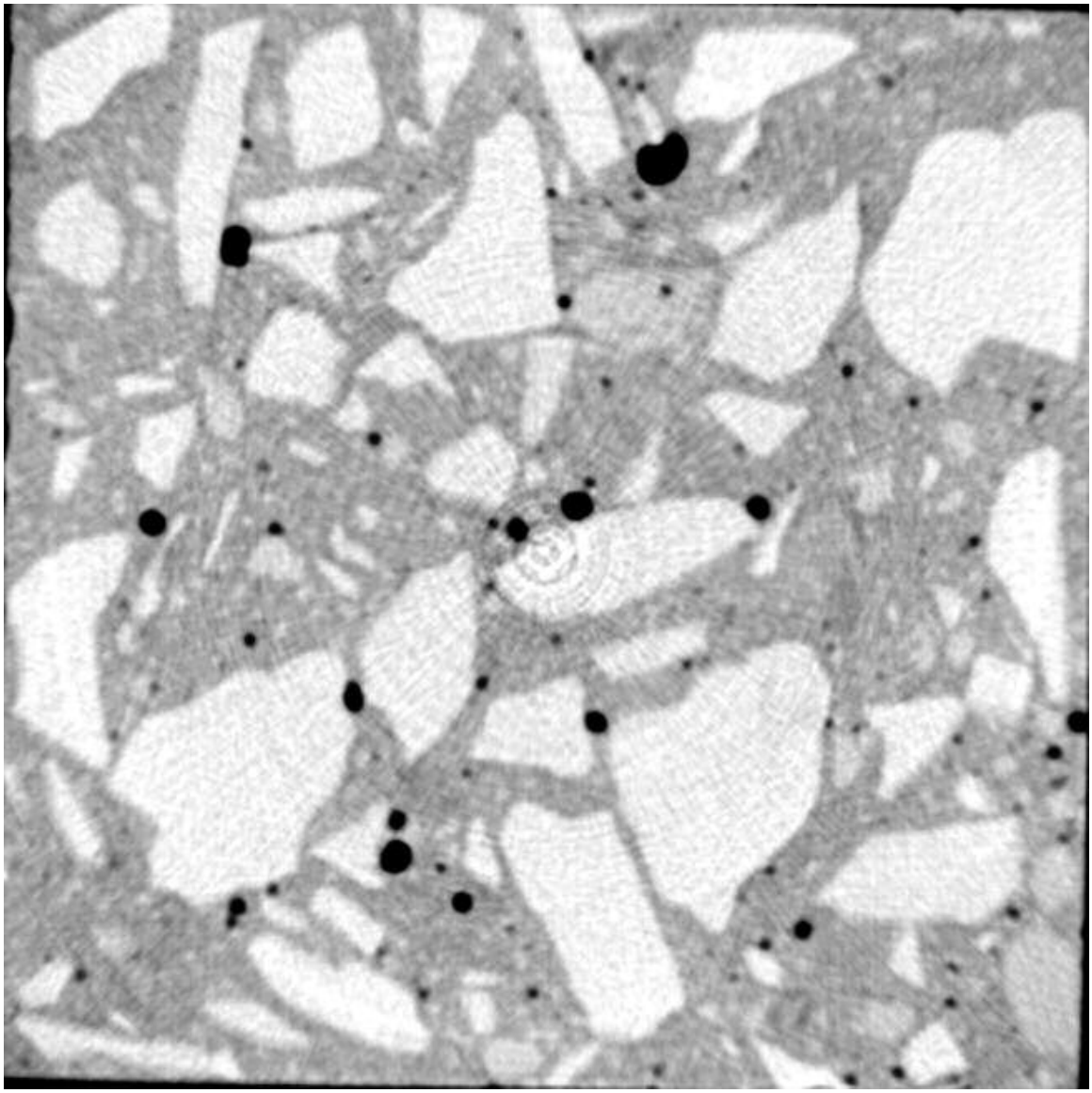

Figure 6.31 X-ray Computed Tomographic Image for Scan #11 of Specimen made with Laurel Sand

Bins (mm)	Frequency	Cumulative %	Relative %
0.1	0	.00%	0.00%
0.5	15	19.23%	19.23%
1	45	76.92%	57.69%
1.5	7	85.90%	8.97%
2	4	91.03%	5.13%
2.5	3	94.87%	3.85%
3	2	97.44%	2.56%
6	2	100.00%	2.56%
13	0	100.00%	0.00%

Table 6.22 Histogram Data of Scan #11 for the Pore Size Distribution on Diameter of Specimen made with Laurel Sand

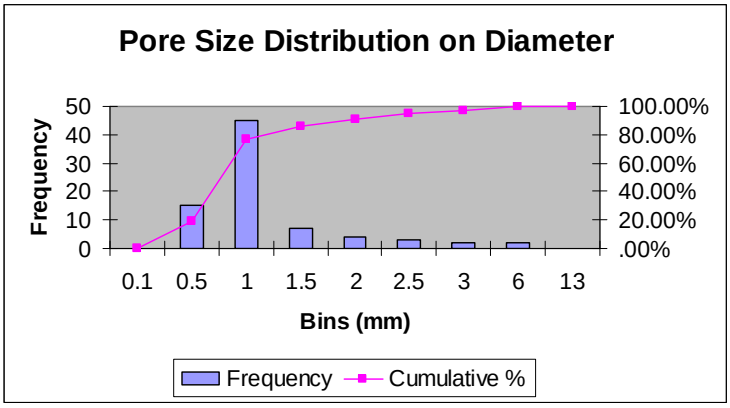

Figure 6.32 Histogram Plot of Scan #11 for the Pore Size Distribution on Diameter of Specimen made with Laurel Sand

Bins (mm^3)	Frequency	Cumulative %	Relative %
0.5	14	17.95%	17.95%
1	6	25.64%	7.69%
2	25	57.69%	32.05%
5	19	82.05%	24.36%
15	10	94.87%	12.82%
30	3	98.72%	3.85%
60	1	100.00%	1.28%
120	0	100.00%	0.00%
210	0	100.00%	0.00%

Table 6.23 Histogram Data of Scan #11 for the Pore Size Distribution on Volume of Specimen made with Laurel Sand

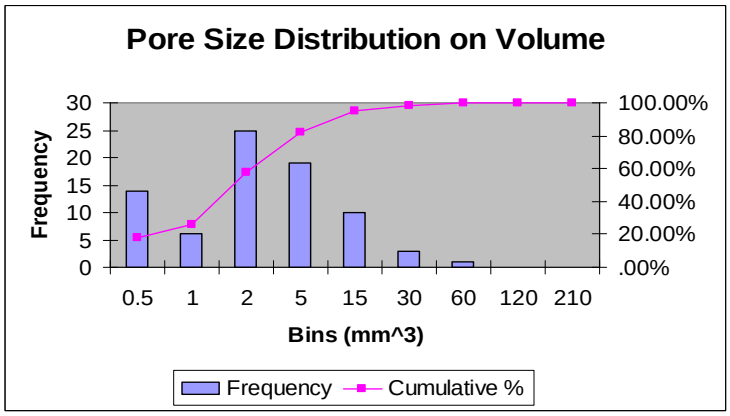

Figure 6.33 Histogram Plot of Scan #11 for the Pore Size Distribution on Volume of Specimen made with Laurel Sand

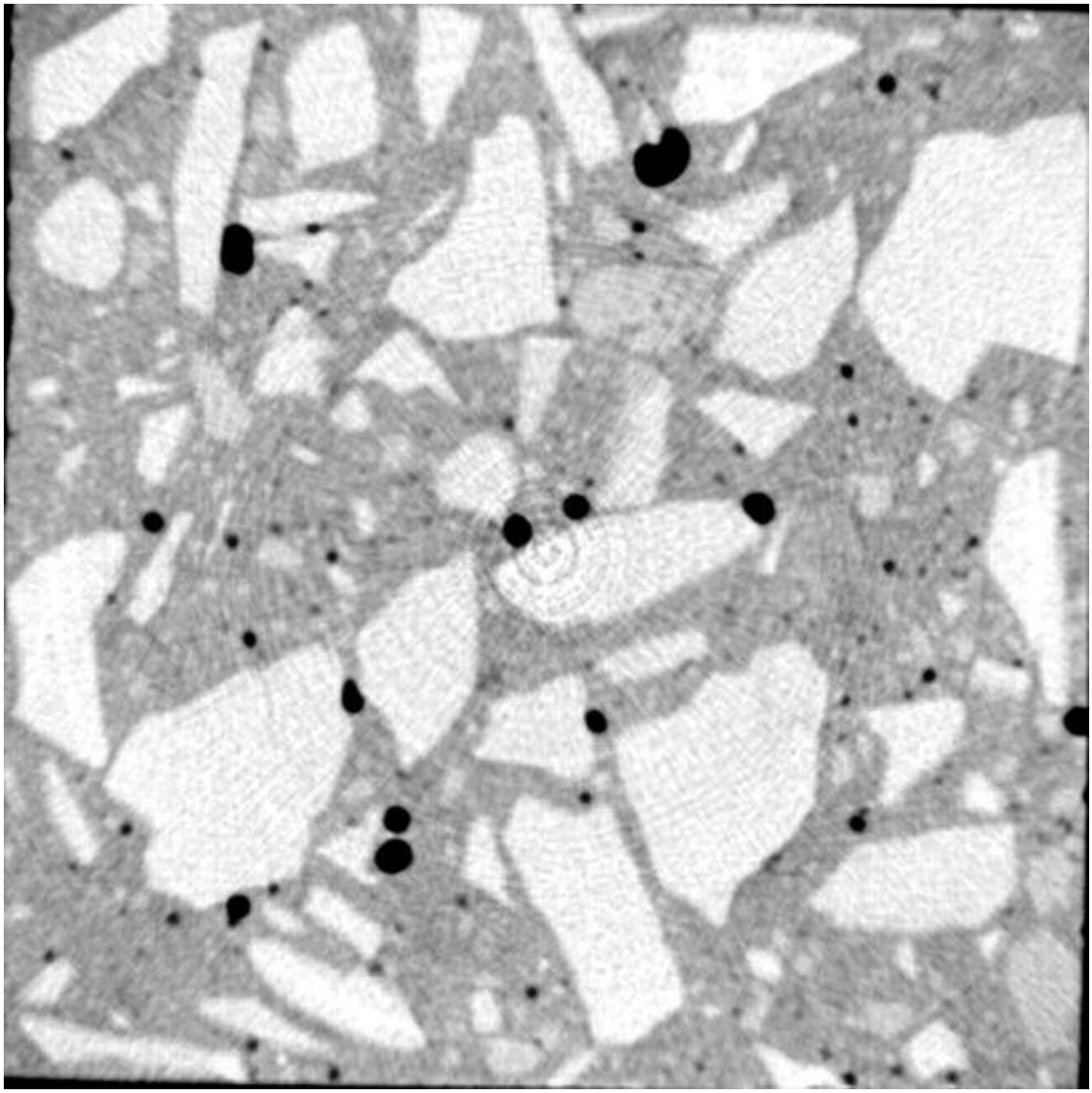

Figure 6.34 X-ray Computed Tomographic Image for Scan #12 of Specimen made with Laurel Sand

Bins (mm)	Frequency	Cumulative %	Relative %
0.1	0	.00%	0.00%
0.5	23	30.67%	30.67%
1	33	74.67%	44.00%
1.5	7	84.00%	9.33%
2	4	89.33%	5.33%
2.5	4	94.67%	5.33%
3	2	97.33%	2.67%
6	2	100.00%	2.67%
13	0	100.00%	0.00%

Table 6.24 Histogram Data of Scan #12 for the Pore Size Distribution on Diameter of Specimen made with Laurel Sand

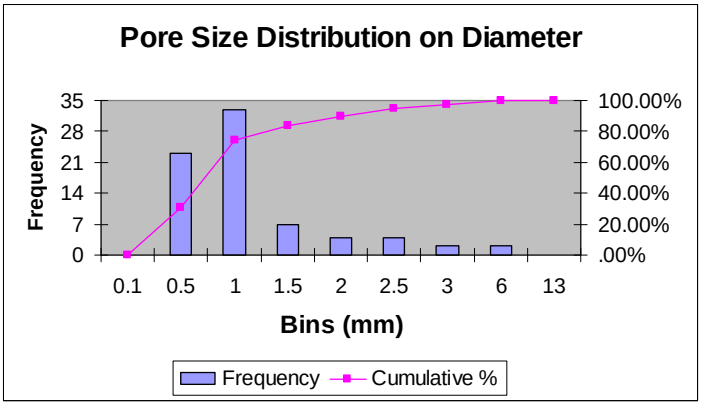

Figure 6.35 Histogram Plot of Scan #12 for the Pore Size Distribution on Diameter of Specimen made with Laurel Sand

Bins (mm^3)	Frequency	Cumulative %	Relative %
0.5	15	20.00%	20.00%
1	14	38.67%	18.67%
2	11	53.33%	14.67%
5	22	82.67%	29.33%
15	8	93.33%	10.67%
30	3	97.33%	4.00%
60	2	100.00%	2.67%
120	0	100.00%	0.00%
210	0	100.00%	0.00%

Table 6.25 Histogram Data of Scan #12 for the Pore Size Distribution on Volume of Specimen made with Laurel Sand

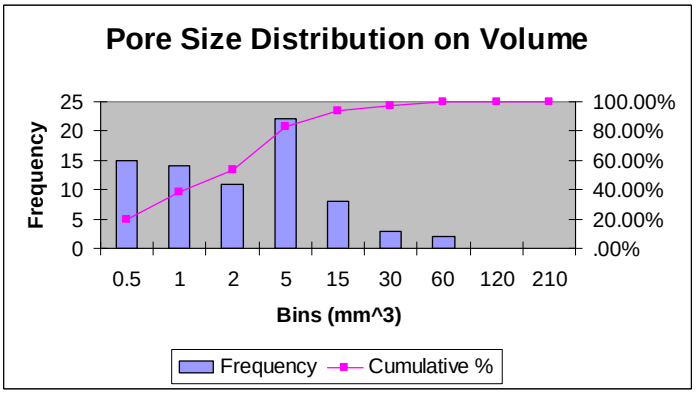

Figure 6.36 Histogram Plot of Scan #12 for the Pore Size Distribution on Volume of Specimen made with Laurel Sand

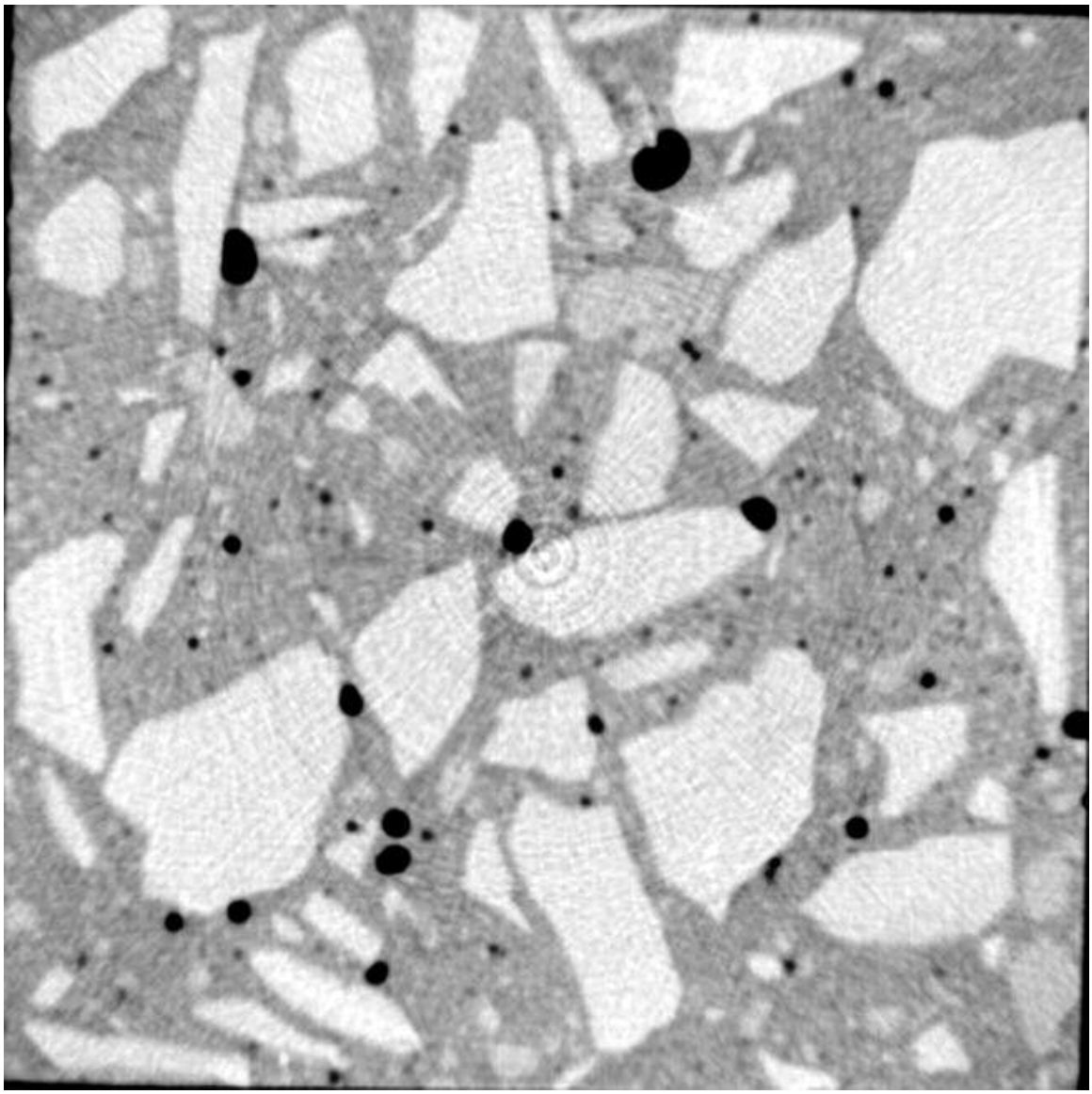

Figure 6.37 X-ray Computed Tomographic Image for Scan #13 of Specimen made with Laurel Sand

Bins (mm)	Frequency	Cumulative %	Relative %
0.1	0	.00%	0.00%
0.5	21	23.60%	23.60%
1	46	75.28%	51.69%
1.5	9	85.39%	10.11%
2	6	92.13%	6.74%
2.5	2	94.38%	2.25%
3	3	97.75%	3.37%
6	2	100.00%	2.25%
13	0	100.00%	0.00%

Table 6.26 Histogram Data of Scan #13 for the Pore Size Distribution on Diameter of Specimen made with Laurel Sand

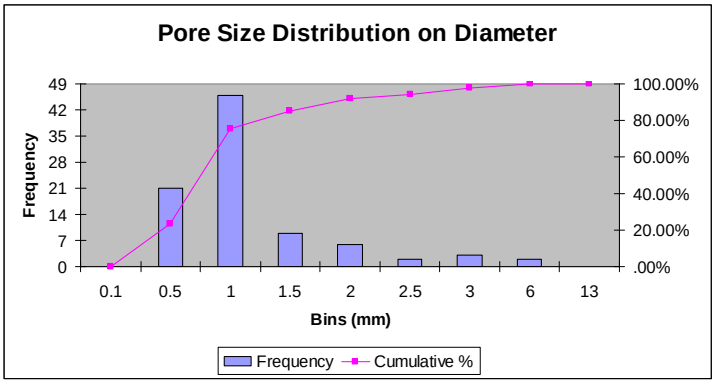

Figure 6.38 Histogram Plot of Scan #13 for the Pore Size Distribution on Diameter of Specimen made with Laurel Sand

Bins (mm^3)	Frequency	Cumulative %	Relative %
0.5	14	15.73%	15.73%
1	15	32.58%	16.85%
2	19	53.93%	21.35%
5	22	78.65%	24.72%
15	12	92.13%	13.48%
30	5	97.75%	5.62%
60	1	98.88%	1.12%
120	1	100.00%	1.12%
210	0	100.00%	0.00%

Table 6.27 Histogram Data of Scan #13 for the Pore Size Distribution on Volume of Specimen made with Laurel Sand

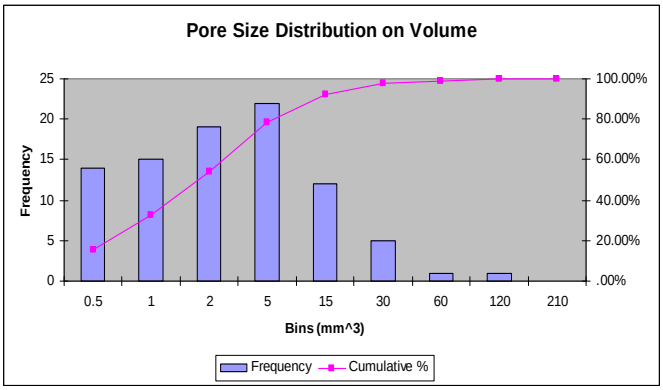

Figure 6.39 Histogram Plot of Scan #13 for the Pore Size Distribution on Volume of Specimen made with Laurel Sand

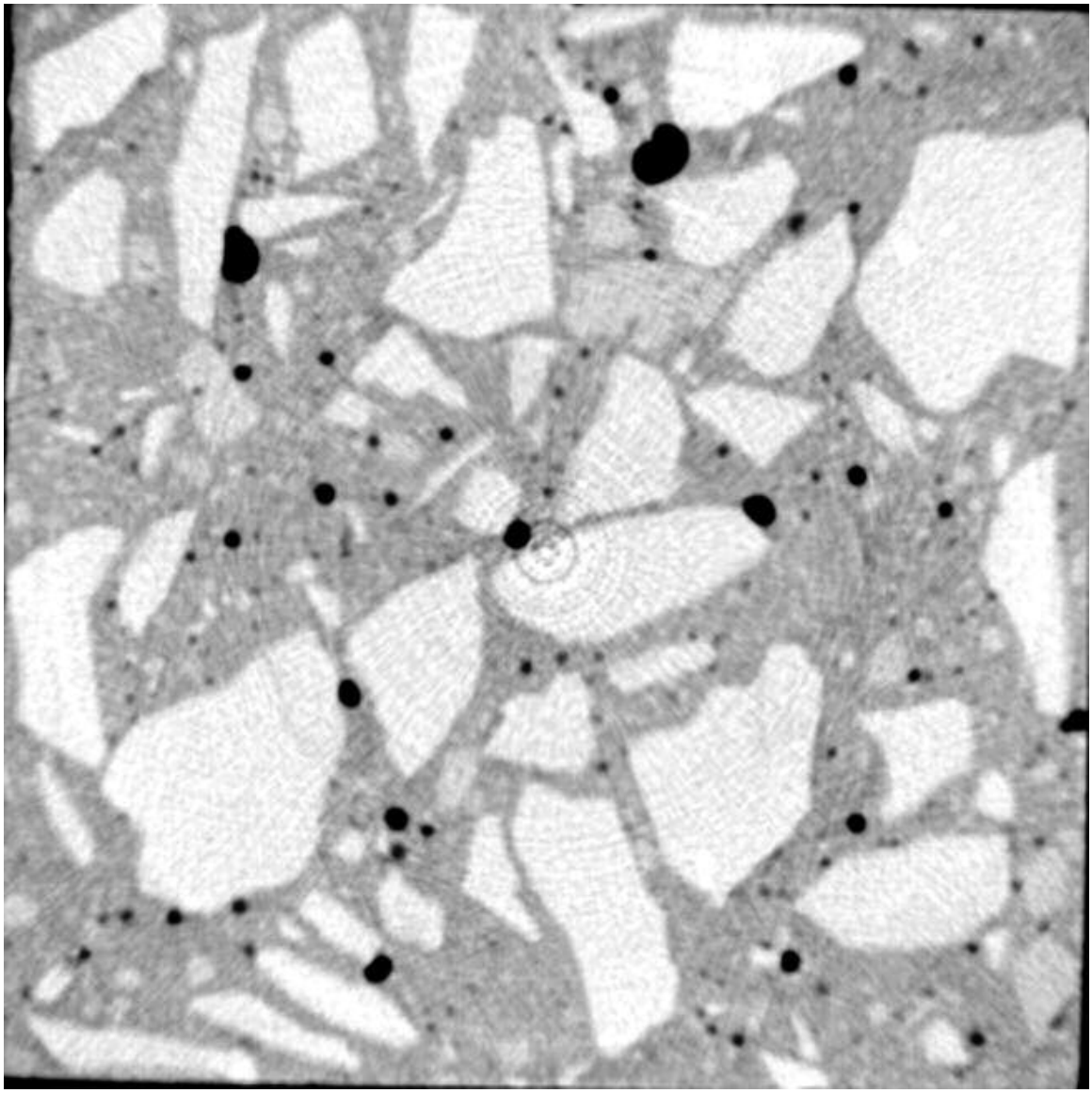

Figure 6.40 X-ray Computed Tomographic Image for Scan #14 of Specimen made with Laurel Sand

Bins (mm)	Frequency	Cumulative %	Relative %
0.1	0	.00%	0.00%
0.5	29	28.43%	28.43%
1	45	72.55%	44.12%
1.5	17	89.22%	16.67%
2	5	94.12%	4.90%
2.5	3	97.06%	2.94%
3	1	98.04%	0.98%
6	2	100.00%	1.96%
13	0	100.00%	0.00%

Table 6.28 Histogram Data of Scan #14 for the Pore Size Distribution on Diameter of Specimen made with Laurel Sand

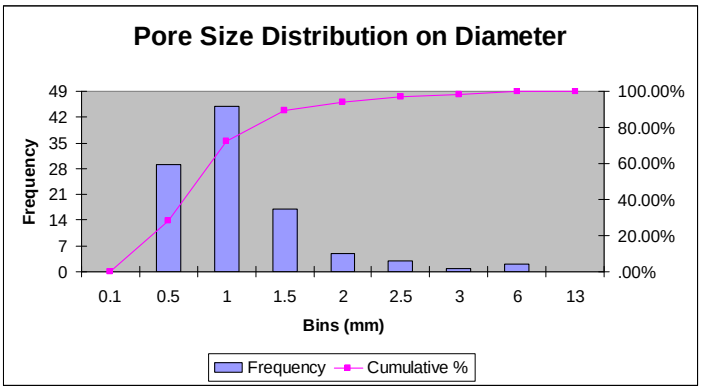

Figure 6.41 Histogram Plot of Scan #14 for the Pore Size Distribution on Diameter of Specimen made with Laurel Sand

Bins (mm^3)	Frequency	Cumulative %	Relative %
0.5	23	22.55%	22.55%
1	17	39.22%	16.67%
2	22	60.78%	21.57%
5	19	79.41%	18.63%
15	16	95.10%	15.69%
30	3	98.04%	2.94%
60	1	99.02%	0.98%
120	1	100.00%	0.98%
210	0	100.00%	0.00%

Table 6.29 Histogram Data of Scan #14 for the Pore Size Distribution on Volume of Specimen made with Laurel Sand

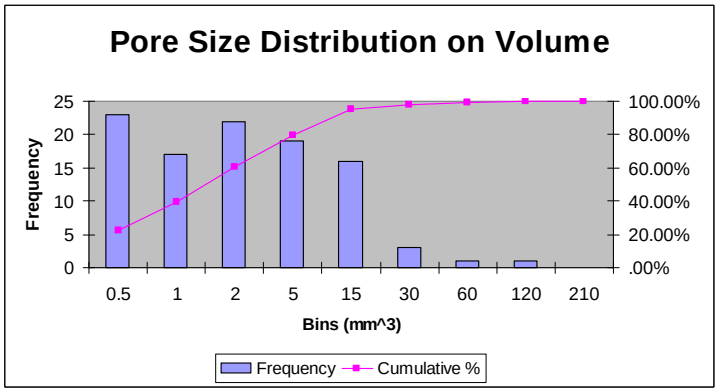

Figure 6.42 Histogram Plot of Scan #14 for the Pore Size Distribution on Volume of Specimen made with Laurel Sand

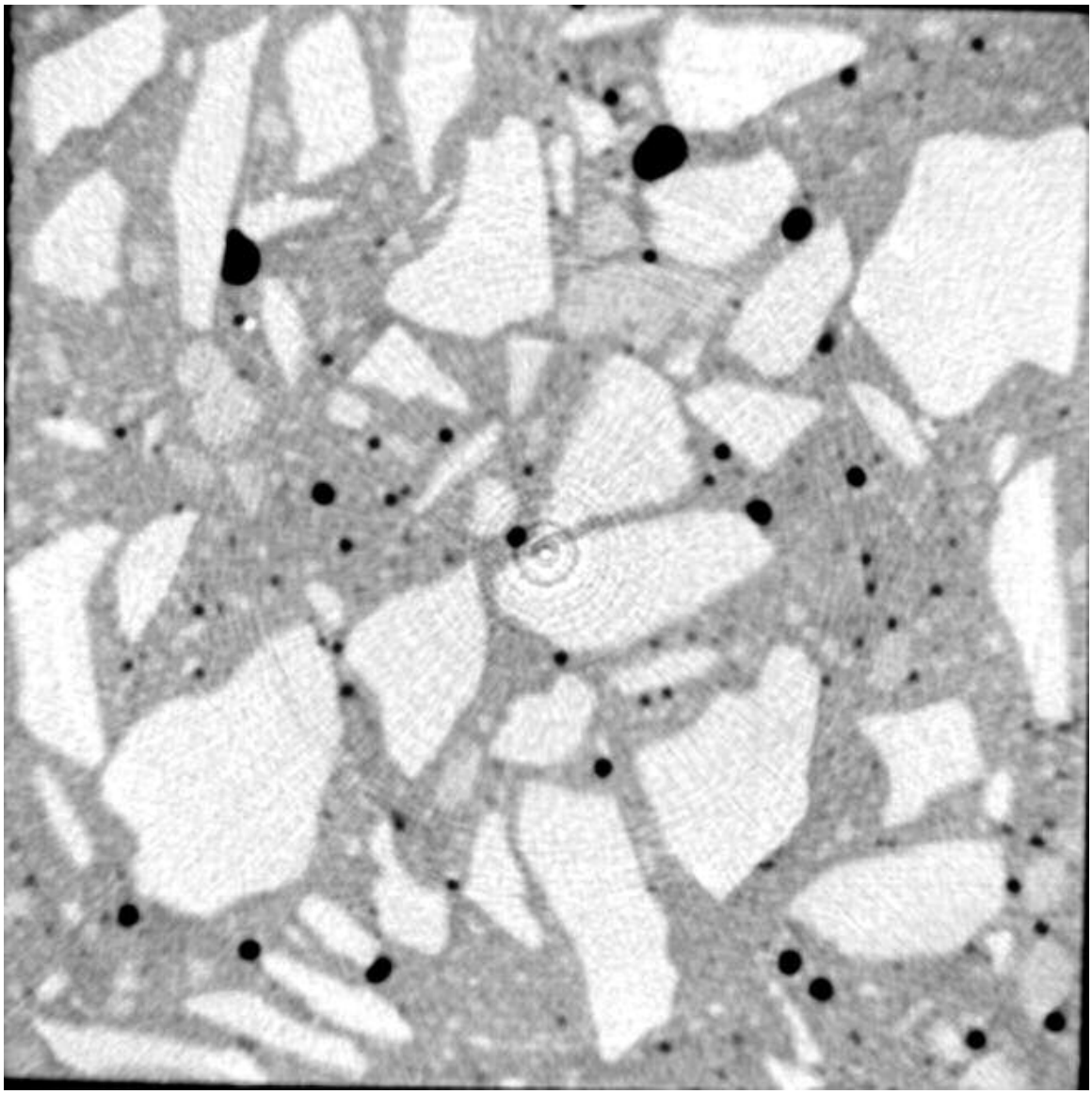

Figure 6.43 X-ray Computed Tomographic Image for Scan #15 of Specimen made with Laurel Sand

Bins (mm)	Frequency	Cumulative %	Relative %
0.1	0	.00%	0.00%
0.5	31	31.63%	31.63%
1	40	72.45%	40.82%
1.5	13	85.71%	13.27%
2	9	94.90%	9.18%
2.5	2	96.94%	2.04%
3	1	97.96%	1.02%
6	2	100.00%	2.04%
13	0	100.00%	0.00%

Table 6.30 Histogram Data of Scan #15 for the Pore Size Distribution on Diameter of Specimen made with Laurel Sand

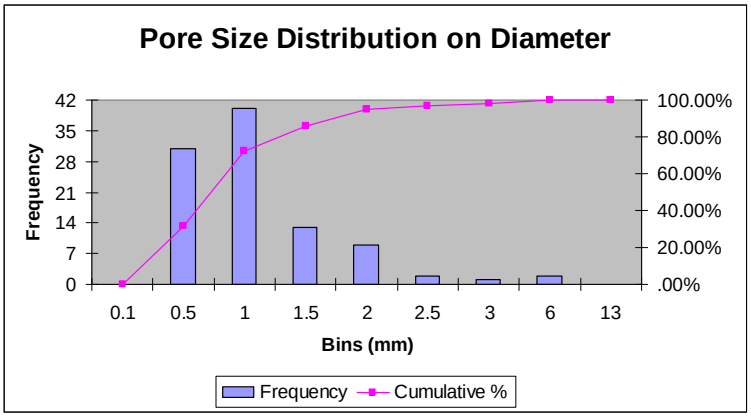

Figure 6.44 Histogram Plot of Scan #15 for the Pore Size Distribution on Diameter of Specimen made with Laurel Sand

Bins (mm^3)	Frequency	Cumulative %	Relative %
0.5	22	22.45%	22.45%
1	15	37.76%	15.31%
2	17	55.10%	17.35%
5	25	80.61%	25.51%
15	16	96.94%	16.33%
30	1	97.96%	1.02%
60	2	100.00%	2.04%
120	0	100.00%	0.00%
210	0	100.00%	0.00%

Table 6.31 Histogram Data of Scan #15 for the Pore Size Distribution on Volume of Specimen made with Laurel Sand

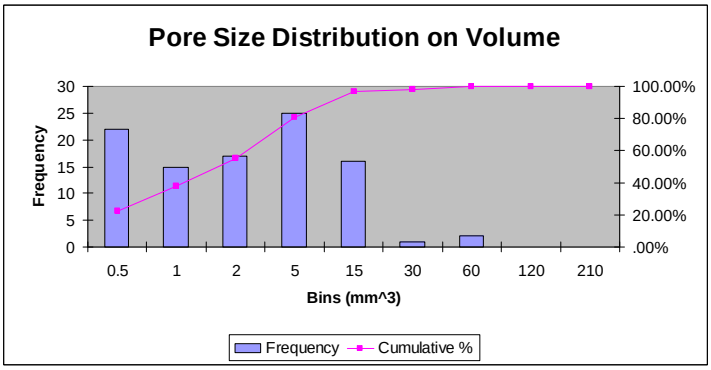

Figure 6.45 Histogram Plot of Scan #15 for the Pore Size Distribution on Volume of Specimen made with Laurel Sand

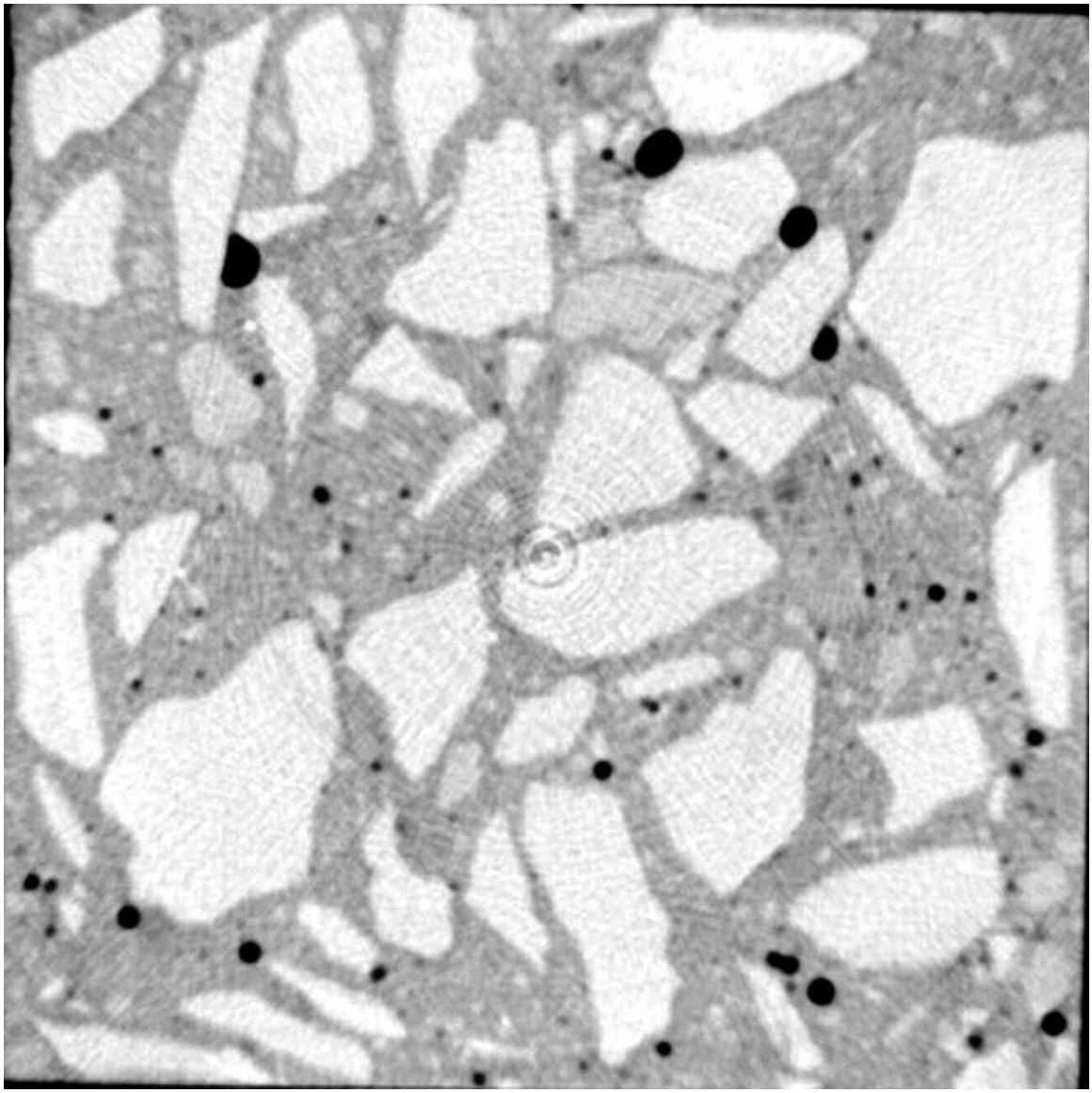

Figure 6.46 X-ray Computed Tomographic Image for Scan #16 of Specimen made with Laurel Sand

Bins (mm)	Frequency	Cumulative %	Relative %
0.1	0	.00%	0.00%
0.5	25	30.49%	30.49%
1	35	73.17%	42.68%
1.5	12	87.80%	14.63%
2	3	91.46%	3.66%
2.5	3	95.12%	3.66%
3	1	96.34%	1.22%
6	3	100.00%	3.66%
13	0	100.00%	0.00%

Table 6.32 Histogram Data of Scan #16 for the Pore Size Distribution on Diameter of Specimen made with Laurel Sand

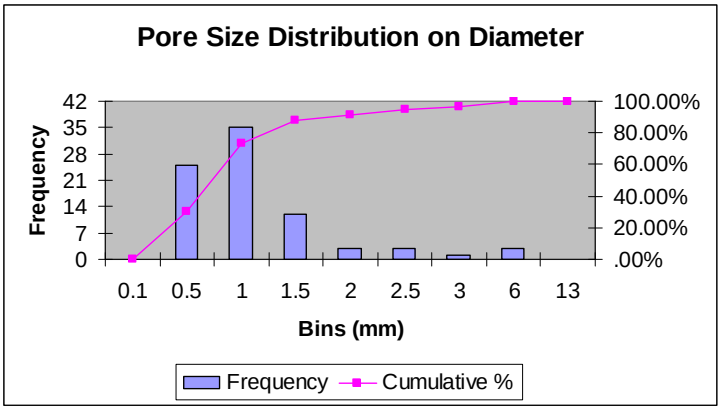

Figure 6.47 Histogram Plot of Scan #16 for the Pore Size Distribution on Diameter of Specimen made with Laurel Sand

Bins (mm^3)	Frequency	Cumulative %	Relative %
0.5	20	24.39%	24.39%
1	11	37.80%	13.41%
2	20	62.20%	24.39%
5	15	80.49%	18.29%
15	11	93.90%	13.41%
30	3	97.56%	3.66%
60	2	100.00%	2.44%
120	0	100.00%	0.00%
210	0	100.00%	0.00%

Table 6.33 Histogram Data of Scan #16 for the Pore Size Distribution on Volume of Specimen made with Laurel Sand

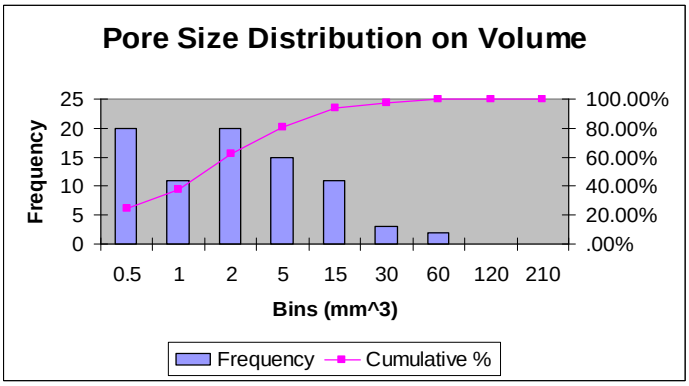

Figure 6.48 Histogram Plot of Scan #16 for the Pore Size Distribution on Volume of Specimen made with Laurel Sand

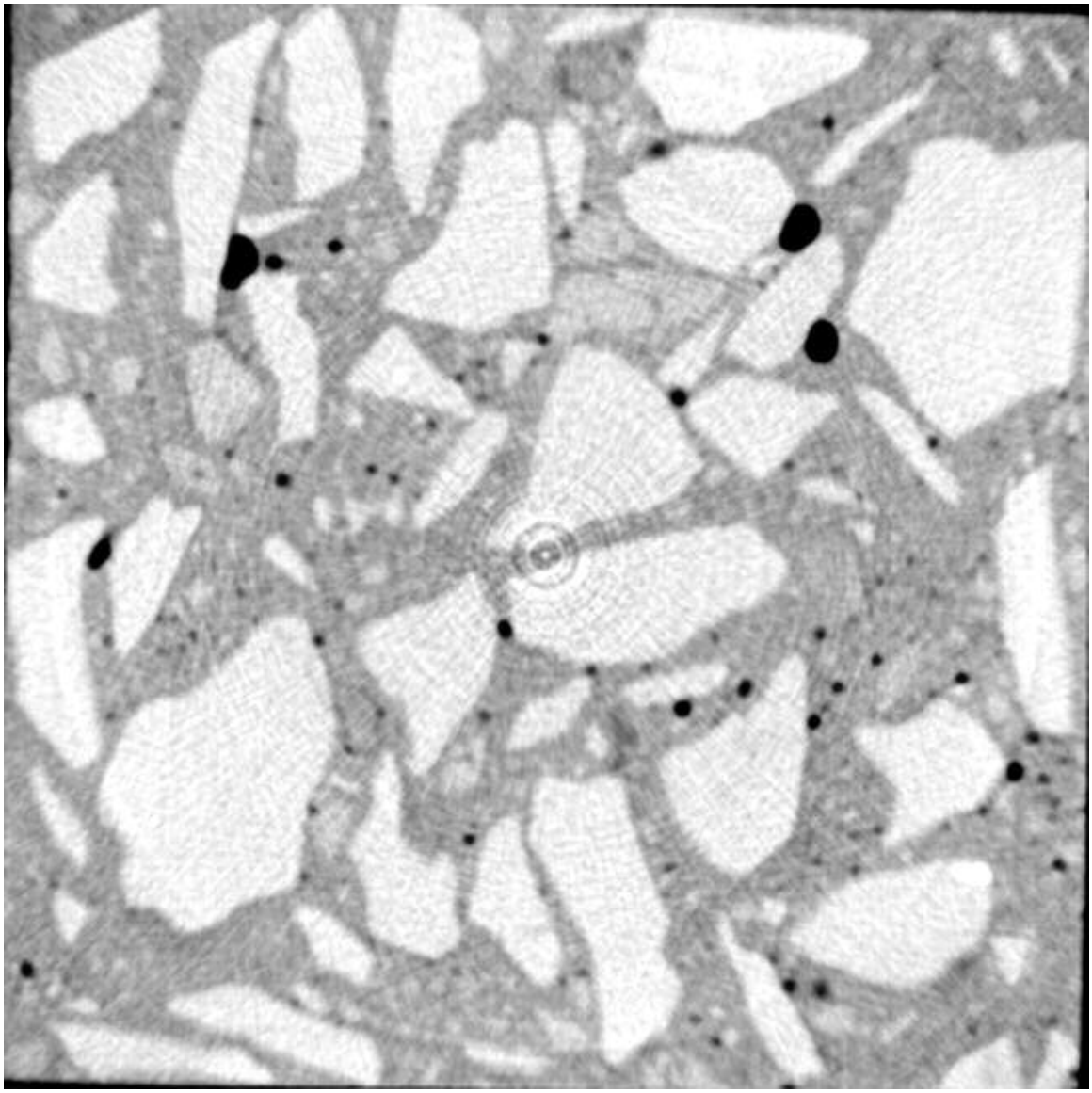

Figure 6.49 X-ray Computed Tomographic Image for Scan #18 of Specimen made with Laurel Sand

Bins (mm)	Frequency	Cumulative %	Relative %
0.1	0	.00%	0.00%
0.5	31	40.79%	40.79%
1	28	77.63%	36.84%
1.5	12	93.42%	15.79%
2	1	94.74%	1.32%
2.5	0	94.74%	0.00%
3	1	96.05%	1.32%
6	3	100.00%	3.95%
13	0	100.00%	0.00%

Table 6.34 Histogram Data of Scan #18 for the Pore Size Distribution on Diameter of Specimen made with Laurel Sand

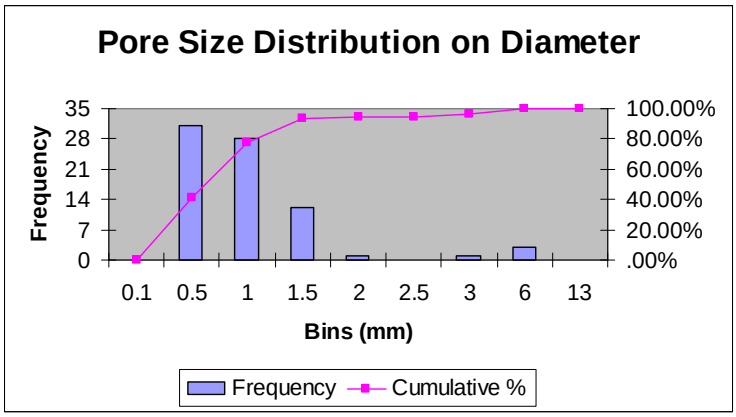

Figure 6.50 Histogram Plot of Scan #18 for the Pore Size Distribution on Diameter of Specimen made with Laurel Sand

Bins (mm^3)	Frequency	Cumulative %	Relative %
0.5	21	27.63%	27.63%
1	20	53.95%	26.32%
2	9	65.79%	11.84%
5	14	84.21%	18.42%
15	9	96.05%	11.84%
30	1	97.37%	1.32%
60	2	100.00%	2.63%
120	0	100.00%	0.00%
210	0	100.00%	0.00%

Table 6.35 Histogram Data of Scan #18 for the Pore Size Distribution on Volume of Specimen made with Laurel Sand

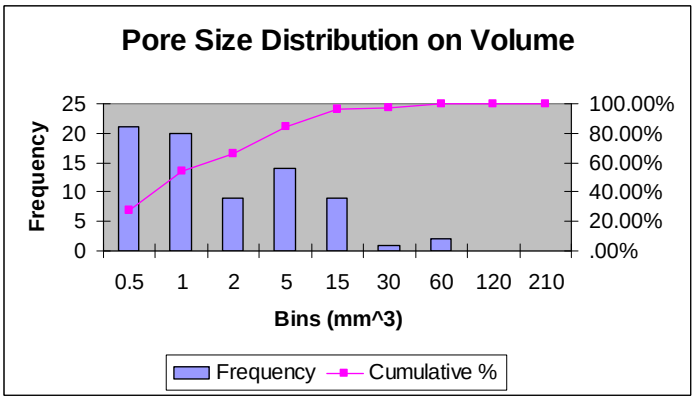

Figure 6.51 Histogram Plot of Scan #18 for the Pore Size Distribution on Volume of Specimen made with Laurel Sand

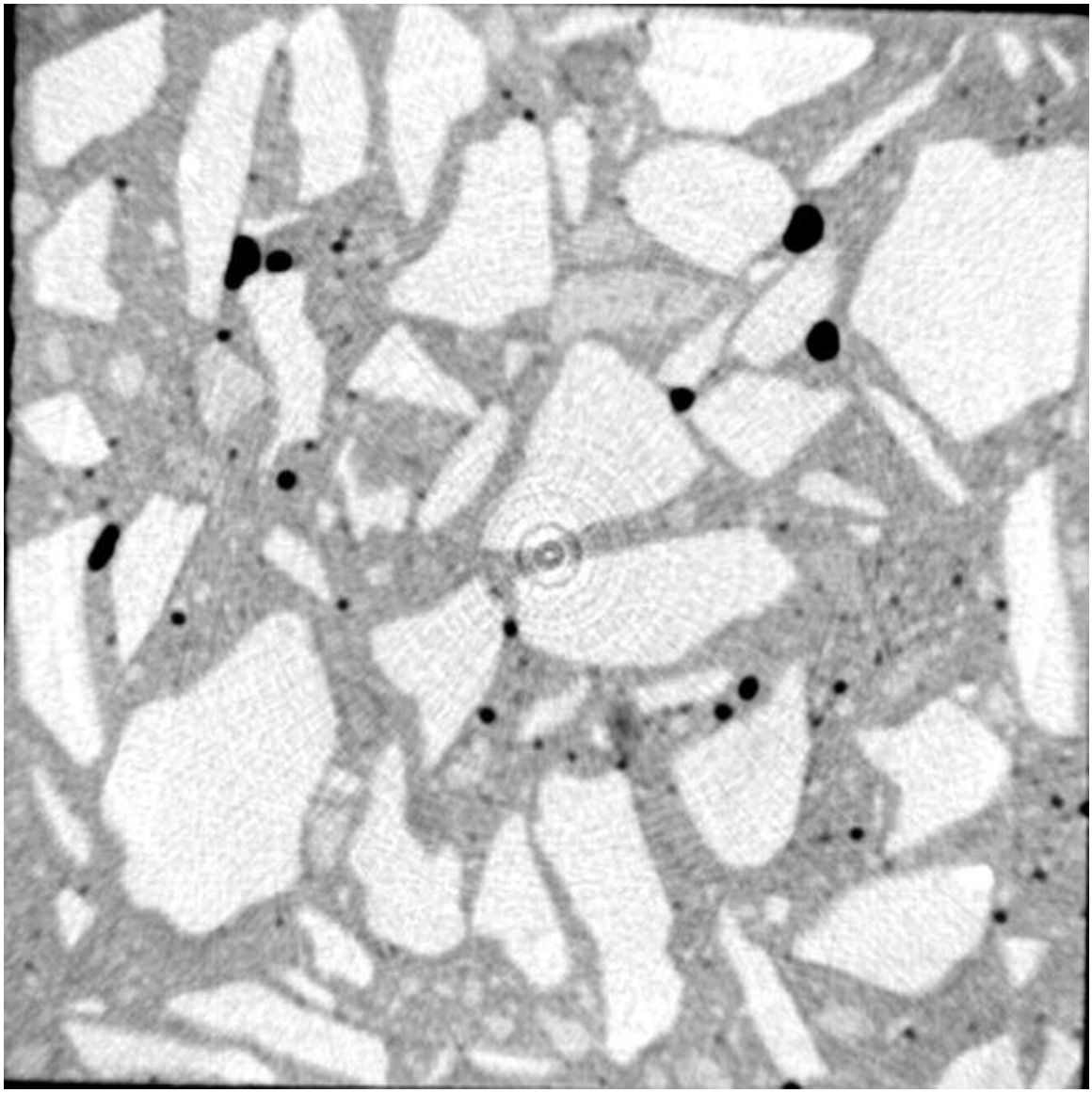

Figure 6.52 X-ray Computed Tomographic Image for Scan #19 of Specimen made with Laurel Sand

Bins (mm)	Frequency	Cumulative %	Relative %
0.1	0	.00%	0.00%
0.5	26	38.24%	38.24%
1	28	79.41%	41.18%
1.5	6	88.24%	8.82%
2	3	92.65%	4.41%
2.5	1	94.12%	1.47%
3	1	95.59%	1.47%
6	3	100.00%	4.41%
13	0	100.00%	0.00%

Table 6.36 Histogram Data of Scan #19 for the Pore Size Distribution on Diameter of Specimen made with Laurel Sand

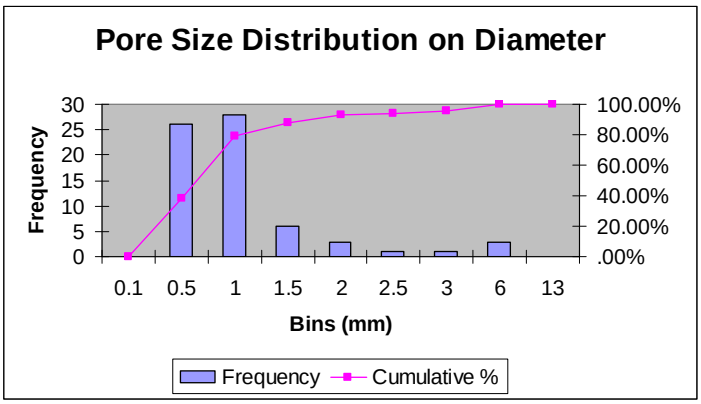

Figure 6.53 Histogram Plot of Scan #19 for the Pore Size Distribution on Diameter of Specimen made with Laurel Sand

Bins (mm^3)	Frequency	Cumulative %	Relative %
0.5	20	29.41%	29.41%
1	10	44.12%	14.71%
2	13	63.24%	19.12%
5	14	83.82%	20.59%
15	7	94.12%	10.29%
30	2	97.06%	2.94%
60	2	100.00%	2.94%
120	0	100.00%	0.00%
210	0	100.00%	0.00%

Table 6.37 Histogram Data of Scan #19 for the Pore Size Distribution on Volume of Specimen made with Laurel Sand

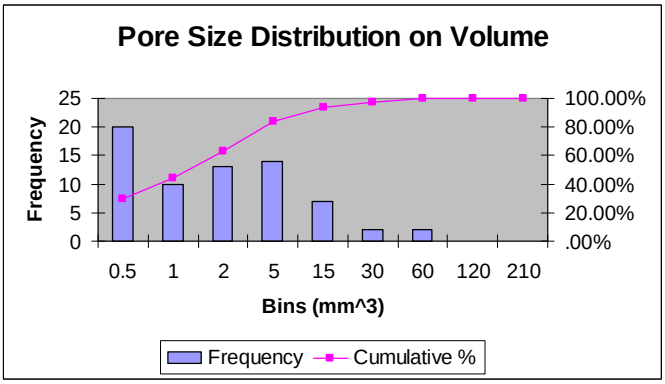

Figure 6.54 Histogram Plot of Scan #19 for the Pore Size Distribution on Volume of Specimen made with Laurel Sand

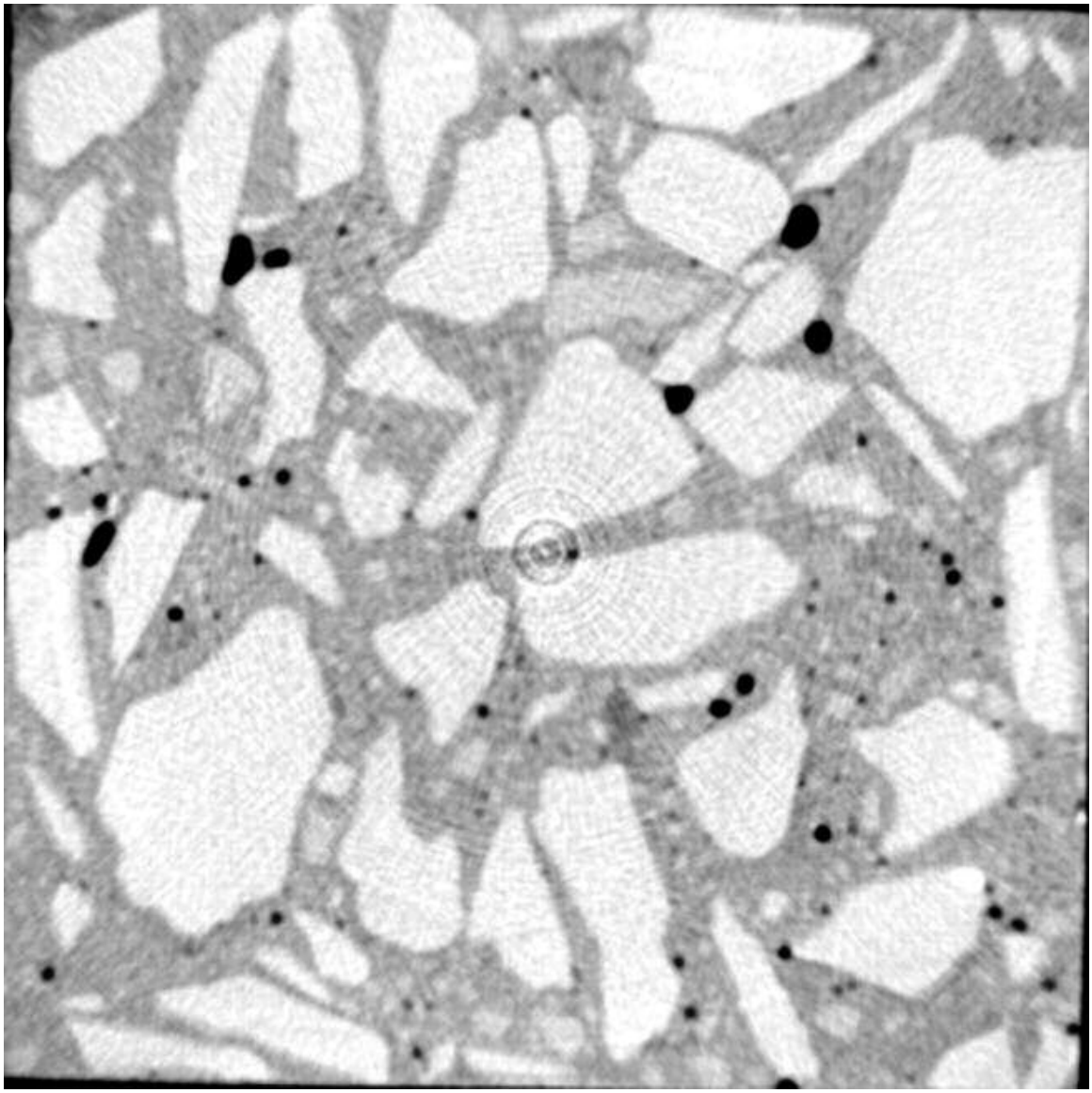

Figure 6.55 X-ray Computed Tomographic Image for Scan #20 of Specimen made with Laurel Sand

Bins (mm)	Frequency	Cumulative %	Relative %
0.1	0	.00%	0.00%
0.5	26	32.91%	32.91%
1	36	78.48%	45.57%
1.5	8	88.61%	10.13%
2	2	91.14%	2.53%
2.5	3	94.94%	3.80%
3	1	96.20%	1.27%
6	3	100.00%	3.80%
13	0	100.00%	0.00%

Table 6.38 Histogram Data of Scan #20 for the Pore Size Distribution on Diameter of Specimen made with Laurel Sand

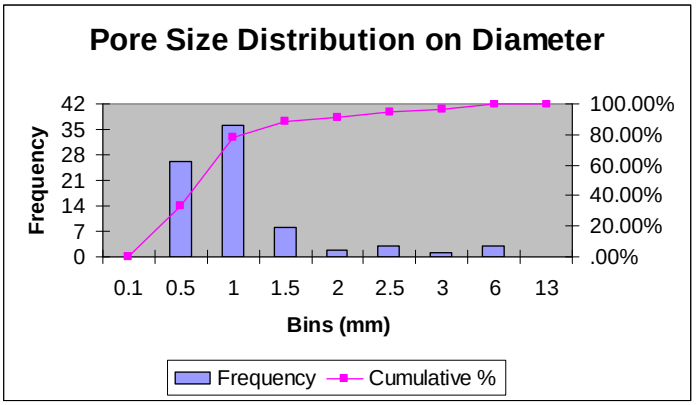

Figure 6.56 Histogram Plot of Scan #20 for the Pore Size Distribution on Diameter of Specimen made with Laurel Sand

Bins (mm^3)	Frequency	Cumulative %	Relative %
0.5	19	24.05%	24.05%
1	16	44.30%	20.25%
2	13	60.76%	16.46%
5	18	83.54%	22.78%
15	8	93.67%	10.13%
30	4	98.73%	5.06%
60	1	100.00%	1.27%
120	0	100.00%	0.00%
210	0	100.00%	0.00%

Table 6.39 Histogram Data of Scan #20 for the Pore Size Distribution on Volume of Specimen made with Laurel Sand

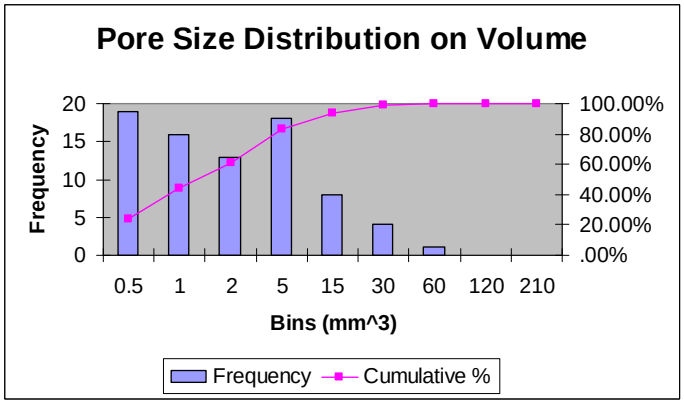

Figure 6.57 Histogram Plot of Scan #20 for the Pore Size Distribution on Volume of Specimen made with Laurel Sand

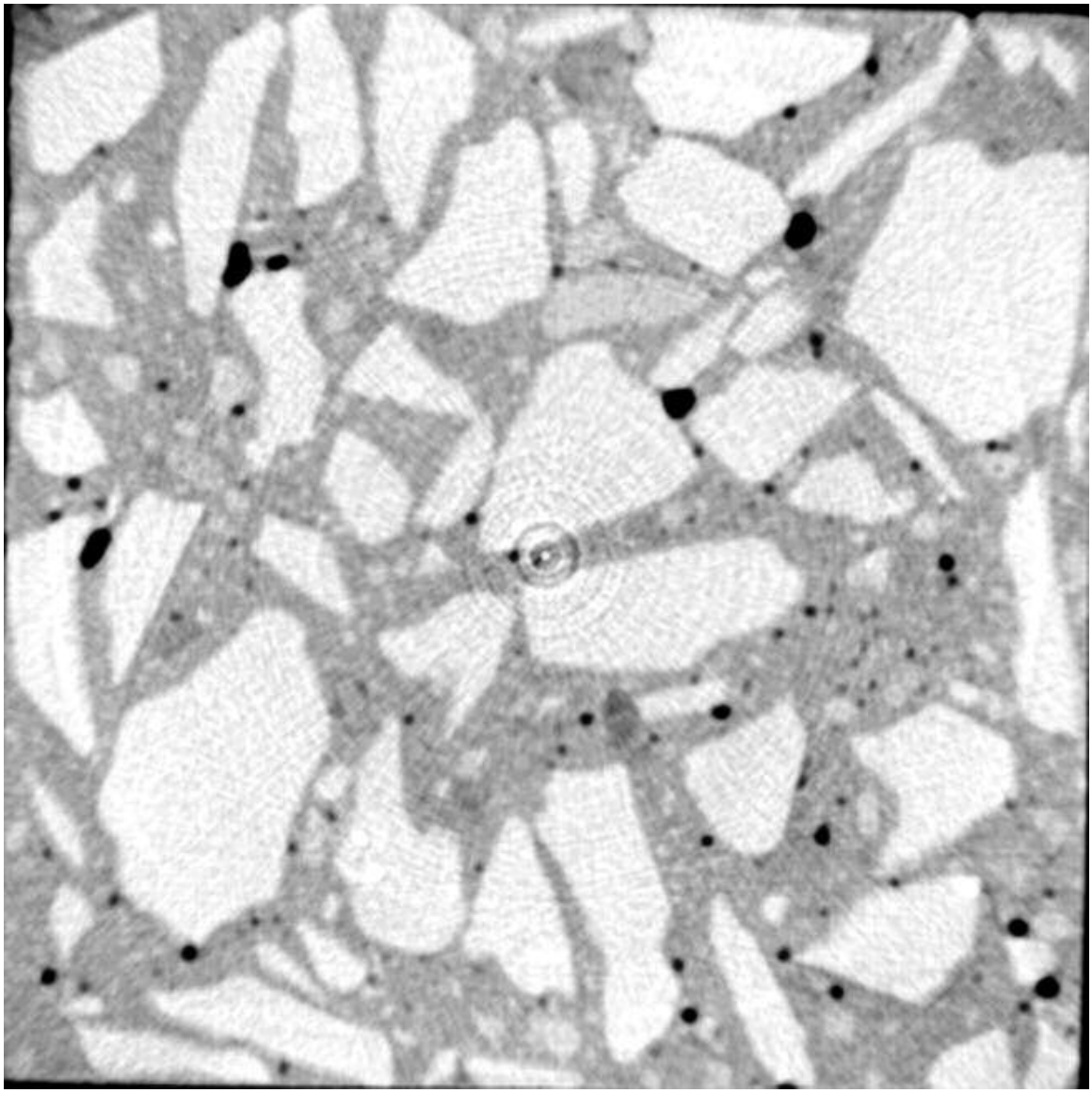

Figure 6.58 X-ray Computed Tomographic Image for Scan #21 of Specimen made with Laurel Sand

Bins (mm)	Frequency	Cumulative %	Relative %
0.1	0	.00%	0.00%
0.5	33	37.08%	37.08%
1	37	78.65%	41.57%
1.5	9	88.76%	10.11%
2	6	95.51%	6.74%
2.5	1	96.63%	1.12%
3	1	97.75%	1.12%
6	2	100.00%	2.25%
13	0	100.00%	0.00%

Table 6.40 Histogram Data of Scan #21 for the Pore Size Distribution on Diameter of Specimen made with Laurel Sand

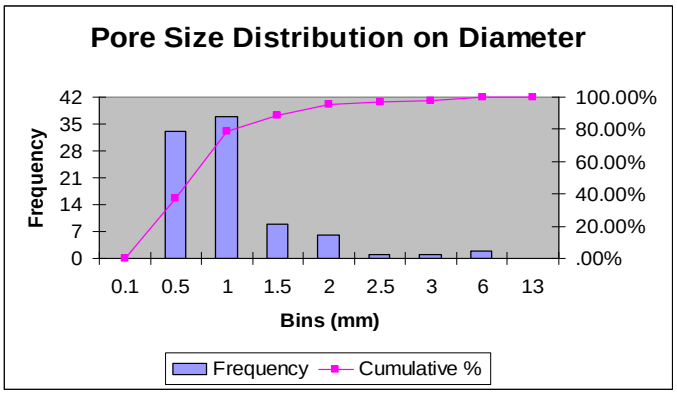

Figure 6.59 Histogram Plot of Scan #21 for the Pore Size Distribution on Diameter of Specimen made with Laurel Sand

Bins (mm^3)	Frequency	Cumulative %	Relative %
0.5	26	29.21%	29.21%
1	9	39.33%	10.11%
2	18	59.55%	20.22%
5	20	82.02%	22.47%
15	12	95.51%	13.48%
30	4	100.00%	4.49%
60	0	100.00%	0.00%
120	0	100.00%	0.00%
210	0	100.00%	0.00%

Table 6.41 Histogram Data of Scan #21 for the Pore Size Distribution on Volume of Specimen made with Laurel Sand

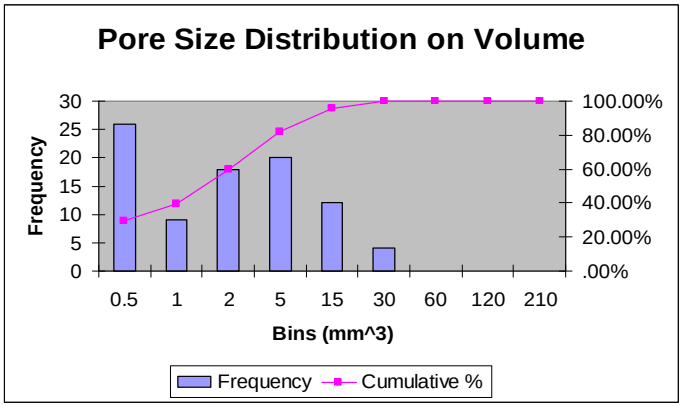

Figure 6.60 Histogram Plot of Scan #21 for the Pore Size Distribution on Volume of Specimen made with Laurel Sand

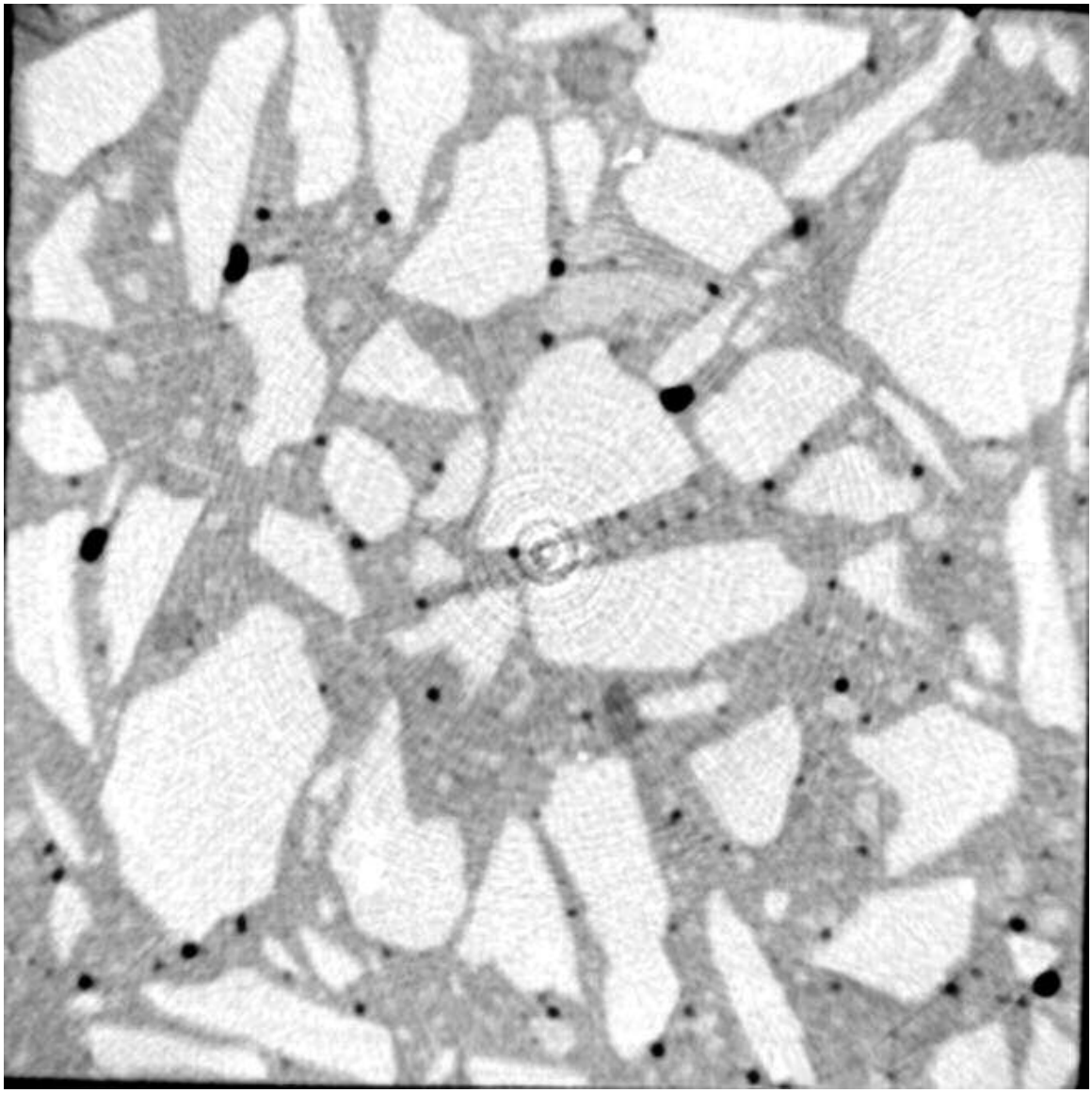

Figure 6.61 X-ray Computed Tomographic Image for Scan #22 of Specimen made with Laurel Sand

Bins (mm)	Frequency	Cumulative %	Relative %
0.1	0	.00%	0.00%
0.5	20	24.10%	24.10%
1	45	78.31%	54.22%
1.5	13	93.98%	15.66%
2	1	95.18%	1.20%
2.5	2	97.59%	2.41%
3	2	100.00%	2.41%
6	0	100.00%	0.00%
13	0	100.00%	0.00%

Table 6.42 Histogram Data of Scan #22 for the Pore Size Distribution on Diameter of Specimen made with Laurel Sand

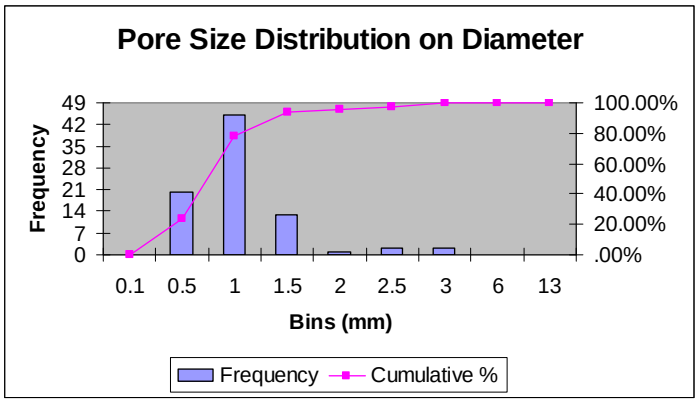

Figure 6.62 Histogram Plot of Scan #22 for the Pore Size Distribution on Diameter of Specimen made with Laurel Sand

Bins (mm^3)	Frequency	Cumulative %	Relative %
0.5	16	19.28%	19.28%
1	13	34.94%	15.66%
2	20	59.04%	24.10%
5	24	87.95%	28.92%
15	7	96.39%	8.43%
30	3	100.00%	3.61%
60	0	100.00%	0.00%
120	0	100.00%	0.00%
210	0	100.00%	0.00%

Table 6.43 Histogram Data of Scan #22 for the Pore Size Distribution on Volume of Specimen made with Laurel Sand

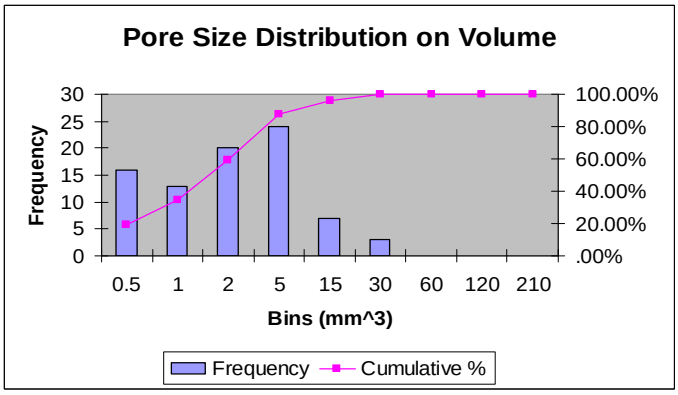

Figure 6.63 Histogram Plot of Scan #22 for the Pore Size Distribution on Volume of Specimen made with Laurel Sand

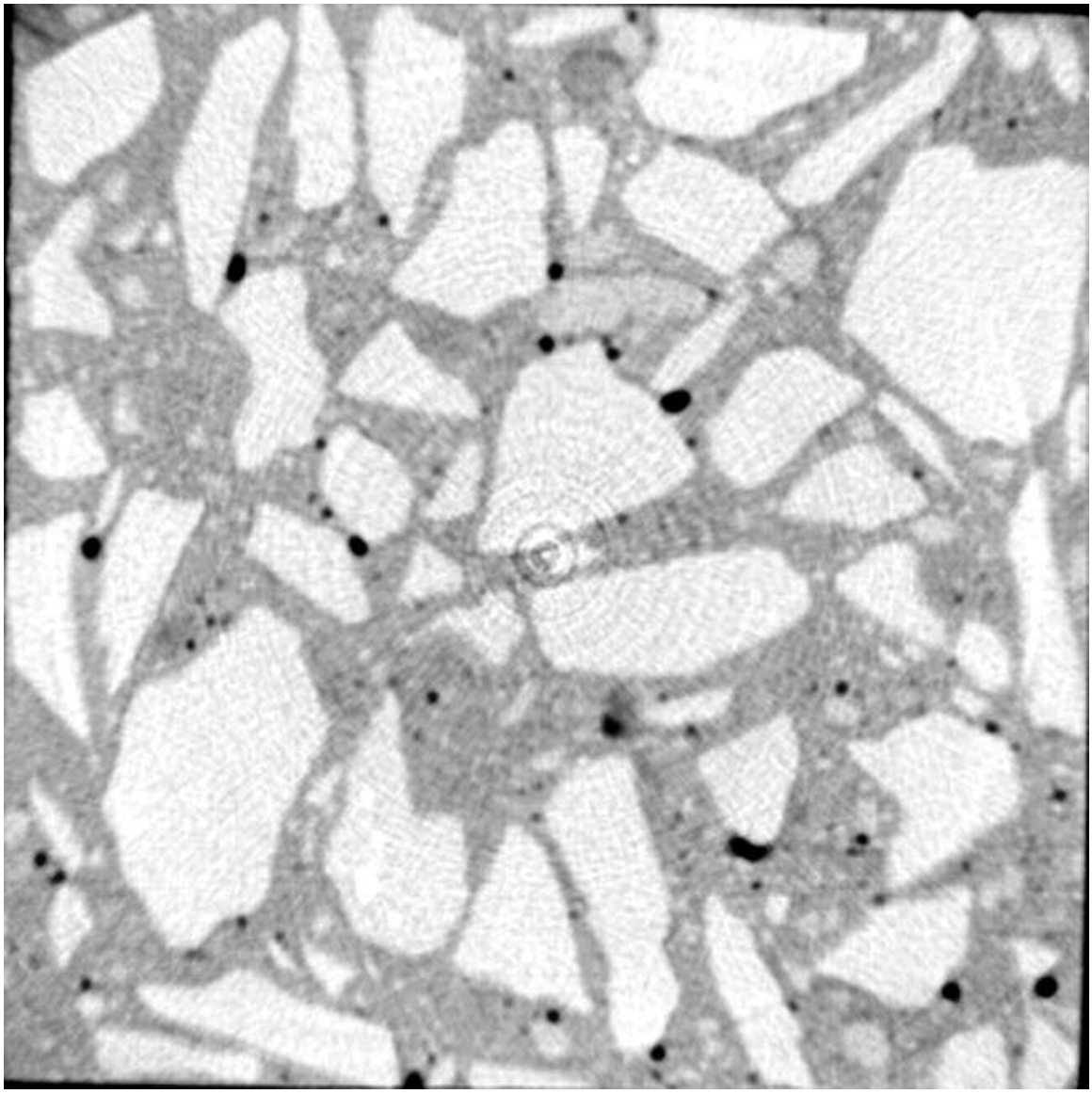

Figure 6.64 X-ray Computed Tomographic Image for Scan #23 of Specimen made with Laurel Sand

Bins (mm)	Frequency	Cumulative %	Relative %
0.1	0	.00%	0.00%
0.5	26	36.62%	36.62%
1	29	77.46%	40.85%
1.5	8	88.73%	11.27%
2	4	94.37%	5.63%
2.5	2	97.18%	2.82%
3	0	97.18%	0.00%
6	2	100.00%	2.82%
13	0	100.00%	0.00%

Table 6.44 Histogram Data of Scan #23 for the Pore Size Distribution on Diameter of Specimen made with Laurel Sand

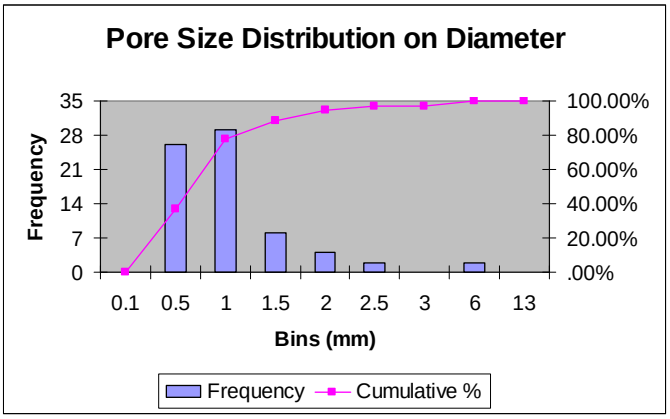

Figure 6.65 Histogram Plot of Scan #23 for the Pore Size Distribution on Diameter of Specimen made with Laurel Sand

Bins (mm^3)	Frequency	Cumulative %	Relative %
0.5	22	30.99%	30.99%
1	8	42.25%	11.27%
2	19	69.01%	26.76%
5	11	84.51%	15.49%
15	9	97.18%	12.68%
30	2	100.00%	2.82%
60	0	100.00%	0.00%
120	0	100.00%	0.00%
210	0	100.00%	0.00%

Table 6.45 Histogram Data of Scan #23 for the Pore Size Distribution on Volume of Specimen made with Laurel Sand

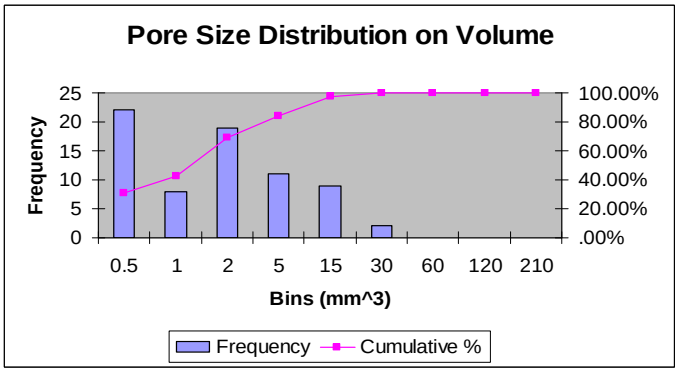

Figure 6.66 Histogram Plot of Scan #23 for the Pore Size Distribution on Volume of Specimen made with Laurel Sand

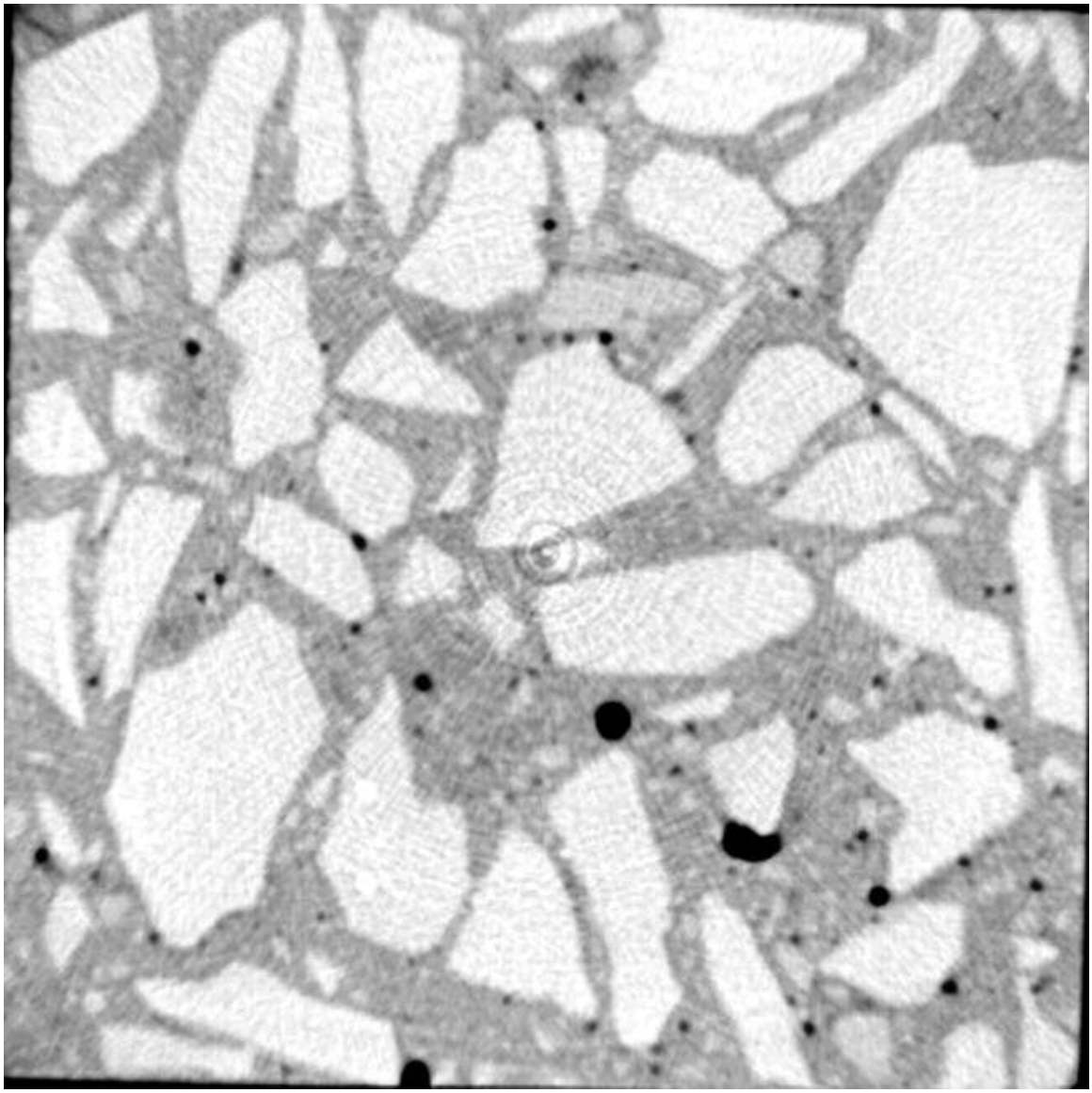

Figure 6.67 X-ray Computed Tomographic Image for Scan #24 of Specimen made with Laurel Sand

Bins (mm)	Frequency	Cumulative %	Relative %
0.1	0	.00%	0.00%
0.5	19	27.54%	27.54%
1	41	86.96%	59.42%
1.5	5	94.20%	7.25%
2	2	97.10%	2.90%
2.5	0	97.10%	0.00%
3	1	98.55%	1.45%
6	1	100.00%	1.45%
13	0	100.00%	0.00%

Table 6.46 Histogram Data of Scan #24 for the Pore Size Distribution on Diameter of Specimen made with Laurel Sand

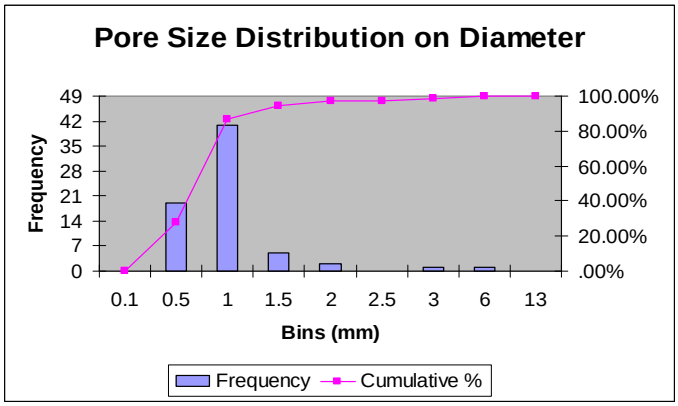

Figure 6.68 Histogram Plot of Scan #24 for the Pore Size Distribution on Diameter of Specimen made with Laurel Sand

Bins (mm^3)	Frequency	Cumulative %	Relative %
0.5	15	21.74%	21.74%
1	11	37.68%	15.94%
2	22	69.57%	31.88%
5	15	91.30%	21.74%
15	4	97.10%	5.80%
30	1	98.55%	1.45%
60	1	100.00%	1.45%
120	0	100.00%	0.00%
210	0	100.00%	0.00%

Table 6.47 Histogram Data of Scan #24 for the Pore Size Distribution on Volume of Specimen made with Laurel Sand

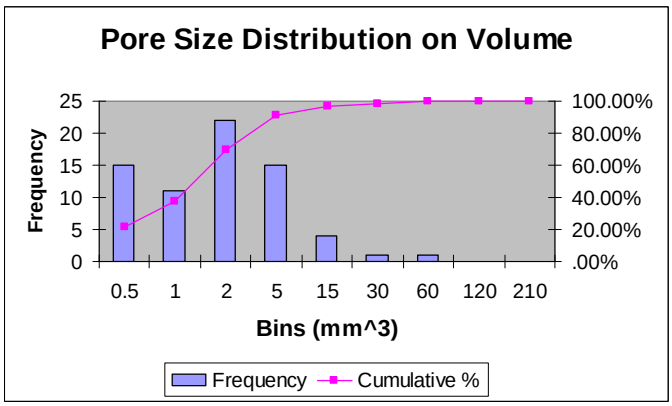

Figure 6.69 Histogram Plot of Scan #24 for the Pore Size Distribution on Volume of Specimen made with Laurel Sand

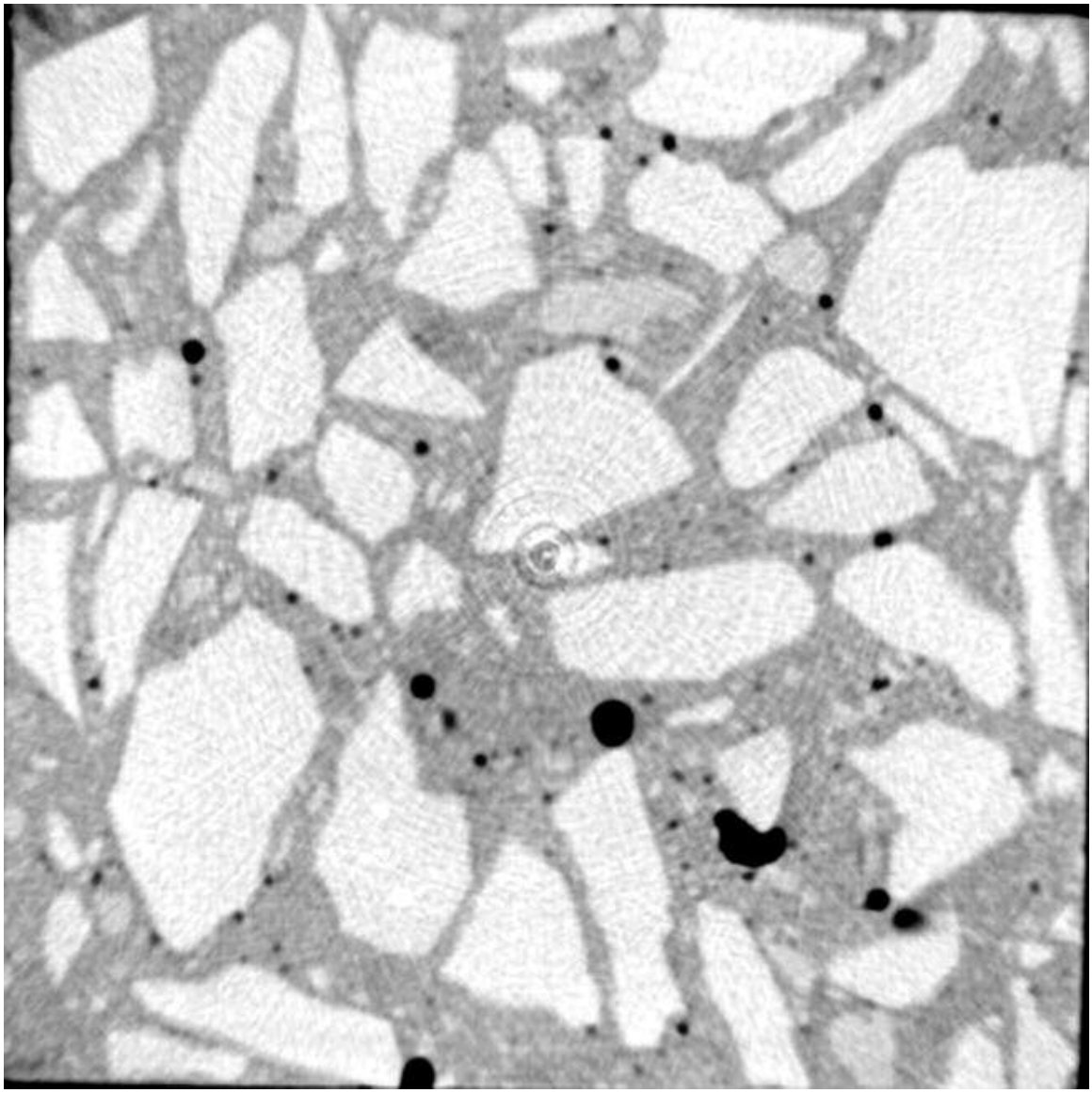

Figure 6.70 X-ray Computed Tomographic Image for Scan #25 of Specimen made with Laurel Sand

Bins (mm)	Frequency	Cumulative %	Relative %
0.1	0	.00%	0.00%
0.5	20	29.85%	29.85%
1	33	79.10%	49.25%
1.5	8	91.04%	11.94%
2	2	94.03%	2.99%
2.5	2	97.01%	2.99%
3	0	97.01%	0.00%
6	2	100.00%	2.99%
13	0	100.00%	0.00%

Table 6.48 Histogram Data of Scan #25 for the Pore Size Distribution on Diameter of Specimen made with Laurel Sand

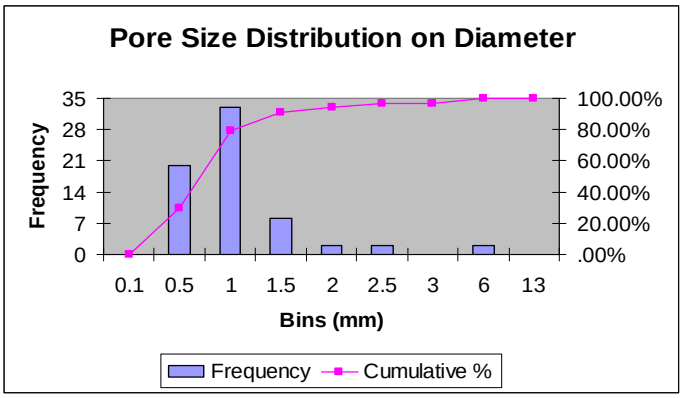

Figure 6.71 Histogram Plot of Scan #25 for the Pore Size Distribution on Diameter of Specimen made with Laurel Sand

Bins (mm^3)	Frequency	Cumulative %	Relative %
0.5	15	22.39%	22.39%
1	12	40.30%	17.91%
2	16	64.18%	23.88%
5	15	86.57%	22.39%
15	7	97.01%	10.45%
30	0	97.01%	0.00%
60	1	98.51%	1.49%
120	1	100.00%	1.49%
210	0	100.00%	0.00%

Table 6.49 Histogram Data of Scan #25 for the Pore Size Distribution on Volume of Specimen made with Laurel Sand

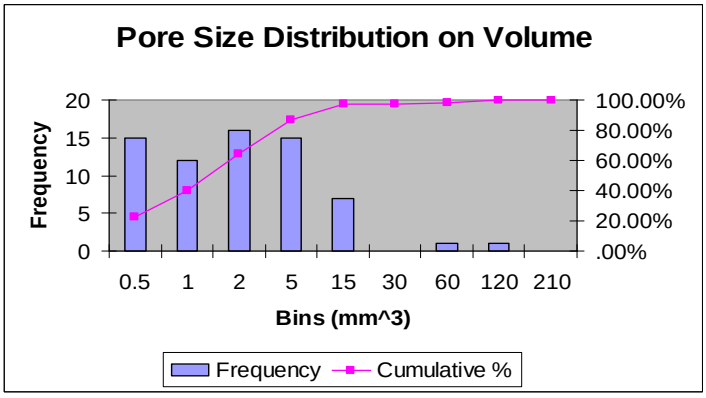

Figure 6.72 Histogram Plot of Scan #25 for the Pore Size Distribution on Volume of Specimen made with Laurel Sand

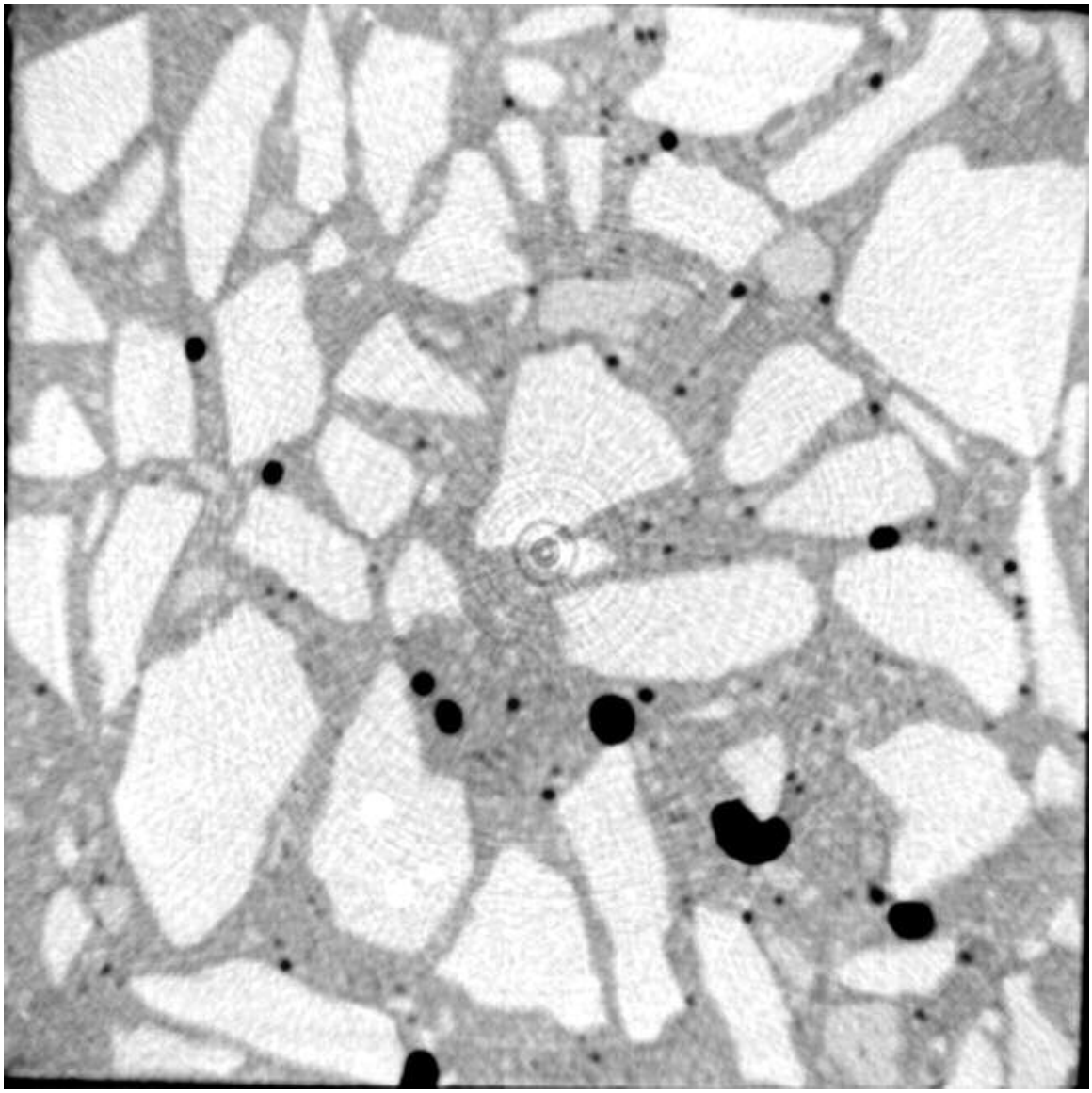

Figure 6.73 X-ray Computed Tomographic Image for Scan #26 of Specimen made with Laurel Sand

Bins (mm)	Frequency	Cumulative %	Relative %
0.1	0	.00%	0.00%
0.5	22	31.88%	31.88%
1	33	79.71%	47.83%
1.5	5	86.96%	7.25%
2	4	92.75%	5.80%
2.5	1	94.20%	1.45%
3	1	95.65%	1.45%
6	3	100.00%	4.35%
13	0	100.00%	0.00%

Table 6.50 Histogram Data of Scan #26 for the Pore Size Distribution on Diameter of Specimen made with Laurel Sand

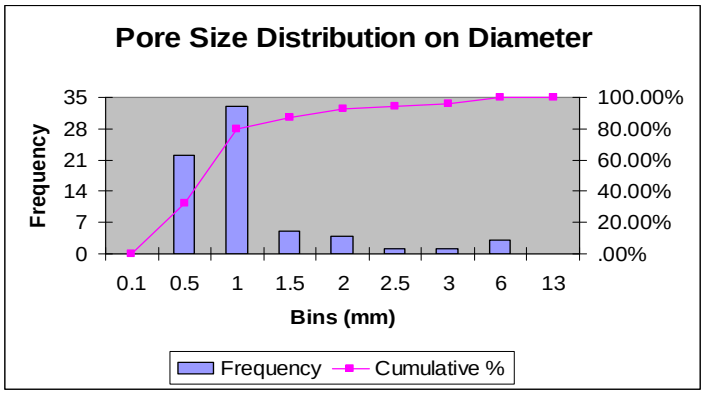

Figure 6.74 Histogram Plot of Scan #26 for the Pore Size Distribution on Diameter of Specimen made with Laurel Sand

Bins (mm^3)	Frequency	Cumulative %	Relative %
0.5	13	18.84%	18.84%
1	12	36.23%	17.39%
2	19	63.77%	27.54%
5	14	84.06%	20.29%
15	7	94.20%	10.14%
30	1	95.65%	1.45%
60	2	98.55%	2.90%
120	1	100.00%	1.45%
210	0	100.00%	0.00%

Table 6.51 Histogram Data of Scan #26 for the Pore Size Distribution on Volume of Specimen made with Laurel Sand

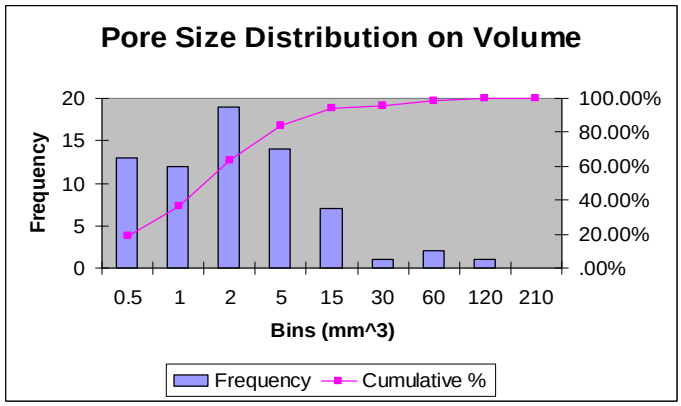

Figure 6.75 Histogram Plot of Scan #26 for the Pore Size Distribution on Volume of Specimen made with Laurel Sand

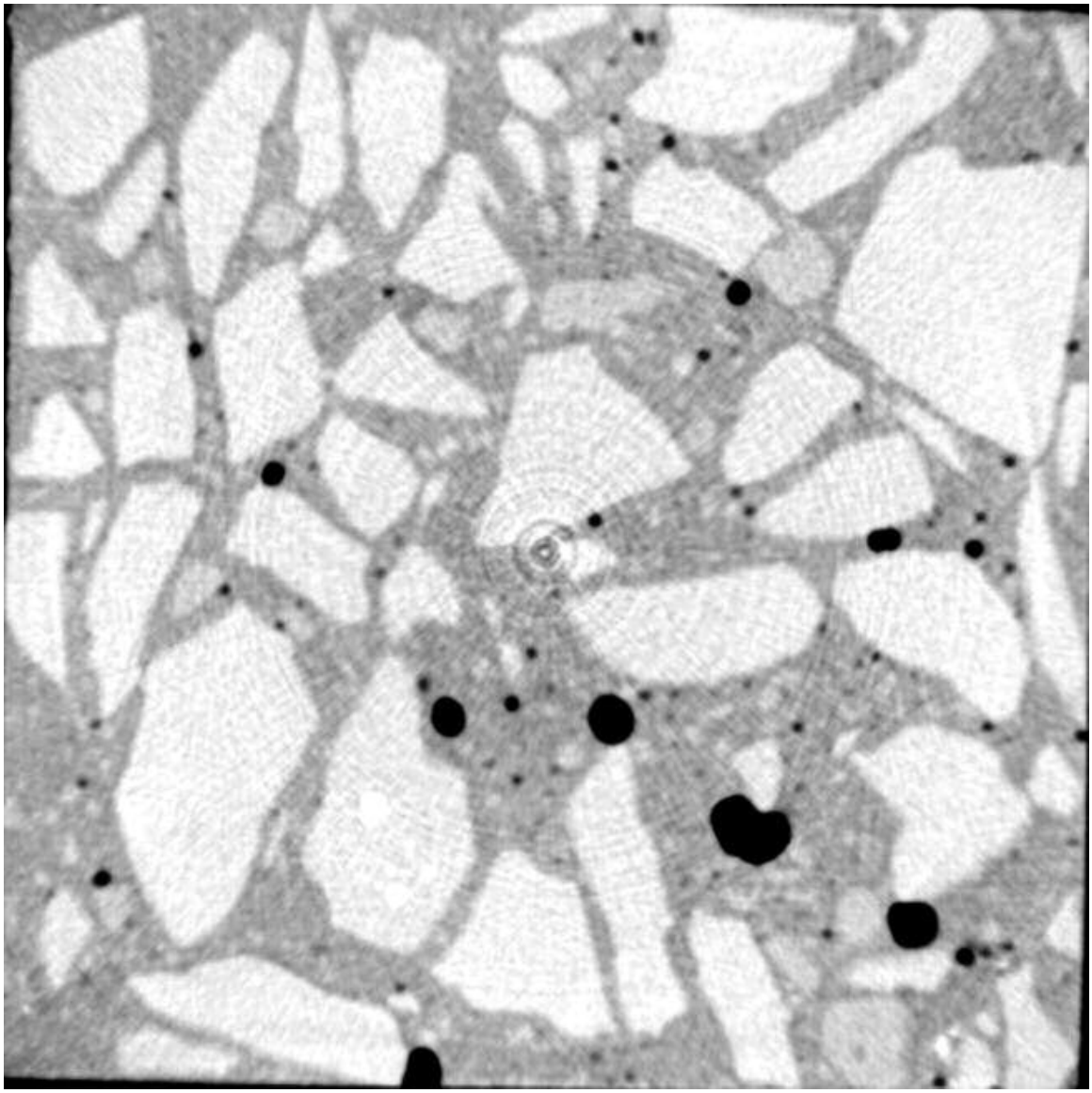

Figure 6.76 X-ray Computed Tomographic Image for Scan #27 of Specimen made with Laurel Sand

Bins (mm)	Frequency	Cumulative %	Relative %
0.1	0	.00%	0.00%
0.5	20	28.99%	28.99%
1	35	79.71%	50.72%
1.5	6	88.41%	8.70%
2	2	91.30%	2.90%
2.5	0	91.30%	0.00%
3	3	95.65%	4.35%
6	3	100.00%	4.35%
13	0	100.00%	0.00%

Table 6.52 Histogram Data of Scan #27 for the Pore Size Distribution on Diameter of Specimen made with Laurel Sand

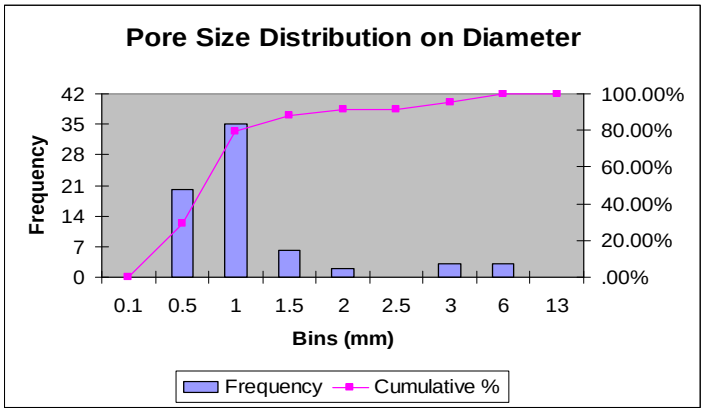

Figure 6.77 Histogram Plot of Scan #27 for the Pore Size Distribution on Diameter of Specimen made with Laurel Sand

Bins (mm^3)	Frequency	Cumulative %	Relative %
0.5	14	20.29%	20.29%
1	13	39.13%	18.84%
2	15	60.87%	21.74%
5	15	82.61%	21.74%
15	7	92.75%	10.14%
30	2	95.65%	2.90%
60	2	98.55%	2.90%
120	1	100.00%	1.45%
210	0	100.00%	0.00%

Table 6.53 Histogram Data of Scan #27 for the Pore Size Distribution on Volume of Specimen made with Laurel Sand

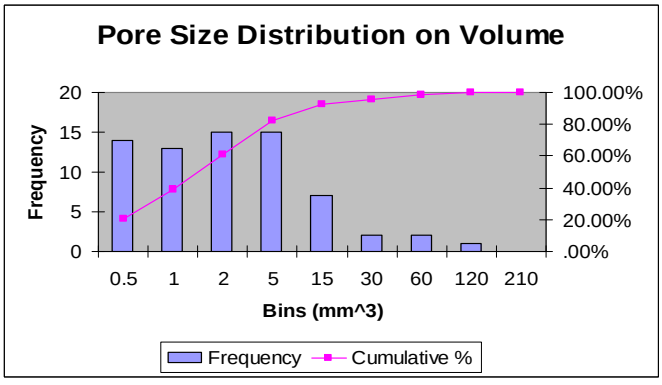

Figure 6.78 Histogram Plot of Scan #27 for the Pore Size Distribution on Volume of Specimen made with Laurel Sand

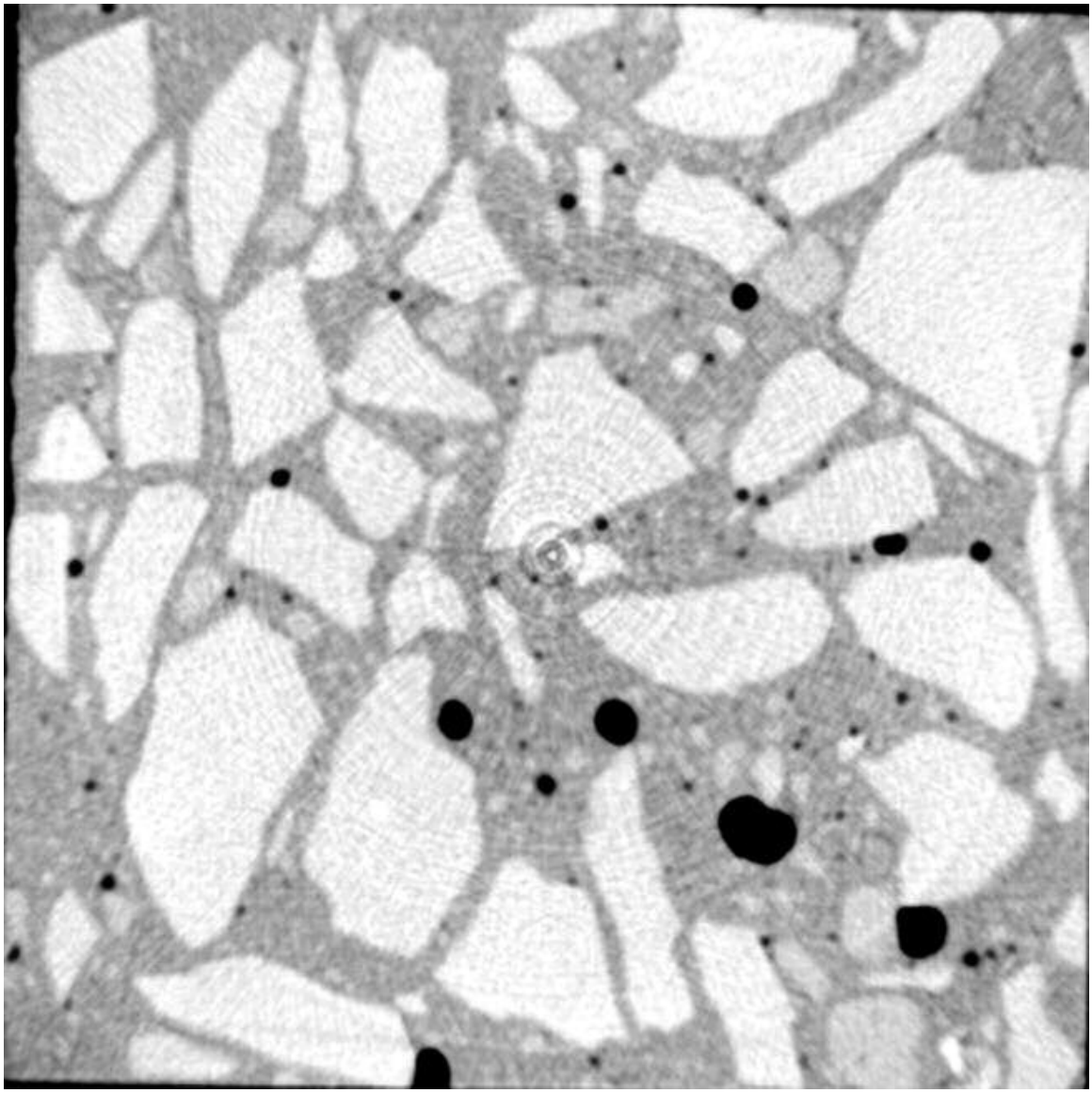

Figure 6.79 X-ray Computed Tomographic Image for Scan #28 of Specimen made with Laurel Sand

Bins (mm)	Frequency	Cumulative %	Relative %
0.1	0	.00%	0.00%
0.5	15	22.73%	22.73%
1	35	75.76%	53.03%
1.5	7	86.36%	10.61%
2	4	92.42%	6.06%
2.5	1	93.94%	1.52%
3	1	95.45%	1.52%
6	3	100.00%	4.55%
13	0	100.00%	0.00%

Table 6.54 Histogram Data of Scan #28 for the Pore Size Distribution on Diameter of Specimen made with Laurel Sand

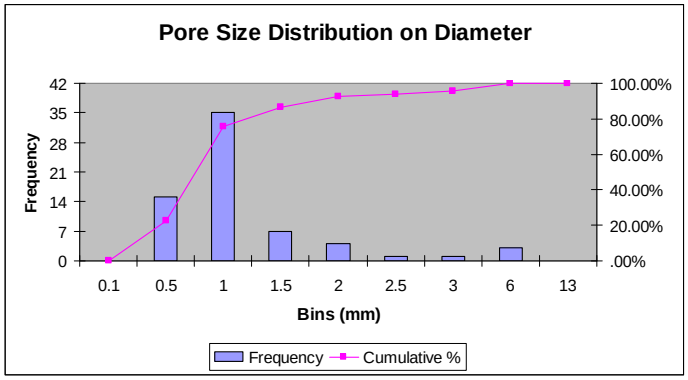

Figure 6.80 Histogram Plot of Scan #28 for the Pore Size Distribution on Diameter of Specimen made with Laurel Sand

Bins (mm^3)	Frequency	Cumulative %	Relative %
0.5	12	18.18%	18.18%
1	12	36.36%	18.18%
2	16	60.61%	24.24%
5	13	80.30%	19.70%
15	8	92.42%	12.12%
30	2	95.45%	3.03%
60	2	98.48%	3.03%
120	1	100.00%	1.52%
210	0	100.00%	0.00%

Table 6.55 Histogram Data of Scan #28 for the Pore Size Distribution on Volume of Specimen made with Laurel Sand

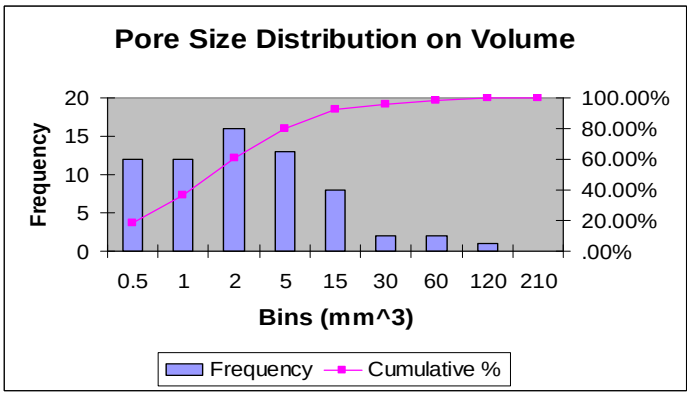

Figure 6.81 Histogram Plot of Scan #28 for the Pore Size Distribution on Volume of Specimen made with Laurel Sand

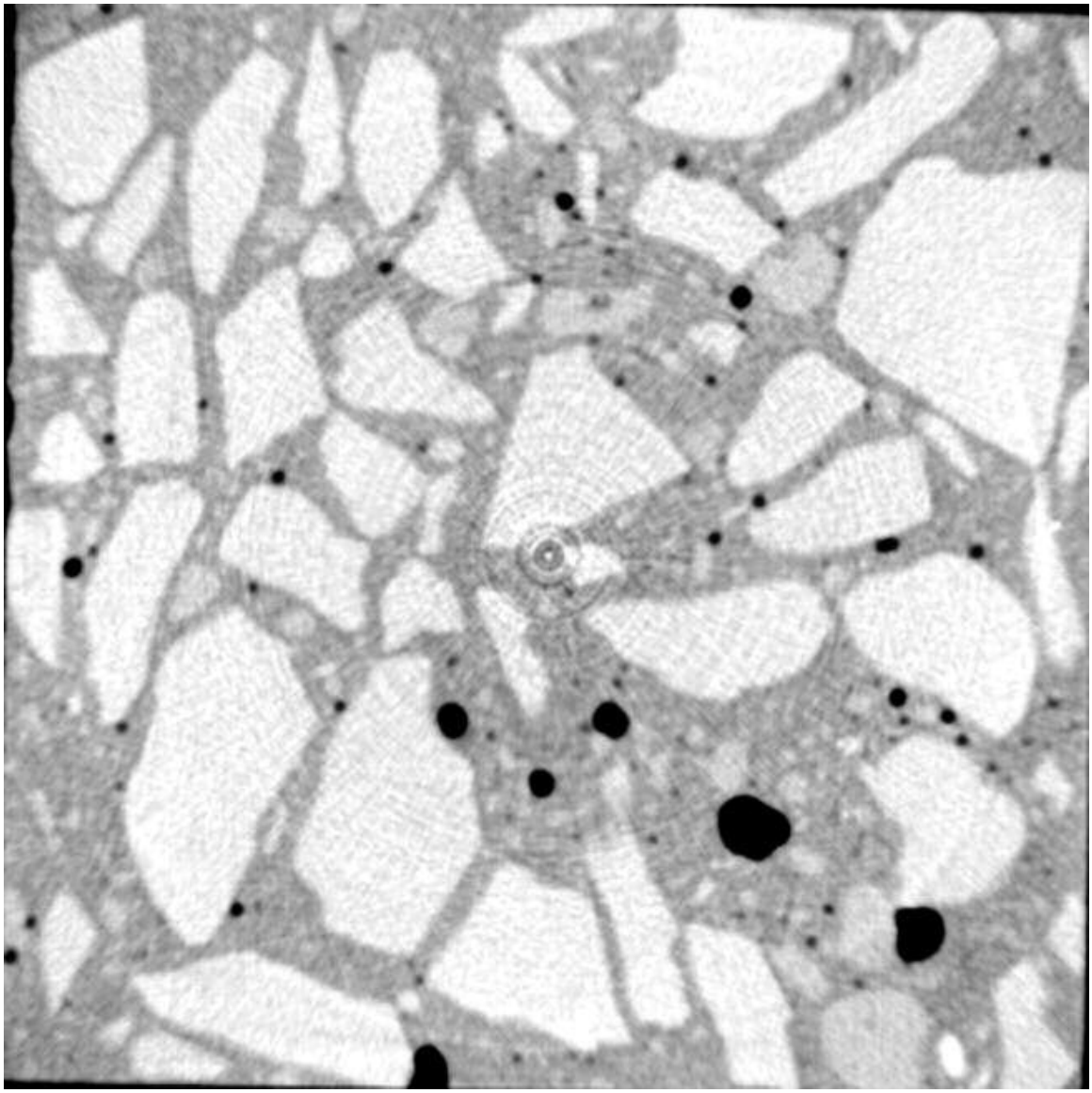

Figure 6.82 X-ray Computed Tomographic Image for Scan #29 of Specimen made with Laurel Sand

Bins (mm)	Frequency	Cumulative %	Relative %
0.1	0	.00%	0.00%
0.5	20	28.57%	28.57%
1	35	78.57%	50.00%
1.5	7	88.57%	10.00%
2	3	92.86%	4.29%
2.5	1	94.29%	1.43%
3	1	95.71%	1.43%
6	3	100.00%	4.29%
13	0	100.00%	0.00%

Table 6.56 Histogram Data of Scan #29 for the Pore Size Distribution on Diameter of Specimen made with Laurel Sand

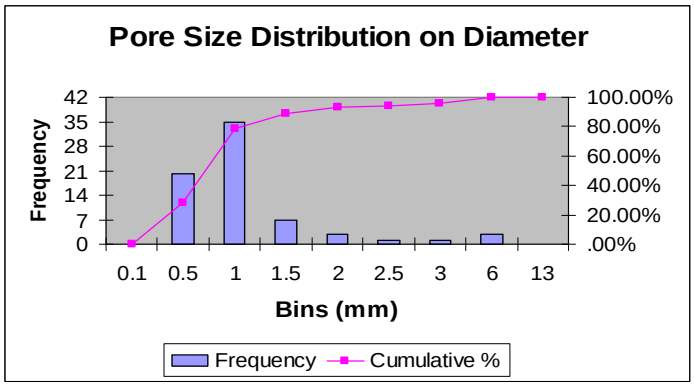

Figure 6.83 Histogram Plot of Scan #29 for the Pore Size Distribution on Diameter of Specimen made with Laurel Sand

Bins (mm^3)	Frequency	Cumulative %	Relative %
0.5	11	15.71%	15.71%
1	15	37.14%	21.43%
2	17	61.43%	24.29%
5	17	85.71%	24.29%
15	5	92.86%	7.14%
30	3	97.14%	4.29%
60	1	98.57%	1.43%
120	1	100.00%	1.43%
210	0	100.00%	0.00%

Table 6.57 Histogram Data of Scan #29 for the Pore Size Distribution on Volume of Specimen made with Laurel Sand

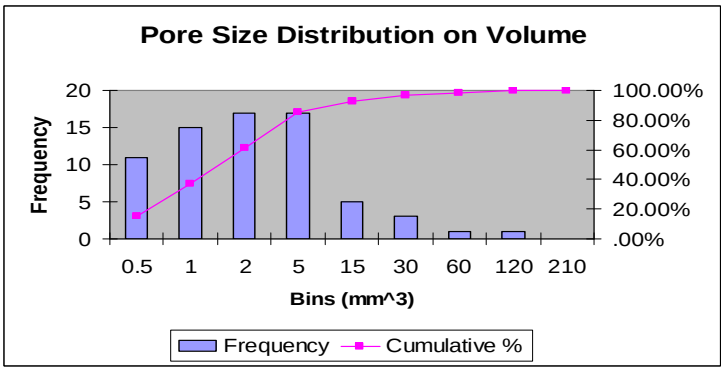

Figure 6.84 Histogram Plot of Scan #29 for the Pore Size Distribution on Volume of Specimen made with Laurel Sand

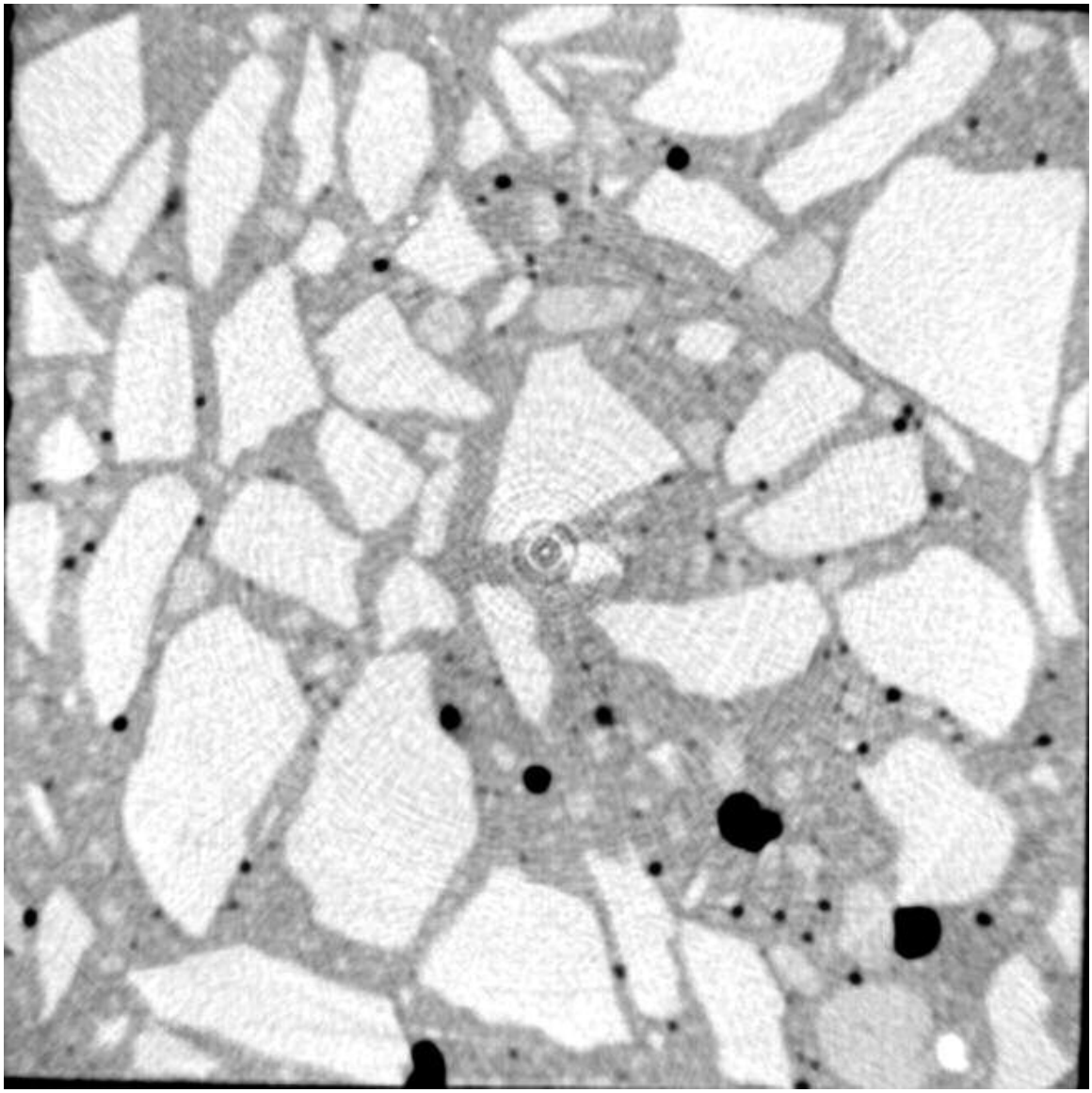

Figure 6.85 X-ray Computed Tomographic Image for Scan #30 of Specimen made with Laurel Sand

Bins (mm)	Frequency	Cumulative %	Relative %
0.1	0	.00%	.00%
0.5	26	32.50%	32.500%
1	38	80.00%	47.500%
1.5	8	90.00%	10.000%
2	3	93.75%	3.750%
2.5	3	97.50%	3.750%
3	0	97.50%	0.000%
6	2	100.00%	2.500%
13	0	100.00%	0.000%

Table 6.58 Histogram Data of Scan #30 for the Pore Size Distribution on Diameter of Specimen made with Laurel Sand

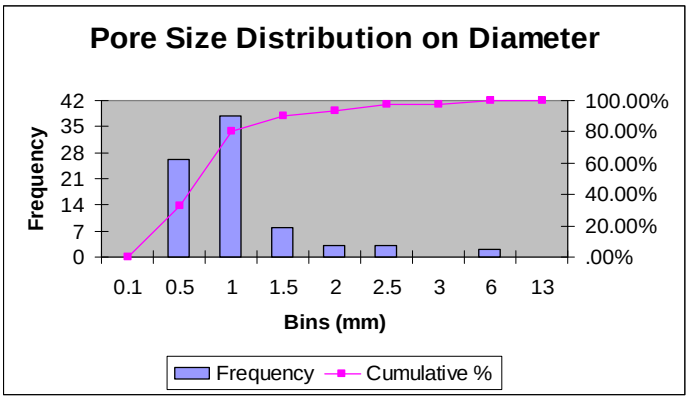

Figure 6.86 Histogram Plot of Scan #30 for the Pore Size Distribution on Diameter of Specimen made with Laurel Sand

Bins (mm^3)	Frequency	Cumulative %	Relative %
0.5	14	17.50%	17.50%
1	21	43.75%	26.2500%
2	14	61.25%	17.5000%
5	20	86.25%	25.0000%
15	8	96.25%	10.0000%
30	1	97.50%	1.2500%
60	1	98.75%	1.2500%
120	1	100.00%	1.2500%
210	0	100.00%	0.0000%

Table 6.59 Histogram Data of Scan #30 for the Pore Size Distribution on Volume of Specimen made with Laurel Sand

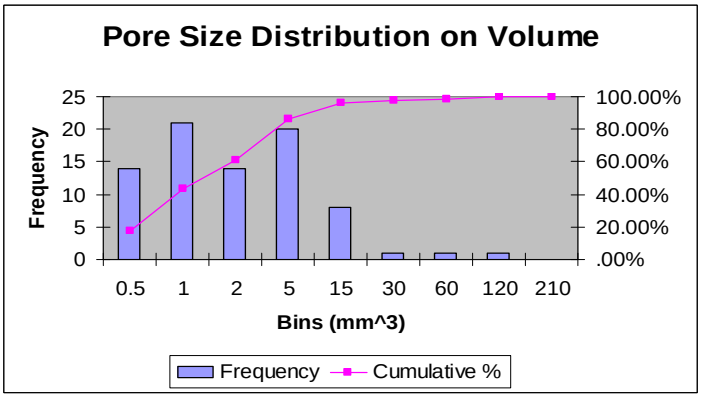

Figure 6.87 Histogram Plot of Scan #30 for the Pore Size Distribution on Volume of Specimen made with Laurel Sand

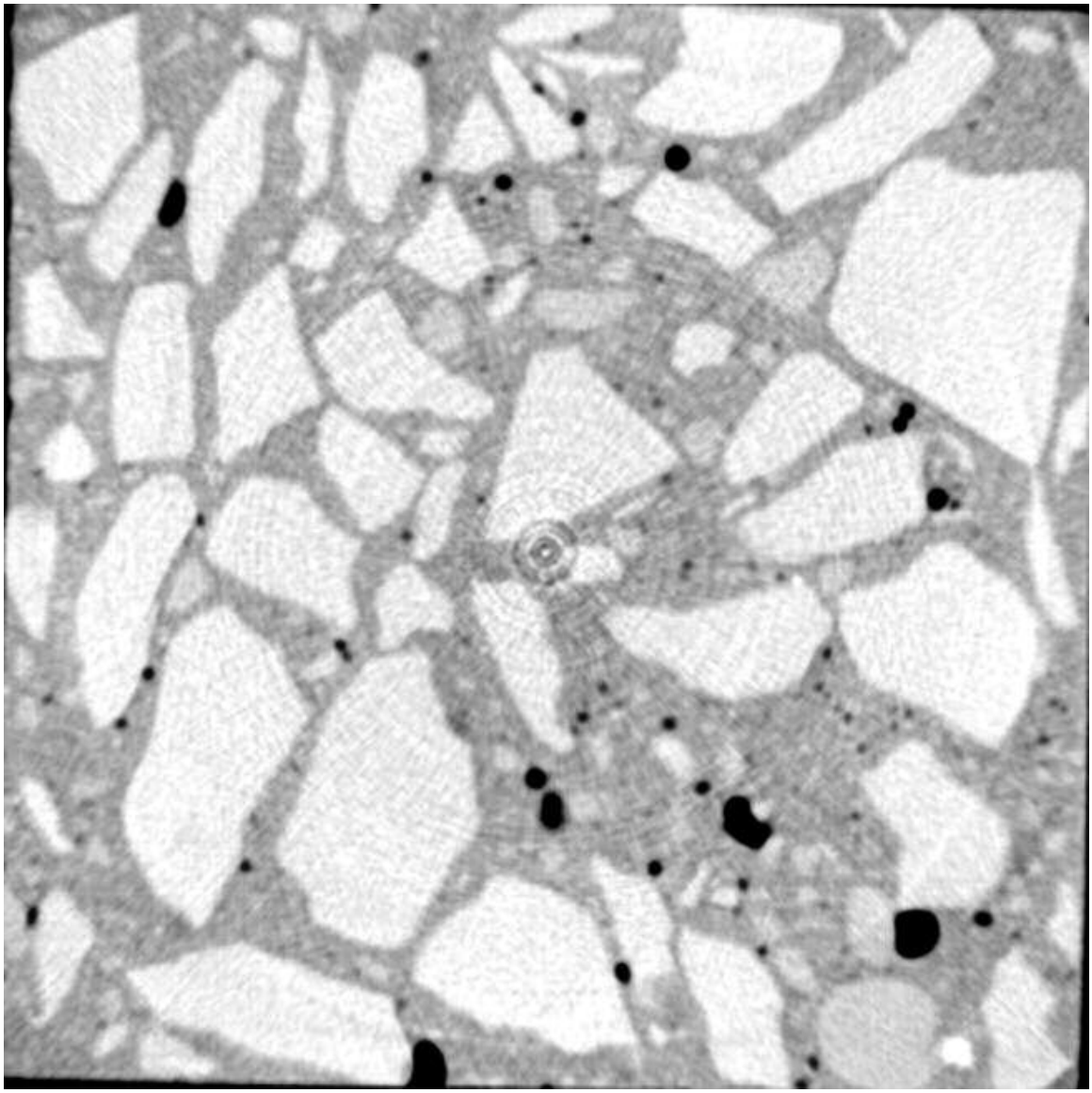

Figure 6.88 X-ray Computed Tomographic Image for Scan #31 of Specimen made with Laurel Sand

Bins (mm)	Frequency	Cumulative %	Relative %
0.1	0	.00%	0.00%
0.5	23	33.33%	33.33%
1	30	76.81%	43.48%
1.5	6	85.51%	8.70%
2	4	91.30%	5.80%
2.5	2	94.20%	2.90%
3	1	95.65%	1.45%
6	3	100.00%	4.35%
13	0	100.00%	0.00%

Table 6.60 Histogram Data of Scan #31 for the Pore Size Distribution on Diameter of Specimen made with Laurel Sand

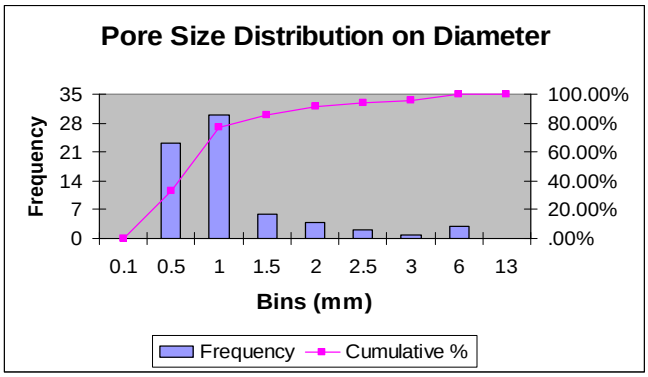

Figure 6.89 Histogram Plot of Scan #31 for the Pore Size Distribution on Diameter of Specimen made with Laurel Sand

Bins (mm^3)	Frequency	Cumulative %	Relative %
0.5	15	21.74%	21.74%
1	15	43.48%	21.74%
2	12	60.87%	17.39%
5	16	84.06%	23.19%
15	7	94.20%	10.14%
30	2	97.10%	2.90%
60	2	100.00%	2.90%
120	0	100.00%	0.00%
210	0	100.00%	0.00%

Table 6.61 Histogram Data of Scan #31 for the Pore Size Distribution on Volume of Specimen made with Laurel Sand

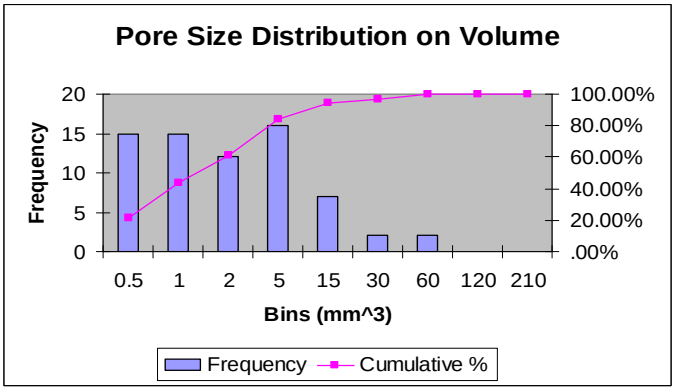

Figure 6.90 Histogram Plot of Scan #31 for the Pore Size Distribution on Volume of Specimen made with Laurel Sand

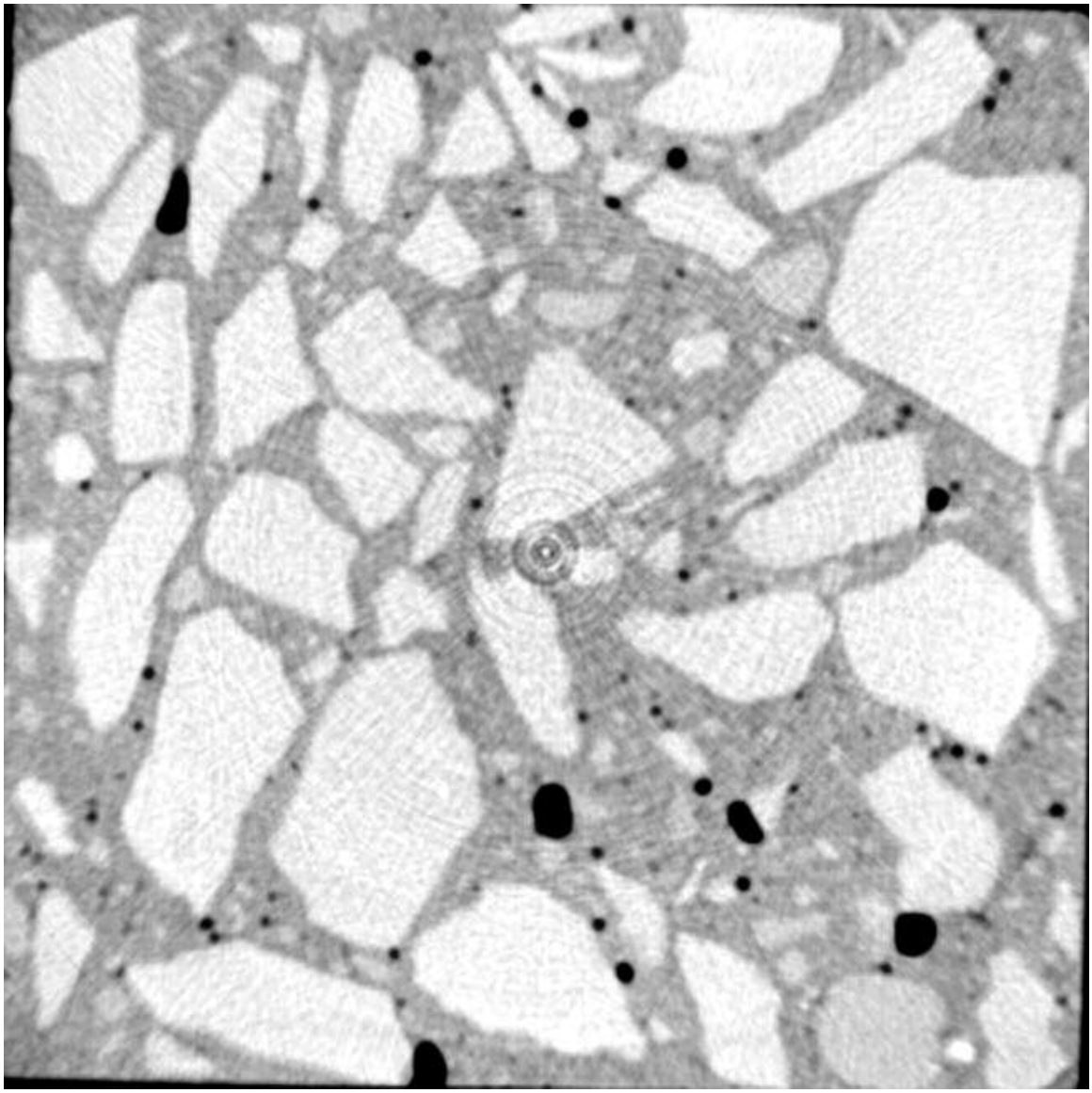

Figure 6.91 X-ray Computed Tomographic Image for Scan #32 of Specimen made with Laurel Sand

Bins (mm)	Frequency	Cumulative %	Relative %
0.1	0	.00%	0.00%
0.5	25	28.09%	28.09%
1	45	78.65%	50.56%
1.5	10	89.89%	11.24%
2	4	94.38%	4.49%
2.5	1	95.51%	1.12%
3	0	95.51%	0.00%
6	4	100.00%	4.49%
13	0	100.00%	0.00%

Table 6.62 Histogram Data of Scan #32 for the Pore Size Distribution on Diameter of Specimen made with Laurel Sand

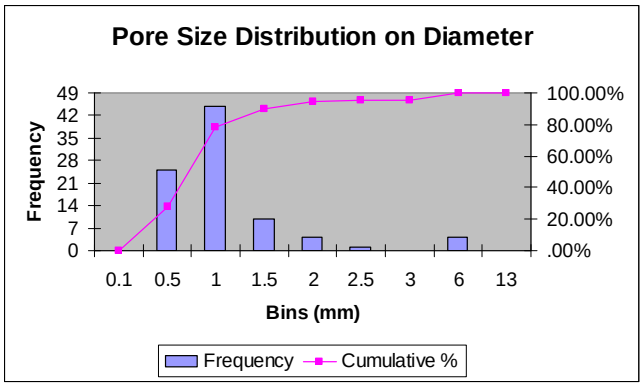

Figure 6.92 Histogram Plot of Scan #32 for the Pore Size Distribution on Diameter of Specimen made with Laurel Sand

Bins (mm^3)	Frequency	Cumulative %	Relative %
0.5	20	22.47%	22.47%
1	14	38.20%	15.73%
2	18	58.43%	20.22%
5	24	85.39%	26.97%
15	9	95.51%	10.11%
30	1	96.63%	1.12%
60	3	100.00%	3.37%
120	0	100.00%	0.00%
210	0	100.00%	0.00%

Table 6.63 Histogram Data of Scan #32 for the Pore Size Distribution on Volume of Specimen made with Laurel Sand

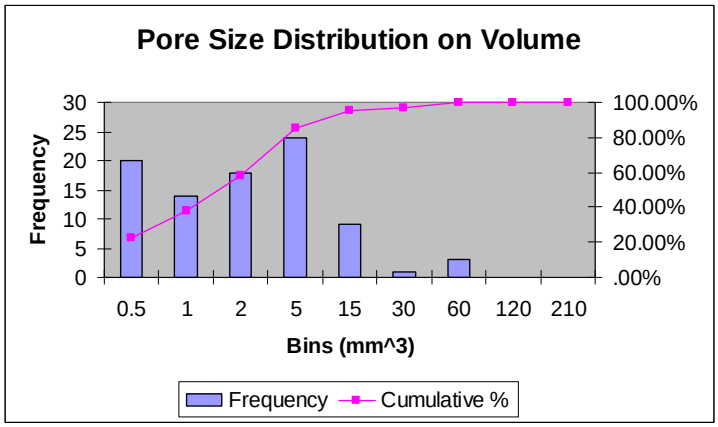

Figure 6.93 Histogram Plot of Scan #32 for the Pore Size Distribution on Volume of Specimen made with Laurel Sand

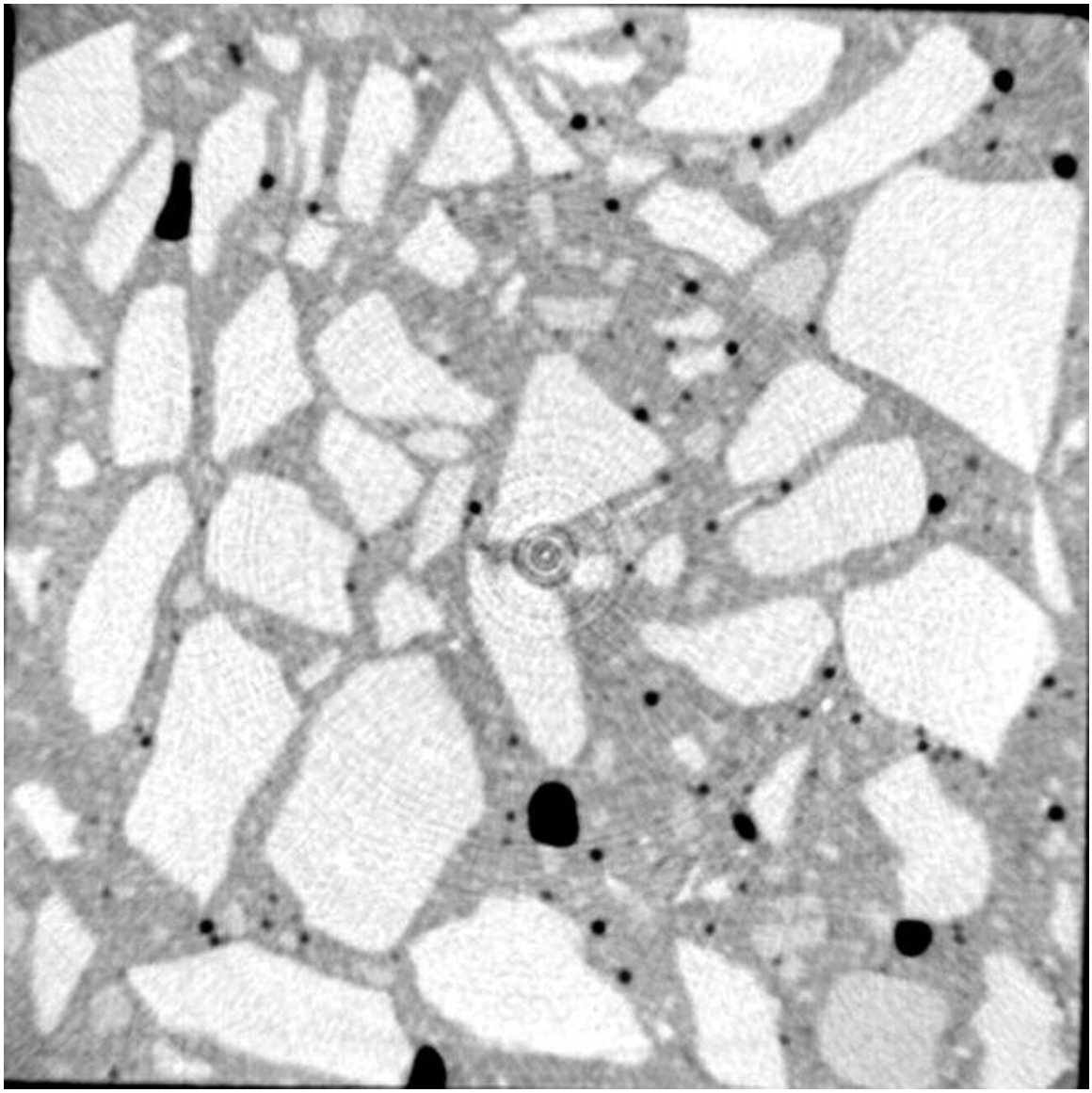

Figure 6.94 X-ray Computed Tomographic Image for Scan #33 of Specimen made with Laurel Sand

Bins (mm)	Frequency	Cumulative %	Relative %
0.1	0	.00%	0.00%
0.5	22	26.83%	26.83%
1	40	75.61%	48.78%
1.5	11	89.02%	13.41%
2	5	95.12%	6.10%
2.5	1	96.34%	1.22%
3	1	97.56%	1.22%
6	2	100.00%	2.44%
13	0	100.00%	0.00%

Table 6.64 Histogram Data of Scan #33 for the Pore Size Distribution on Diameter of Specimen made with Laurel Sand

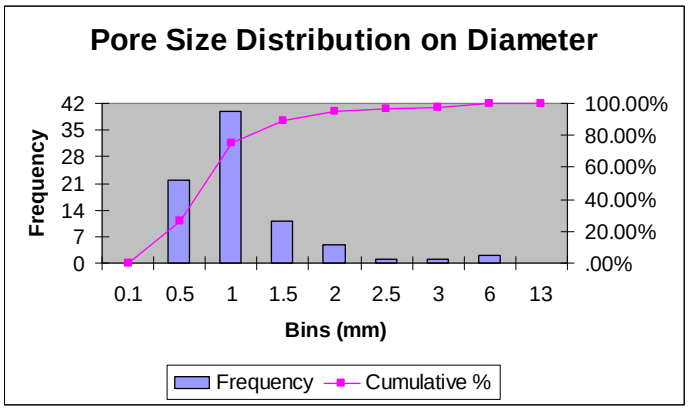

Figure 6.95 Histogram Plot of Scan #33 for the Pore Size Distribution on Diameter of Specimen made with Laurel Sand

Bins (mm^3)	Frequency	Cumulative %	Relative %
0.5	15	18.29%	18.29%
1	14	35.37%	17.07%
2	22	62.20%	26.83%
5	20	86.59%	24.39%
15	8	96.34%	9.76%
30	1	97.56%	1.22%
60	1	98.78%	1.22%
120	1	100.00%	1.22%
210	0	100.00%	0.00%

Table 6.65 Histogram Data of Scan #33 for the Pore Size Distribution on Volume of Specimen made with Laurel Sand

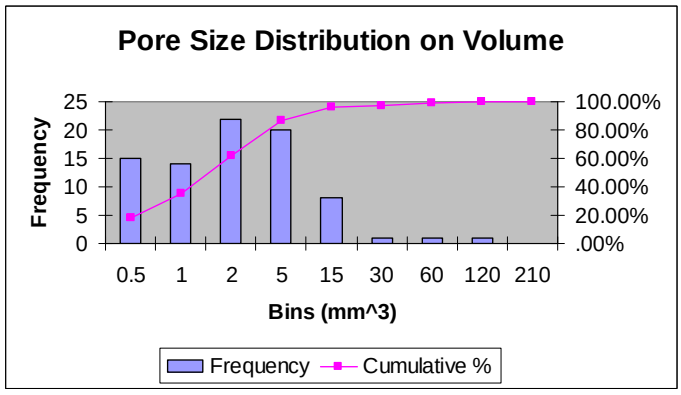

Figure 6.96 Histogram Plot of Scan #33 for the Pore Size Distribution on Volume of Specimen made with Laurel Sand

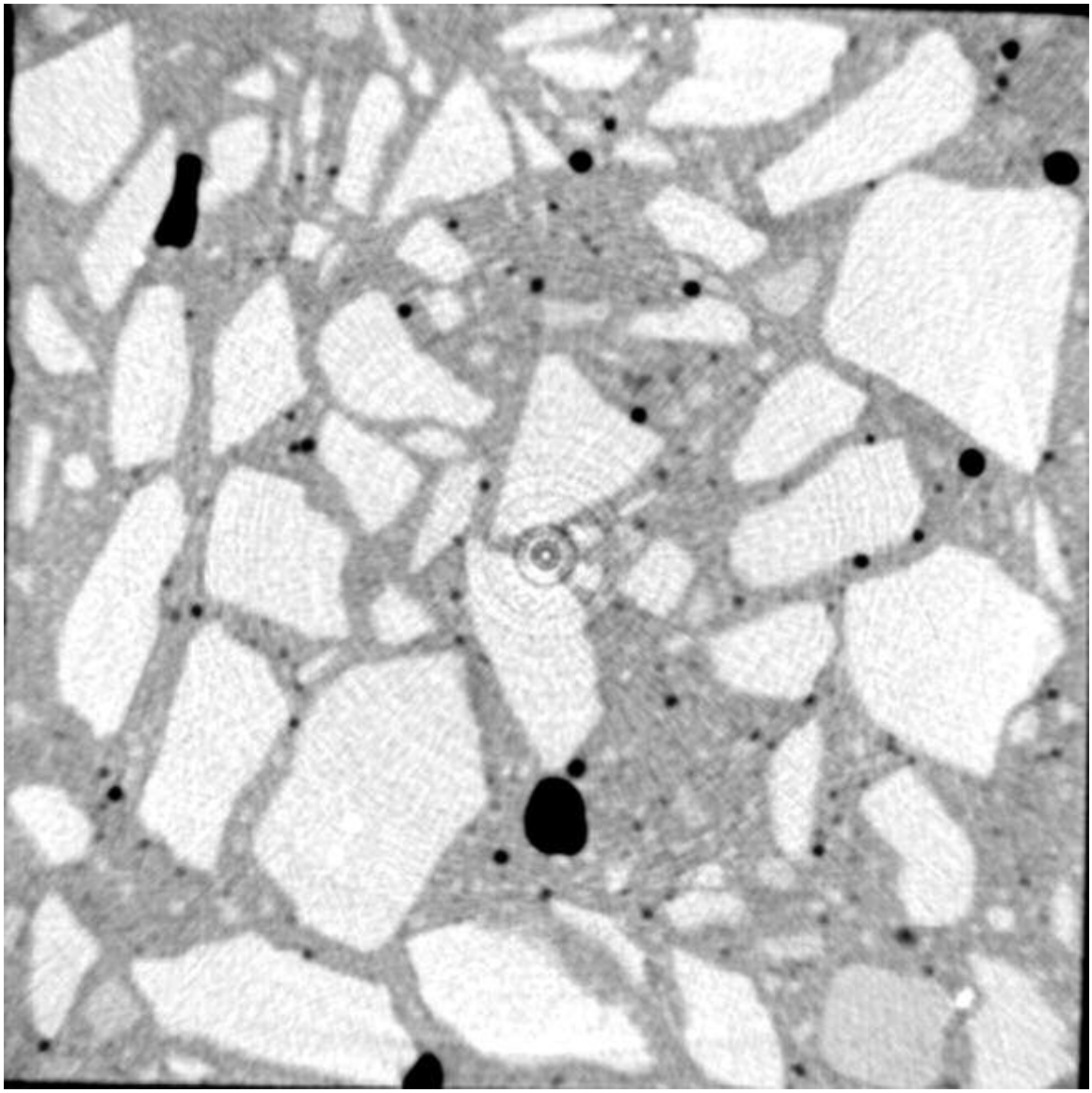

Figure 6.97 X-ray Computed Tomographic Image for Scan #35 of Specimen made with Laurel Sand

Bins (mm)	Frequency	Cumulative %	Relative %
0.1	0	.00%	0.00%
0.5	29	32.95%	32.95%
1	43	81.82%	48.86%
1.5	10	93.18%	11.36%
2	3	96.59%	3.41%
2.5	0	96.59%	0.00%
3	1	97.73%	1.14%
6	1	98.86%	1.14%
13	1	100.00%	1.14%

Table 6.66 Histogram Data of Scan #35 for the Pore Size Distribution on Diameter of Specimen made with Laurel Sand

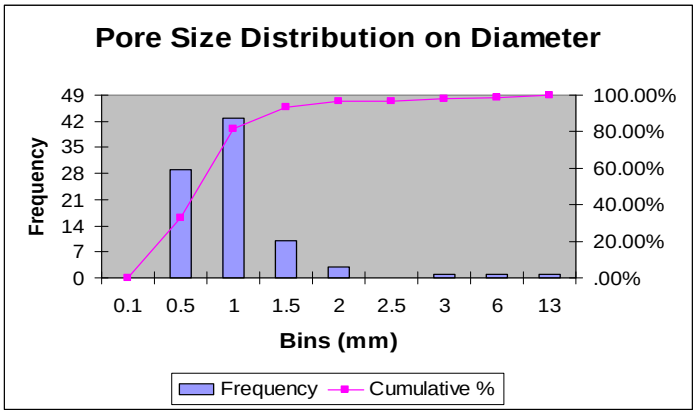

Figure 6.98 Histogram Plot of Scan #35 for the Pore Size Distribution on Diameter of Specimen made with Laurel Sand

Bins (mm^3)	Frequency	Cumulative %	Relative %
0.5	22	25.00%	25.00%
1	18	45.45%	20.45%
2	22	70.45%	25.00%
5	16	88.64%	18.18%
15	6	95.45%	6.82%
30	2	97.73%	2.27%
60	0	97.73%	0.00%
120	2	100.00%	2.27%
210	0	100.00%	0.00%

Table 6.67 Histogram Data of Scan #35 for the Pore Size Distribution on Volume of Specimen made with Laurel Sand

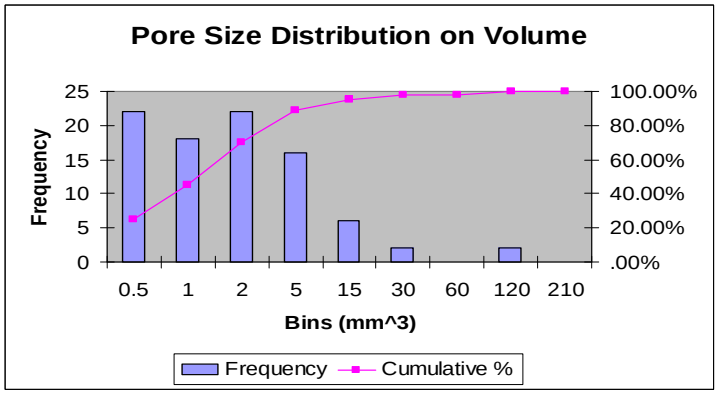

Figure 6.99 Histogram Plot of Scan #35 for the Pore Size Distribution on Volume of Specimen made with Laurel Sand

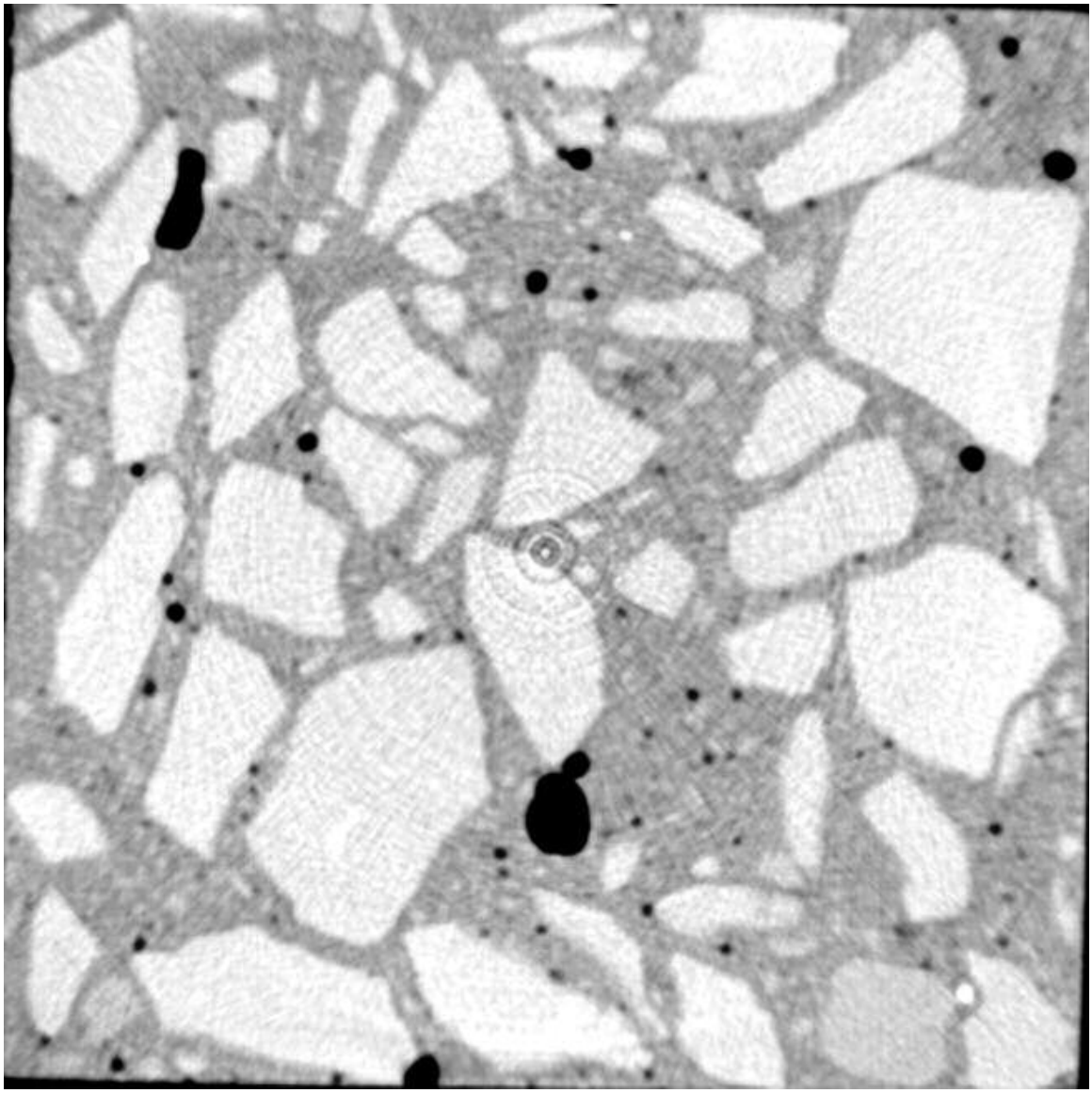

Figure 6.100 X-ray Computed Tomographic Image for Scan #36 of Specimen made with Laurel Sand

Bins (mm)	Frequency	Cumulative %	Relative %
0.1	0	.00%	0.00%
0.5	27	33.75%	33.75%
1	40	83.75%	50.00%
1.5	5	90.00%	6.25%
2	4	95.00%	5.00%
2.5	0	95.00%	0.00%
3	2	97.50%	2.50%
6	0	97.50%	0.00%
13	2	100.00%	2.50%

Table 6.68 Histogram Data of Scan #36 for the Pore Size Distribution on Diameter of Specimen made with Laurel Sand

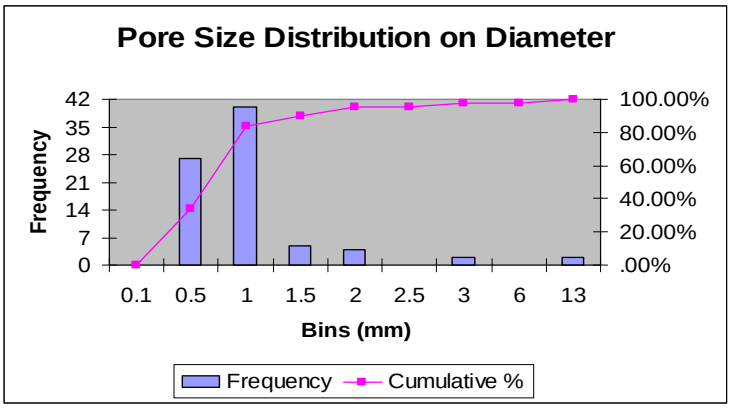

Figure 6.101 Histogram Plot of Scan #36 for the Pore Size Distribution on Diameter of Specimen made with Laurel Sand

Bins (mm^3)	Frequency	Cumulative %	Relative %
0.5	19	23.75%	23.75%
1	16	43.75%	20.00%
2	19	67.50%	23.75%
5	17	88.75%	21.25%
15	6	96.25%	7.50%
30	1	97.50%	1.25%
60	0	97.50%	0.00%
120	2	100.00%	2.50%
210	0	100.00%	0.00%

Table 6.69 Histogram Data of Scan #36 for the Pore Size Distribution on Volume of Specimen made with Laurel Sand

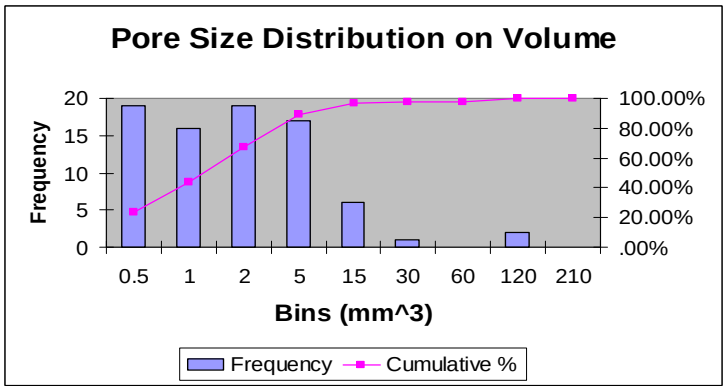

Figure 6.102 Histogram Plot of Scan #36 for the Pore Size Distribution on Volume of Specimen made with Laurel Sand

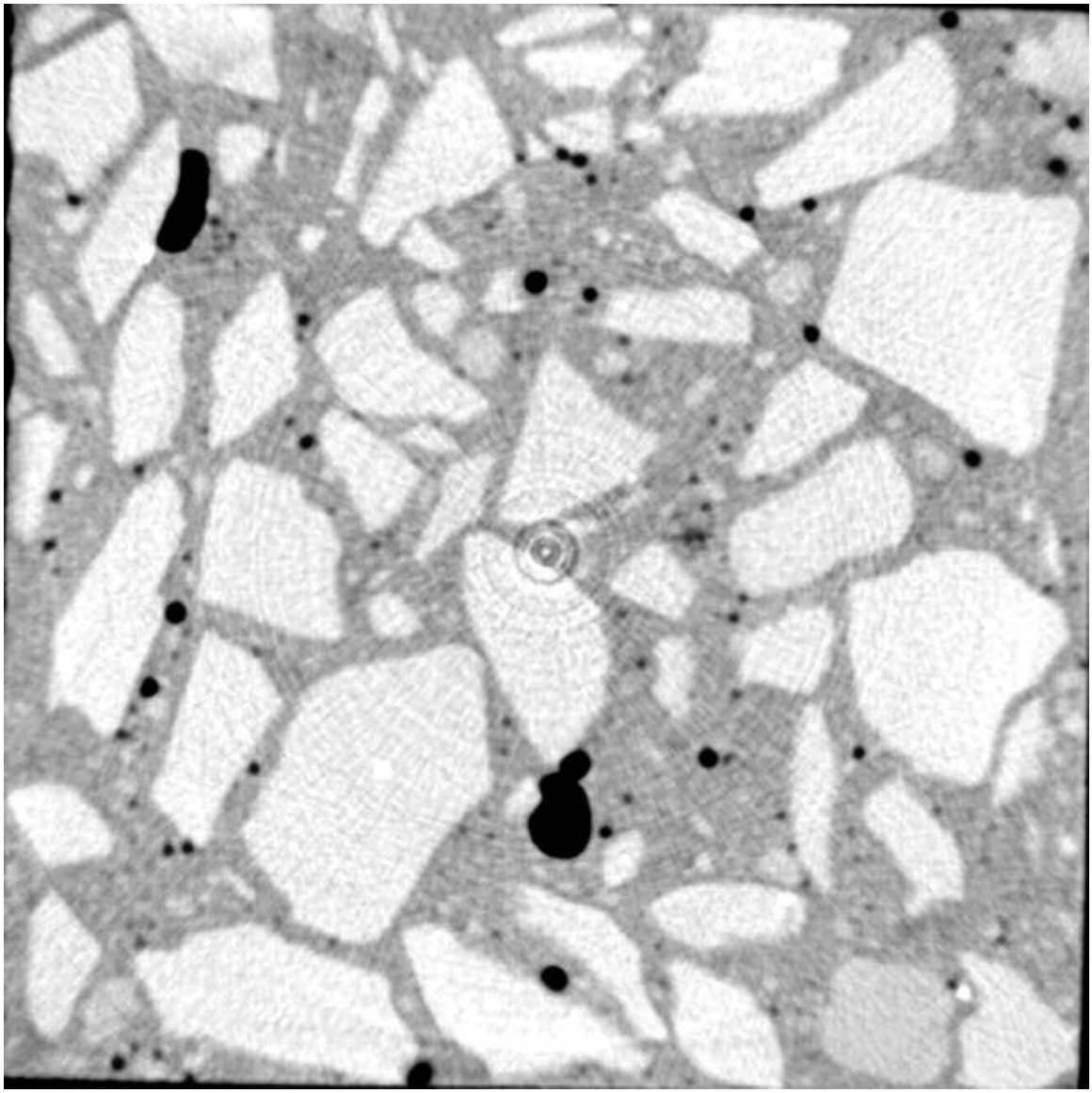

Figure 6.103 X-ray Computed Tomographic Image for Scan #37 of Specimen made with Laurel Sand

Bins (mm)	Frequency	Cumulative %	Relative %
0.1	0	.00%	0.00%
0.5	28	33.33%	33.33%
1	40	80.95%	47.62%
1.5	6	88.10%	7.14%
2	6	95.24%	7.14%
2.5	2	97.62%	2.38%
3	0	97.62%	0.00%
6	0	97.62%	0.00%
13	2	100.00%	2.38%

Table 6.70 Histogram Data of Scan #37 for the Pore Size Distribution on Diameter of Specimen made with Laurel Sand

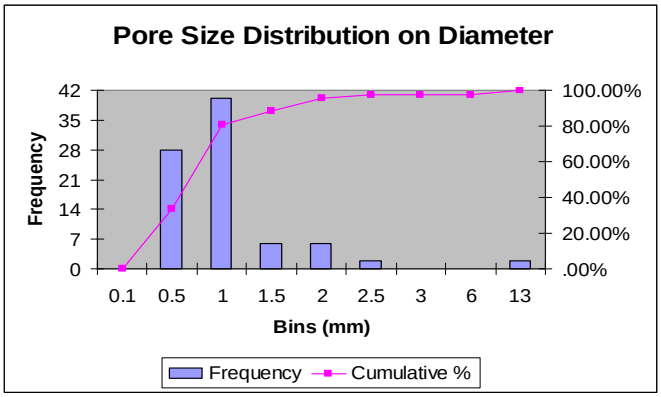

Figure 6.104 Histogram Plot of Scan #37 for the Pore Size Distribution on Diameter of Specimen made with Laurel Sand

Bins (mm^3)	Frequency	Cumulative %	Relative %
0.5	17	20.24%	20.24%
1	23	47.62%	27.38%
2	14	64.29%	16.67%
5	17	84.52%	20.24%
15	11	97.62%	13.10%
30	0	97.62%	0.00%
60	0	97.62%	0.00%
120	2	100.00%	2.38%
210	0	100.00%	0.00%

Table 6.71 Histogram Data of Scan #37 for the Pore Size Distribution on Volume of Specimen made with Laurel Sand

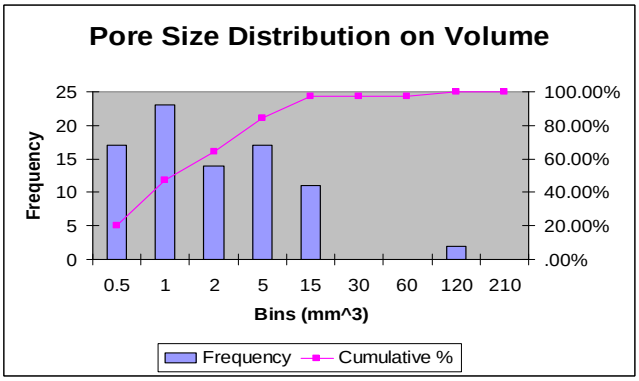

Figure 6.105 Histogram Plot of Scan #37 for the Pore Size Distribution on Volume of Specimen made with Laurel Sand

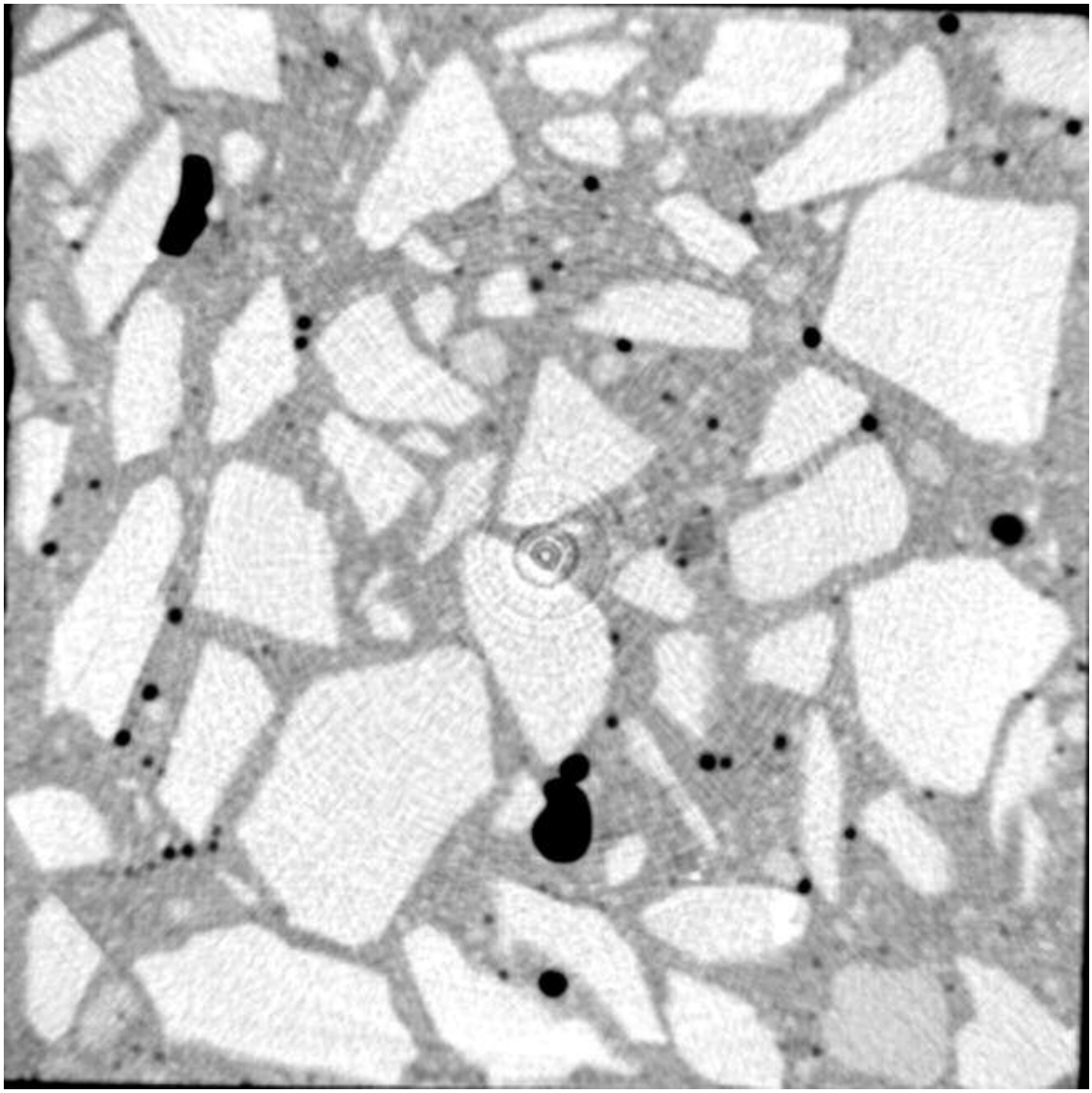

Figure 6.106 X-ray Computed Tomographic Image for Scan #38 of Specimen made with Laurel Sand

Bins (mm)	Frequency	Cumulative %	Relative %
0.1	0	.00%	0.00%
0.5	23	32.86%	32.86%
1	28	72.86%	40.00%
1.5	12	90.00%	17.14%
2	1	91.43%	1.43%
2.5	3	95.71%	4.29%
3	1	97.14%	1.43%
6	0	97.14%	0.00%
13	2	100.00%	2.86%

Table 6.72 Histogram Data of Scan #38 for the Pore Size Distribution on Diameter of Specimen made with Laurel Sand

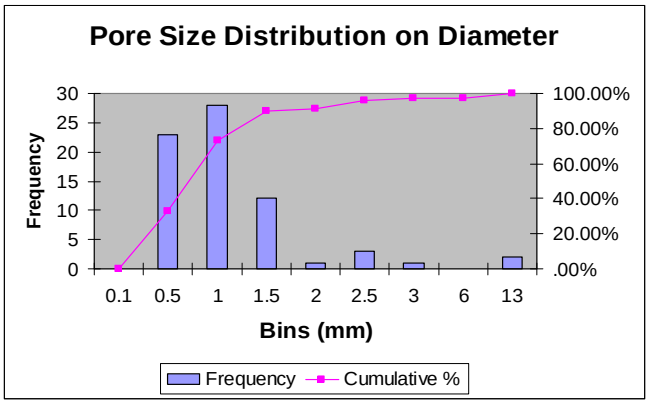

Figure 6.107 Histogram Plot of Scan #38 for the Pore Size Distribution on Diameter of Specimen made with Laurel Sand

Bins (mm^3)	Frequency	Cumulative %	Relative %
0.5	18	25.71%	25.71%
1	12	42.86%	17.14%
2	8	54.29%	11.43%
5	18	80.00%	25.71%
15	10	94.29%	14.29%
30	2	97.14%	2.86%
60	0	97.14%	0.00%
120	2	100.00%	2.86%
210	0	100.00%	0.00%

Table 6.73 Histogram Data of Scan #38 for the Pore Size Distribution on Volume of Specimen made with Laurel Sand

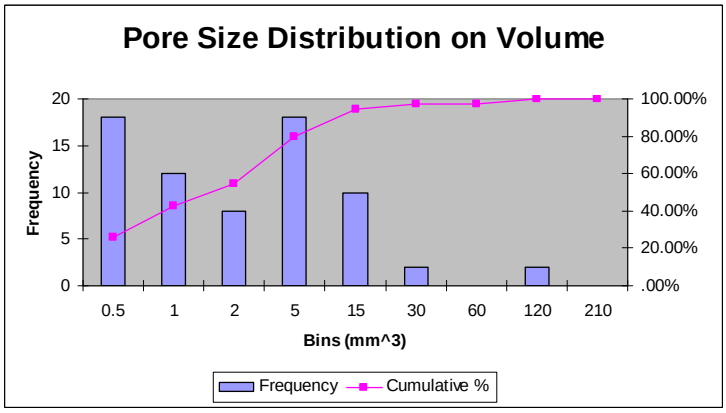

Figure 6.108 Histogram Plot of Scan #38 for the Pore Size Distribution on Volume of Specimen made with Laurel Sand

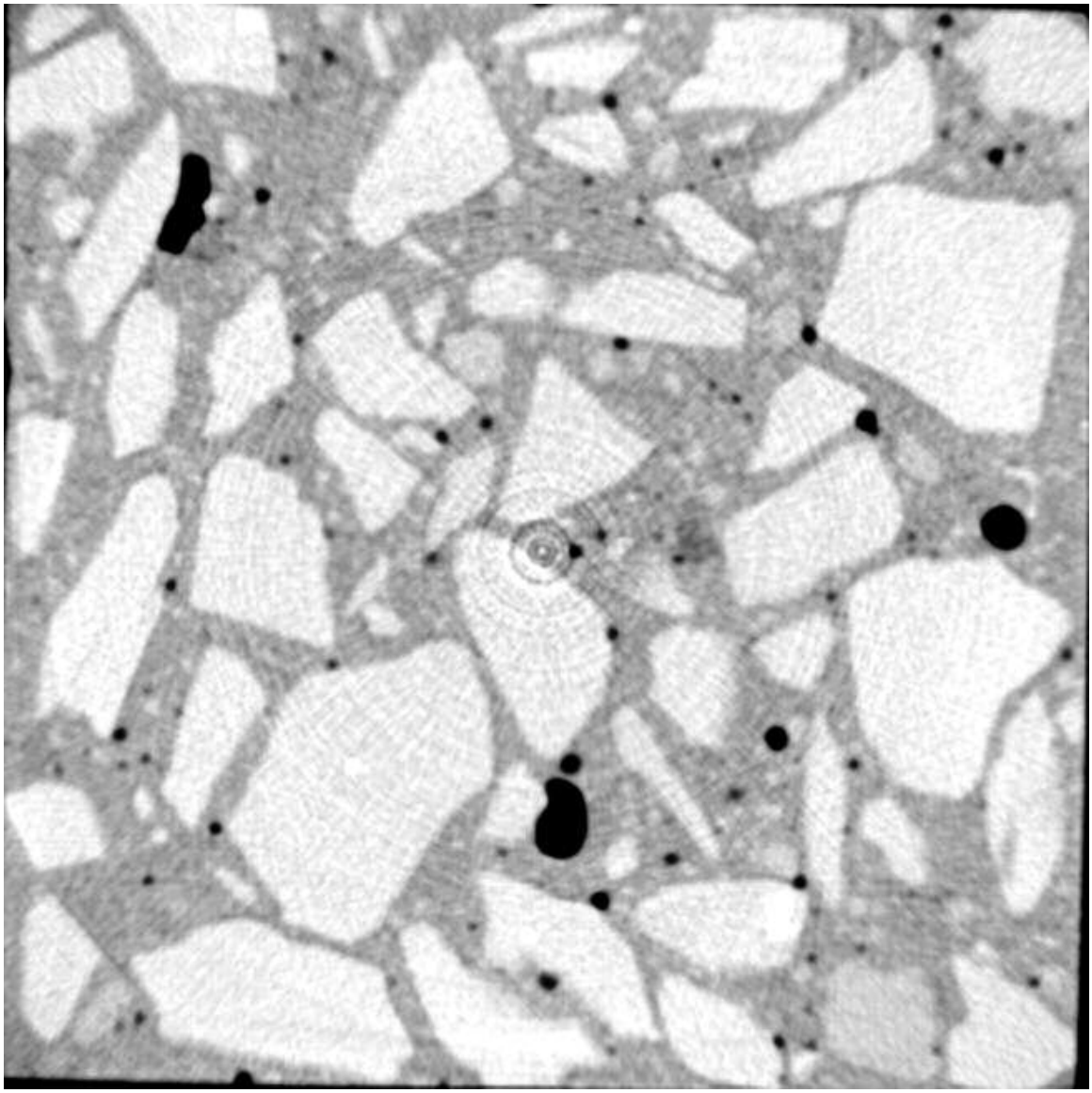

Figure 6.109 X-ray Computed Tomographic Image for Scan #39 of Specimen made with Laurel Sand

Bins (mm)	Frequency	Cumulative %	Relative %
0.1	0	.00%	0.00%
0.5	21	27.63%	27.63%
1	34	72.37%	44.74%
1.5	15	92.11%	19.74%
2	2	94.74%	2.63%
2.5	1	96.05%	1.32%
3	0	96.05%	0.00%
6	2	98.68%	2.63%
13	1	100.00%	1.32%

Table 6.74 Histogram Data of Scan #39 for the Pore Size Distribution on Diameter of Specimen made with Laurel Sand

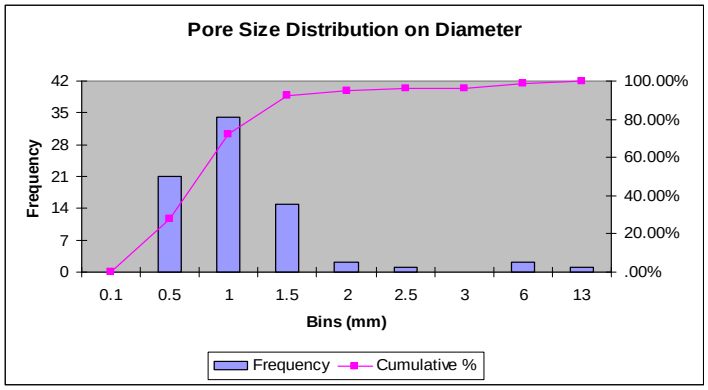

Figure 6.110 Histogram Plot of Scan #39 for the Pore Size Distribution on Diameter of Specimen made with Laurel Sand

Bins (mm^3)	Frequency	Cumulative %	Relative %
0.5	18	23.68%	23.68%
1	7	32.89%	9.21%
2	17	55.26%	22.37%
5	23	85.53%	30.26%
15	8	96.05%	10.53%
30	0	96.05%	0.00%
60	1	97.37%	1.32%
120	2	100.00%	2.63%
210	0	100.00%	0.00%

Table 6.75 Histogram Data of Scan #39 for the Pore Size Distribution on Volume of Specimen made with Laurel Sand

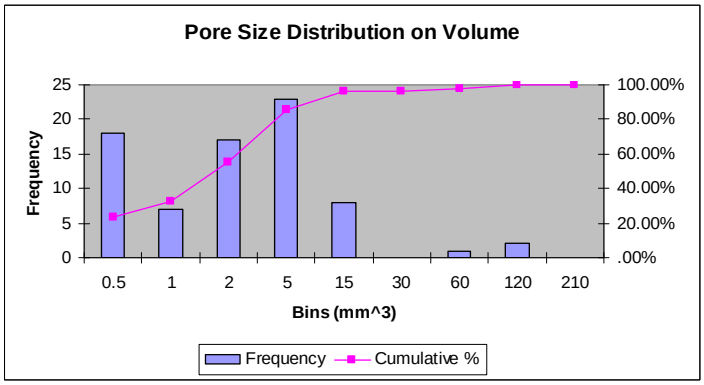

Figure 6.111 Histogram Plot of Scan #39 for the Pore Size Distribution on Volume of Specimen made with Laurel Sand

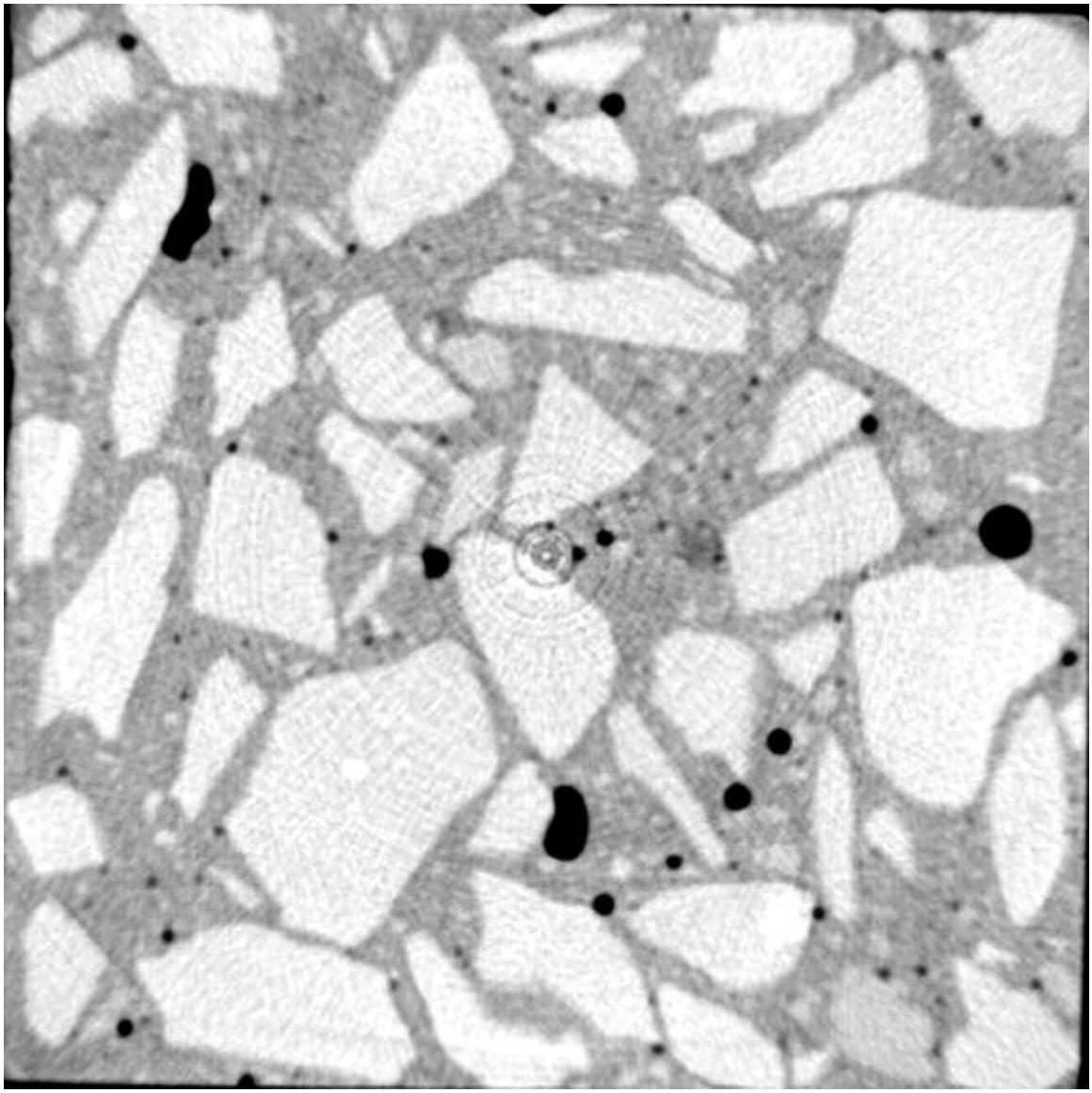

Figure 6.112 X-ray Computed Tomographic Image for Scan #40 of Specimen made with Laurel Sand

Bins (mm)	Frequency	Cumulative %	Relative %
0.1	0	.00%	0.00%
0.5	23	32.39%	32.39%
1	32	77.46%	45.07%
1.5	8	88.73%	11.27%
2	3	92.96%	4.23%
2.5	2	95.77%	2.82%
3	0	95.77%	0.00%
6	2	98.59%	2.82%
13	1	100.00%	1.41%

Table 6.76 Histogram Data of Scan #40 for the Pore Size Distribution on Diameter of Specimen made with Laurel Sand

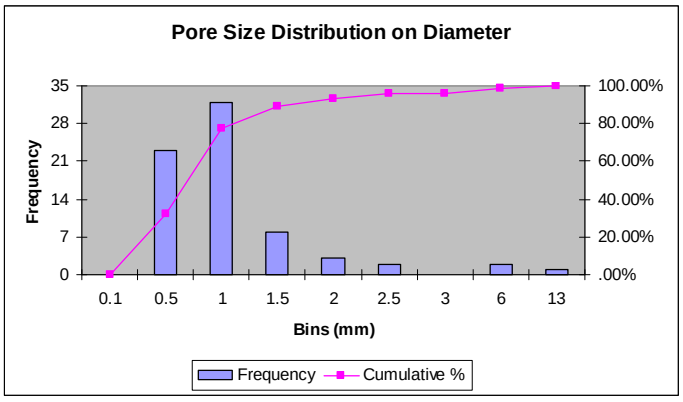

Figure 6.113 Histogram Plot of Scan #40 for the Pore Size Distribution on Diameter of Specimen made with Laurel Sand

Bins (mm^3)	Frequency	Cumulative %	Relative %
0.5	16	22.54%	22.54%
1	17	46.48%	23.94%
2	15	67.61%	21.13%
5	9	80.28%	12.68%
15	9	92.96%	12.68%
30	2	95.77%	2.82%
60	1	97.18%	1.41%
120	2	100.00%	2.82%
210	0	100.00%	0.00%

Table 6.77 Histogram Data of Scan #40 for the Pore Size Distribution on Volume of Specimen made with Laurel Sand

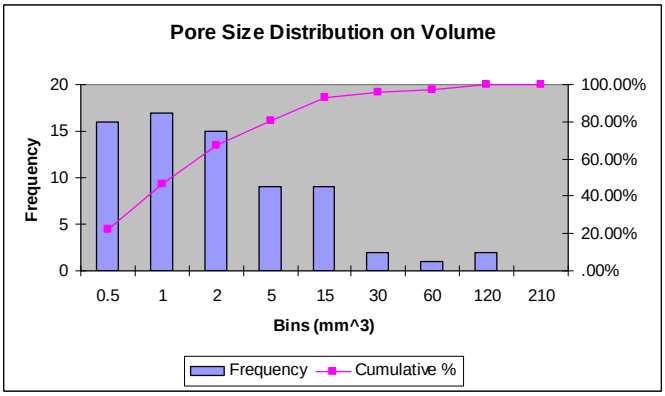

Figure 6.114 Histogram Plot of Scan #40 for the Pore Size Distribution on Volume of Specimen made with Laurel Sand

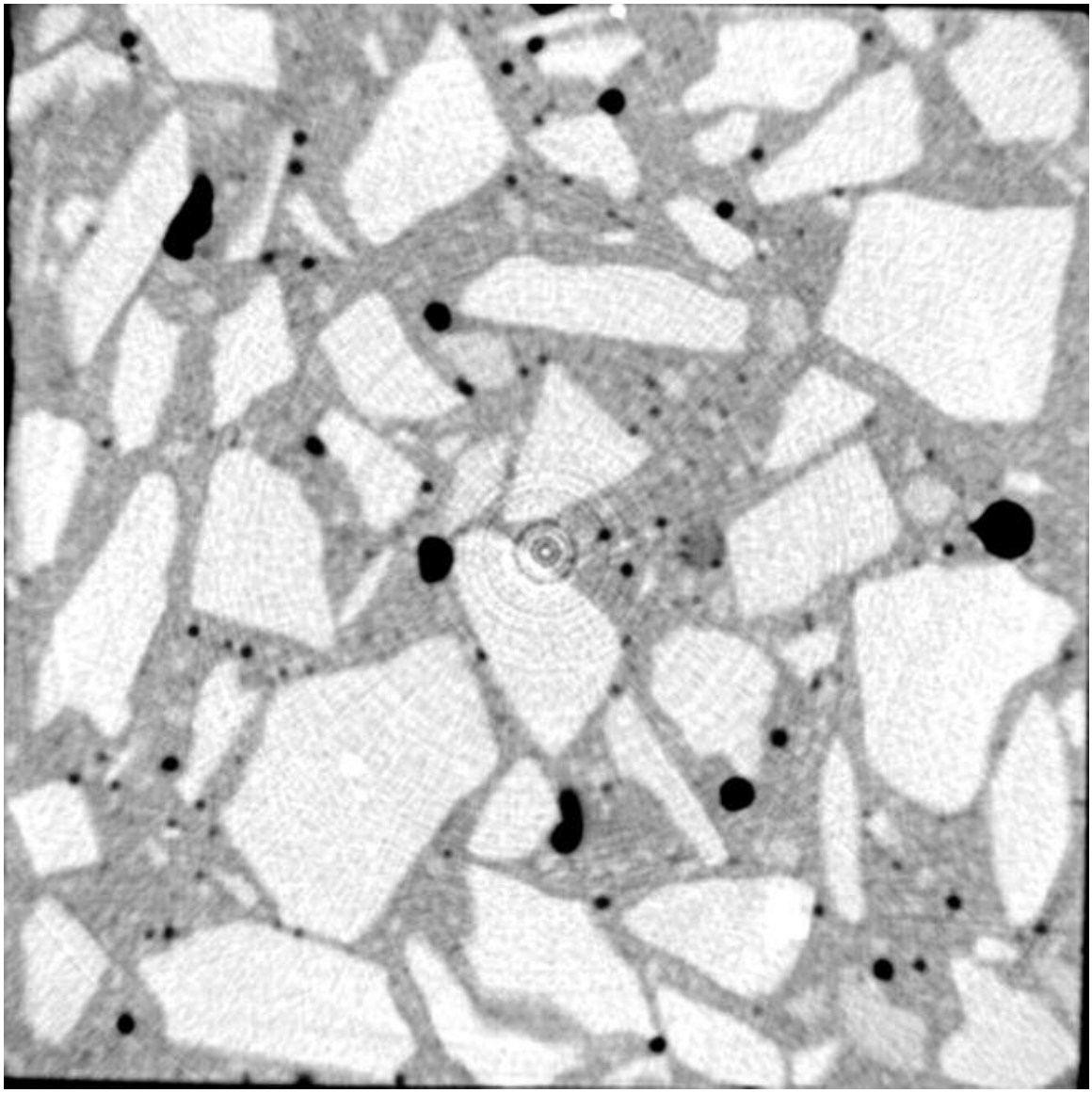

Figure 6.115 X-ray Computed Tomographic Image for Scan #41 of Specimen made with Laurel Sand

Bins (mm)	Frequency	Cumulative %	Relative %
0.1	0	.00%	0.00%
0.5	22	23.91%	23.91%
1	44	71.74%	47.83%
1.5	14	86.96%	15.22%
2	5	92.39%	5.43%
2.5	2	94.57%	2.17%
3	1	95.65%	1.09%
6	3	98.91%	3.26%
13	1	100.00%	1.09%

Table 6.78 Histogram Data of Scan #41 for the Pore Size Distribution on Diameter of Specimen made with Laurel Sand

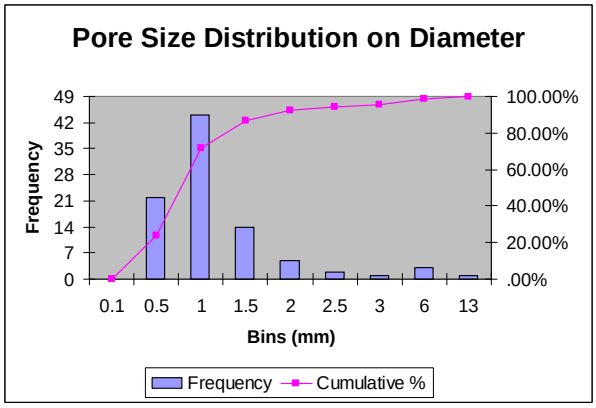

Figure 6.116 Histogram Plot of Scan #41 for the Pore Size Distribution on Diameter of Specimen made with Laurel Sand

Bins (mm^3)	Frequency	Cumulative %	Relative %
0.5	13	14.13%	14.13%
1	19	34.78%	20.65%
2	18	54.35%	19.57%
5	24	80.43%	26.09%
15	12	93.48%	13.04%
30	2	95.65%	2.17%
60	2	97.83%	2.17%
120	2	100.00%	2.17%
210	0	100.00%	0.00%

Table 6.79 Histogram Data of Scan #41 for the Pore Size Distribution on Volume of Specimen made with Laurel Sand

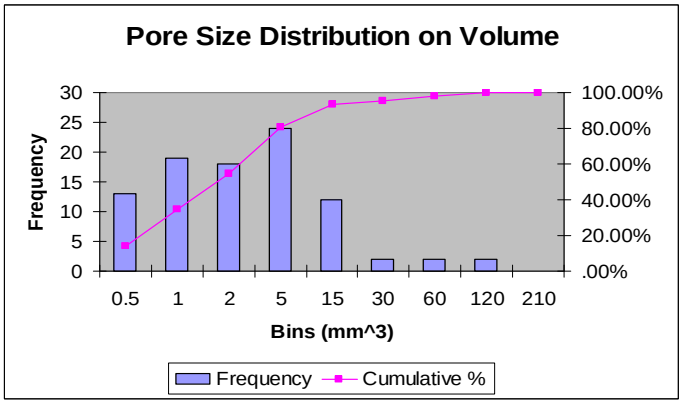

Figure 6.117 Histogram Plot of Scan #41 for the Pore Size Distribution on Volume of Specimen made with Laurel Sand

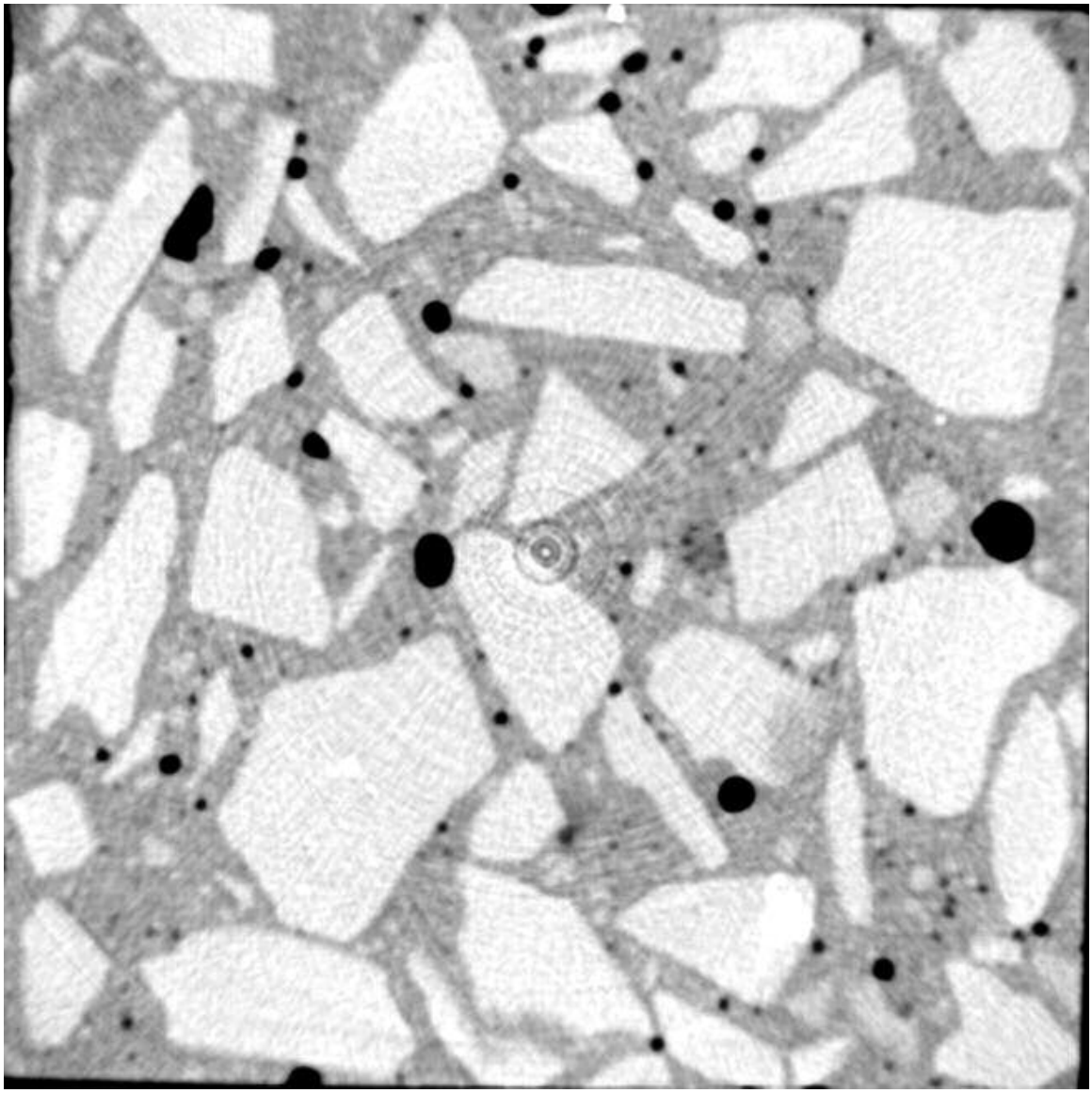

Figure 6.118 X-ray Computed Tomographic Image for Scan #42 of Specimen made with Laurel Sand

Bins (mm)	Frequency	Cumulative %	Relative %
0.1	0	.00%	0.00%
0.5	34	33.01%	33.01%
1	43	74.76%	41.75%
1.5	11	85.44%	10.68%
2	7	92.23%	6.80%
2.5	4	96.12%	3.88%
3	1	97.09%	0.97%
6	3	100.00%	2.91%
13	0	100.00%	0.00%

Table 6.80 Histogram Data of Scan #42 for the Pore Size Distribution on Diameter of Specimen made with Laurel Sand

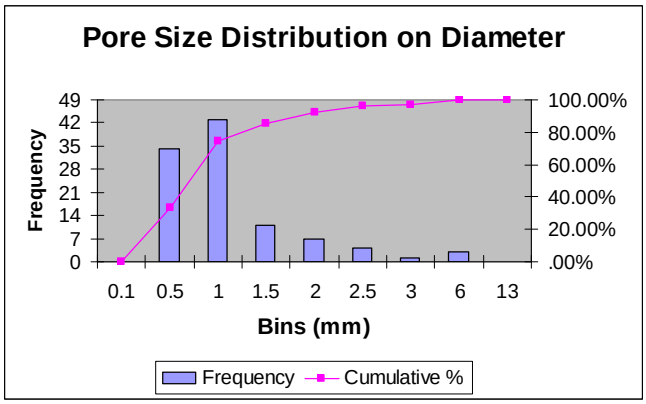

Figure 6.119 Histogram Plot of Scan #42 for the Pore Size Distribution on Diameter of Specimen made with Laurel Sand

Bins (mm^3)	Frequency	Cumulative %	Relative %
0.5	22	21.36%	21.36%
1	17	37.86%	16.50%
2	19	56.31%	18.45%
5	24	79.61%	23.30%
15	16	95.15%	15.53%
30	2	97.09%	1.94%
60	2	99.03%	1.94%
120	1	100.00%	0.97%
210	0	100.00%	0.00%

Table 6.81 Histogram Data of Scan #42 for the Pore Size Distribution on Volume of Specimen made with Laurel Sand

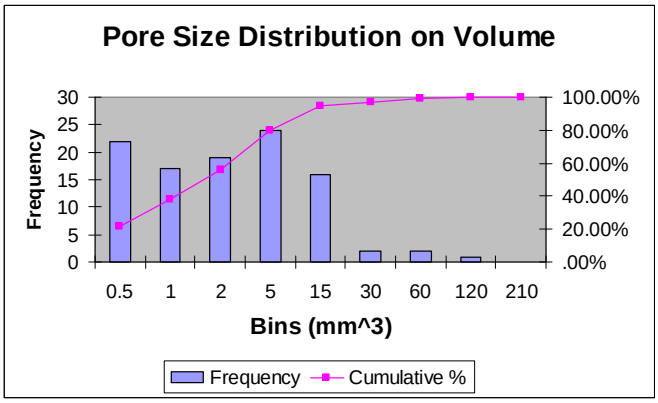

Figure 6.120 Histogram Plot of Scan #42 for the Pore Size Distribution on Volume of Specimen made with Laurel Sand

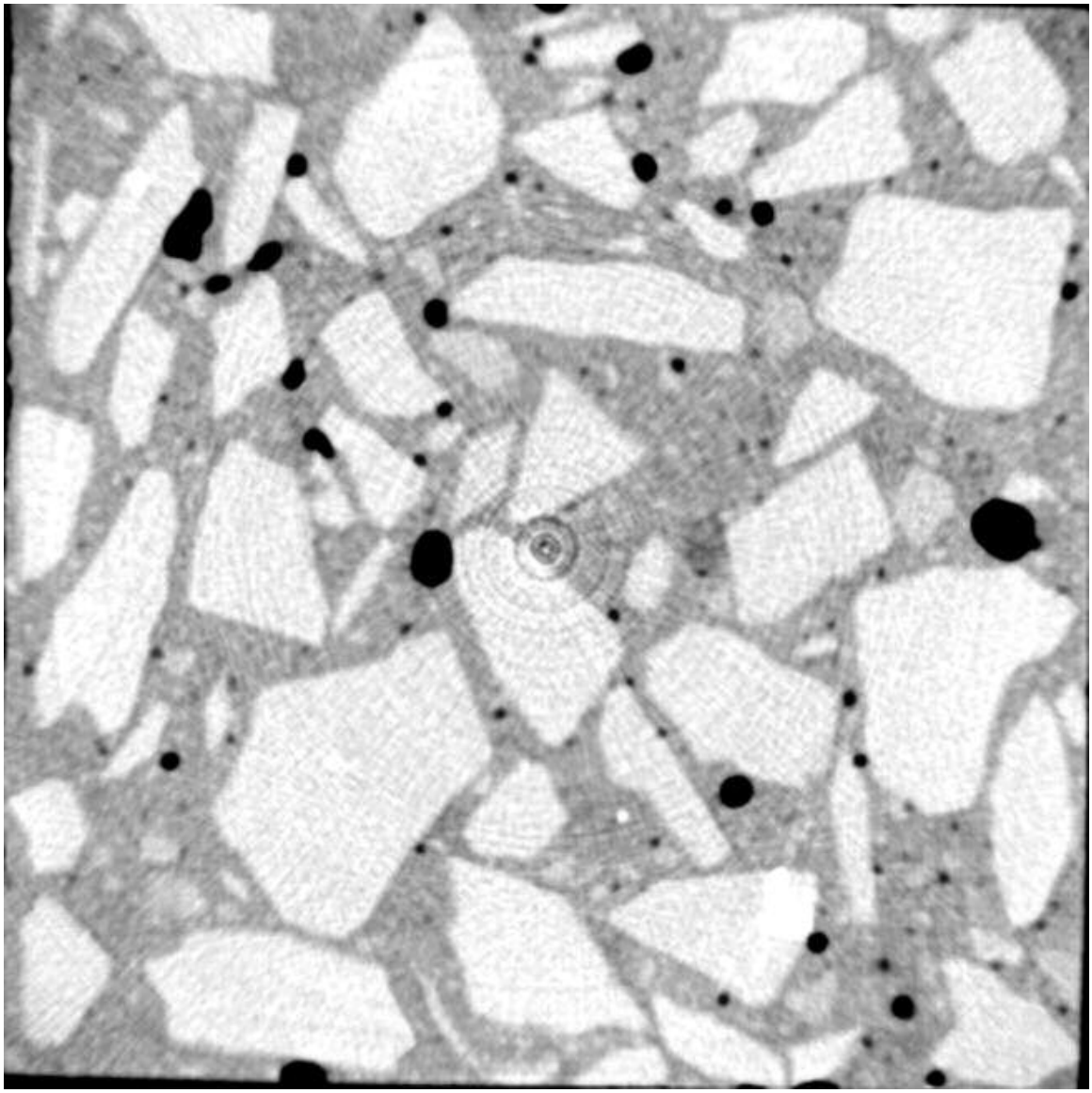

Figure 6.121 X-ray Computed Tomographic Image for Scan #43 of Specimen made with Laurel Sand

Bins (mm)	Frequency	Cumulative %	Relative %
0.1	0	.00%	0.00%
0.5	30	31.25%	31.25%
1	43	76.04%	44.79%
1.5	8	84.38%	8.33%
2	4	88.54%	4.17%
2.5	4	92.71%	4.17%
3	3	95.83%	3.13%
6	4	100.00%	4.17%
13	0	100.00%	0.00%

Table 6.82 Histogram Data of Scan #43 for the Pore Size Distribution on Diameter of Specimen made with Laurel Sand

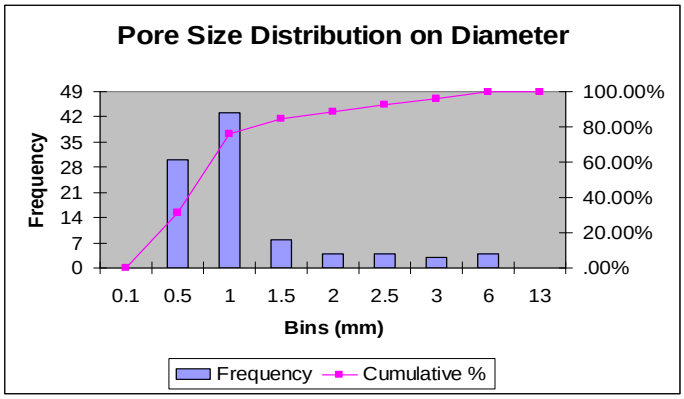

Figure 6.122 Histogram Plot of Scan #43 for the Pore Size Distribution on Diameter of Specimen made with Laurel Sand

Bins (mm^3)	Frequency	Cumulative %	Relative %
0.5	19	19.79%	19.79%
1	22	42.71%	22.92%
2	19	62.50%	19.79%
5	16	79.17%	16.67%
15	12	91.67%	12.50%
30	5	96.88%	5.21%
60	2	98.96%	2.08%
120	1	100.00%	1.04%
210	0	100.00%	0.00%

Table 6.83 Histogram Data of Scan #43 for the Pore Size Distribution on Volume of Specimen made with Laurel Sand

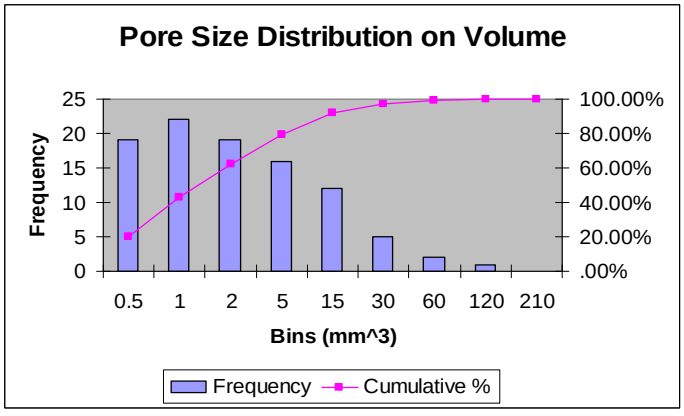

Figure 6.123 Histogram Plot of Scan #43 for the Pore Size Distribution on Volume of Specimen made with Laurel Sand

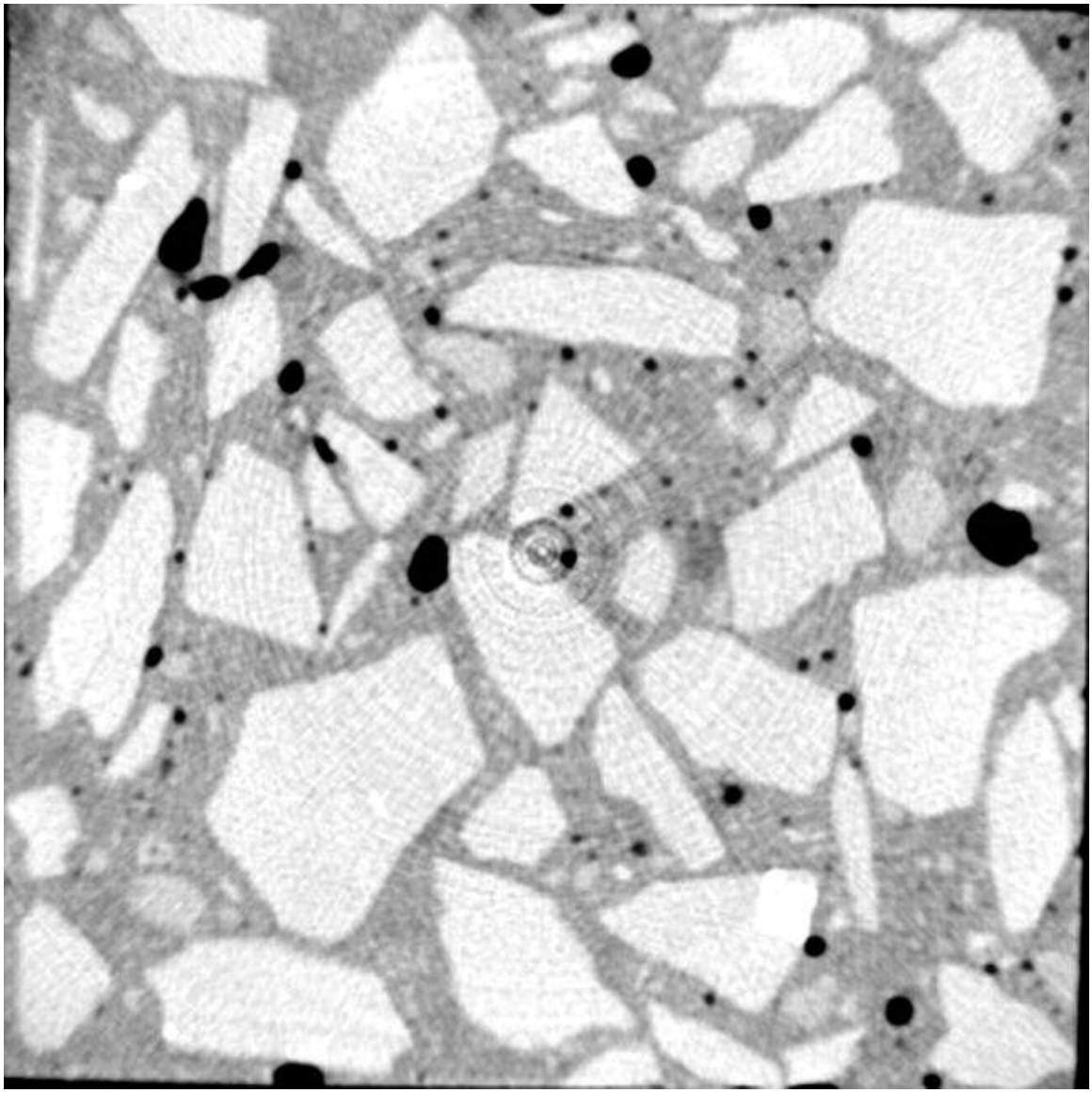

Figure 6.124 X-ray Computed Tomographic Image for Scan #44 of Specimen made with Laurel Sand

Bins (mm)	Frequency	Cumulative %	Relative %
0.1	0	.00%	0.00%
0.5	17	19.54%	19.54%
1	43	68.97%	49.43%
1.5	9	79.31%	10.34%
2	7	87.36%	8.05%
2.5	4	91.95%	4.60%
3	2	94.25%	2.30%
6	5	100.00%	5.75%
13	0	100.00%	0.00%

Table 6.84 Histogram Data of Scan #44 for the Pore Size Distribution on Diameter of Specimen made with Laurel Sand

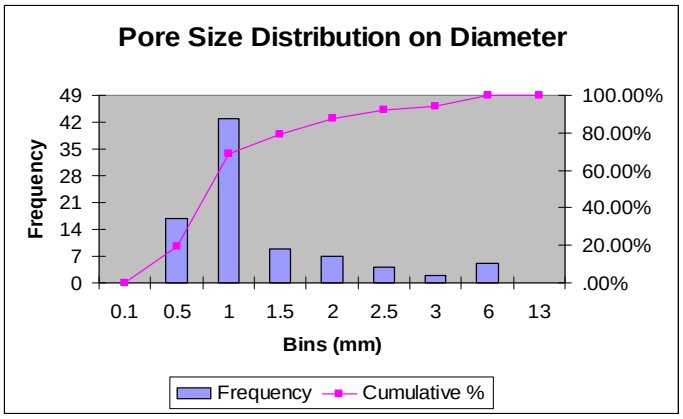

Figure 6.125 Histogram Plot of Scan #44 for the Pore Size Distribution on Diameter of Specimen made with Laurel Sand

Bins (mm^3)	Frequency	Cumulative %	Relative %
0.5	13	14.94%	14.94%
1	13	29.89%	14.94%
2	17	49.43%	19.54%
5	22	74.71%	25.29%
15	13	89.66%	14.94%
30	6	96.55%	6.90%
60	1	97.70%	1.15%
120	2	100.00%	2.30%
210	0	100.00%	0.00%

Table 6.85 Histogram Data of Scan #44 for the Pore Size Distribution on Volume of Specimen made with Laurel Sand

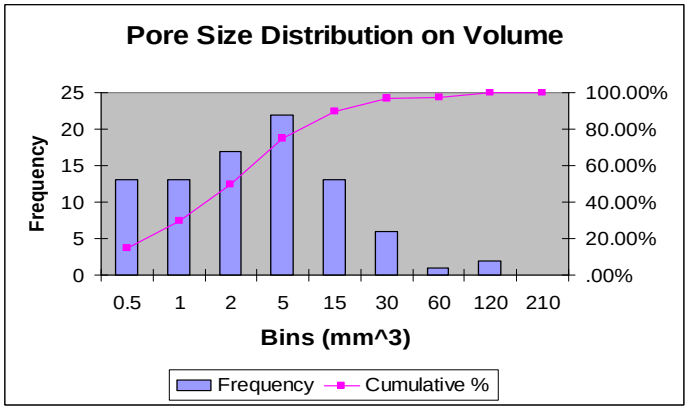

Figure 6.126 Histogram Plot of Scan #44 for the Pore Size Distribution on Volume of Specimen made with Laurel Sand

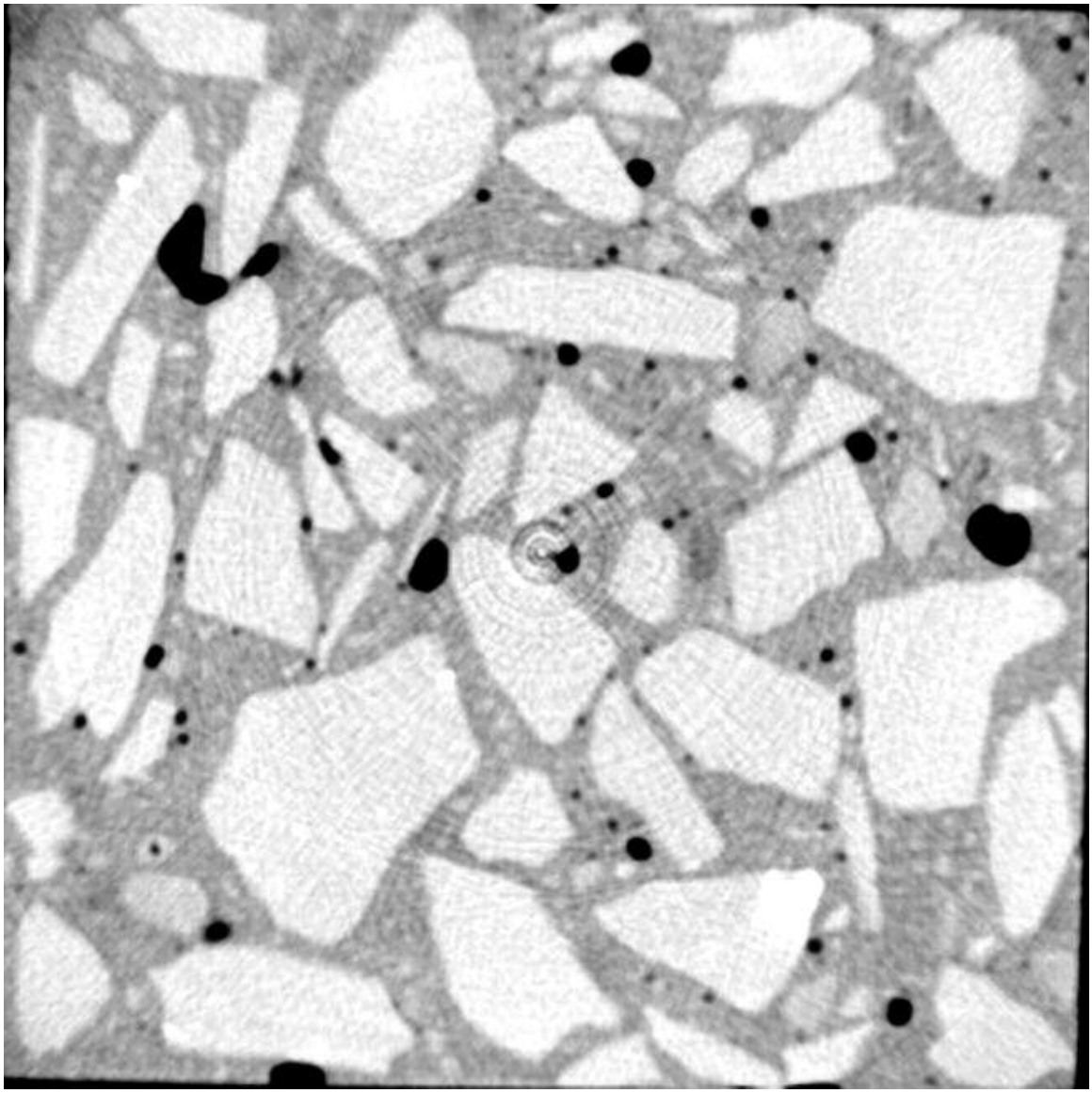

Figure 6.127 X-ray Computed Tomographic Image for Scan #45 of Specimen made with Laurel Sand

Bins (mm)	Frequency	Cumulative %	Relative %
0.1	0	.00%	0.00%
0.5	18	23.38%	23.38%
1	35	68.83%	45.45%
1.5	8	79.22%	10.39%
2	4	84.42%	5.19%
2.5	7	93.51%	9.09%
3	1	94.81%	1.30%
6	3	98.70%	3.90%
13	1	100.00%	1.30%

Table 6.86 Histogram Data of Scan #45 for the Pore Size Distribution on Diameter of Specimen made with Laurel Sand

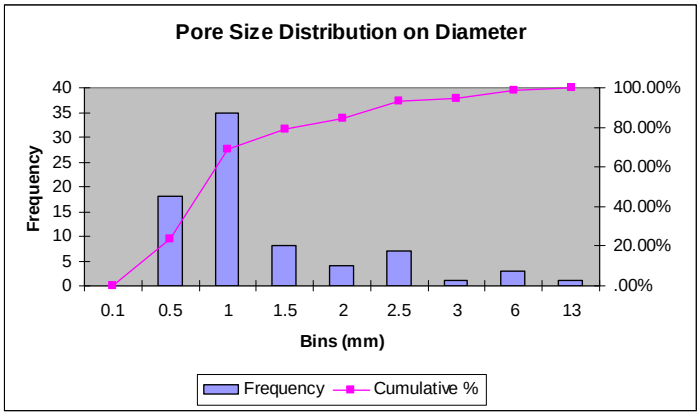

Figure 6.128 Histogram Plot of Scan #45 for the Pore Size Distribution on Diameter of Specimen made with Laurel Sand

Bins (mm^3)	Frequency	Cumulative %	Relative %
0.5	17	22.08%	22.08%
1	6	29.87%	7.79%
2	14	48.05%	18.18%
5	21	75.32%	27.27%
15	11	89.61%	14.29%
30	5	96.10%	6.49%
60	1	97.40%	1.30%
120	2	100.00%	2.60%
210	0	100.00%	0.00%

Table 6.87 Histogram Data of Scan #45 for the Pore Size Distribution on Volume of Specimen made with Laurel Sand

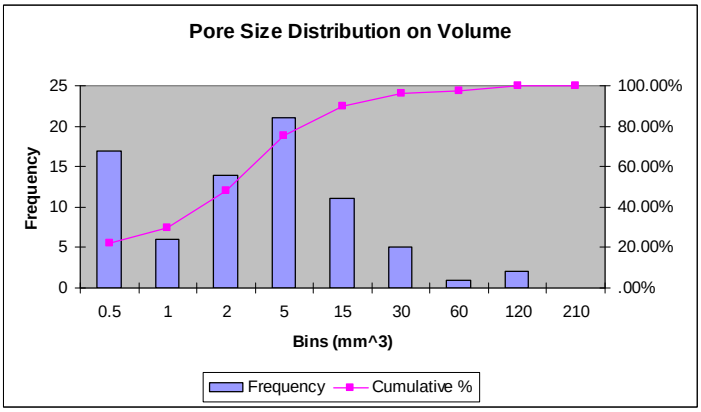

Figure 6.129 Histogram Plot of Scan #45 for the Pore Size Distribution on Volume of Specimen made with Laurel Sand

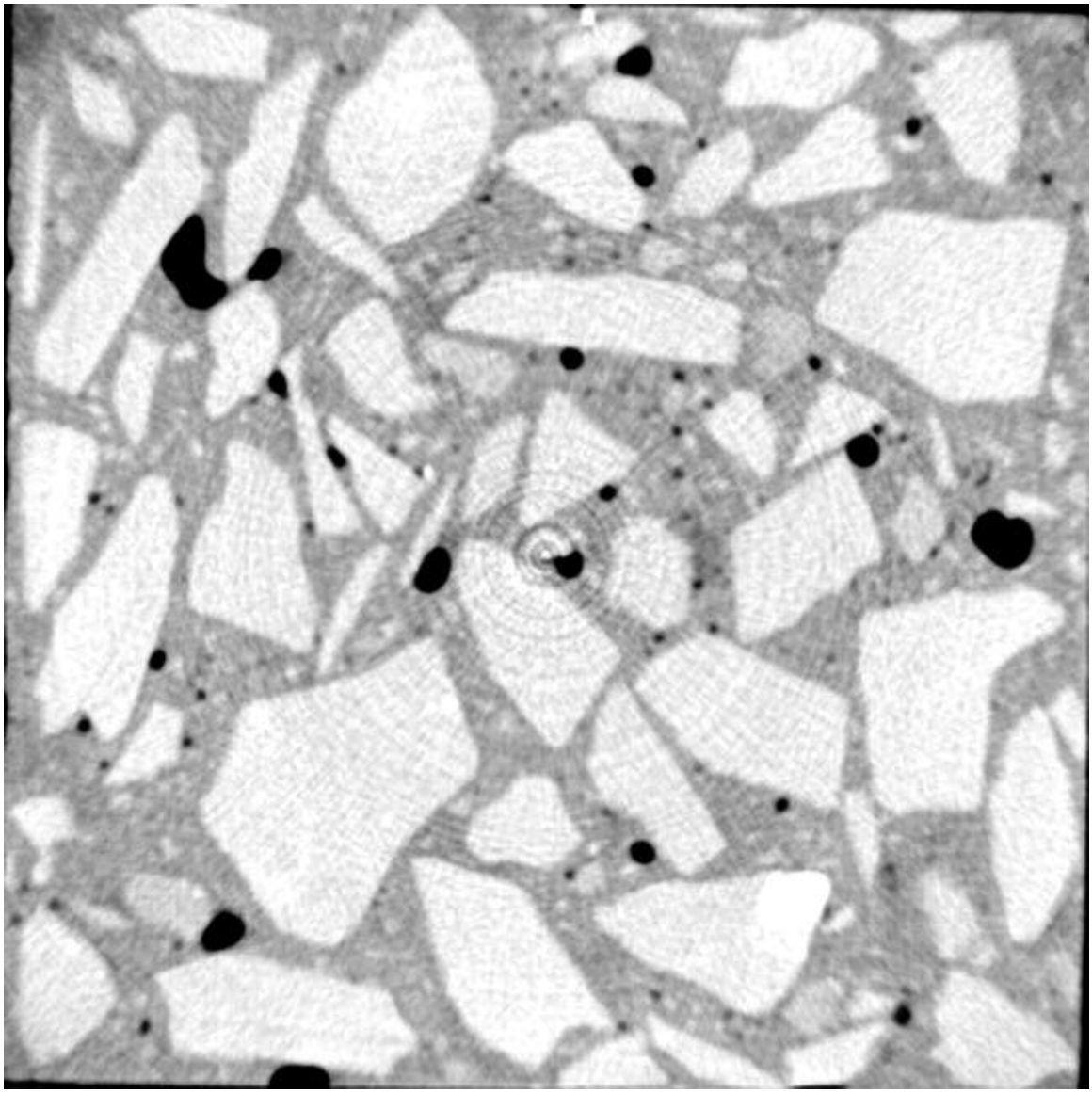

Figure 6.130 X-ray Computed Tomographic Image for Scan #46 of Specimen made with Laurel Sand

Bins (mm)	Frequency	Cumulative %	Relative %
0.1	0	.00%	0.00%
0.5	21	28.77%	28.77%
1	33	73.97%	45.21%
1.5	4	79.45%	5.48%
2	6	87.67%	8.22%
2.5	2	90.41%	2.74%
3	2	93.15%	2.74%
6	4	98.63%	5.48%
13	1	100.00%	1.37%

Table 6.88 Histogram Data of Scan #46 for the Pore Size Distribution on Diameter of Specimen made with Laurel Sand

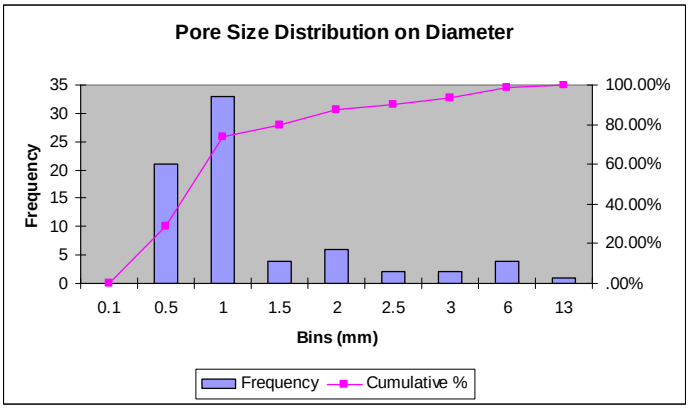

Figure 6.131 Histogram Plot of Scan #46 for the Pore Size Distribution on Diameter of Specimen made with Laurel Sand

Bins (mm^3)	Frequency	Cumulative %	Relative %
0.5	18	24.66%	24.66%
1	13	42.47%	17.81%
2	17	65.75%	23.29%
5	8	76.71%	10.96%
15	9	89.04%	12.33%
30	4	94.52%	5.48%
60	2	97.26%	2.74%
120	2	100.00%	2.74%
210	0	100.00%	0.00%

Table 6.89 Histogram Data of Scan #46 for the Pore Size Distribution on Volume of Specimen made with Laurel Sand

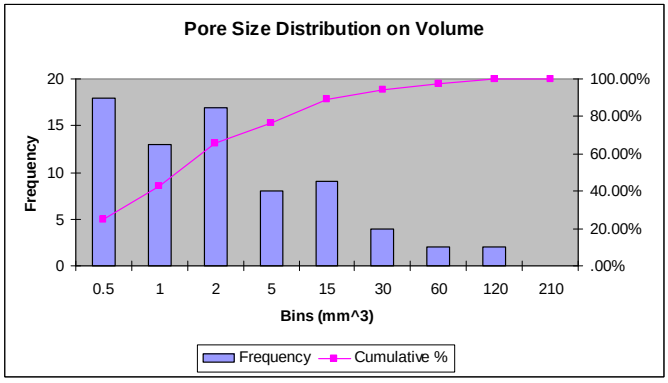

Figure 6.132 Histogram Plot of Scan #46 for the Pore Size Distribution on Volume of Specimen made with Laurel Sand

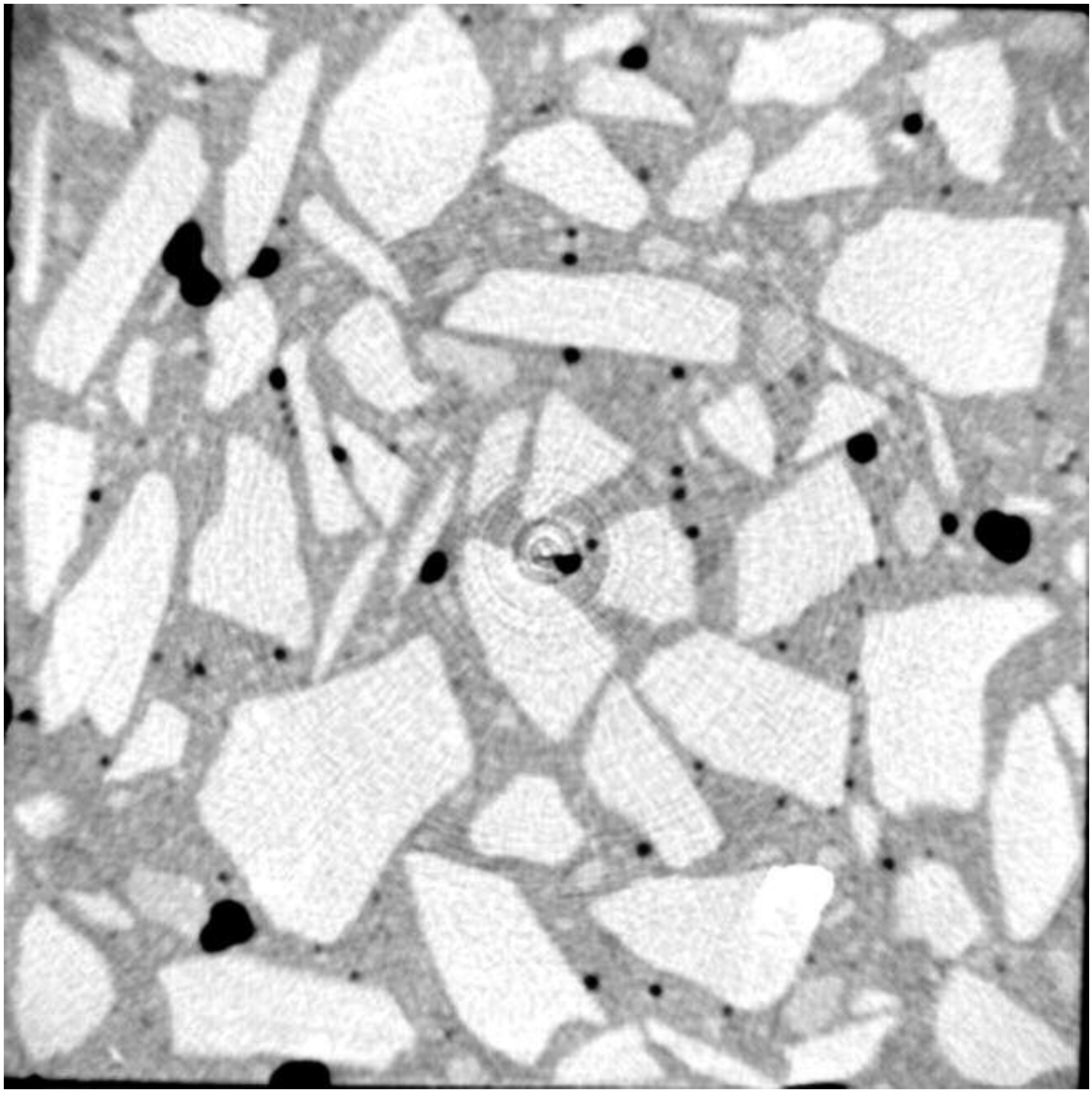

Figure 6.133 X-ray Computed Tomographic Image for Scan #47 of Specimen made with Laurel Sand

Bins (mm)	Frequency	Cumulative %	Relative %
0.1	0	.00%	0.00%
0.5	17	24.29%	24.29%
1	35	74.29%	50.00%
1.5	6	82.86%	8.57%
2	4	88.57%	5.71%
2.5	2	91.43%	2.86%
3	3	95.71%	4.29%
6	2	98.57%	2.86%
13	1	100.00%	1.43%

Table 6.90 Histogram Data of Scan #47 for the Pore Size Distribution on Diameter of Specimen made with Laurel Sand

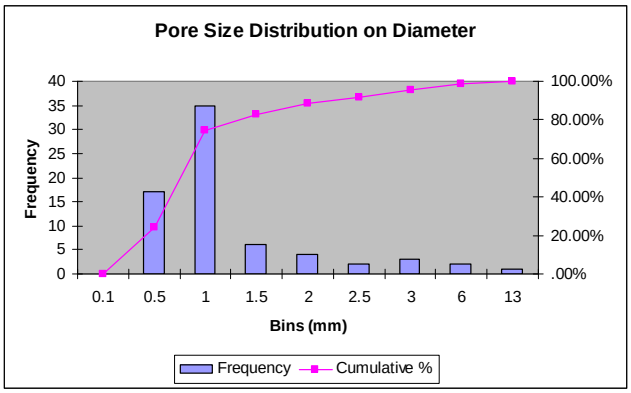

Figure 6.134 Histogram Plot of Scan #47 for the Pore Size Distribution on Diameter of Specimen made with Laurel Sand

Bins (mm^3)	Frequency	Cumulative %	Relative %
0.5	14	20.00%	20.00%
1	9	32.86%	12.86%
2	18	58.57%	25.71%
5	15	80.00%	21.43%
15	8	91.43%	11.43%
30	3	95.71%	4.29%
60	2	98.57%	2.86%
120	1	100.00%	1.43%
210	0	100.00%	0.00%

Table 6.91 Histogram Data of Scan #47 for the Pore Size Distribution on Volume of Specimen made with Laurel Sand

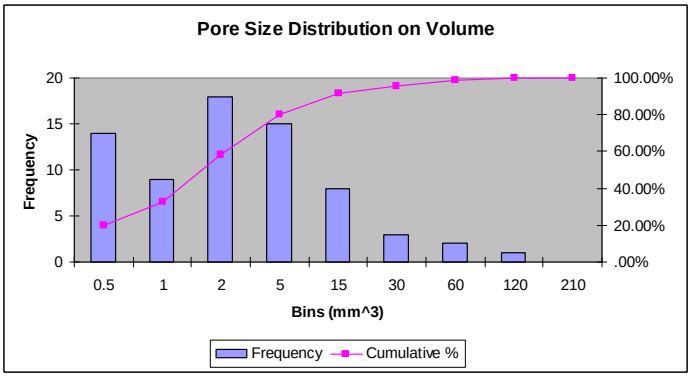

Figure 6.135 Histogram Plot of Scan #47 for the Pore Size Distribution on Volume of Specimen made with Laurel Sand

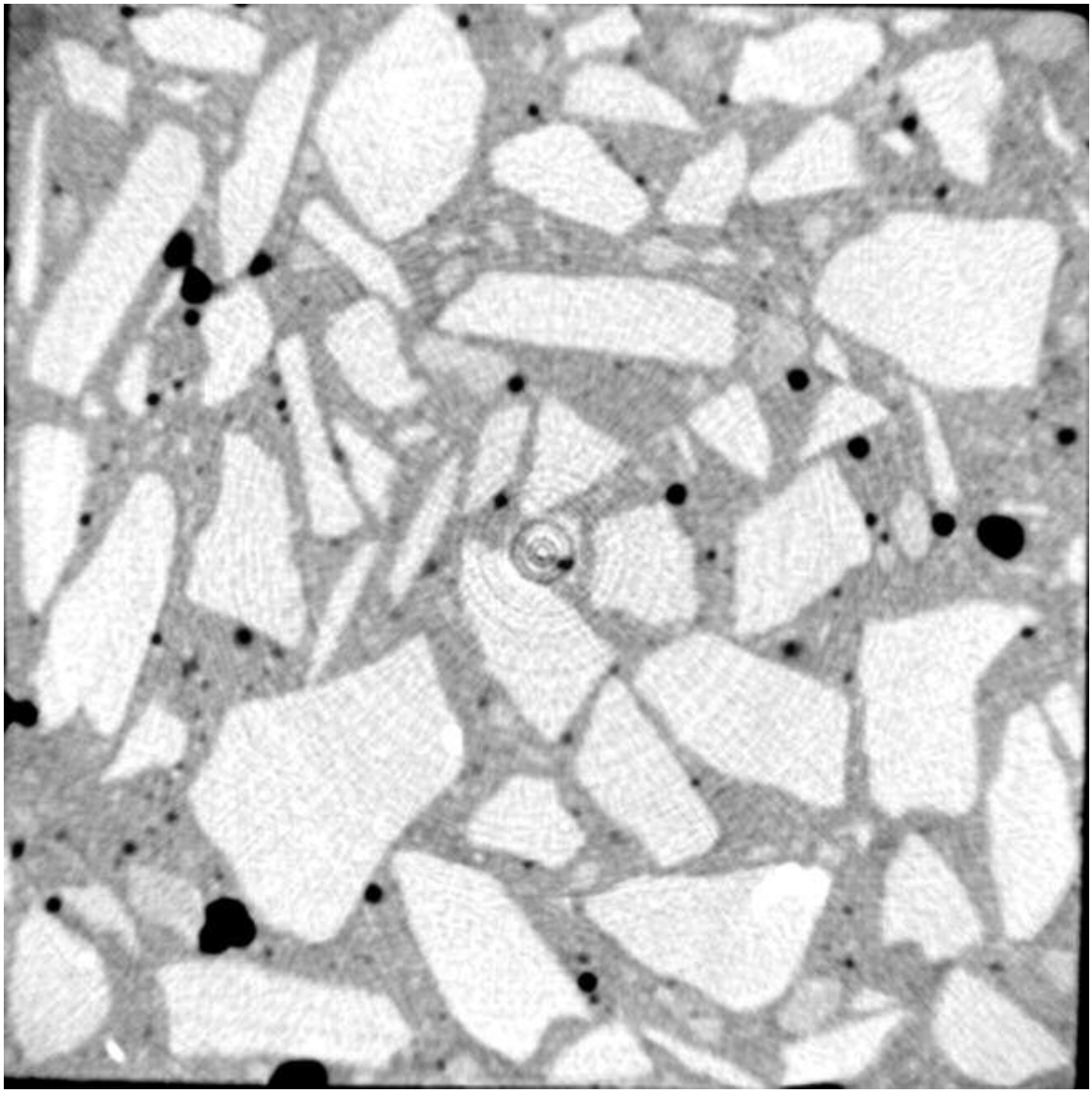

Figure 6.136 X-ray Computed Tomographic Image for Scan #48 of Specimen made with Laurel Sand

Bins (mm)	Frequency	Cumulative %	Relative %
0.1	0	.00%	0.00%
0.5	19	24.36%	24.36%
1	36	70.51%	46.15%
1.5	14	88.46%	17.95%
2	5	94.87%	6.41%
2.5	1	96.15%	1.28%
3	0	96.15%	0.00%
6	3	100.00%	3.85%
13	0	100.00%	0.00%

Table 6.92 Histogram Data of Scan #48 for the Pore Size Distribution on Diameter of Specimen made with Laurel Sand

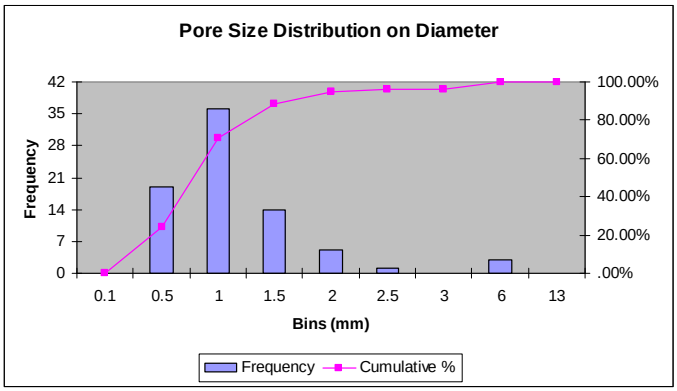

Figure 6.137 Histogram Plot of Scan #48 for the Pore Size Distribution on Diameter of Specimen made with Laurel Sand

Bins (mm^3)	Frequency	Cumulative %	Relative %
0.5	18	23.08%	23.08%
1	8	33.33%	10.26%
2	18	56.41%	23.08%
5	16	76.92%	20.51%
15	15	96.15%	19.23%
30	0	96.15%	0.00%
60	3	100.00%	3.85%
120	0	100.00%	0.00%
210	0	100.00%	0.00%

Table 6.93 Histogram Data of Scan #48 for the Pore Size Distribution on Volume of Specimen made with Laurel Sand

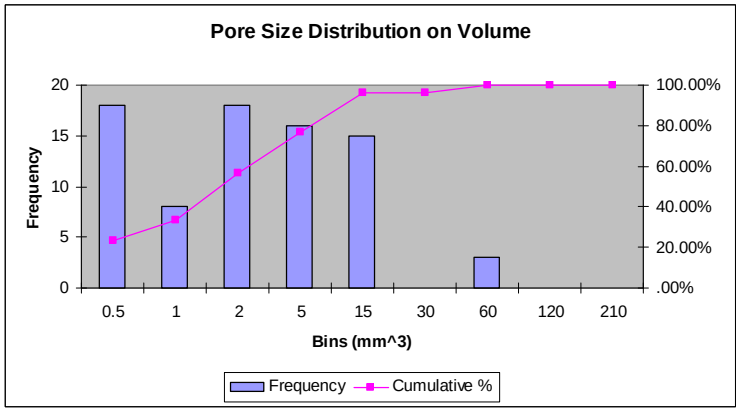

Figure 6.138 Histogram Plot of Scan #48 for the Pore Size Distribution on Volume of Specimen made with Laurel Sand

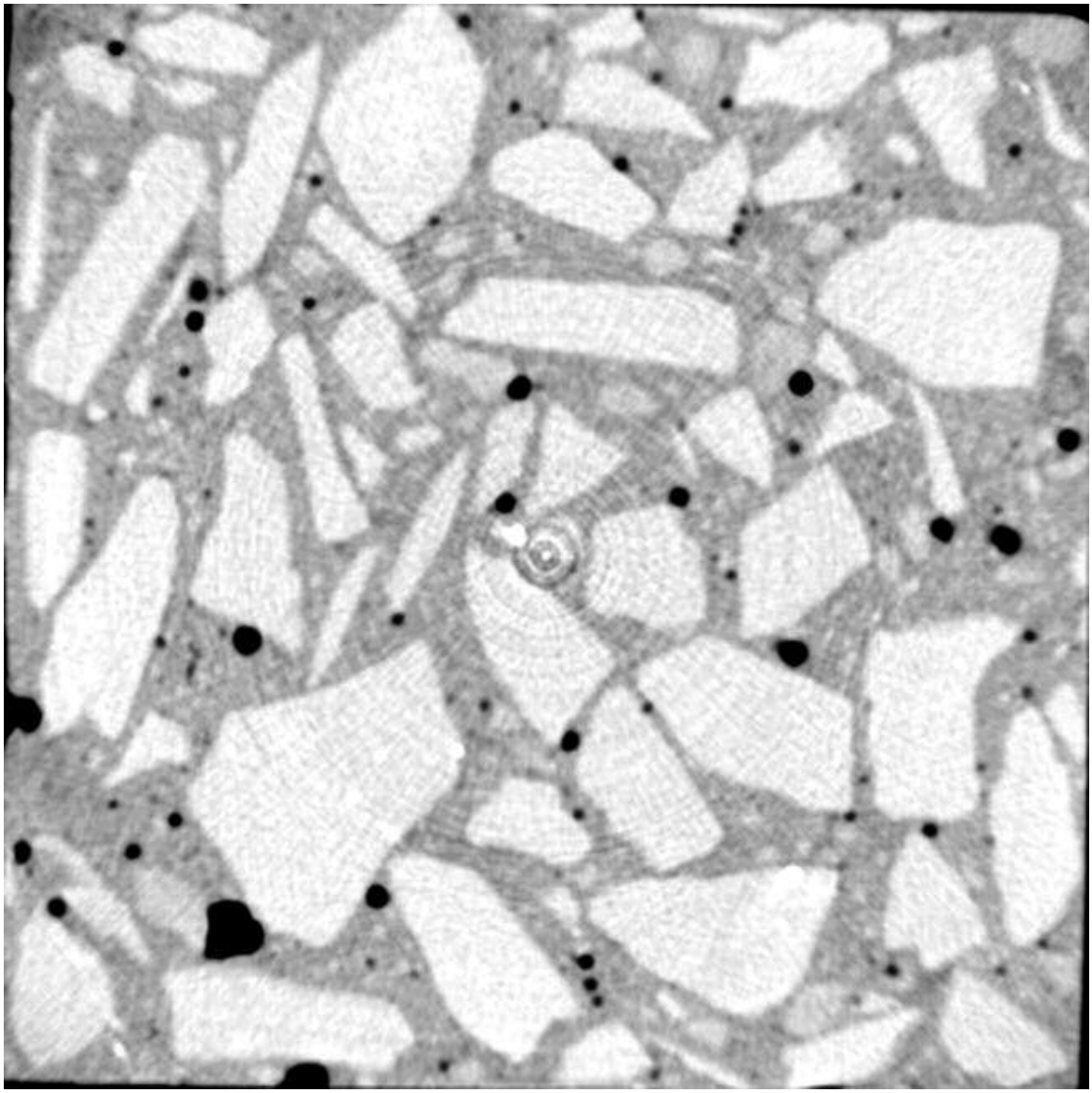

Figure 6.139 X-ray Computed Tomographic Image for Scan #49 of Specimen made with Laurel Sand

Bins (mm)	Frequency	Cumulative %	Relative %
0.1	0	.00%	0.00%
0.5	19	22.35%	22.35%
1	40	69.41%	47.06%
1.5	9	80.00%	10.59%
2	11	92.94%	12.94%
2.5	3	96.47%	3.53%
3	2	98.82%	2.35%
6	1	100.00%	1.18%
13	0	100.00%	0.00%

Table 6.94 Histogram Data of Scan #49 for the Pore Size Distribution on Diameter of Specimen made with Laurel Sand

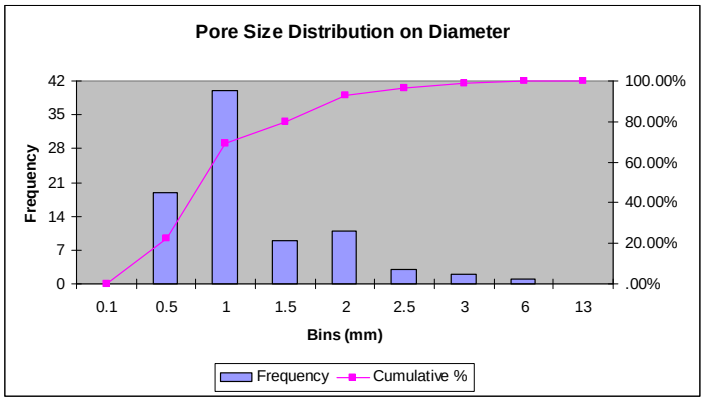

Figure 6.140 Histogram Plot of Scan #49 for the Pore Size Distribution on Diameter of Specimen made with Laurel Sand

Bins (mm^3)	Frequency	Cumulative %	Relative %
0.5	12	14.12%	14.12%
1	15	31.76%	17.65%
2	14	48.24%	16.47%
5	24	76.47%	28.24%
15	16	95.29%	18.82%
30	3	98.82%	3.53%
60	0	98.82%	0.00%
120	1	100.00%	1.18%
210	0	100.00%	0.00%

Table 6.95 Histogram Data of Scan #49 for the Pore Size Distribution on Volume of Specimen made with Laurel Sand

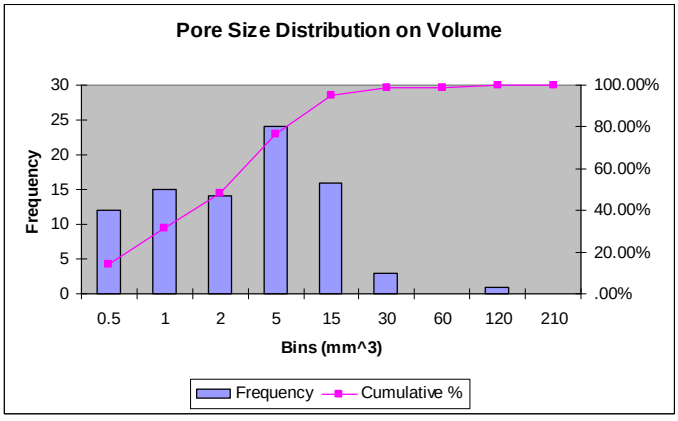

Figure 6.141 Histogram Plot of Scan #49 for the Pore Size Distribution on Volume of Specimen made with Laurel Sand

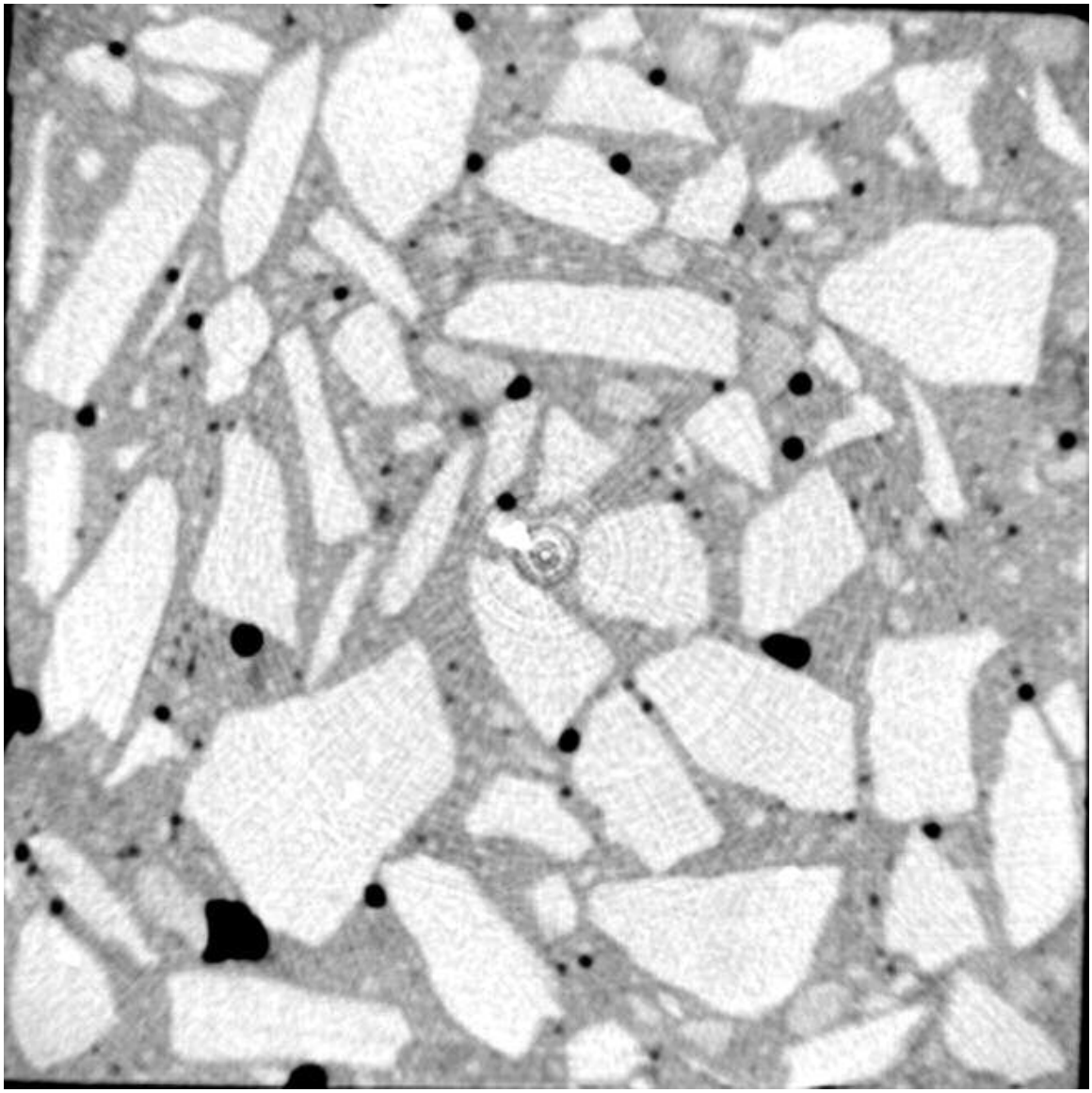

Figure 6.142 X-ray Computed Tomographic Image for Scan #50 of Specimen made with Laurel Sand

Bins (mm)	Frequency	Cumulative %	Relative %
0.1	0	.00%	0.00%
0.5	21	22.11%	22.11%
1	43	67.37%	45.26%
1.5	20	88.42%	21.05%
2	8	96.84%	8.42%
2.5	1	97.89%	1.05%
3	0	97.89%	0.00%
6	2	100.00%	2.11%
13	0	100.00%	0.00%

Table 6.96 Histogram Data of Scan #50 for the Pore Size Distribution on Diameter of Specimen made with Laurel Sand

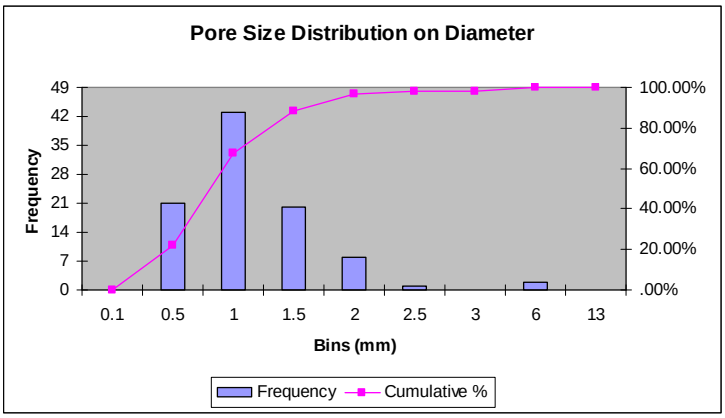

Figure 6.143 Histogram Plot of Scan #50 for the Pore Size Distribution on Diameter of Specimen made with Laurel Sand

Bins (mm^3)	Frequency	Cumulative %	Relative %
0.5	15	15.79%	15.79%
1	15	31.58%	15.79%
2	26	58.95%	27.37%
5	16	75.79%	16.84%
15	20	96.84%	21.05%
30	1	97.89%	1.05%
60	1	98.95%	1.05%
120	1	100.00%	1.05%
210	0	100.00%	0.00%

Table 6.97 Histogram Data of Scan #50 for the Pore Size Distribution on Volume of Specimen made with Laurel Sand

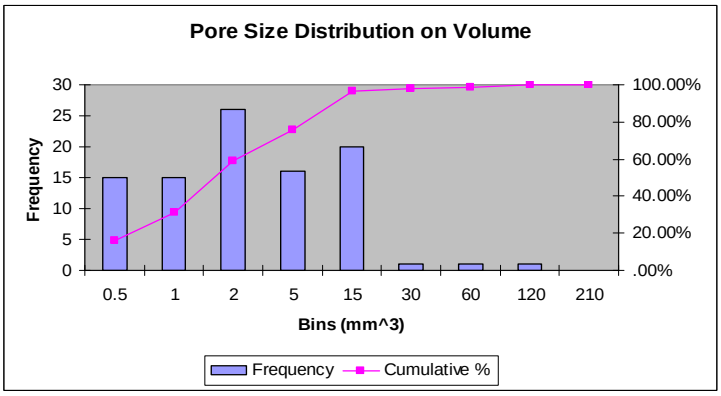

Figure 6.144 Histogram Plot of Scan #50 for the Pore Size Distribution on Volume of Specimen made with Laurel Sand

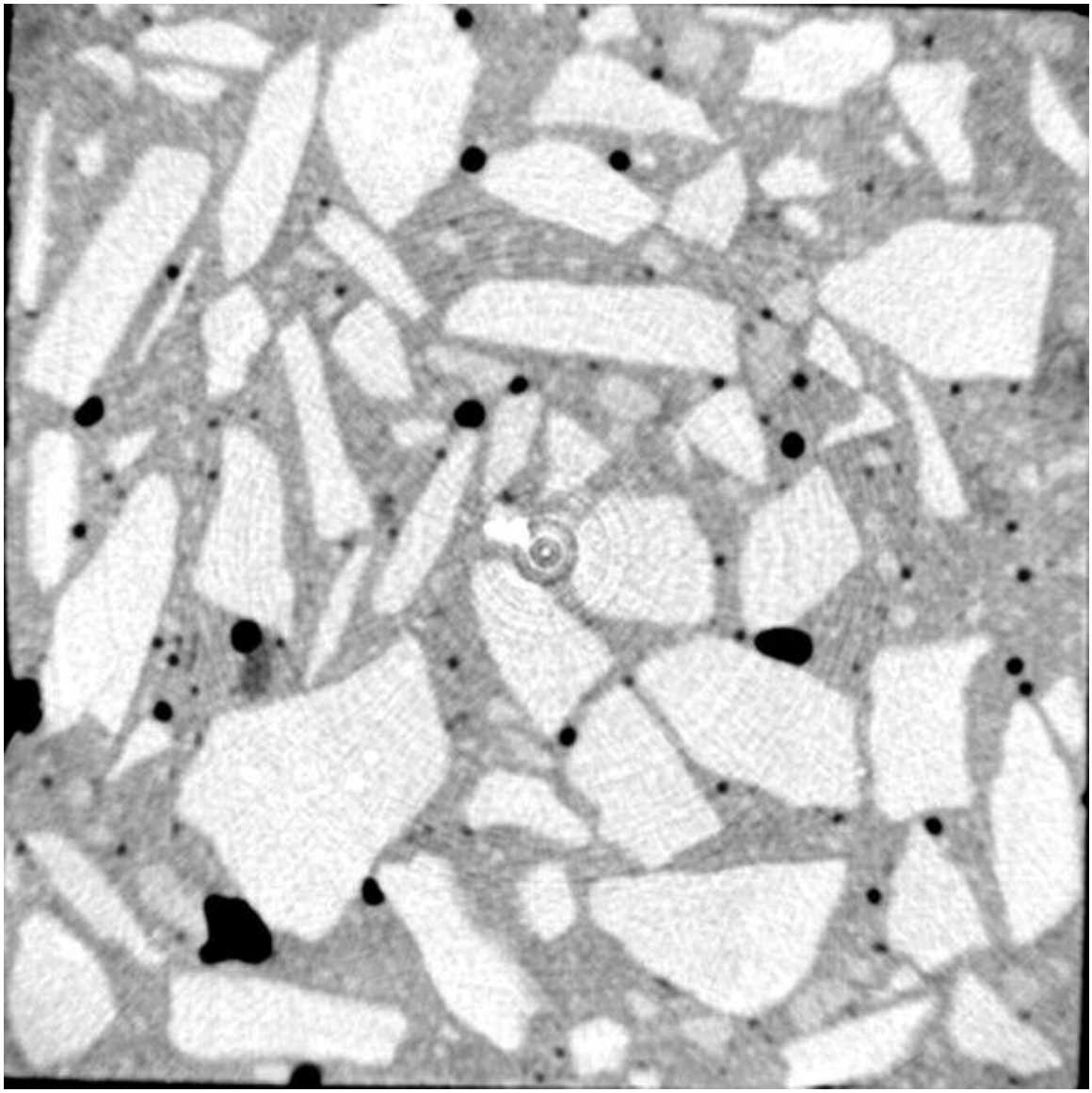

Figure 6.145 X-ray Computed Tomographic Image for Scan #51 of Specimen made with Laurel Sand

Bins (mm)	Frequency	Cumulative %	Relative %
0.1	0	.00%	0.00%
0.5	22	24.18%	24.18%
1	49	78.02%	53.85%
1.5	10	89.01%	10.99%
2	5	94.51%	5.49%
2.5	2	96.70%	2.20%
3	1	97.80%	1.10%
6	2	100.00%	2.20%
13	0	100.00%	0.00%

Table 6.98 Histogram Data of Scan #51 for the Pore Size Distribution on Diameter of Specimen made with Laurel Sand

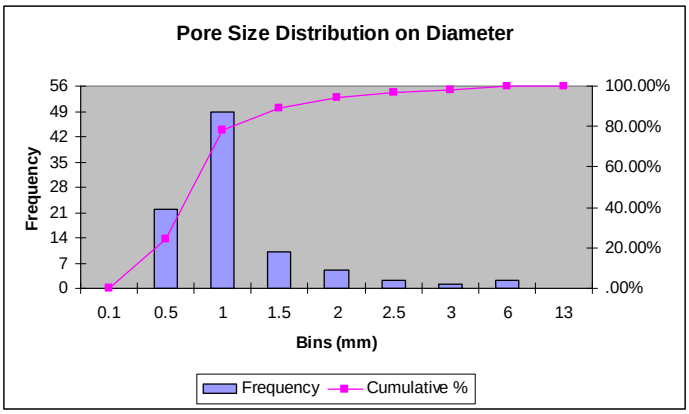

Figure 6.146 Histogram Plot of Scan #51 for the Pore Size Distribution on Diameter of Specimen made with Laurel Sand

Bins (mm^3)	Frequency	Cumulative %	Relative %
0.5	17	18.68%	18.68%
1	15	35.16%	16.48%
2	25	62.64%	27.47%
5	18	82.42%	19.78%
15	11	94.51%	12.09%
30	3	97.80%	3.30%
60	1	98.90%	1.10%
120	1	100.00%	1.10%
210	0	100.00%	0.00%

Table 6.99 Histogram Data of Scan #51 for the Pore Size Distribution on Volume of Specimen made with Laurel Sand

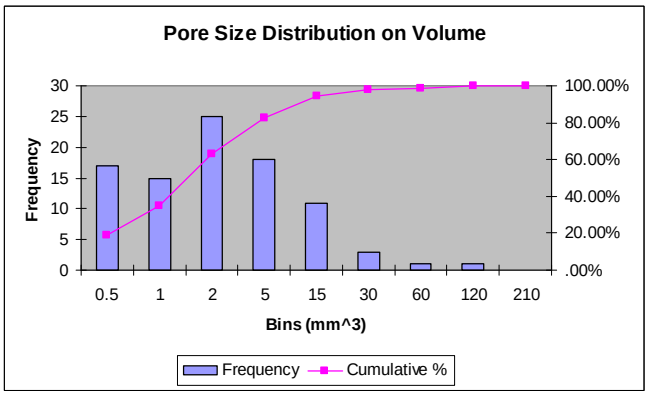

Figure 6.147 Histogram Plot of Scan #51 for the Pore Size Distribution on Volume of Specimen made with Laurel Sand

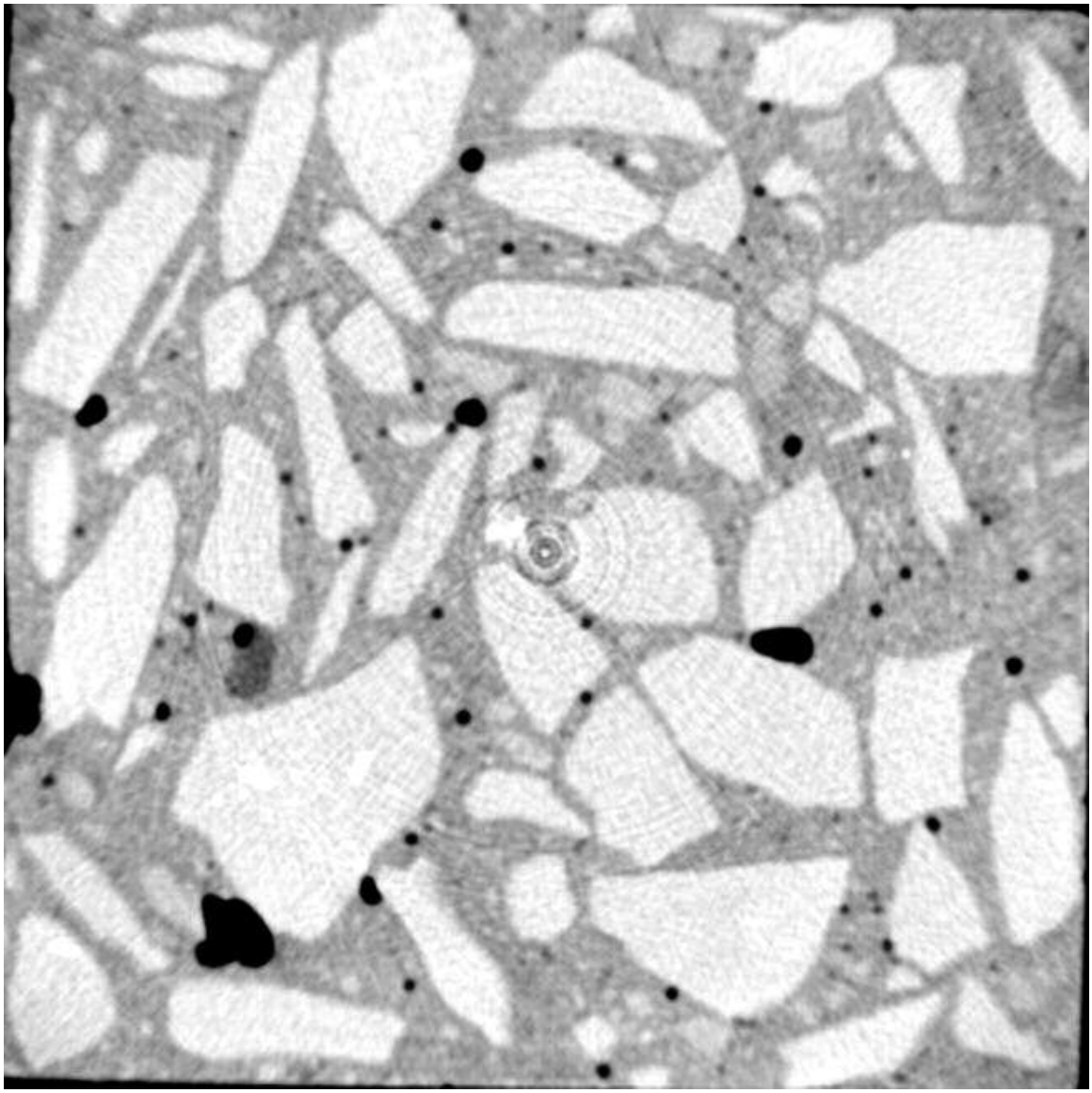

Figure 6.148 X-ray Computed Tomographic Image for Scan #52 of Specimen made with Laurel Sand

Bins (mm)	Frequency	Cumulative %	Relative %
0.1	0	.00%	0.00%
0.5	27	31.76%	31.76%
1	44	83.53%	51.76%
1.5	6	90.59%	7.06%
2	2	92.94%	2.35%
2.5	1	94.12%	1.18%
3	1	95.29%	1.18%
6	3	98.82%	3.53%
13	1	100.00%	1.18%

Table 6.100 Histogram Data of Scan #52 for the Pore Size Distribution on Diameter of Specimen made with Laurel Sand

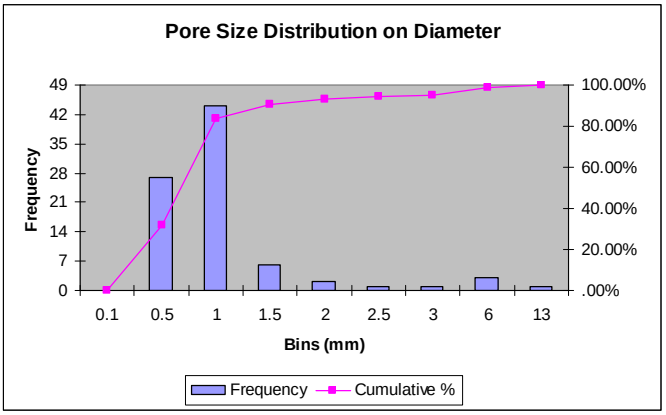

Figure 6.149 Histogram Plot of Scan #52 for the Pore Size Distribution on Diameter of Specimen made with Laurel Sand

Bins (mm^3)	Frequency	Cumulative %	Relative %
0.5	22	25.88%	25.88%
1	13	41.18%	15.29%
2	14	57.65%	16.47%
5	25	87.06%	29.41%
15	6	94.12%	7.06%
30	2	96.47%	2.35%
60	2	98.82%	2.35%
120	1	100.00%	1.18%
210	0	100.00%	0.00%

Table 6.101 Histogram Data of Scan #52 for the Pore Size Distribution on Volume of Specimen made with Laurel Sand

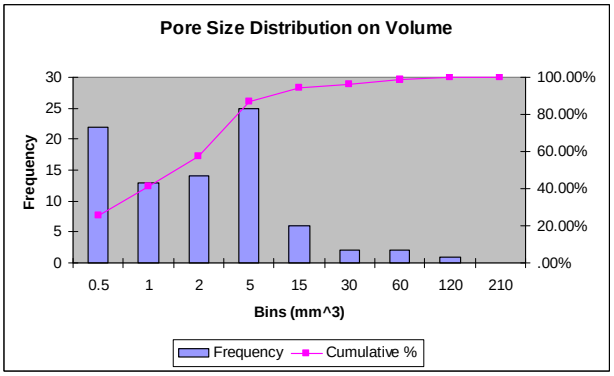

Figure 6.150 Histogram Plot of Scan #52 for the Pore Size Distribution on Volume of Specimen made with Laurel Sand

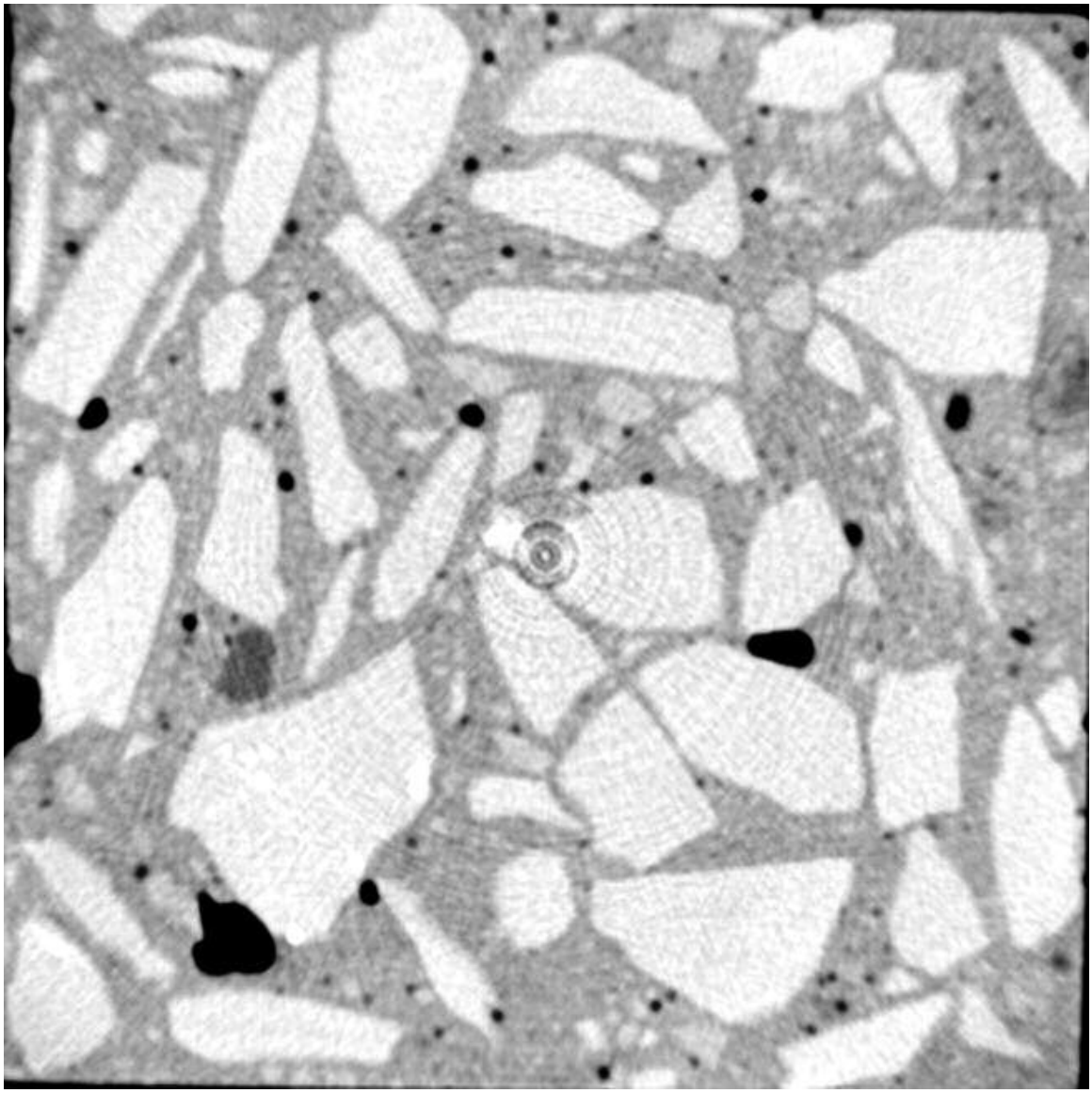

Figure 6.151 X-ray Computed Tomographic Image for Scan #53 of Specimen made with Laurel Sand

Bins (mm)	Frequency	Cumulative %	Relative %
0.1	0	.00%	0.00%
0.5	33	34.74%	34.74%
1	43	80.00%	45.26%
1.5	9	89.47%	9.47%
2	5	94.74%	5.26%
2.5	2	96.84%	2.11%
3	1	97.89%	1.05%
6	1	98.95%	1.05%
13	1	100.00%	1.05%

Table 6.102 Histogram Data of Scan #53 for the Pore Size Distribution on Diameter of Specimen made with Laurel Sand

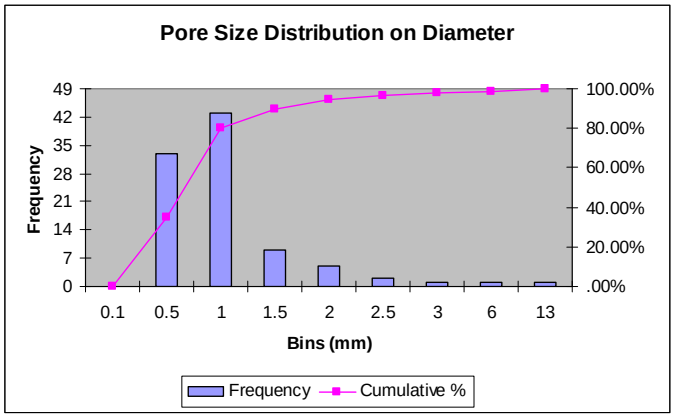

Figure 6.152 Histogram Plot of Scan #53 for the Pore Size Distribution on Diameter of Specimen made with Laurel Sand

Bins (mm^3)	Frequency	Cumulative %	Relative %
0.5	24	25.26%	25.26%
1	18	44.21%	18.95%
2	21	66.32%	22.11%
5	20	87.37%	21.05%
15	8	95.79%	8.42%
30	2	97.89%	2.11%
60	1	98.95%	1.05%
120	0	98.95%	0.00%
210	1	100.00%	1.05%

Table 6.103 Histogram Data of Scan #53 for the Pore Size Distribution on Volume of Specimen made with Laurel Sand

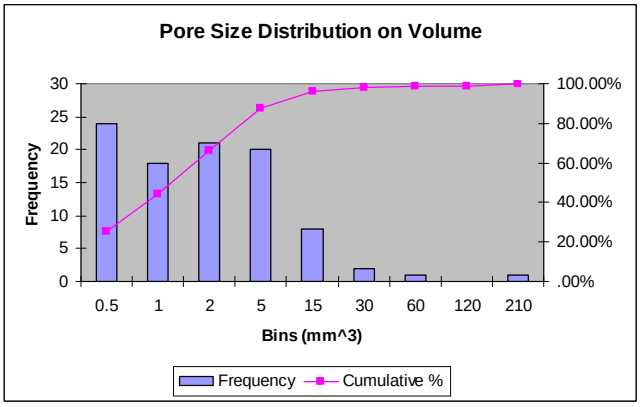

Figure 6.153 Histogram Plot of Scan #53 for the Pore Size Distribution on Volume of Specimen made with Laurel Sand

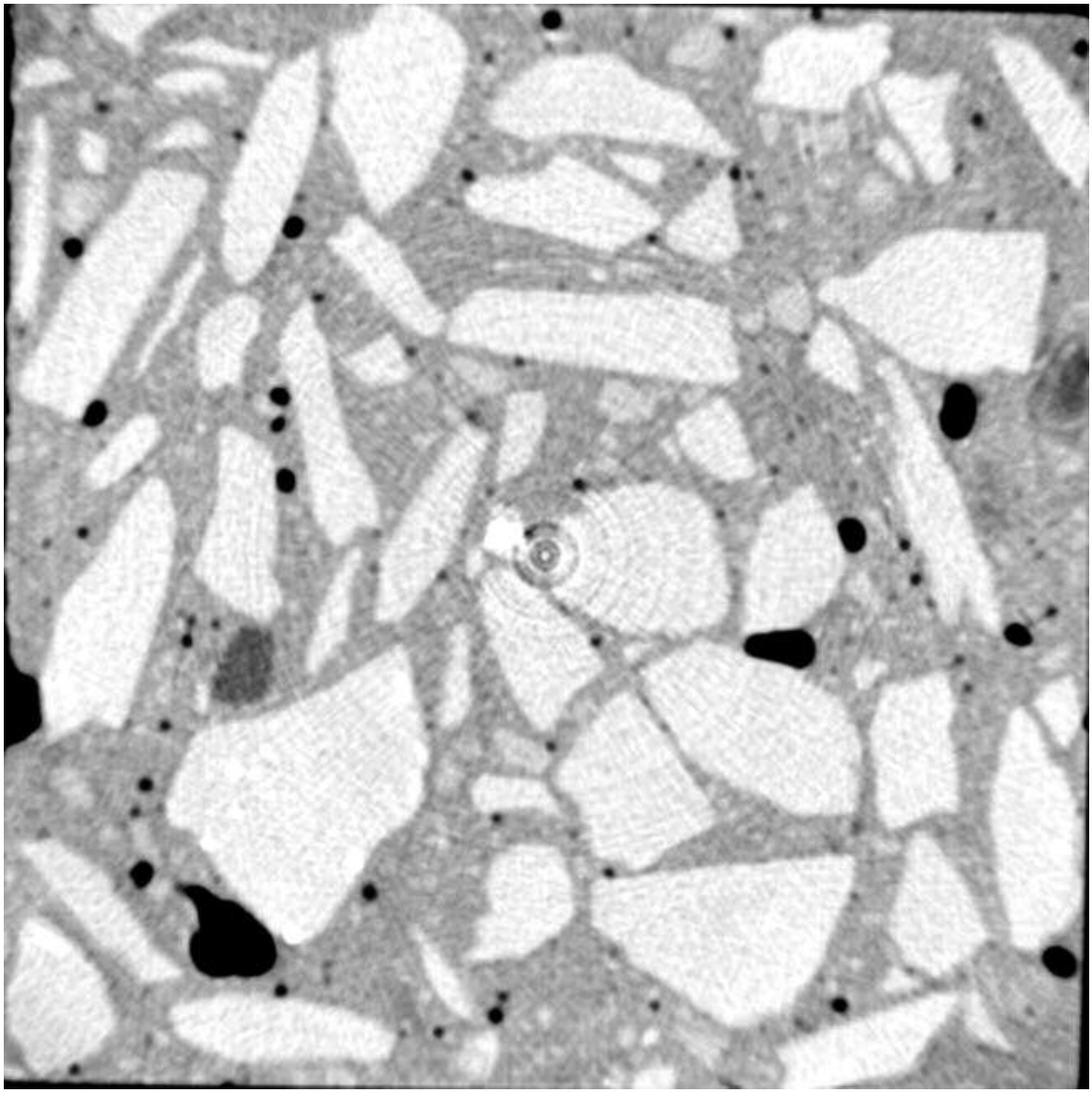

Figure 6.154 X-ray Computed Tomographic Image for Scan #54 of Specimen made with Laurel Sand

Bins (mm)	Frequency	Cumulative %	Relative %
0.1	0	.00%	0.00%
0.5	20	25.32%	25.32%
1	37	72.15%	46.84%
1.5	10	84.81%	12.66%
2	3	88.61%	3.80%
2.5	4	93.67%	5.06%
3	1	94.94%	1.27%
6	3	98.73%	3.80%
13	1	100.00%	1.27%

Table 6.104 Histogram Data of Scan #54 for the Pore Size Distribution on Diameter of Specimen made with Laurel Sand

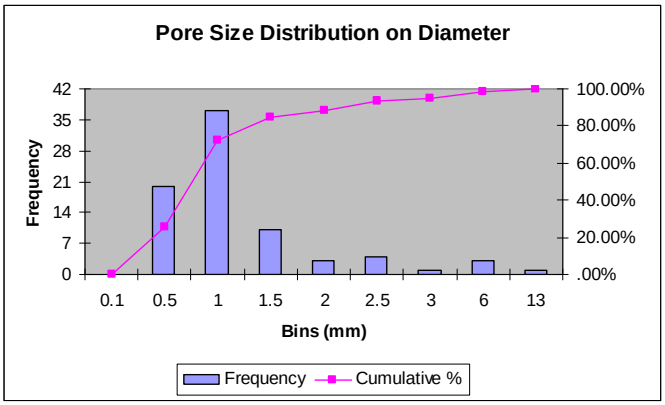

Figure 6.155 Histogram Plot of Scan #54 for the Pore Size Distribution on Diameter of Specimen made with Laurel Sand

Bins (mm^3)	Frequency	Cumulative %	Relative %
0.5	13	16.46%	16.46%
1	15	35.44%	18.99%
2	17	56.96%	21.52%
5	16	77.22%	20.25%
15	13	93.67%	16.46%
30	1	94.94%	1.27%
60	2	97.47%	2.53%
120	1	98.73%	1.27%
210	1	100.00%	1.27%

Table 6.105 Histogram Data of Scan #54 for the Pore Size Distribution on Volume of Specimen made with Laurel Sand

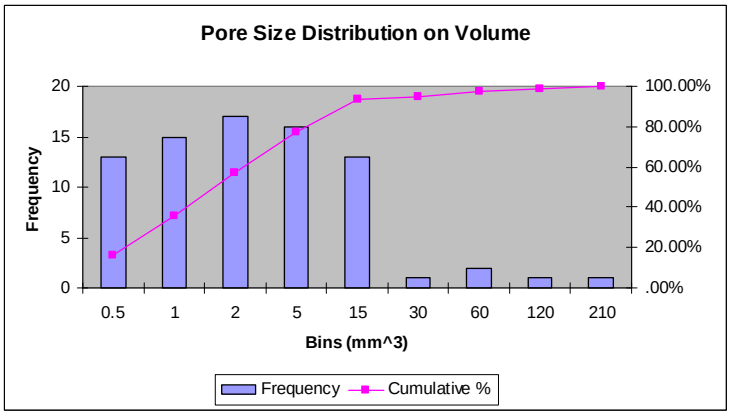

Figure 6.156 Histogram Plot of Scan #54 for the Pore Size Distribution on Volume of Specimen made with Laurel Sand

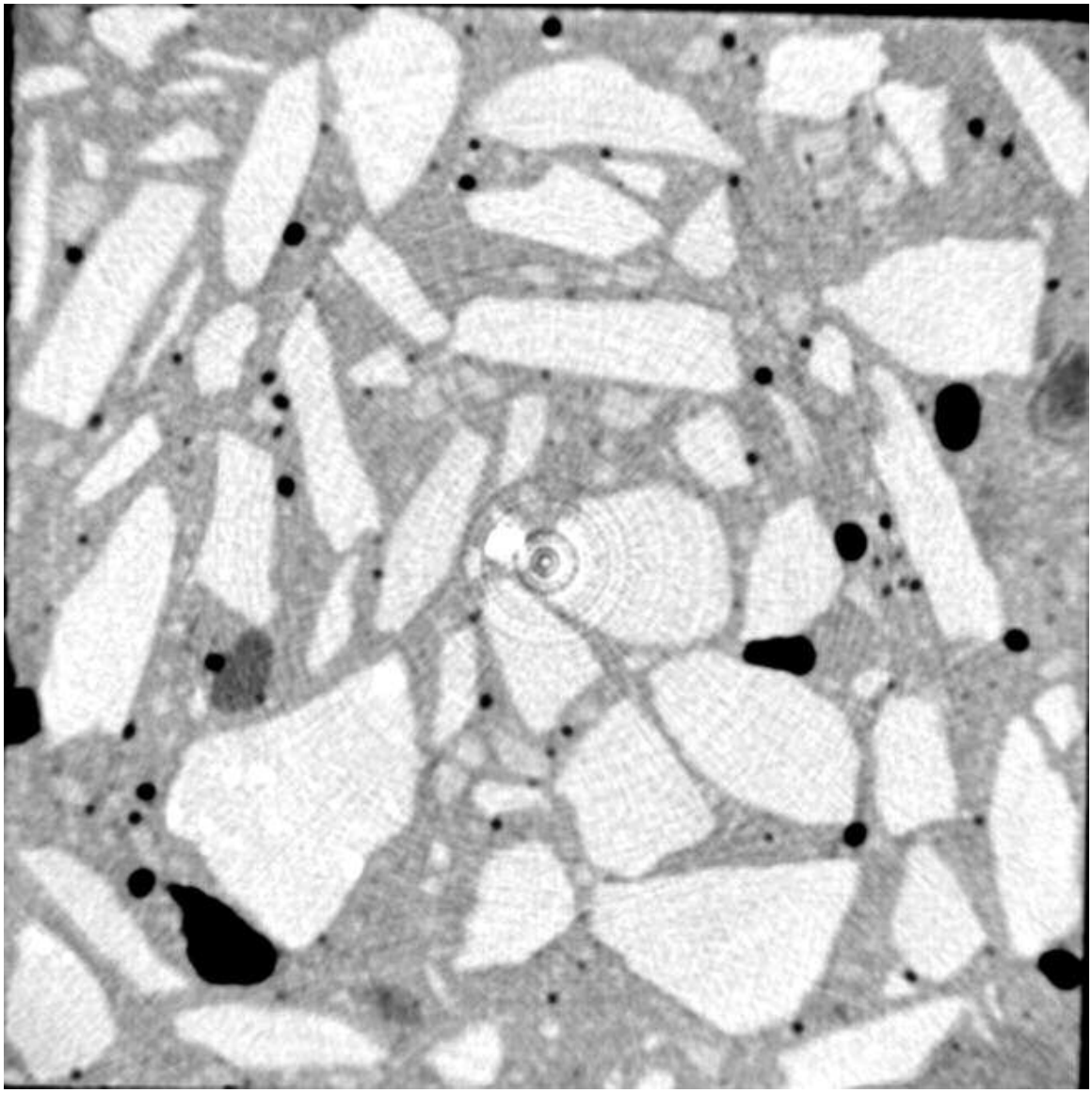

Figure 6.157 X-ray Computed Tomographic Image for Scan #55 of Specimen made with Laurel Sand

Bins (mm)	Frequency	Cumulative %	Relative %
0.1	0	.00%	0.00%
0.5	21	26.25%	26.25%
1	38	73.75%	47.50%
1.5	8	83.75%	10.00%
2	8	93.75%	10.00%
2.5	1	95.00%	1.25%
3	1	96.25%	1.25%
6	2	98.75%	2.50%
13	1	100.00%	1.25%

Table 6.106 Histogram Data of Scan #55 for the Pore Size Distribution on Diameter of Specimen made with Laurel Sand

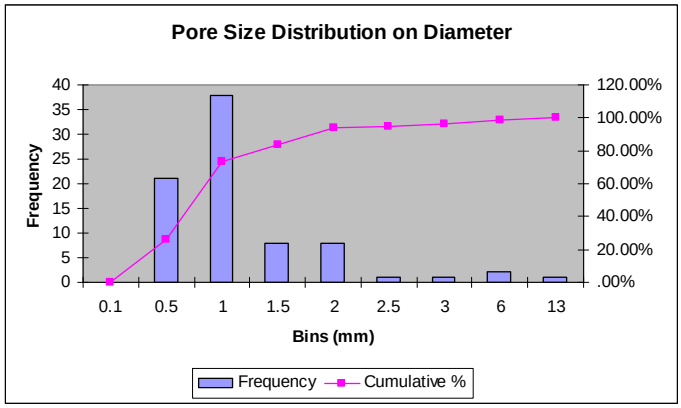

Figure 6.158 Histogram Plot of Scan #55 for the Pore Size Distribution on Diameter of Specimen made with Laurel Sand

Bins (mm^3)	Frequency	Cumulative %	Relative %
0.5	10	12.50%	12.50%
1	16	32.50%	20.00%
2	16	52.50%	20.00%
5	20	77.50%	25.00%
15	13	93.75%	16.25%
30	2	96.25%	2.50%
60	1	97.50%	1.25%
120	1	98.75%	1.25%
210	1	100.00%	1.25%

Table 6.107 Histogram Data of Scan #55 for the Pore Size Distribution on Volume of Specimen made with Laurel Sand

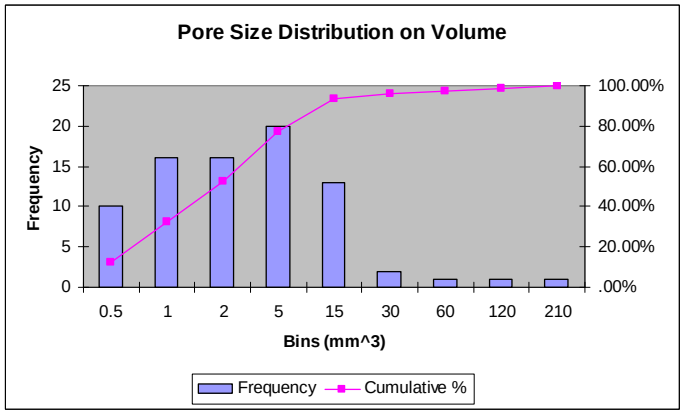

Figure 6.159 Histogram Plot of Scan #55 for the Pore Size Distribution on Volume of Specimen made with Laurel Sand

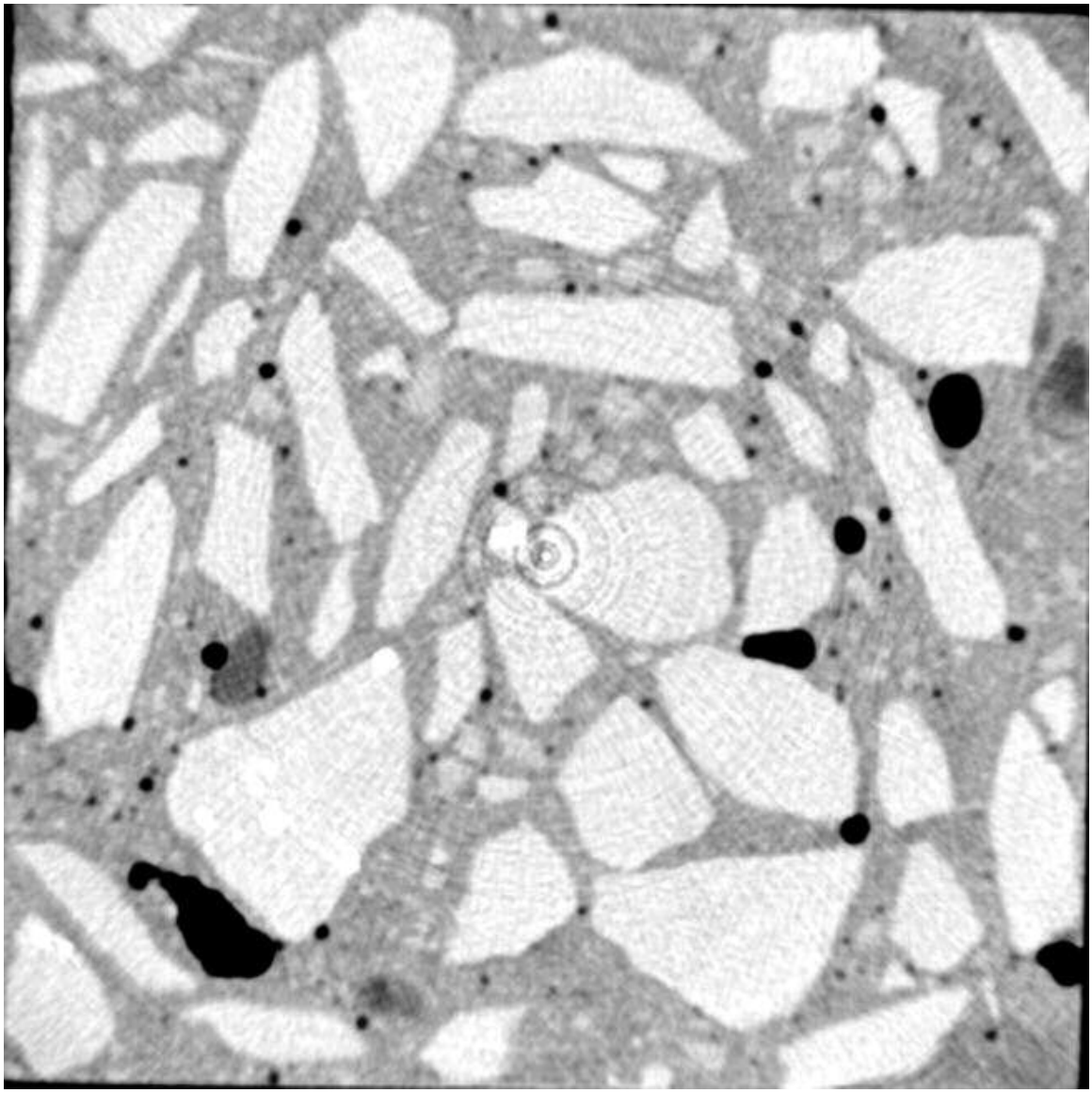

Figure 6.160 X-ray Computed Tomographic Image for Scan #56 of Specimen made with Laurel Sand

Bins (mm)	Frequency	Cumulative %	Relative %
0.1	0	.00%	0.00%
0.5	20	28.17%	28.17%
1	32	73.24%	45.07%
1.5	13	91.55%	18.31%
2	0	91.55%	0.00%
2.5	2	94.37%	2.82%
3	1	95.77%	1.41%
6	2	98.59%	2.82%
13	1	100.00%	1.41%

Table 6.108 Histogram Data of Scan #56 for the Pore Size Distribution on Diameter of Specimen made with Laurel Sand

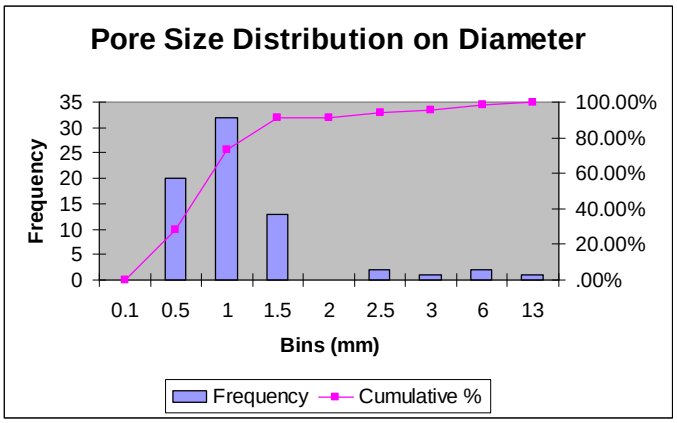

Figure 6.161 Histogram Plot of Scan #56 for the Pore Size Distribution on Diameter of Specimen made with Laurel Sand

Bins (mm^3)	Frequency	Cumulative %	Relative %
0.5	14	19.72%	19.72%
1	9	32.39%	12.68%
2	16	54.93%	22.54%
5	21	84.51%	29.58%
15	5	91.55%	7.04%
30	3	95.77%	4.23%
60	1	97.18%	1.41%
120	1	98.59%	1.41%
210	1	100.00%	1.41%

Table 6.109 Histogram Data of Scan #56 for the Pore Size Distribution on Volume of Specimen made with Laurel Sand

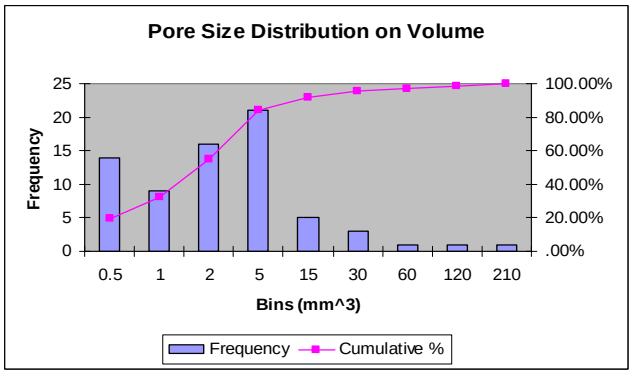

Figure 6.162 Histogram Plot of Scan #56 for the Pore Size Distribution on Volume of Specimen made with Laurel Sand

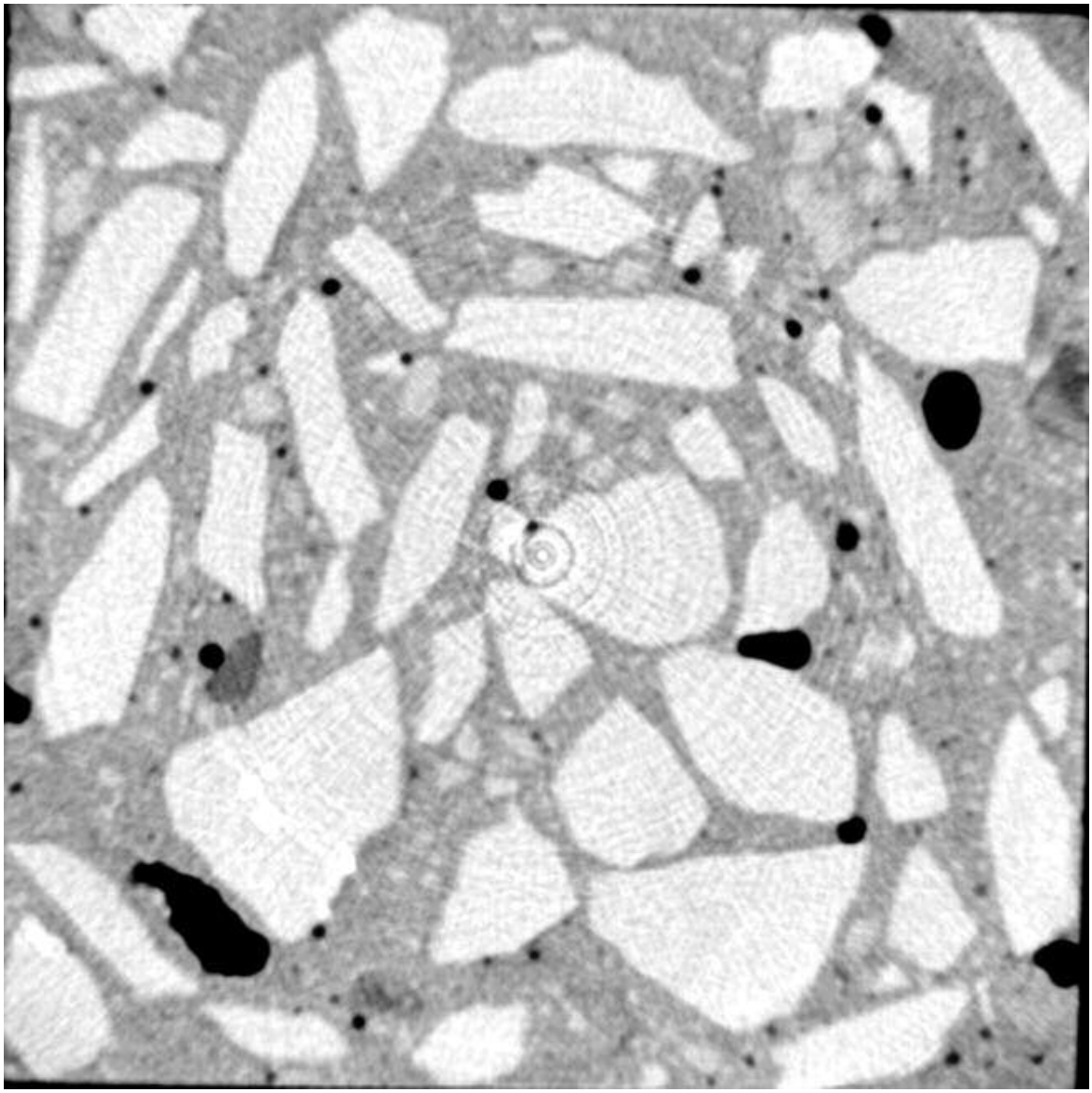

Figure 6.163 X-ray Computed Tomographic Image for Scan #57 of Specimen made with Laurel Sand

Bins (mm)	Frequency	Cumulative %	Relative %
0.1	0	.00%	0.00%
0.5	30	37.97%	37.97%
1	32	78.48%	40.51%
1.5	7	87.34%	8.86%
2	2	89.87%	2.53%
2.5	3	93.67%	3.80%
3	1	94.94%	1.27%
6	3	98.73%	3.80%
13	1	100.00%	1.27%

Table 6.110 Histogram Data of Scan #57 for the Pore Size Distribution on Diameter of Specimen made with Laurel Sand

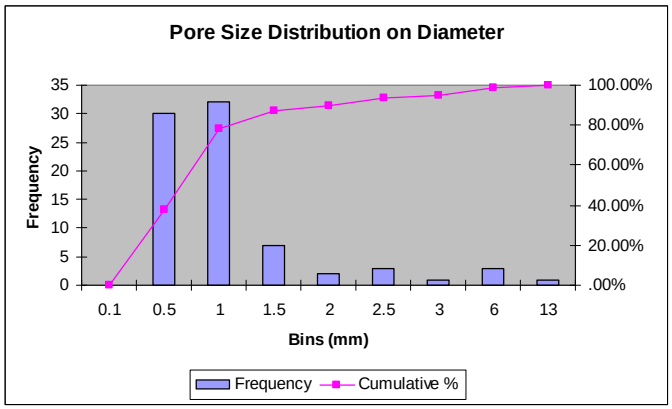

Figure 6.164 Histogram Plot of Scan #57 for the Pore Size Distribution on Diameter of Specimen made with Laurel Sand

Bins (mm^3)	Frequency	Cumulative %	Relative %
0.5	20	25.32%	25.32%
1	18	48.10%	22.78%
2	10	60.76%	12.66%
5	17	82.28%	21.52%
15	8	92.41%	10.13%
30	3	96.20%	3.80%
60	1	97.47%	1.27%
120	1	98.73%	1.27%
210	1	100.00%	1.27%

Table 6.111 Histogram Data of Scan #57 for the Pore Size Distribution on Volume of Specimen made with Laurel Sand

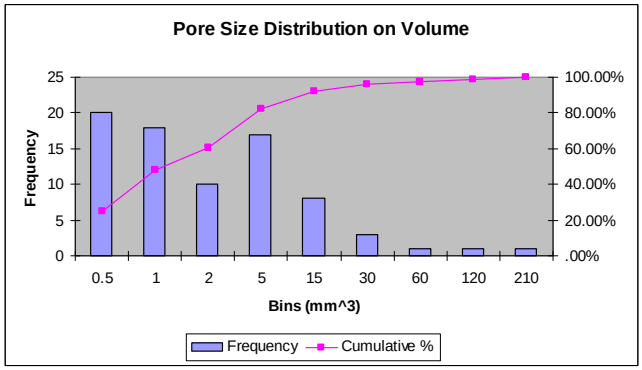

Figure 6.165 Histogram Plot of Scan #57 for the Pore Size Distribution on Volume of Specimen made with Laurel Sand

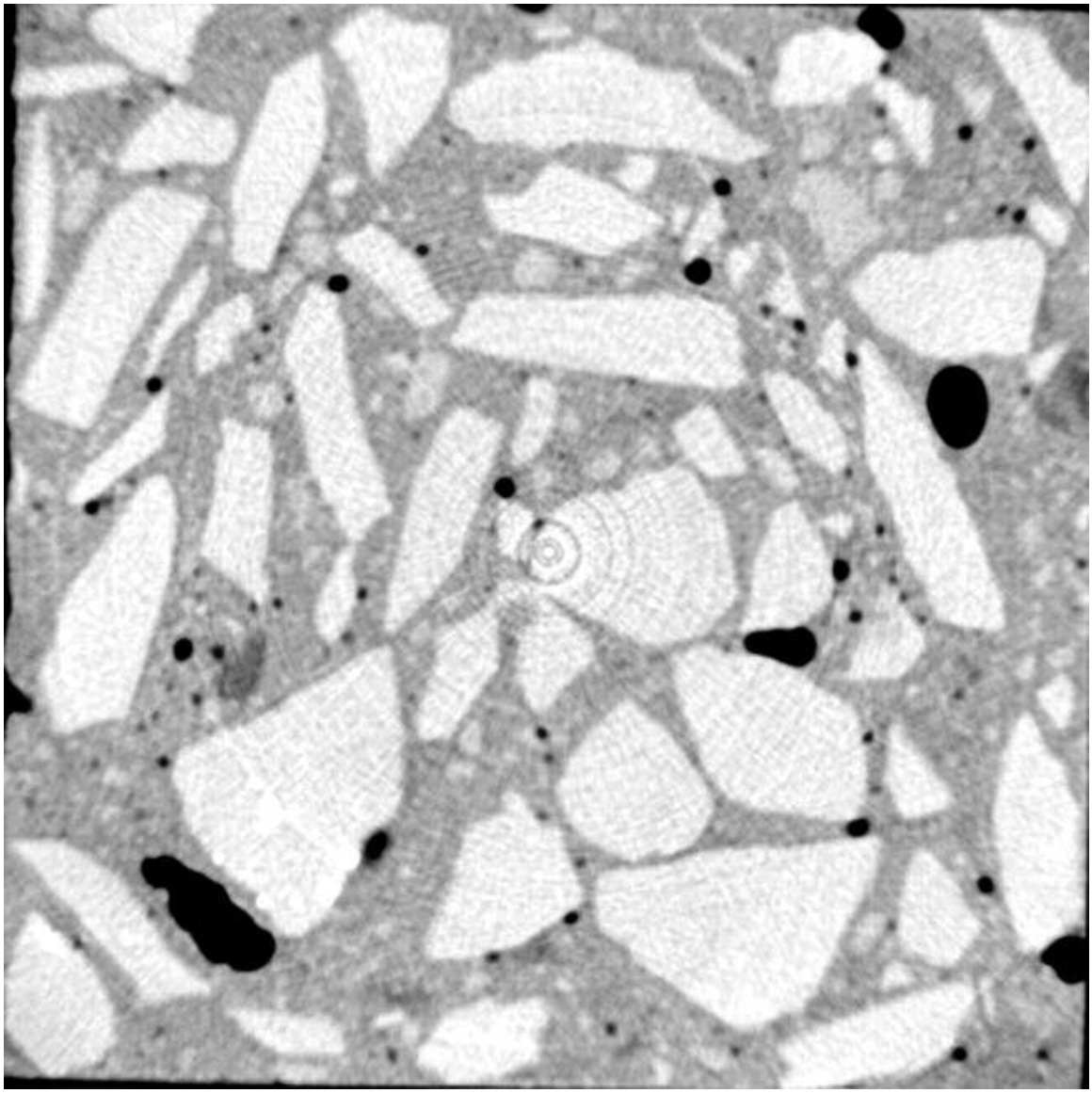

Figure 6.166 X-ray Computed Tomographic Image for Scan #58 of Specimen made with Laurel Sand

Bins (mm)	Frequency	Cumulative %	Relative %
0.1	0	.00%	0.00%
0.5	28	30.43%	30.43%
1	42	76.09%	45.65%
1.5	11	88.04%	11.96%
2	7	95.65%	7.61%
2.5	0	95.65%	0.00%
3	1	96.74%	1.09%
6	2	98.91%	2.17%
13	1	100.00%	1.09%

Table 6.112 Histogram Data of Scan #58 for the Pore Size Distribution on Diameter of Specimen made with Laurel Sand

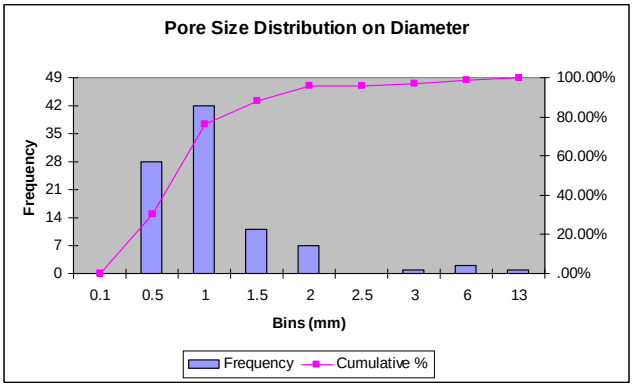

Figure 6.167 Histogram Plot of Scan #58 for the Pore Size Distribution on Diameter of Specimen made with Laurel Sand

Bins (mm^3)	Frequency	Cumulative %	Relative %
0.5	18	19.57%	19.57%
1	19	40.22%	20.65%
2	23	65.22%	25.00%
5	16	82.61%	17.39%
15	12	95.65%	13.04%
30	1	96.74%	1.09%
60	1	97.83%	1.09%
120	1	98.91%	1.09%
210	1	100.00%	1.09%

Table 6.113 Histogram Data of Scan #58 for the Pore Size Distribution on Volume of Specimen made with Laurel Sand

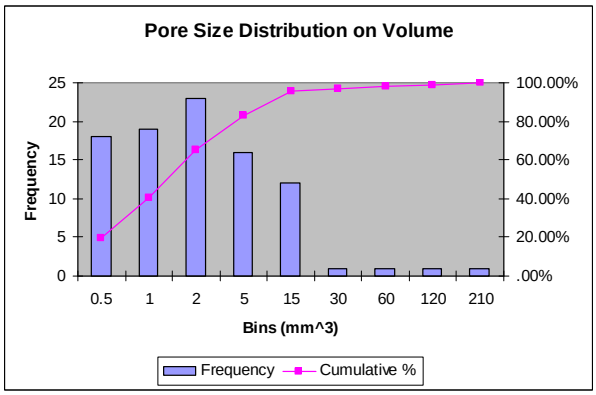

Figure 6.168 Histogram Plot of Scan #58 for the Pore Size Distribution on Volume of Specimen made with Laurel Sand

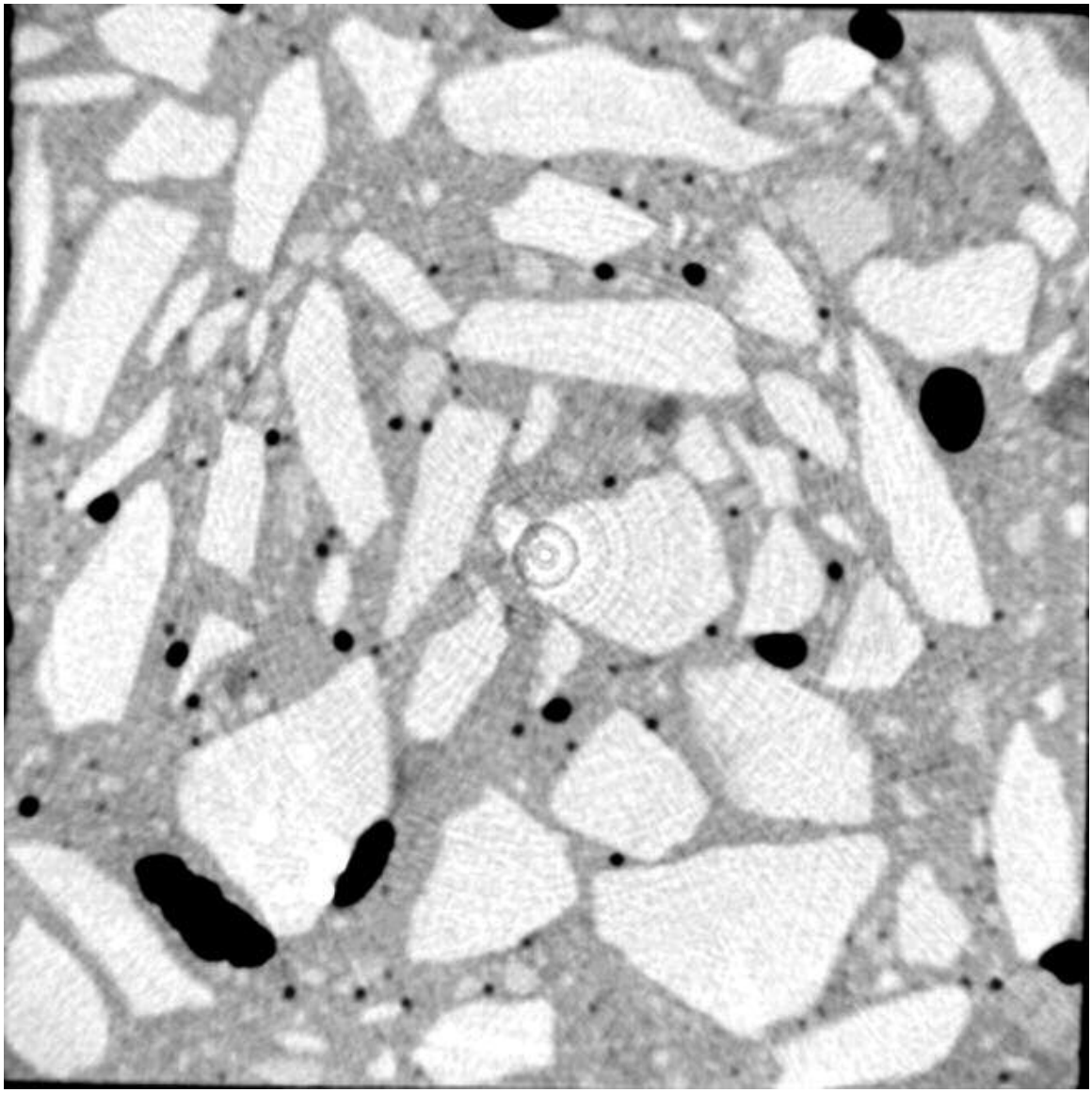

Figure 6.169 X-ray Computed Tomographic Image for Scan #60 of Specimen made with Laurel Sand

Bins (mm)	Frequency	Cumulative %	Relative %
0.1	0	.00%	0.00%
0.5	27	30.00%	30.00%
1	44	78.89%	48.89%
1.5	7	86.67%	7.78%
2	5	92.22%	5.56%
2.5	2	94.44%	2.22%
3	1	95.56%	1.11%
6	1	96.67%	1.11%
13	3	100.00%	3.33%

Table 6.114 Histogram Data of Scan #60 for the Pore Size Distribution on Diameter of Specimen made with Laurel Sand

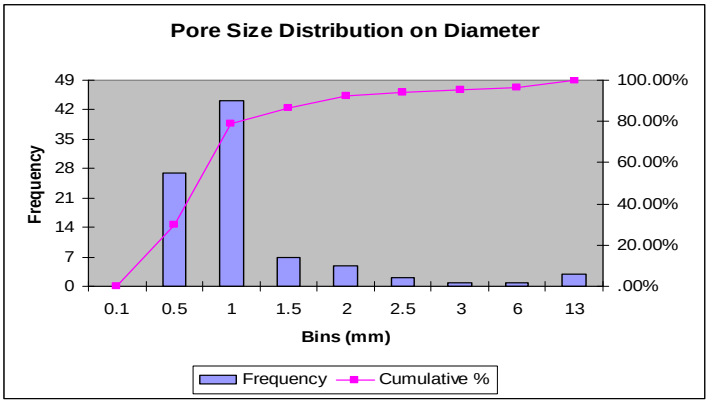

Figure 6.170 Histogram Plot of Scan #60 for the Pore Size Distribution on Diameter of Specimen made with Laurel Sand

Bins (mm^3)	Frequency	Cumulative %	Relative %
0.5	21	23.33%	23.33%
1	14	38.89%	15.56%
2	23	64.44%	25.56%
5	18	84.44%	20.00%
15	8	93.33%	8.89%
30	2	95.56%	2.22%
60	1	96.67%	1.11%
120	2	98.89%	2.22%
210	1	100.00%	1.11%

Table 6.115 Histogram Data of Scan #60 for the Pore Size Distribution on Volume of Specimen made with Laurel Sand

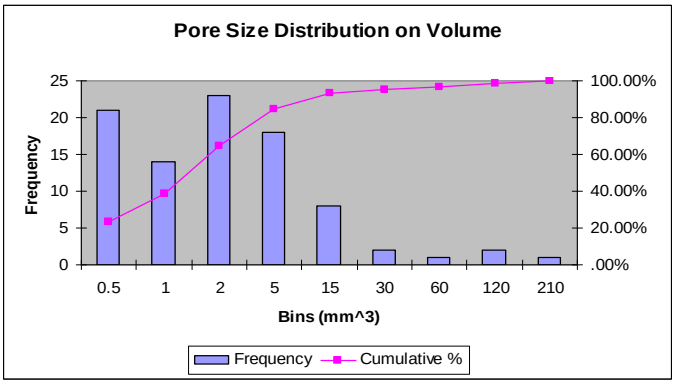

Figure 6.171 Histogram Plot of Scan #60 for the Pore Size Distribution on Volume of Specimen made with Laurel Sand

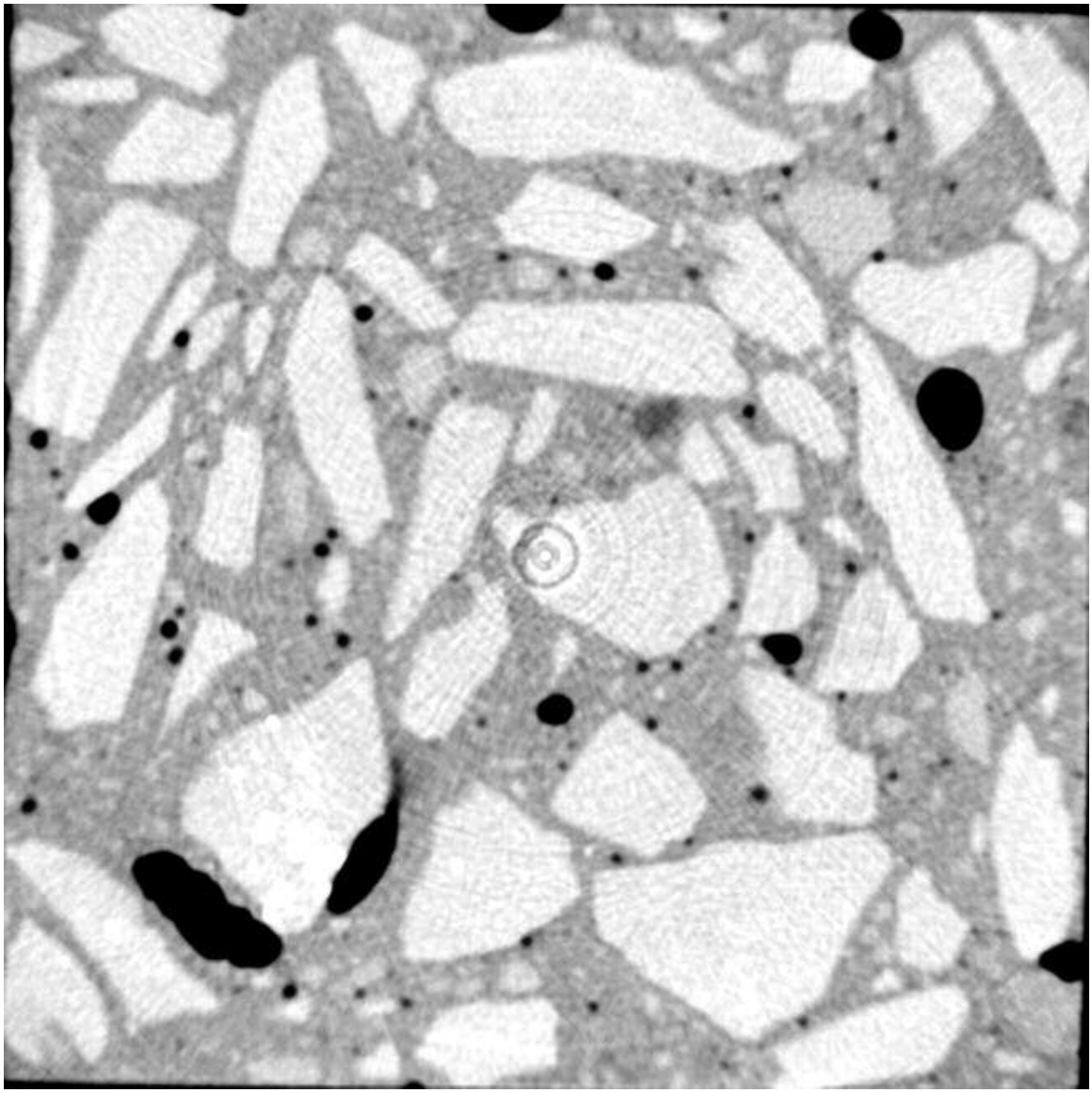

Figure 6.172 X-ray Computed Tomographic Image for Scan #61 of Specimen made with Laurel Sand

Bins (mm)	Frequency	Cumulative %	Relative %
0.1	0	.00%	0.00%
0.5	17	22.97%	22.97%
1	38	74.32%	51.35%
1.5	13	91.89%	17.57%
2	0	91.89%	0.00%
2.5	0	91.89%	0.00%
3	2	94.59%	2.70%
6	1	95.95%	1.35%
13	3	100.00%	4.05%

Table 6.116 Histogram Data of Scan #61 for the Pore Size Distribution on Diameter of Specimen made with Laurel Sand

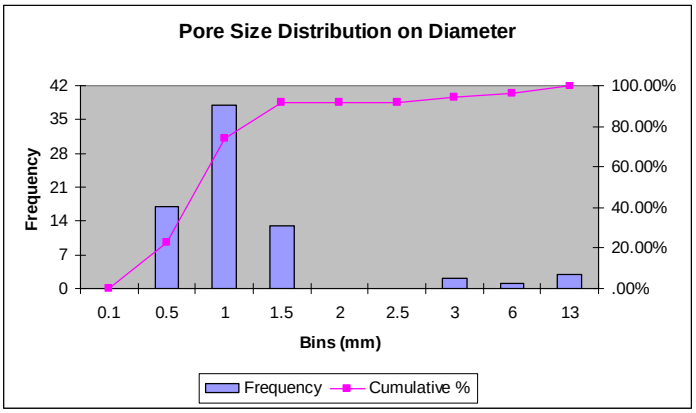

Figure 6.173 Histogram Plot of Scan #61 for the Pore Size Distribution on Diameter of Specimen made with Laurel Sand

Bins (mm^3)	Frequency	Cumulative %	Relative %
0.5	12	16.22%	16.22%
1	11	31.08%	14.86%
2	19	56.76%	25.68%
5	17	79.73%	22.97%
15	9	91.89%	12.16%
30	3	95.95%	4.05%
60	0	95.95%	0.00%
120	2	98.65%	2.70%
210	0	98.65%	0.00%

Table 6.117 Histogram Data of Scan #61 for the Pore Size Distribution on Volume of Specimen made with Laurel Sand

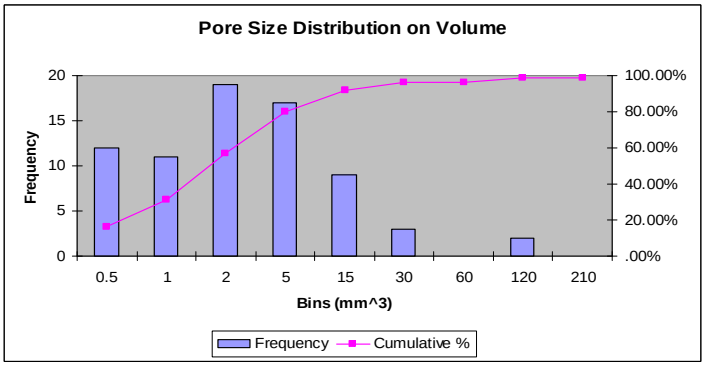

Figure 6.174 Histogram Plot of Scan #61 for the Pore Size Distribution on Volume of Specimen made with Laurel Sand

Bins (mm)	Frequency	Cumulative %	Relative %
0.1	0	.00%	0.00%
0.5	1362	29.58%	29.58%
1	2162	76.53%	46.95%
1.5	521	87.84%	11.31%
2	233	92.90%	5.06%
2.5	117	95.44%	2.54%
3	64	96.83%	1.39%
6	120	99.44%	2.61%
13	26	100.00%	0.56%

Table 6.118 Total Histogram Data for the Pore Size Distribution on Diameter of Specimen made with Laurel Sand

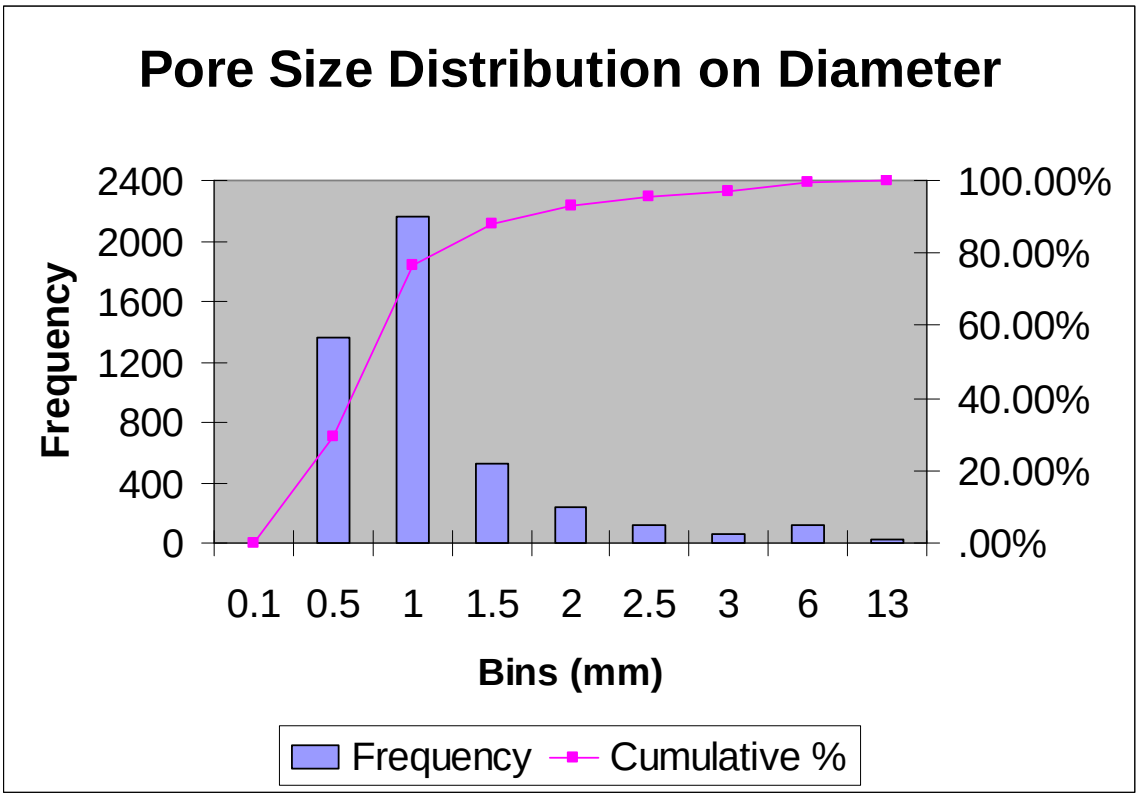

Figure 6.175 Total Histogram Plot for the Pore Size Distribution on Diameter of Specimen made with Laurel Sand

Bins (mm^3)	Frequency	Cumulative %	Relative %
0.5	993	21.56%	21.56%
1	788	38.68%	17.11%
2	999	60.37%	21.69%
5	1010	82.30%	21.93%
15	562	94.51%	12.20%
30	129	97.31%	2.80%
60	71	98.85%	1.54%
120	45	99.83%	0.98%
210	7	99.98%	0.15%

Table 6.119 Total Histogram Data for the Pore Size Distribution on Volume of Specimen made with Laurel Sand

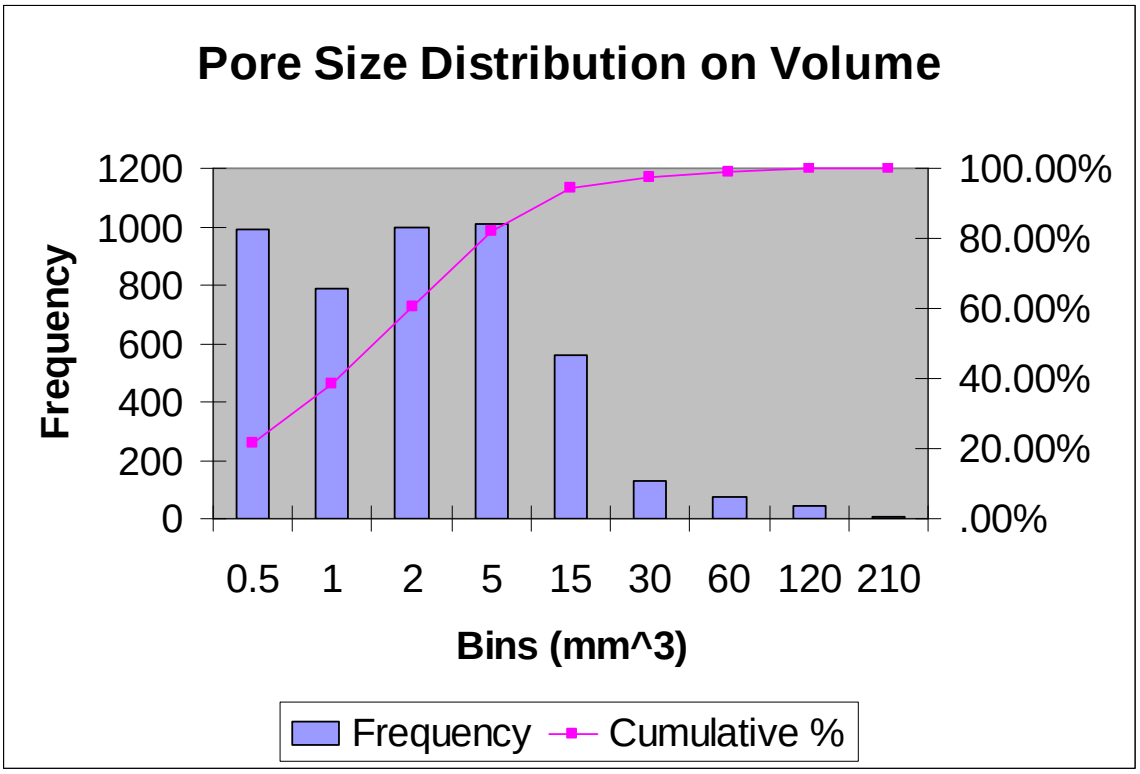

Figure 6.176 Total Histogram Plot for the Pore Size Distribution on Volume of Specimen made with Laurel Sand

Bins (mm)	Frequency	Cumulative %	Relative %
0.1	0	.00%	0.00%
0.5	659	27.69%	27.69%
1	1130	75.17%	47.48%
1.5	268	86.43%	11.26%
2	144	92.48%	6.05%
2.5	68	95.34%	2.86%
3	39	96.97%	1.64%
6	53	99.20%	2.23%
13	19	100.00%	0.80%

Table 6.120 Total Histogram Data for the Pore Size Distribution on Diameter of Specimen made with Medford Sand

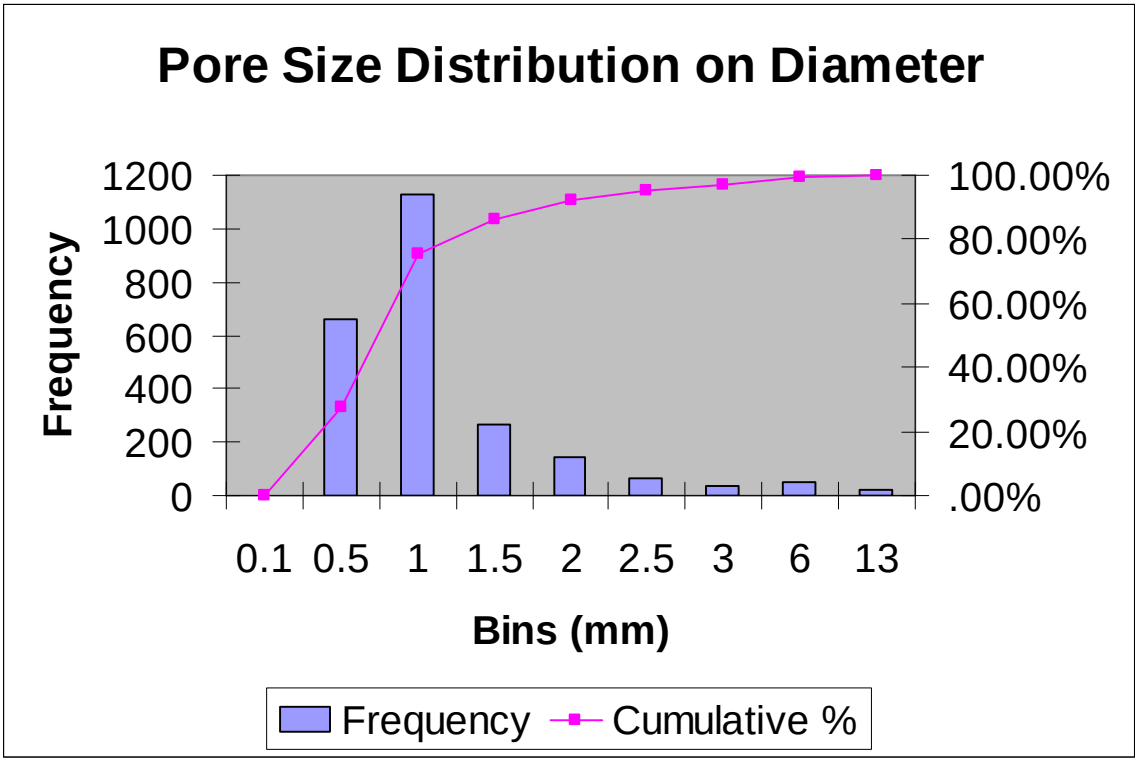

Figure 6.177 Total Histogram Plot for the Pore Size Distribution on Diameter of Specimen made with Medford Sand

Bins (mm^3)	Frequency	Cumulative %	Relative %
0.5	507	21.30%	21.30%
1	387	37.56%	16.26%
2	486	57.98%	20.42%
5	530	80.25%	22.27%
15	317	93.57%	13.32%
30	99	97.73%	4.16%
60	42	99.50%	1.76%
120	12	100.00%	0.50%
210	0	100.00%	0.00%

Table 6.121 Total Histogram Data for the Pore Size Distribution on Volume of Specimen made with Medford Sand

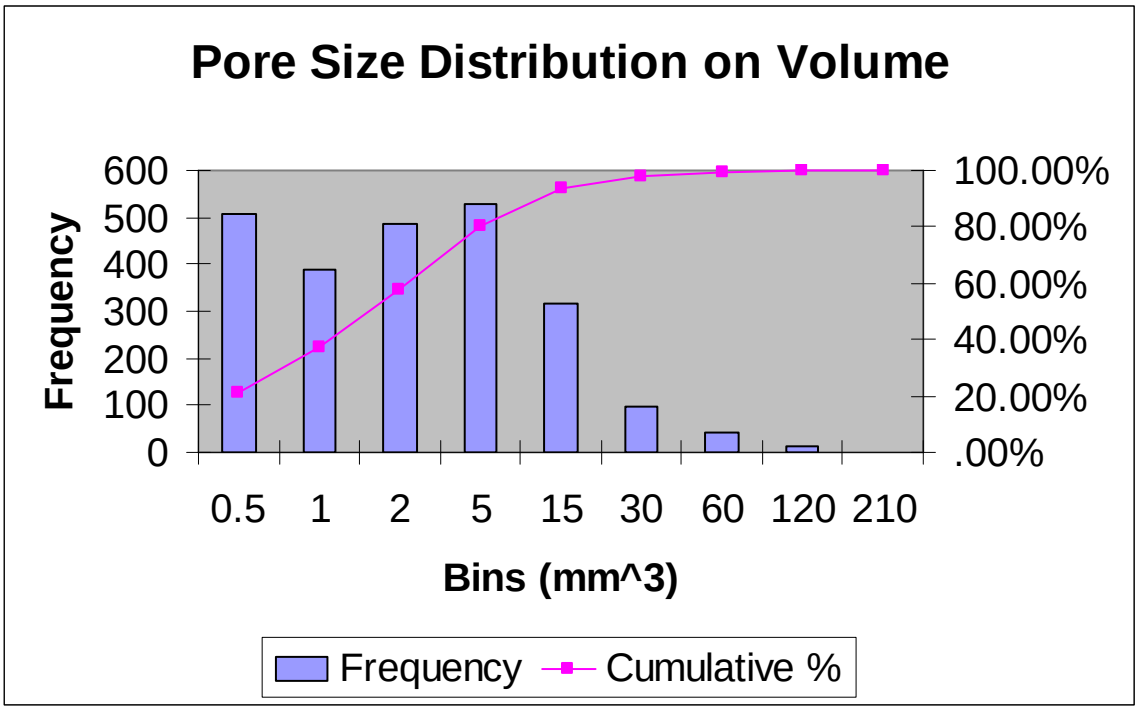

Figure 6.178 Total Histogram Plot for the Pore Size Distribution on Volume of Specimen made with Medford Sand

Bins (mm)	Frequency	Cumulative %	Relative %
0.1	0	.00%	0.00%
0.5	1096	33.44%	33.44%
1	1528	80.05%	46.61%
1.5	372	91.40%	11.35%
2	163	96.37%	4.97%
2.5	76	98.69%	2.32%
3	25	99.45%	0.76%
6	18	100.00%	0.55%
13	0	100.00%	0.00%

Table 6.122 Total Histogram Data for the Pore Size Distribution on Diameter of Specimen made with Frederick Sand

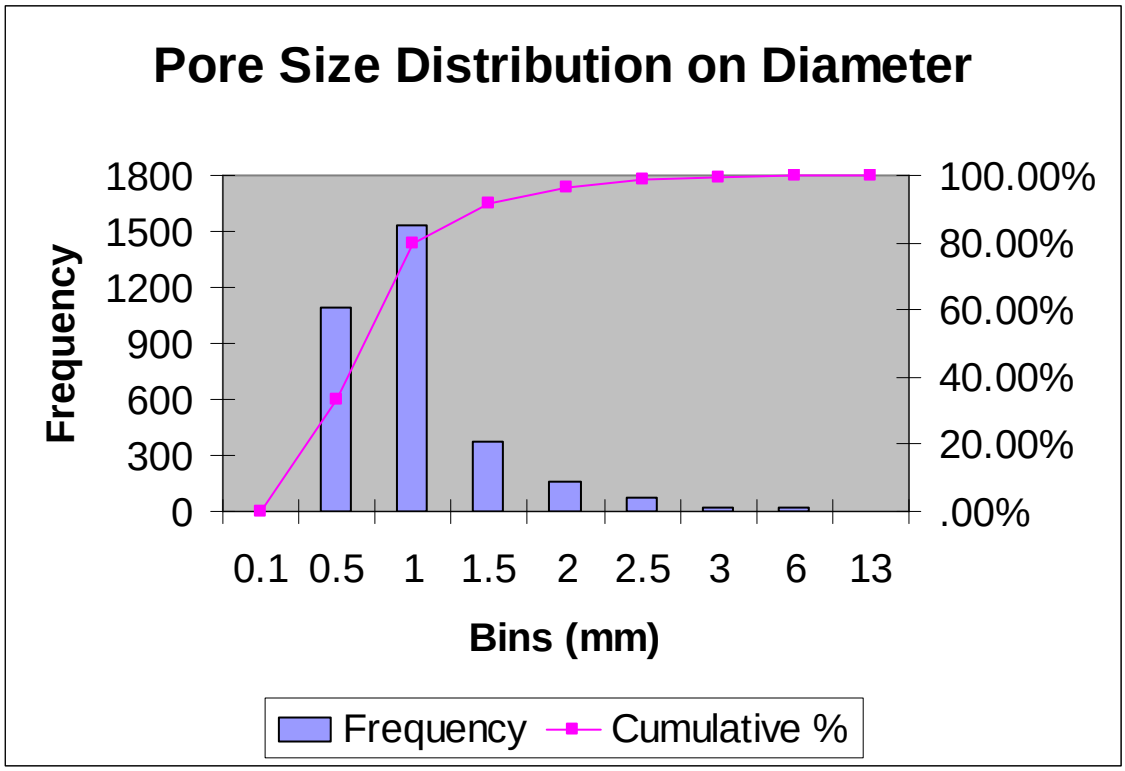

Figure 6.179 Total Histogram Plot for the Pore Size Distribution on Diameter of Specimen made with Frederick Sand

Bins (mm^3)	Frequency	Cumulative %	Relative %
0.5	831	25.35%	25.35%
1	585	43.20%	17.85%
2	697	64.46%	21.26%
5	691	85.54%	21.08%
15	386	97.32%	11.78%
30	76	99.63%	2.32%
60	12	100.00%	0.37%
120	0	100.00%	0.00%
210	0	100.00%	0.00%

Table 6.123 Total Histogram Data for the Pore Size Distribution on Volume of Specimen made with Frederick Sand

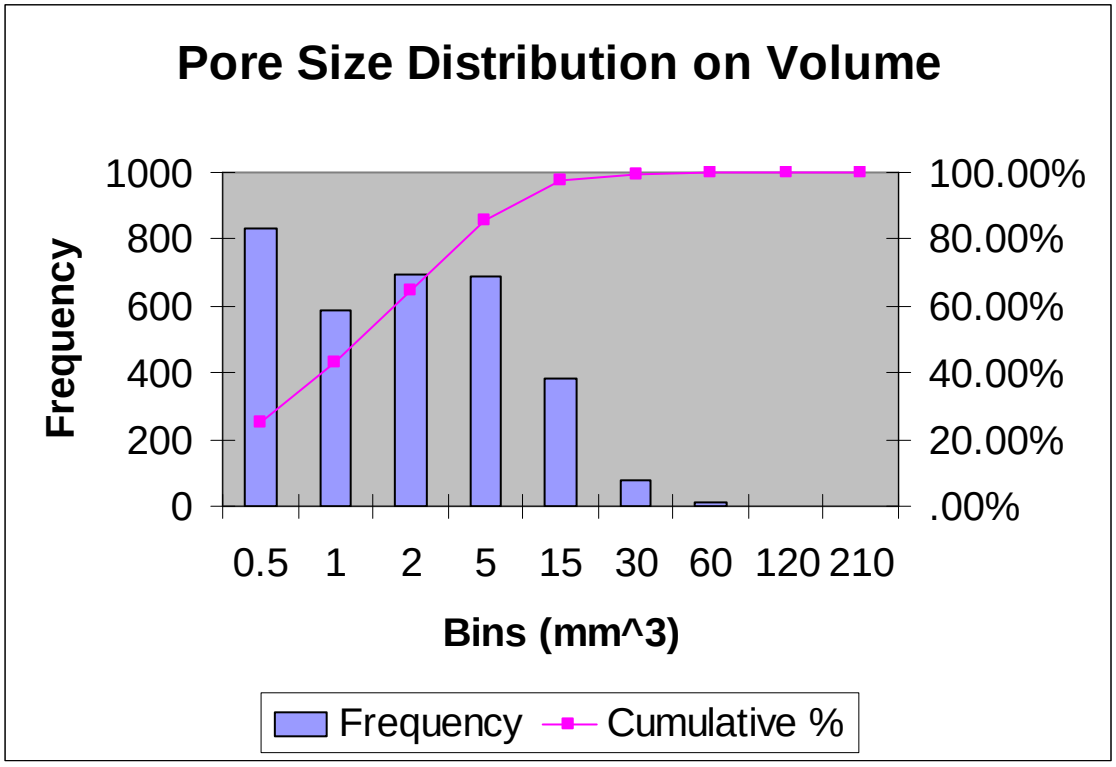

Figure 6.180 Total Histogram Plot for the Pore Size Distribution on Volume of Specimen made with Frederick Sand

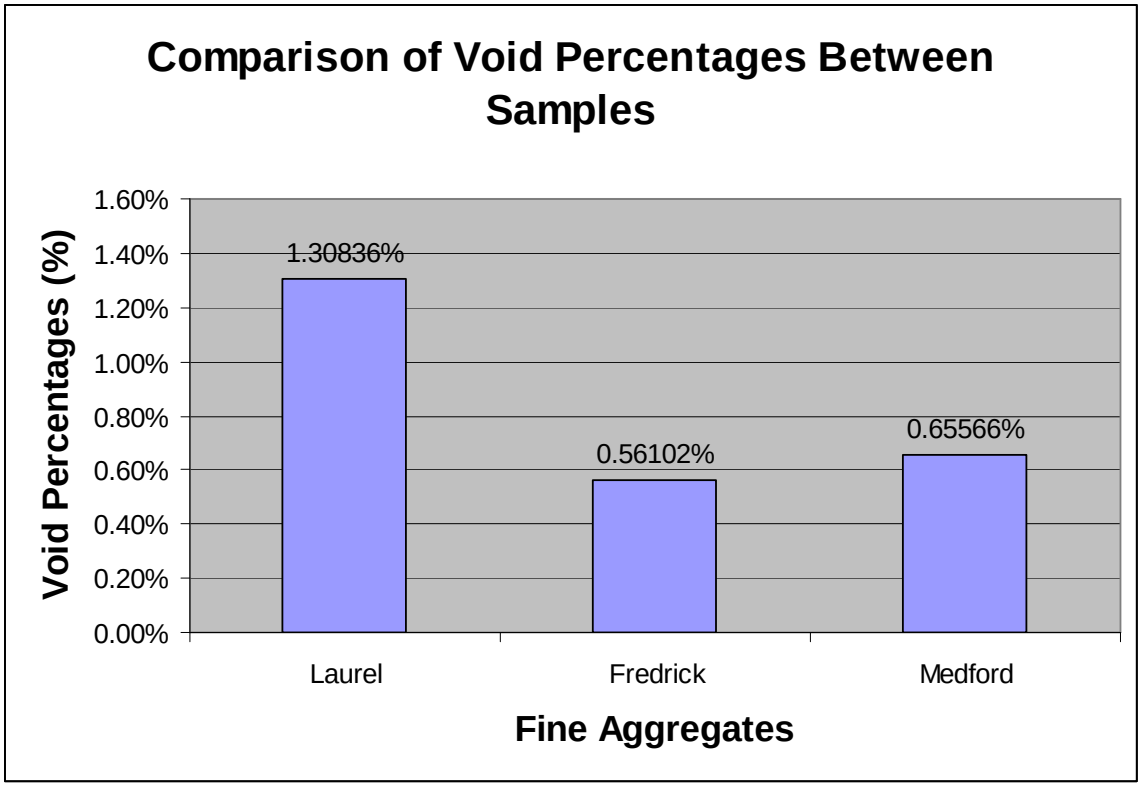

Figure 6.181 Comparisons of Void Percentages Between Laurel Frederick and Medford Specimens

Bins (mm)	Frequency	Cumulative %	Relative %
0.1	0	.00%	0.00%
0.5	1137	31.53%	31.53%
1	1346	68.86%	37.33%
1.5	620	86.05%	17.19%
2	253	93.07%	7.02%
2.5	68	94.95%	1.89%
3	58	96.56%	1.61%
6	116	99.78%	3.22%
13	8	100.00%	0.22%

Table 6.124 Total Histogram Data for the Pore Size Distribution on Diameter of Specimen made with 0% Fly Ash

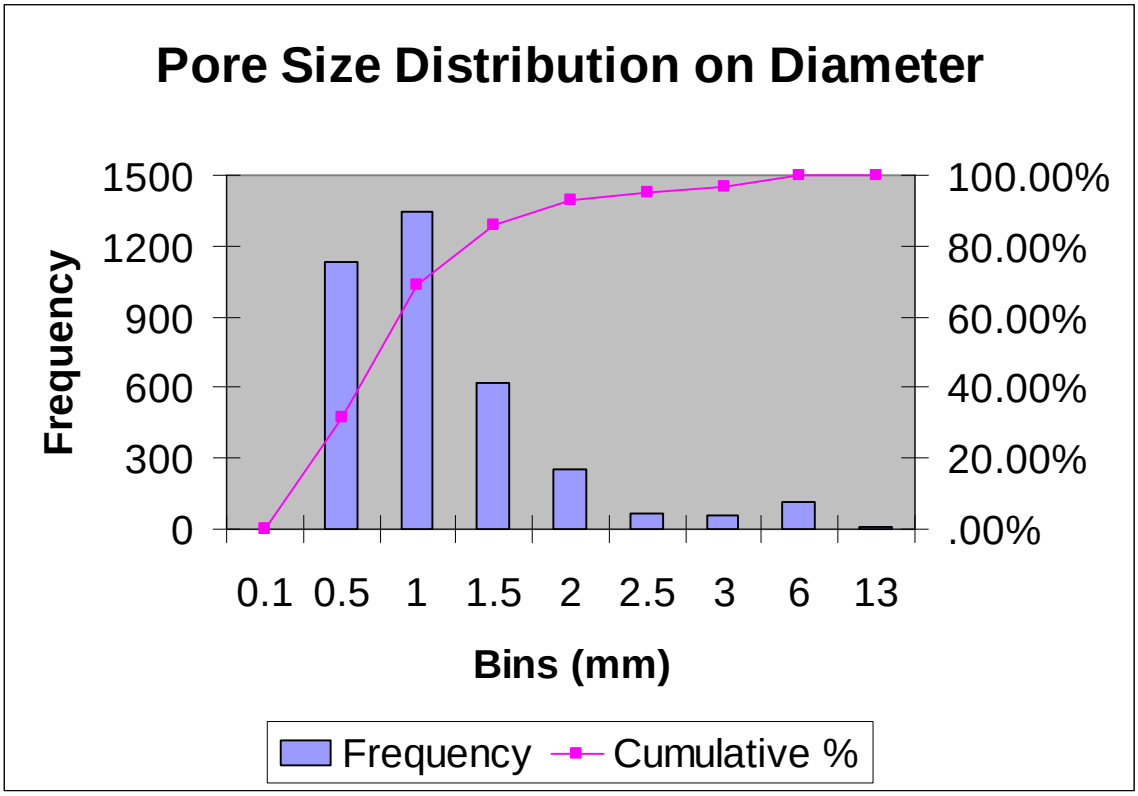

Figure 6.182 Total Histogram Plot for the Pore Size Distribution on Diameter of Specimen made with 0% Fly Ash

Bins (mm^3)	Frequency	Cumulative %	Relative %
0.5	511	14.17%	14.17%
1	591	30.56%	16.39%
2	891	55.27%	24.71%
5	924	80.89%	25.62%
15	451	93.40%	12.51%
30	127	96.92%	3.52%
60	80	99.14%	2.22%
120	31	100.00%	0.86%
210	0	100.00%	0.00%

Table 6.125 Total Histogram Data for the Pore Size Distribution on Volume of Specimen made with 0% Fly Ash

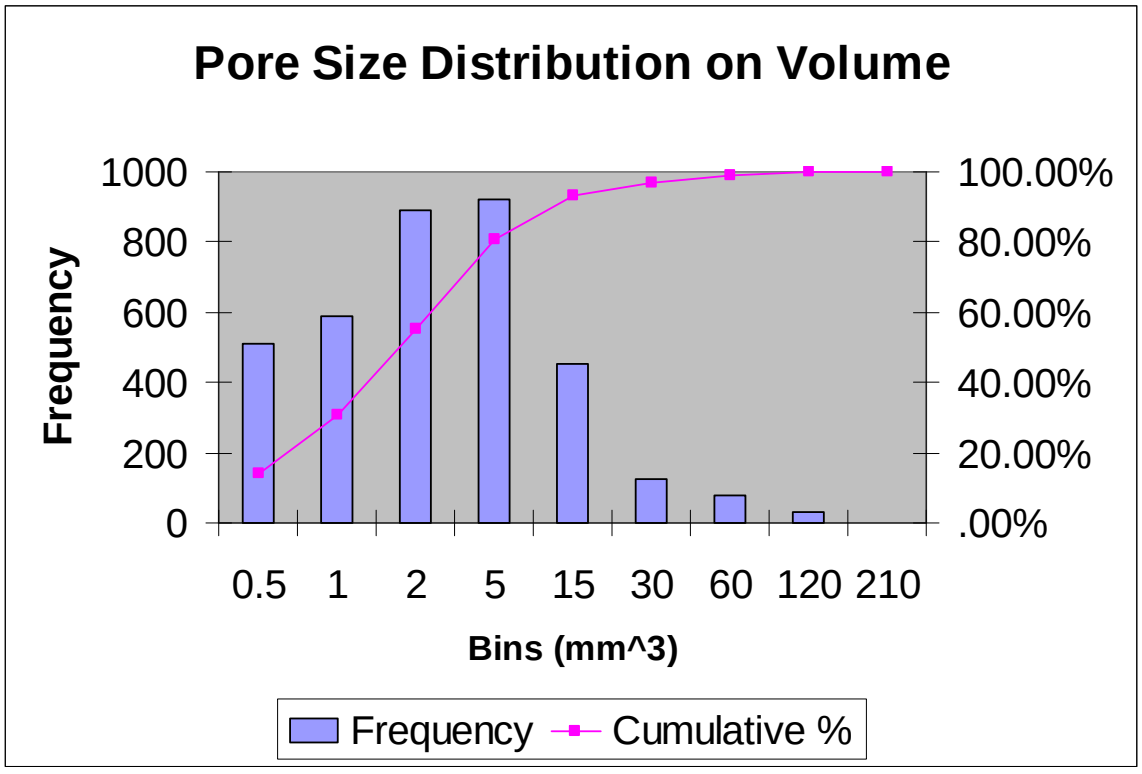

Figure 6.183 Total Histogram Plot for the Pore Size Distribution on Volume of Specimen made with 0% Fly Ash

Bins (mm)	Frequency	Cumulative %	Relative %
0.1	0	.00%	0.00%
0.5	301	24.63%	24.63%
1	410	58.18%	33.55%
1.5	252	78.81%	20.62%
2	137	90.02%	11.21%
2.5	35	92.88%	2.86%
3	39	96.07%	3.19%
6	48	100.00%	3.93%
13	0	100.00%	0.00%

Table 6.126 Total Histogram Data for the Pore Size Distribution on Diameter of Specimen made with 10% Fly Ash

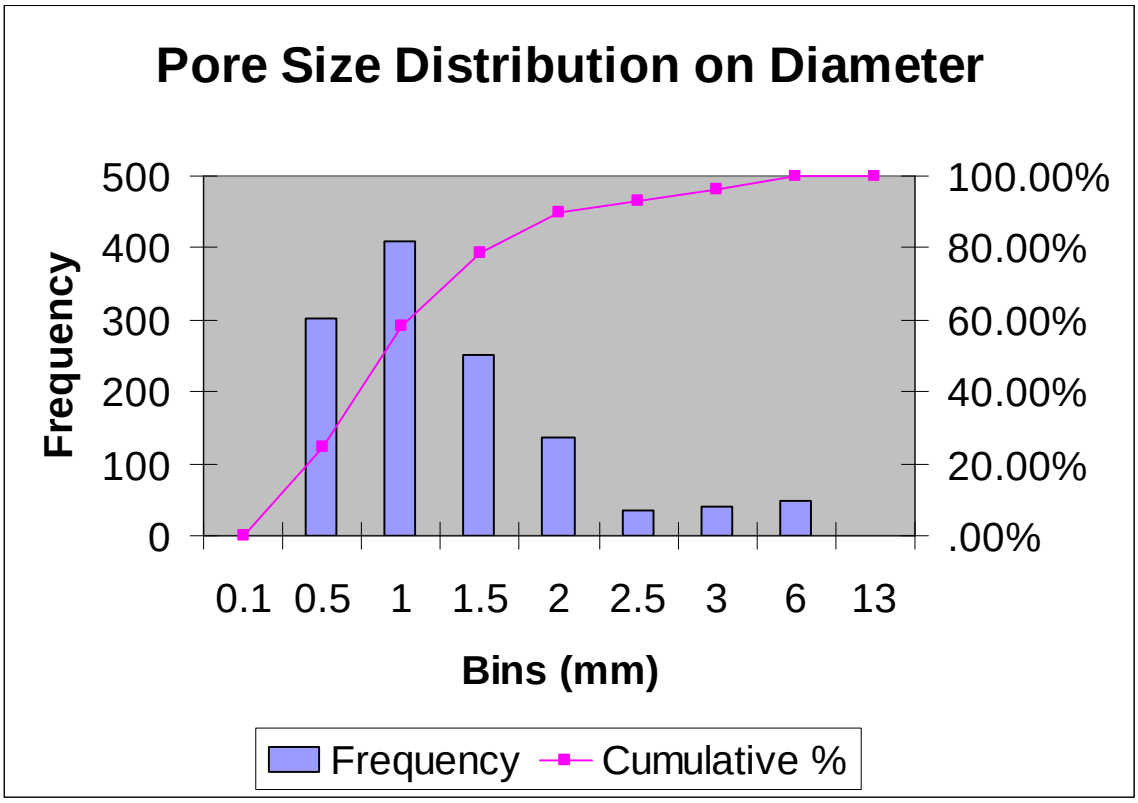

Figure 6.184 Total Histogram Plot for the Pore Size Distribution on Diameter of Specimen made with 10% Fly Ash

Bins (mm^3)	Frequency	Cumulative %	Relative %
0.5	131	10.72%	10.72%
1	165	24.22%	13.50%
2	247	44.44%	20.21%
5	339	72.18%	27.74%
15	222	90.34%	18.17%
30	78	96.73%	6.38%
60	32	99.35%	2.62%
120	8	100.00%	0.65%
210	0	100.00%	0.00%

Table 6.127 Total Histogram Data for the Pore Size Distribution on Volume of Specimen made with 10% Fly Ash

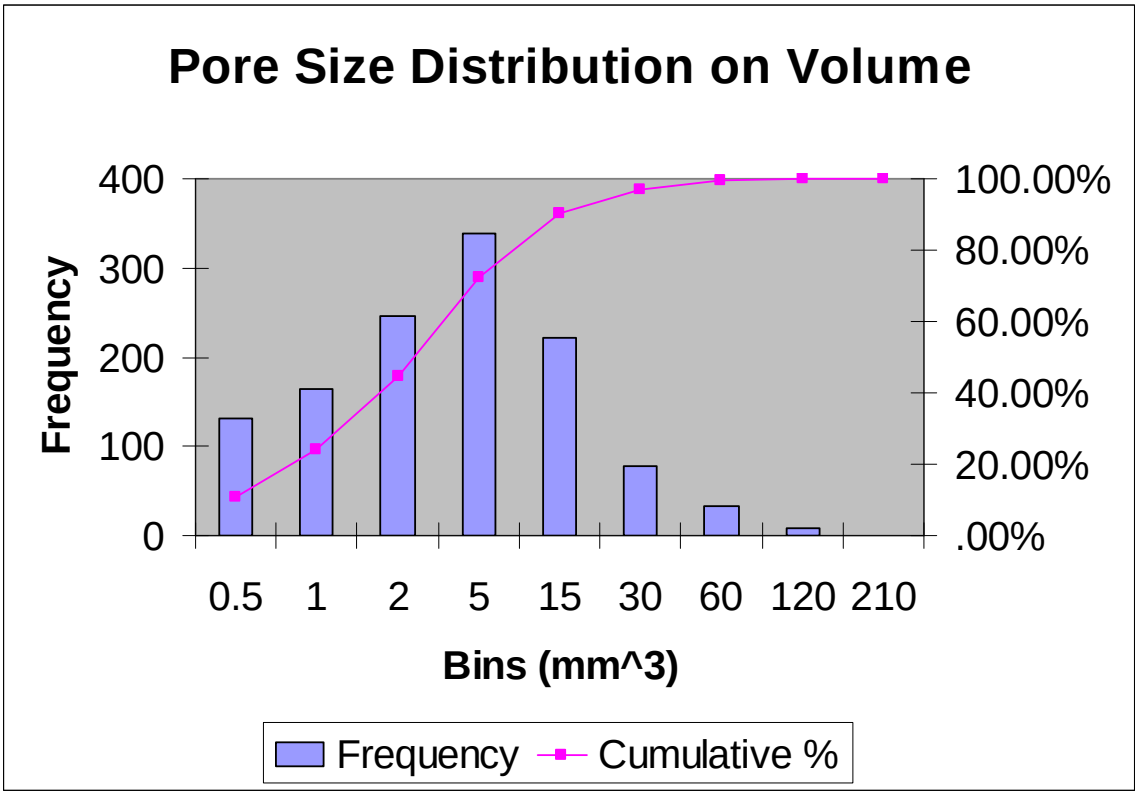

Figure 6.185 Total Histogram Plot for the Pore Size Distribution on Volume of Specimen made with 10% Fly Ash

Bins (mm)	Frequency	Cumulative %	Relative %
0.1	0	.00%	0.00%
0.5	484	21.85%	21.85%
1	976	65.91%	44.06%
1.5	457	86.55%	20.63%
2	174	94.40%	7.86%
2.5	56	96.93%	2.53%
3	42	98.83%	1.90%
6	26	100.00%	1.17%
13	0	100.00%	0.00%

Table 6.128 Total Histogram Data for the Pore Size Distribution on Diameter of Specimen made with 20% Fly Ash

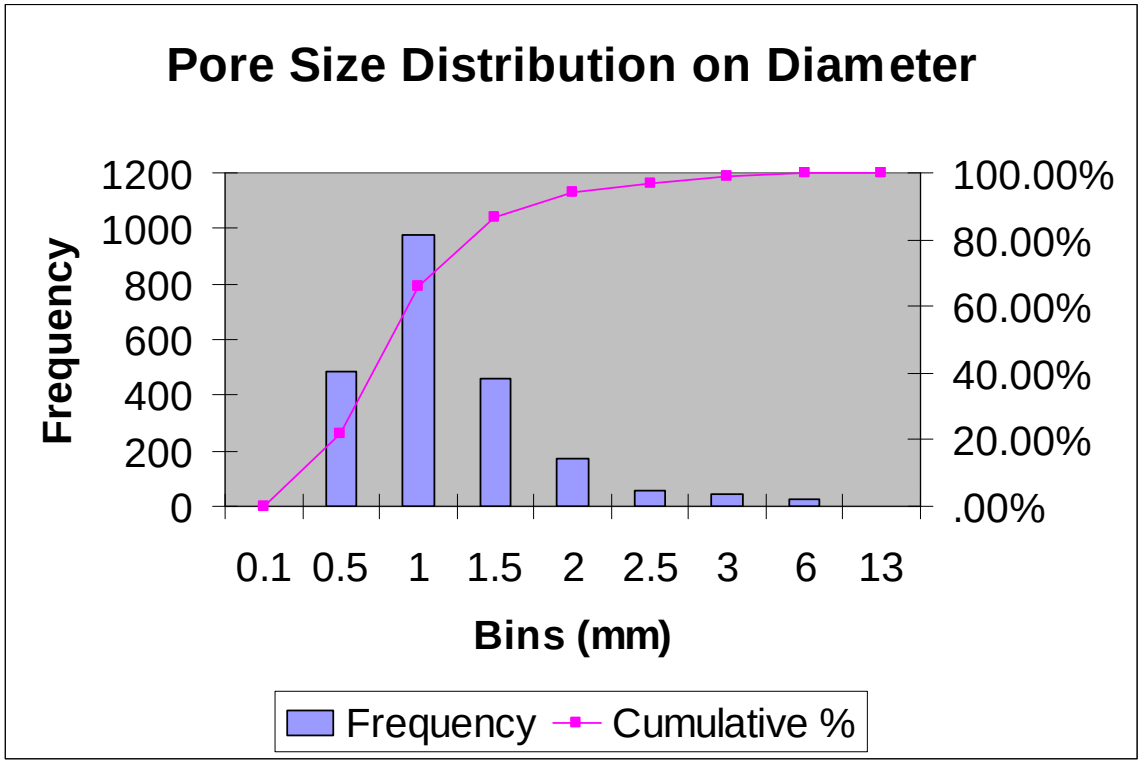

Figure 6.186 Total Histogram Plot for the Pore Size Distribution on Diameter of Specimen made with 20% Fly Ash

Bins (mm^3)	Frequency	Cumulative %	Relative %
0.5	280	12.64%	12.64%
1	348	28.35%	15.71%
2	576	54.36%	26.00%
5	590	80.99%	26.64%
15	303	94.67%	13.68%
30	90	98.74%	4.06%
60	28	100.00%	1.26%
120	0	100.00%	0.00%
210	0	100.00%	0.00%

Table 6.129 Total Histogram Data for the Pore Size Distribution on Volume of Specimen made with 20% Fly Ash

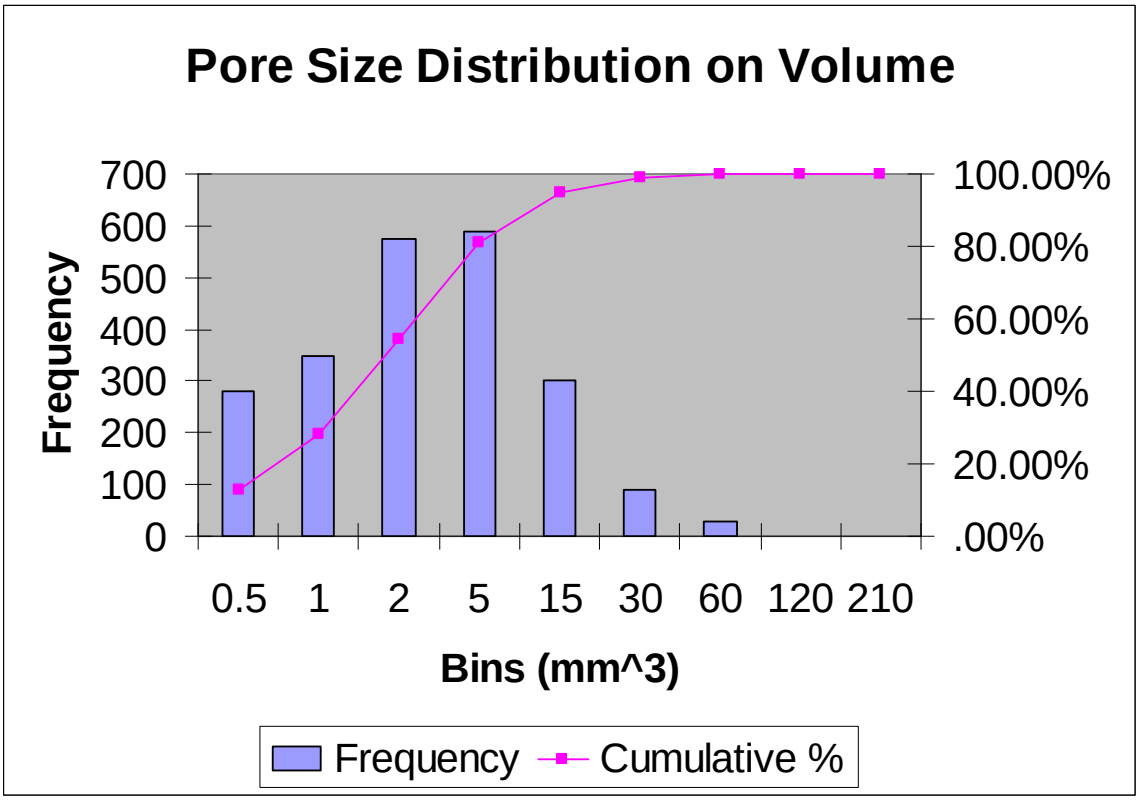

Figure 6.187 Total Histogram Plot for the Pore Size Distribution on Volume of Specimen made with 20% Fly Ash

Bins (mm)	Frequency	Cumulative %	Relative %
0.1	0	.00%	0.00%
0.5	676	27.30%	27.30%
1	1180	74.96%	47.66%
1.5	279	86.23%	11.27%
2	153	92.41%	6.18%
2.5	67	95.11%	2.71%
3	44	96.89%	1.78%
6	55	99.11%	2.22%
13	22	100.00%	0.89%

Table 6.130 Total Histogram Data for the Pore Size Distribution on Diameter of Specimen made with 30% Fly Ash

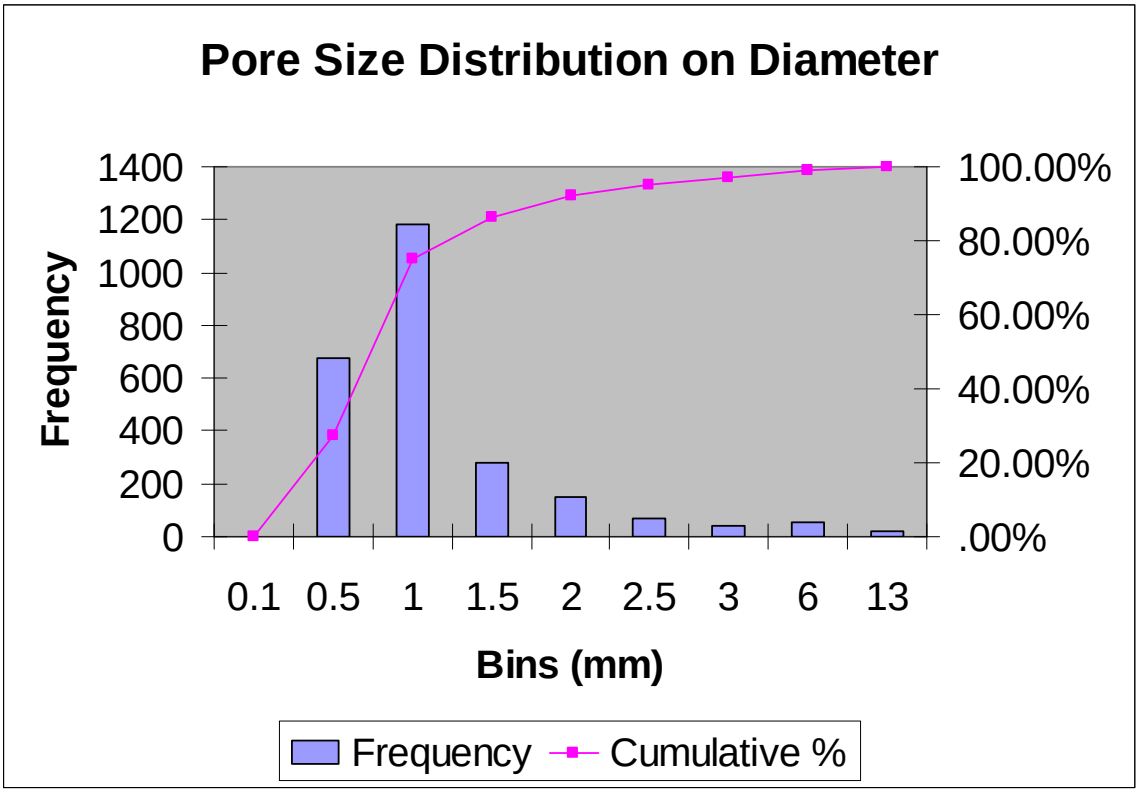

Figure 6.188 Total Histogram Plot for the Pore Size Distribution on Diameter of Specimen made with 30% Fly Ash

Bins (mm^3)	Frequency	Cumulative %	Relative %
0.5	506	20.44%	20.44%
1	413	37.12%	16.68%
2	523	58.24%	21.12%
5	539	80.01%	21.77%
15	336	93.58%	13.57%
30	101	97.66%	4.08%
60	38	99.19%	1.53%
120	19	99.96%	0.77%
210	1	100.00%	0.04%

Table 6.131 Total Histogram Data for the Pore Size Distribution on Volume of Specimen made with 30% Fly Ash

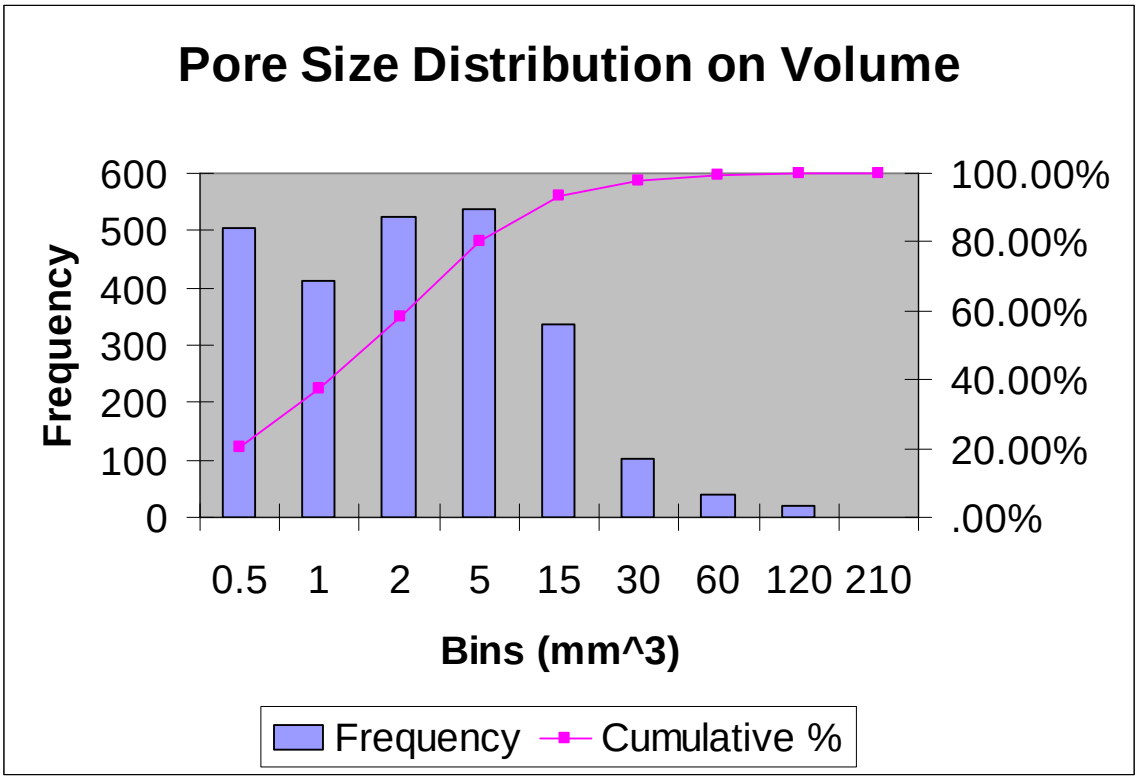

Figure 6.189 Total Histogram Plot for the Pore Size Distribution on Volume of Specimen made with 30% Fly Ash

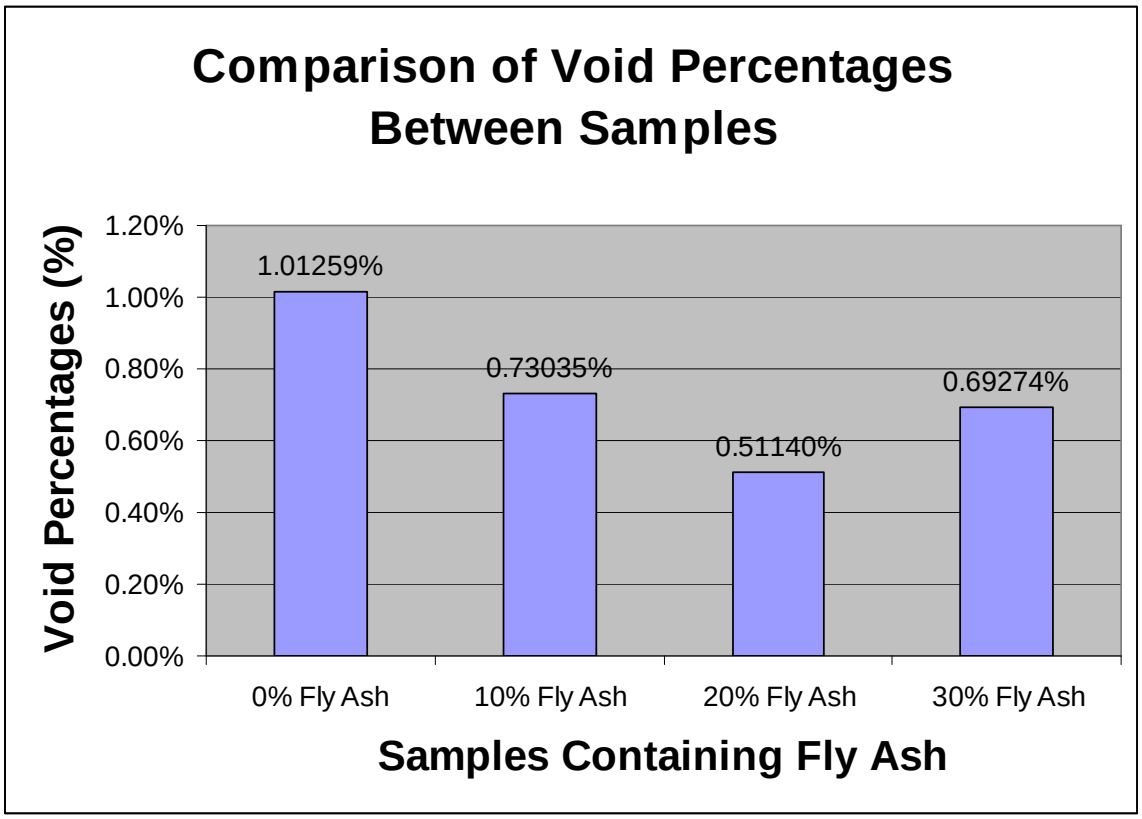

Figure 6.190 Comparison of Void Percentages Between Samples Containing 0%, 10%, 20% and 30% of Fly Ash

Bin Range	Laurel	Frederick	Medford
0.1mm - 0.5mm	29.58%	35.44%	27.69%
0.5mm - 1mm	46.95%	46.61%	47.48%
1mm - 13mm	23.74%	17.95%	24.83%

Table 6.132 Comparison of Pore Size Distribution for Samples Containing Different Sands Based on Diameter

	% Fly Ash			
Bin Range	**0**	**10**	**20**	**30**
0.1mm - 0.5mm	31.53%	24.63%	21.85%	27.30%
0.5mm - 1mm	37.33%	33.55%	44.06%	47.66%
1mm - 13mm	31.14%	41.82%	34.09%	25.04%

Table 6.133 Comparison of Pore Size Distribution for Samples Containing Different Percentage of Fly Ash Based on Diameter

CHAPTER 7

Conclusions and Recommendations

7.1 General

This experiment was aimed at utilizing the method of computed tomography to quantify and analyze concrete specimens. The specific purpose was to quantify the pore structure in concrete, and identify cracking caused by delayed ettringite formation. Computed tomography has proved to be a useful technique providing results that would not be achieved with other existing test methods. The conclusions of the experiment are summarized below:

- X-ray CT scanning was successful in capturing the interior pores of the specimens within the millimeter to micrometer range.
- Pore size distribution revealed that almost 50% of the pores for all three specimens in series one had diameters within the range of 0.5 and 1mm
- Computed tomography is capable of three dimensional analyses producing a volume unit of measurement for the pore sizes.
- The pore size distribution of an individual scan was reasonably representative of the pore size distribution of the entire specimen
- Ettringite development in concrete has influenced the pore structure and void percentage which will consequently affect the durability of the concrete
- Total Porosity for samples made with Laurel, Frederick and Medford aggregates are 1.31%, 0.56% and 0.66% respectively.
- Internal Cracking was not quantitatively determined in either the reactive aggregates or the non-reactive aggregates.

- Inclusion of Fly Ash mitigated the formation of ettringite causing an overall decrease in the void percentage of the samples as Fly Ash percentage increased.
- Pore Size distribution in series two showed that the occurrence of larger size pores (1 to 13mm) decreased as Fly Ash percent increased up to 20%.

7.2 Recommendations

1. In the CT analysis the number of scans taken per specimen should be increased to improve the accuracy of the results. This can be done by reducing the scan thickness even further.
2. Utilizing a three dimension reconstructive software which would stack up and connect all scans to obtain a visual three dimensional representation of the specimen and its pore structure.

REFERENCES

ASTM, 1993, Annual Book of ASTM Standards. Volume 04.02 concrete and aggregates. American Society for testing and Materials, Philadelphia.

Azzam, A., 2002, "Delayed Ettringite Formation, The Influence of Aggregate Types, Curing Conditions, Exposure Conditions, Alkali Content, Fly Ash, Mix Water Conditioner (MWC)," Ph. D. Dissertation, University of Maryland, College Park.

Bergeson, K. L., Schlorholtz, S. and Demirel, T., 1988, "Development of a rational Characterization Method for Iowa Fly Ash," final report, Iowa Department of Transportation Project HR-286, ERI Project 1847, ISU-ERI 86-450.

Berry, E. E. and Malhotra, V. M., 1982, "Fly Ash for Use in Concrete – A Critical Review," ACI Journal Vol. 2, No. 3, pp. 59-73

Bouge, R. H., 1955, "The Chemistry of Portland Cement," 2nd Edition, New York: Reinhold Publishing Corp.

Bouge, R. H. and Lerch, W., 1934, "Hydration of Portland Cement Compounds," Industrial and Engineering Chemistry, Vol. 26, No. 8, pp. 837-847.

Bye, G. C., 1999, "Portland Cement: Composition, Production and Properties," 2nd Edition, London: Thomas Telford.

Daerr, G. M., Punzet, M. and Ludwig, U., 1977, "On the Chemical and Thermal Stability of Ettringite," React. Aluminates Setting Cem., sum. Contrib. Semin., 42-45.

Diamond, S., 1996, "Delayed Ettringite Formation-Processes and Problems," Cement and Concrete Composites, Vol. 18, pp. 205-215.

Diamond, S. and Ong, S., 1993, "Combined Effects of Alkali Silica Reaction and Secondary Ettringite Deposition in Steam Cured Mortars," Cement Technology Symposium, American Ceramic Society PAC-Rim Conference, Honolulu, Ceramic Trans., in the press.

Diamond, S., 1983, "On the Glass Present in Low-Ca and High-Ca Fly Ash," Cement and Concrete Research, Vol. 18, pp. 205-215.

Diamond, S. and Lopez-Flores, F., 1981, "On the Distribution Between Physical and Chemical Characteristics Between Lignitic and Bituminous Fly Ashes," Symposium Proceedings on Effects of Fly Ash Incorporation in Cement and Concrete, Materials Research Society, pp. 34-44.

Diamond, S., 1976, "C/S mole ratio of C-S-H gel in a mature C_3S paste as determined by EDXA," Cement and Concrete Research, Vol. 6, No. 3, pp. 413-416.

Feldman, R. F., 1981, "Pore Structure Formation During Hydration of Fly Ash and Slag Cements Blends, Symposium Proceedings on Effects of Fly Ash Incorporation in Cement and Concrete, Materials Research Society, pp. 124-133.

Flannery, B. P., Deckman, H. W., Roberge, W. G. and D'Amico, K. L., 1987, "Three-Dimensional X-ray Microtomography," Science, Vol. 237, No. 4821, pp. 1439-1444.

Flint, E. P., and Wells, L. S., 1934, "Study of the system CaO-SiO_2-H_2O at 30° C and the reaction of water on the anhydrous calcium silicates," J. Res. Nat. Bur. Stand., Vol. 12, No. 687, pp. 751-783.

Fu, Y., Gu, P., Xie, P. and Beaudoin, J. J., 1995, "Kinetic Study of Delayed Ettringite Formation in Hydrated Portland Cement Paste," Cement and Concrete Research, Vol. 25, No. 1, pp. 63-70.

Giertz-Hedstrom, S., 1938, "The physical structure of hydrated cements," 2nd Intl. Symposium Proceedings on the Chemistry of Cement, pp. 505-534.

Glasser, F. P., 1992, "Progress in the immobilization of radioactive wastes in cement," Cement and concrete Research, Vol. 22, Nos 2/3, pp. 201-216.

Goldbeck, A. J., 1956, "Needed Research," ASTM Sp. Tech. Publ. No. 169, pp.26-34.

Gress, D., 1997, "Early Distress of Concrete Pavements," Federal Highway Administration. Publication No. FHWA-SA-97-045.

Heinz, D. and Ludwig, U., 1987, "Mechanism of Secondary Ettringite Formation in Mortars and Concretes Subjected to Heat Treatment," Concrete Durability, ACI SP 100, Vol. 2, American Concrete Institute, Farmington Hills, MI. pp. 2059-2071.

Heinz, D. and Ludwig, U., 1986, "Mechanisms of Subsequent Ettringite Formation in Mortars and Concretes after Heat Treatment," 8th Intl. Cong. Chem. Cem. Secretaria General de 8th CIQC, Rio de Janeiro, Vol. V, pp. 189-194.

Herman, G. T., 1980, "Image Reconstruction from Projections: The Fundamentals of Computerized Tomography," Academic Press, New York.

Hubbell, J. H., 1969, "Photon Cross Sections, Attenuation Coefficients, and Energy Absorption Coefficients from 10 keV to 100 GeV," National Bureau of Standards, National Standard Reference Data Series, Vol. 29.

Isenberger, K., 1981, "Report on Fly Ash Variability," Highway Division, Office of Materials, Iowa Department of Transportation.

Ketcham, A., Denison, C. and Carlson, W. D., 1997, "Three-dimensional Quantitative Textural Analysis of Metamorphic Rocks Using High-Resolution Computed X-ray Tomography: Part I. Methods and Techniques," Journal of Metamorphic Geology, Vol. 15, pp. 29-44.

Klieger, P., 1978, "Air Entraining Admixtures," ASTM, STP 169B: 787.

Landis, E. N., Nagy, E. N. and Keane, D. T., 2003, "Microstructure and Fracture in Three Dimensions," Engineering Fracture Mechanics, Vol. 70, No. 7, pp. 911-925.

Landis, E. N., Petrell, A. L., Lu, S. and Nagy, E. N., 2000, "Examination of Pore Structure Using Three-Dimensional Image Analysis of Microtomographic Data," Concrete Science and Engineering, Vol. 2, No. 8, pp. 162-169.

Lane, R. O. and Best, J. F., 1982, "Properties and Use of Fly Ash in Portland Cement Concrete," Concrete International, Vol. 4, No. 7, pp. 81-92.

Lawrence, C. D., Dalziel, J. A. and Hobbs, D. W., May 1990, "Sulphate Attack Arising from Delayed Ettringite Formation, Interim Technical note, 12, British Cement Association, Wexham Springs, Slough, U.K.

Lea, F. M., 1956, "The Chemistry of Cement and Concrete," Revised Edition of Lea, F. M. and Desch, C. H., New York: St. Martin's Press Inc.

Lee, C., 1989, "Active Alkalis in Cement Fly Ash Paste," 8th Intl. Conference Proceedings on Alkali-Aggregate Reaction, Kyoto, pp. 223-228.

Lee, C., Schlorholtz, S. and Demirel, T., 1986, "Available Alkalies in Fly Ash," MRS Symposium Proceedings, Vol. 65, Materials Research Society, Pittsburgh, pp. 125-130

McCullough, E. C., 1975, "Photon Attenuation in Computed Tomography," Medical Physics, Vol. 2. pp. 307-320.

Media Cybernetics, 1993, "Image-Pro Plus Start-Up Guide For Windows," Media Cybernetics, Inc., Silver Spring, Maryland.

Mehta, P. K., 1983, "Pozzolanic and Cementitious Byproducts as Mineral Admixtures for Concrete – A Critical Review," Intl. Proceedings on the Use of Fly Ash, Slags and Silica Fume in Concrete, Montebello, Canada ACI/SP-79.

Mindess, S., Young, J. F., Bentur, A., Gray, R. J., 1998, "The Science and Technology of Civil Engineering Materials," 1st Edition, Prentice Hall Inc.

Neville, A. M., 1996, "Properties of Concrete," 4th Edition, New York: John Wiley and Sons Inc.

Pettifer, K. and Nixon, P. J., 1980, "Alkali Metal Sulphate-A factor Common to Both Alkali Aggregate Reaction and Sulphate Attack on Concrete," Cement, Concrete Research, Vol. 10, pp. 173-181.

Powers, T. C., 1958, "Structure and physical properties of hardened Portland cement paste, " Journal of the American Ceramic Society, Vol. 41, No. 1, pp. 1-6.

Powers, T. C., May 1949, "The non-evaporable water content of hydrated cements," Proc. ASTM, Bul. No. 158, pp. 68-76.

Ramachandran, V. S., 1984, "Concrete Admixtures Handbook: Properties, Science and Technology," 1st Edition, Noyes Publications.

Ronne, M. and Hammer, T. A., Dec. 1999, "Delayed Ettringite Formation (DEF) in Structural Lightweight Aggregate Concrete: Effect of Curing Temperature, Moisture, and Silica Fume Content," Cement, Concrete and Aggregates. CCAGDP, Vol. 21, No. 2, pp. 202-211.

Schlorholtz, S. and Bergeson, K. L., 1993, "Evaluation of the Chemical Durability of Iowa Fly Ash Concrete," final report, Iowa Department of Transportation project HR-327, ERI project 3295, ISU-ERI Ames 93-411.

Shayan, A. and Ivanusec, I., 1996, "An Experimental Clarification of the Association of Delayed Ettringite Formation with Alkali Aggregate Reaction," Cem. Concr. Comp., Vol. 18, pp. 161-171.

Steinour, H. H., 1952, "The reactions and thermochemistry of cement hydration at ordinary temperature," 3rd Intl. Symposium Proceedings on the Chemistry of Cement, pp. 261-89.

Taylor, H. F. W., 1989, "Modification of the Bogue calculation," Advances in Cement Research, Vol. 2, No. 6, pp. 73-79.

Tepponen, P. and Eriksson, B. E., 1987, "Damages in Concrete Railway Sleepers in Finland," Nordic Concrete Research, Vol. 6, pp. 199-209.

Tikalsky, P. J., 1989, "The Effect of Fly Ash on the Sulfate Resistance of Concrete," Ph.D. Dissertation, University of Texas at Austin.

Tishmack, J. K., Olek, J. and Diamond, S., 1999, "Characterization of High-Calcium Fly Ashes and Their Potential Influences on Ettringite Formation in Cementitious Systems," Cement, Concrete and Aggregates, CCAGDP. Vol. 21, No. 1, June, pp. 82-92.

Wellington, S. L. and Vinegar, H. J., 1987, "X-ray Computerized Tomography," Journal of Petroleum Technology, August, pp. 885-898.

Worall, W. E., 1986, "Clays and Ceramic Raw Materials," 2nd Edition, Elsevier Applied Science Publishers Ltd.

Young, J. F., Mindess, S. and Darwin, D., 2002, "Concrete," 2nd Edition, Prentice Hall Inc.

Young, J.F. and Mindess, S., 1981, "Concrete," 1st Edition, Prentice Hall Inc.